THE EFFECT OF PHYSICAL PARAMETERS ON THE RUPTURE OF BUBBLE FILMS IN TWO-PHASE FOAMS

BY

WYNAND ANDRÉ VAN DYK

Dissertation submitted in partial fulfilment of the requirements for the degree of Doctor of Philosophy in Engineering (Metallurgical Engineering) in the Department of Chemical Engineering at the University of Stellenbosch

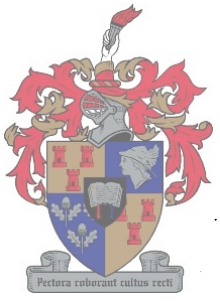

Promoters: Prof. L. Lorenzen
Prof. J.S.J. van Deventer

November 1999

DECLARATION

I hereby declare that, unless otherwise indicated, all the work in this dissertation was done by myself and that this dissertation has not been submitted to this, or any other institution of learning, in support of an application for any degree or qualification.

W.A. van Dyk
November 1999

ABSTRACT

The effects of various physical parameters on the rupture of bubble films in two-phase foams were investigated in order to develop a better understanding of the behaviour of coarse particles in the froth phase of a novel flotation cell. This novel flotation technique is based on the fact that coarse particles, if they are selectively rendered hydrophobic by conditioning, would act as bubble film breakers. If the feed was introduced onto the surface of the froth, such particles would settle through the froth under gravity to be recovered as an underflow (concentrate) product, while the gangue would be supported by the bubble films and be recovered as a float (tailings) product.

The efficiency of this technique – reverse froth flotation - depends on the interaction between various characteristics of particles and the froth. In order to simulate the experimentally observed trends, and hence investigate the various mechanisms qualitatively, a fundamental model of these interactions was developed. Various particle properties were taken into account, including surface properties, shape, size and density. To account for the changing nature of the froth at different positions in the cell, the model predicts the trajectory of a particle over discrete time events. This was accomplished by calculating bubble flow streamlines and modelling the bubble size, thickness of bubble films, air hold-up and bubble velocity at any point on the streamline.

The experimental results showed that the behaviour of particles (within the size range tested) in the froth phase of the cell is primarily dependent on the mass of a particle. In general, the higher the mass, the steeper the trajectory of the particle in the froth, i.e. an increase in particle mass results in an increased recovery to the concentrate. The contact angle on the particle surface has only a secondary influence on the overall particle trajectory, in that an increase in the equilibrium contact angle will result in an increased recovery. However, the particle contact angle has very little influence on the behaviour of large, high-density particles, as well as small, low-density particles.

Particles will therefore only separate on the basis of contact angle as long as their mass is between an upper and lower critical value. Any particle with a mass greater that the critical value will fall through the froth irrespective of the contact angle. Similarly, the upward force component acting on a particle with mass less than the lower critical value will dominate the force balance. The particle will therefore remain supported by the froth, irrespective of the particle contact angle and bubble film rupture time. For particles within these mass limits, the effect of the contact angle increases with a decreased mass.

It was further concluded that these mass limits are dependent on the operating conditions of the cell as well as the particle shape. The particle shape influences the mass to cross-sectional surface area ratio (M/A_0). Where particles therefore have the same mass, the M/A_0 ratio would govern the particle trajectory. The higher the M/A_0 ratio, the more particles would be recovered to the concentrate, while a decrease in the M/A_0 ratio would result in flatter particle trajectories in the froth, thereby increasing the probability of a particle reporting to the tailings. The model provided a unique understanding of the interrelationship between the various parameters which would not have been gained to the same extent by alternative modelling methods.

Two potential industrial applications for the reverse froth flotation process were evaluated. As a coarse particle flotation technique for sulphide bearing ores, it was found that Xanthate pre-conditioning of the ore results in concentrating the sulphur bearing particles to the concentrate. By increasing the Xanthate addition, the relative % mass recovery as well as % sulphur recovery increases. This increase in mass and sulphur recovery, however, is not linear. The greatest concentration effect was obtained by the initial Xanthate addition. An economically optimum Xanthate addition point therefore exists. These results were very promising in terms of finding a coarse particle flotation technique for the pre-concentration of sulphide bearing minerals. However, it is recognised that several potential problems might exist with the technique.

The results further indicated that the reverse froth flotation process is not suitable for the replacement of grease belts for fine (-3 mm) diamond recovery. The major concern is the high potential losses of valuable material to the tailings. These losses are mainly due to the fact that the major separation process in the reverse froth flotation cell is based on particle mass. The surface properties of the particle account only for a secondary separation process.

ACKNOWLEDGEMENTS

The author would like to express his sincere thanks and gratitude to the following people and organisations:

- My promoters, Prof. J.S.J. van Deventer and Prof. L. Lorenzen, for their continued support, valuable suggestions, hours of discussion and invaluable motivation when I needed it most.

- De Beers Industrial Diamond Division for sponsoring the initial project. The financial assistance and permission to convert to a PhD are greatly appreciated.

- Anglo American Corporation for sponsoring the latter parts of the project.

- Dr V.E. Ross for his brilliant ideas, the fruit of a lateral thinking mind.

- HATCH Africa for allowing me to complete this dissertation during a period of study leave. The time is greatly appreciated.

- My wife, parents and friends for their encouragement, motivation and understanding during this time. For the opportunities that you gave me, I will always be grateful.

DEDICATION

To Marie, for her love, understanding, encouragement and friendship…

TABLE OF CONTENTS

List of Figures

List of Tables

1. INTRODUCTION

The earliest possible recovery of valuable material from a mineral processing circuit could have numerous advantages, such as preventing over-grinding of minerals, reducing flotation time and increasing the recovery of valuable minerals. The decrease in size of the later stages of the circuit will moreover reduce the capital and working cost of the process, while the energy efficiency of the overall process will improve.

Although various coarse particle separation techniques exist (i.e. screening, cycloning, magnetic separation, etc.) these techniques are only effective if an adequate difference in size, density or magnetic susceptibility of the particles exists. Should it be impossible for conventional separation techniques to differentiate on these basic physical properties, the process operator/designer must revert to separation techniques based on other physical properties, such as particle wettability. Grease belts are such a recovery technique, currently being used at several diamond mines throughout the world in the final recovery process. Although a workhorse of the industry for several decades, grease belts suffer from a large degree of messiness, while "black magic" plays an important part in its successful operation. The substitution of such cumbersome recovery techniques by efficient low cost technology would offer substantial financial benefits to any mining company.

In the view of above, Ross[1] developed a novel flotation technique for the recovery of fine diamonds (-3+1mm) from gravel by reverse flotation in the froth phase of a pneumatic type of flotation cell. Although the technique was originally intended to solve the grease belt problem for fine diamond recovery, various applications were found through the work of several researchers that ventured into the field of early valuable mineral recovery.

The majority of flotation research and development has, up to date, been focused on the recovery of relatively fine particles (-500 micron), leaving the flotation fraternity with techniques and processes that are skewed in its operating size range. In the conventional coal preparation process the minus 500 micron particles are normally recovered by flotation, however, particles up to 2mm may be present due to poor upstream screening and classification. These large particles are difficult to recover with conventional techniques leading to studies that were aimed at the use of alternative flotation reagents to improve the yield of coarse coal particles (Moxon & Keast-Jones[2], Moxon, Keast-Jones & Aston[3]). Although some degree of success was achieved this size fraction still accounted for the largest losses during coal preparation.

A system was proposed by Lloyd[4] in which gold and other valuable minerals could be concentrated underground by coarse milling and flotation. A model of the process, however, indicated that the flotation step would be able to recover only 75 percent of the valuable minerals due to the large losses in the coarser particle sizes.

Schubert[5] investigated the development of an impeller type and impeller-stator flotation system that would recover coarse particles in the treatment of quartz sands and sylvanite. The aim of the research was to suspend coarse particles in the pulp phase without having to agitate the pulp phase to such an extent that would impose unnecessary turbulent stresses on the bubble-particle aggregates. The design resulted in lower power consumption, but although it appeared successful for particles up to 400 micron, difficulties were encountered at the coarser size ranges.

These investigations have shown that a need exists for a coarse particle separation technique based on particle wettability, with low operating costs, such as power consumption and inexpensive flotation reagents. The reverse froth flotation technique satisfies this need and is based on the fact that coarse particles, if they are selectively rendered hydrophobic by conditioning, would act as bubble film breakers if the feed is introduced on the surface of the froth. Such particles would settle through the froth under gravity to be recovered as an underflow (concentrate) product, while the gangue would be supported by the bubble films and therefore be recovered as a float (tailings) product. This process differs from conventional reverse flotation (in which the valuable mineral is depressed in the pulp phase) in that the separation is effected in the froth phase only. It could therefore be called "reverse froth flotation".

The efficiency of the technique depends on the interrelation between various particle and froth characteristics. Decisive parameters of the particles in the feed include density, shape, surface characteristics (wettability and roughness) and size. The bubble size, residence time of the bubbles in the flotation cell, and rigidity and thickness of the bubble films, are important froth characteristics. In order to improve and optimise the process, a more fundamental understanding of the principles involved and interaction of parameters is required. Various key questions relating to the technique were therefore considered during the project:

- What is the required relationship between the characteristics of the particles (wettability, etc.) and those of the froth (bubble film thickness, etc.) to ensure reverse froth flotation of particles under a particular set of operating conditions?
- Do particles separate on the basis of density if they have similar surface properties; if so, to what extent?
- What is the effect of shape, orientation and/or surface irregularities on the flotation of coarse particles?
- Would it be possible to develop a simulation model capable of qualitatively describing the observed experimental trends, and hence be used to investigate variables in isolation, which is not always possible in experimental work?

This introduction provides a brief background to the need in the metallurgical industry for a coarse particle separation technique that incorporates the degree of wettability of the particles. The aim of this dissertation is to investigate the effects of various physical parameters on the rupture of bubble films in two-phase foams, in order to develop a better understanding of the behaviour of coarse particles in the froth phase of the novel flotation cell.

2. LITERATURE SURVEY

Chapter 1 outlined the background as to why the new flotation technique was developed. However, it does not provide an overview of the published work of previous researchers that provided the impetus for the development. This literature survey therefore commences with a general overview of the flotation process, together with an overview of research into the influence of particle size on the flotation process and the rupture of bubble films by coarse particles. The concept of particle wettability and various associated measurement techniques are then discussed. The chapter closes with a discussion on how each of these research fields contributed to the subsequent development of the flotation cell.

2.1 General Flotation Overview

2.1.1 Definition

Flotation is a mineral separation (or concentration) process based on the interfacial chemistry of mineral particles in a solution (or pulp). In basic terms, it can be described as the process, whereby valuable mineral particles are separated from waste (also called gangue), by contacting the particles with air bubbles in an agitated vessel. Particles with a resistance to wetting of the liquid phase (hydrophobic particles) will attach to the bubble surfaces, and float to the surface of the agitated vessel where it can be removed as a concentrate. Particles that are easily wetted by the liquid phase (hydrophilic particles), however, will not form a strong enough bond with the bubble surface, allowing it to be removed as a discard from the bottom discharge of the vessel. The process is therefore dependent on the difference in surface characteristics (or wettability) of the particles, which is usually enhanced by conditioning the particles prior to flotation with chemical reagents.

2.1.2 History

Although the first commercial application of the flotation process was early in the 20th century at Broken Hill in Australia[6] it was already anticipated in a 19th century patent to Haynes[6]. In the 25 years following this first application, tremendous strides were made in both equipment development and the chemistry of the flotation process. According to Fowkes[7], Taggart listed nearly a thousand patents covering the application of different reagents and processes, together with 170 patents on machine development. These early patents on the application of various chemicals and processes have laid the foundation to the modern flotation practice. However, equipment development has continuously evolved to the point where today's modern flotation machines have only penetrated the market in the last two decades.

Today, due to the international trend towards the treatment of lower-grade and more finely disseminated ores, flotation is clearly the dominant mineral concentration method. It is used for the primary concentration of virtually all sulphide minerals together with all platinum group metals. In addition, it is used in a wide range of non-sulphide metallic minerals; coal and industrial minerals. This is mainly due to

the process being relatively selective in the separation and concentration of minerals in complex ores. In addition, it has a broad applicability with respect to particle size and can be effectively applied from 400 μm to below 10 μm[8]. Finally, the flotation process has virtually no limitations in separating minerals. With other separation processes (gravity, magnetic, etc.) the process is restricted to certain mineral combinations. However, the wide range of reagents and surface chemical differences among minerals can be utilised effectively in flotation.

Due to the wide range of commercially available flotation reagents, as well as the virtually unlimited number of mineral combinations and permutations in nature, flotation is one of the most published research areas in the field of mineral processing. It would therefore not only be impractical, but also irrelevant to provide a literature review of all the flotation research fields. This dissertation, however, focuses on the dynamic behaviour of coarse particles in the froth phase of the reverse froth flotation cell. It is therefore relevant to review the work of a number of researchers into the influence of particle size (especially coarse particles) on the flotation process, as well as the rupture of bubble films by coarse particles.

2.2 The Influence of Particle Size on the Flotation Process

As early as 1931, Gaudin, Groh and Henderson[9] published the first significant work on the effects of particle size on the flotation process. In the fifty years that followed this ground-breaking paper (up to 1981), various authors published a huge amount of operational and experimental data describing the influence of particle size on the flotation process[8]. Unfortunately, this left the flotation fraternity with the formidable task of sifting through large volumes of data in order to resolve some of the uncertainties associated with this field of study. It was not until 1981 that Trahar[8] compiled a selection of data into a single, comprehensive paper that identified the essential effects of particle size for which reliable experimental evidence existed.

Most of the data presented by Trahar[8] is in the form of recovery by size curves (see Figure 2-1) where the recovery of a particular particle size fraction is plotted against the average particle size in such a fraction. Trahar showed that such recovery-size curves have a characteristic shape and can be divided into three arbitrary regions:

- ***Fine region:*** This region comprises particles below 10 μm and is usually difficult to float, as well as to achieve selective separation.
- ***Intermediate region:*** Particles in this region are usually easy to float with high degrees of selectivity. The typical size range for this region is from about 10 μm to 70 μm.
- ***Coarse region:*** Effective flotation in this region may vary significantly depending on the flotation conditions present. Typically this region encompasses particles from about 70 μm in size to an ill-defined upper limit (up to 400 μm in certain cases).

Since the boundaries between these regions are typically very vague, it has become customary for the flotation community to refer to fine, intermediate and coarse particle behaviour, rather than to a specific particle size range.

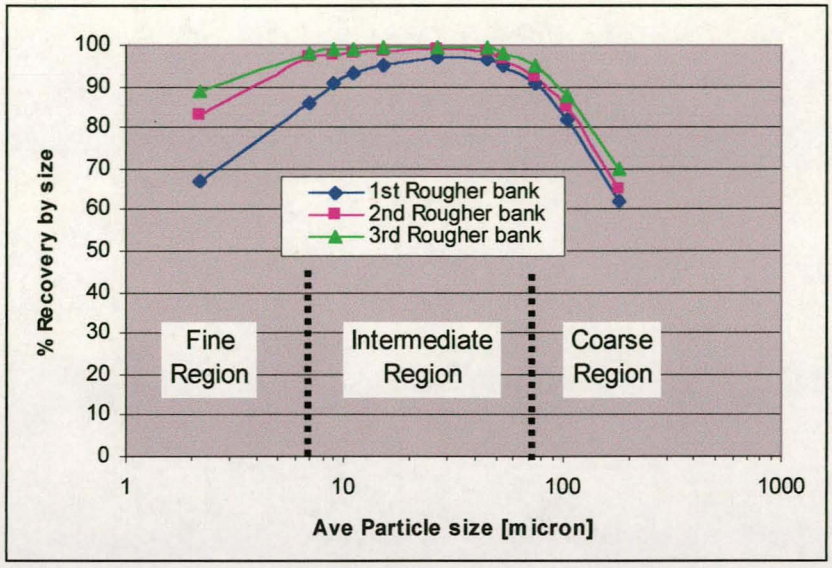

Figure 2-1: Typical cumulative recovery by size profiles with increasing flotation residence time (from Trahar[8]).

Since this dissertation focuses on the behaviour of coarse particles in the new flotation cell, only general comments on the behaviour of fine and intermediate particles in the flotation process will suffice. Trahar[8] concluded that the behaviour of fine particles can be attributed to two factors, namely:

1. A slow true flotation rate, primarily due to a decrease in the probability of collision between particles and air bubbles as the particle size is reduced, and
2. entrainment, which is the major contributor to the recovery of fine particles.

This entrainment of both floatable and non-floatable minerals, coupled with the low rate of true flotation, accounts for the poor selectivity usually associated with fine particle flotation (Li, Hoberg & Schneider[10]). In addition, it also explains the typical poor response to an increase in collector dosage for fine particle flotation (Dobby & Finch[11]), as shown in Figure 2-2. Although a substantial increase in fine particle recovery is typically observed on initial collector addition, usually no further improvement results with increasing collector additions due to the entrainment mechanism dominating the overall recovery process.

Conversely, the principal mechanism for the recovery of intermediate particles is by true flotation (Trahar[8]), with the entrainment mechanism in general, contributing towards the overall recovery in the smaller particle sizes. Typically, particles in this size range do not pose a problem in obtaining very good recoveries at very high grades. It therefore does not warrant any further discussion, other than to mention that the upper boundary of the size range is usually vague and depends on the mineral system and chemical environment present.

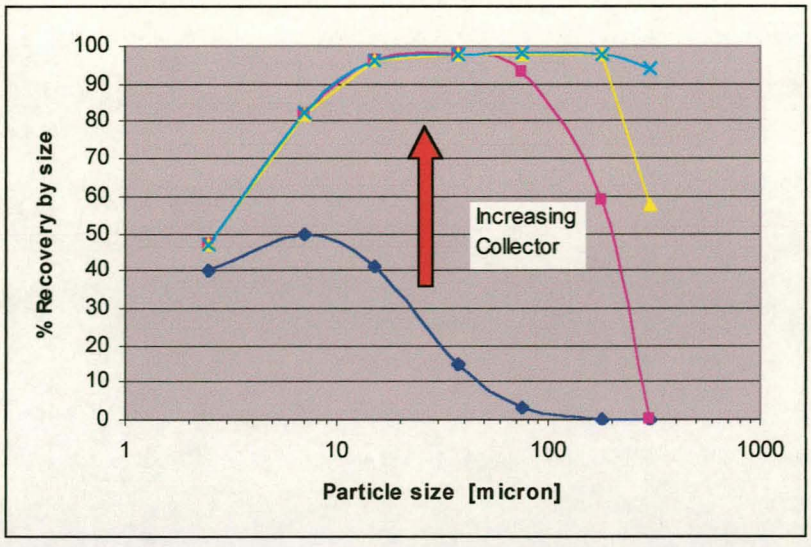

Figure 2-2: Influence of increased collector addition on recovery by size profiles (from Trahar[8]).

From the above discussion it is evident that the flotation behaviour of particles in the fine and intermediate size ranges is predominantly dependent on the interaction between true flotation response and entrainment. However, due to the mass of coarse particles, the recovery of these particles is predominantly attributed to true flotation with a negligible contribution from entrainment[8]. Dobby and Finch[11] were capable of predicting the shape of typical recovery-size curves (Figure 2-1 and 2-2) by applying their collection efficiency model.

According to Dobby and Finch[11] the collection efficiency (E_k) is the product of the collision efficiency (E_c) and the attachment efficiency (E_a) and is directly proportional to the flotation rate constant. Their model does not consider detachment, but they showed that the poor recovery of intermediate and coarse particles could be sufficiently described without the detachment component in the model. They further argue that with an increase in particle size, the collision efficiency (E_c) increases while the attachment efficiency (E_a) decreases. In addition, at a given induction time, or hydrophobicity, the attachment efficiency (E_a) increases with decreasing particle size. This trend in E_a coupled with E_c predicts the typical recovery-size curves observed in flotation concentrators (Trahar[8]).

Figure 2-2 above shows one such typical trend of the effect of increased collector dosage on the recovery of coarse particles. As the collector dosage increases, the recovery of coarse particles increases. Two mechanisms (Trahar[8]) have been proposed to account for this behaviour of coarse particles, namely:

1. As the particle size increases, the degree of hydrophobicity required to achieve a high flotation recovery increases (i.e. the required collector dosage increases).
2. Fine particles consume collector at a more rapid rate than coarse particles, leading to the surface coverage of coarse particles being proportionally less than that of fine particles and the subsequent decrease in flotation response.

Trahar[8] investigated each of these mechanisms based on published data and stated that:
"...the evidence is in favour of the first postulate, i.e. that the degree of hydrophobicity required for maximum floatability increase with particle size. In a range of sizes, no single collector addition will be appropriate for all sizes and the most efficient compromise will depend on the size distribution of the important minerals. Insufficient evidence exist to support the view that fine particles consume reagent disproportionately to surface area..."

Furthermore he concluded that:
"...there is a qualitative but a clear and fundamental relationship between the degree of hydrophobicity necessary to effect flotation and the particle size."

Crawford and Ralston[12] therefore set out to establish a quantitative link between particle size, hydrophobicity and its influence on the overall flotation recovery, and proved the existence of a flotation domain (see Figure 2-3).

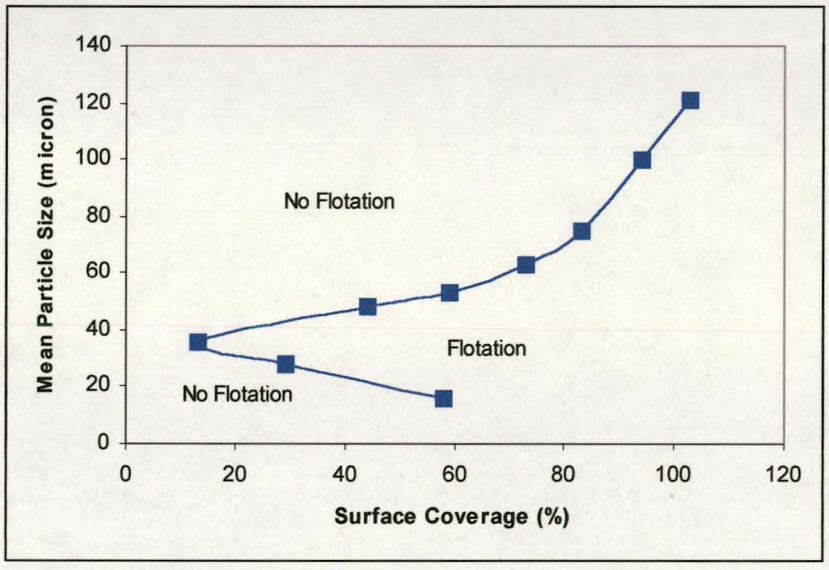

Figure 2-3: Particle surface coverage as a function of particle size showing the existence of a flotation domain (from Crawford & Ralston[12]).

Crawford and Ralston[12] conducted their experiments in a modified Hallimond tube with a model system where the surface of quartz particles were tailored to known surface coverages by a methylation reaction with trimethylchlorosilane. Since they found that the percentage surface coverage and contact angle may be readily correlated, Figure 2-3 shows a quantitative link between particle size, hydrophobicity and its influence on the overall flotation recovery. At this stage it must also be noted that the flotation domain shown in Figure 2-3 is not a universal one, and will alter as the physical and chemical conditions of the system change[12].

Nonetheless, the existence of a flotation domain is of practical importance. A typical milling circuit would produce a distribution of particle sizes of say between 5 μm and 120 μm. In order to minimise operating cost, many flotation concentrators run at the lowest possible collector dosage rates. At these collector dosage rates, the valuable particles should all adsorb the same collector concentrations per unit area, and thereby have the same contact angle or hydrophobicity. Should the flotation domain of Figure 2-3 be valid and the surface coverage of particles be in the region of 40%, only particles between 20 μm and 50 μm would readily float, whilst coarser and finer particles would consume collector and will not float. This therefore suggests that split conditioning and the separate treatment of fine, intermediate and coarse particles would be desirable.

2.3 The Rupture of Bubble Films by Coarse Particles

Based on the work of Trahar[8] and Crawford and Ralston[12] it is clear that as the particle size increases, the degree of hydrophobicity required to achieve a high flotation recovery increases. This is mainly due to the interaction of bubbles and particles and the associated efficiencies of collision and attachment in the pulp phase (i.e. below the pulp-froth interface). However, the separation in the reverse froth flotation cell takes place in the froth phase alone. It is therefore necessary to review previous work done on the interaction between coarse particles and bubble films.

When a gas bubble in a liquid approaches the surface of that liquid, or another bubble in that liquid, a liquid film is formed. It could therefore follow that the stability of the resulting froth will be related to the stability of such films. However, throughout the literature it is found that flotation froth stability depends more on the amount and properties of solids it may contain than on the properties of these films.

The instability of flotation froths and liquid lamella in the presence of hydrophobic particles have been studied extensively. Livshitz and Dudenkov[13] showed that froth instability was not due to a reduction in aqueous surfactant concentration as initially proposed, but rather associated with the presence of hydrophobic particles. Following this work, Garrett[14] proposed that spontaneous dewetting of a particle that has protruded both air-liquid interfaces (bridged the liquid lamella) will form a hole in the lamella leading to film rupture.

This theory was verified by Dippenaar[15] in a study on the interaction of a solid with a thin liquid film using high speed cinematography. He found that moderately hydrophobic particles can be transformed into very effective film-breakers if they are coated with a reagent that produces a static contact angle of more than 90° on the solid.

It is geometrically impossible that two contact angles, both larger than 90°, can exist on the same point on a solid surface. The instantaneous contact angle formed at the newly developed three-phase boundary is therefore much smaller than the equilibrium contact

angle[1] when such a particle is introduced into a lamellar froth (where the particle bridges the liquid films). The movement of the three-phase boundary over the particle to attain an equilibrium contact angle causes the bubble film to thin and rupture when a critical bubble film thickness is reached. This would result in a localised destabilisation of the froth resulting in the settling of such particles through the froth. It was also found that the migration of the two three-phase boundaries to the same discontinuity on the particle, for example a particle with an irregular surface texture, could rupture the bubble films even if the static contact angle is less than 90°. This process of bubble film thinning and rupture occurs in a few milli-seconds, and could be applied in the selective recovery of highly hydrophobic particles if the right froth and operating conditions are maintained.

Dippenaar[16] further found that for particles smaller than 400 μm the natural thinning of the liquid films will be the rate determining step during the film rupture process. However, for particles larger that 400 μm the time of interaction between the particle and the liquid film becomes the rate-determining step. Although not proven it was proposed that this might be due to the very rapid thinning of the relatively thick films that can support these particles.

Hemmings[17] postulated a protruding particle theory to explain the effect of hydrophobic particles with diameters greater than the thickness of the supporting liquid films on flotation froth stability. The basis of this theory is a quantification of the tensile and compressive stresses caused by particles protruding through the liquid films of bubbles. Figure 2-4(a) gives a schematic representation of a spherical particle protruding through both sides of a bubble film. Interfacial forces will tend to cause the particle to protrude further into the gas phase on each side of the film if

$$\cos\theta < \frac{T}{d_p} < \cos\frac{\theta}{2} \qquad \textbf{Equation 2-1}$$

where θ is the contact angle, T is the bubble film thickness in μm and d_p is the effective diameter of the particle in μm. The equal and opposite reaction to this interfacial force is a destructive compressive stress that promotes film thinning and is therefore a latent cause of froth instability. Interfacial forces tend to cause a particle to immerse itself in the liquid on both sides of the film if

$$0 < \frac{T}{d_p} < \cos\theta \qquad \textbf{Equation 2-2}$$

The equal and opposite reaction to this is a supportive tensile stress that tends to prevent film thinning. From equations (2-1) and (2-2) it is obvious that no region of supportive tensile stress exists if θ > 90°, which means that a large particle with a contact angle of more than 90° will cause bubble film thinning and rupture.

[1] Contact angles are static or dynamic depending on whether the liquid-solid-air boundary is stationary or moving during the measurement. When the system has come to equilibrium the liquid-solid-air boundary has stopped moving and the contact angle, θ, is said to reach its equilibrium value.

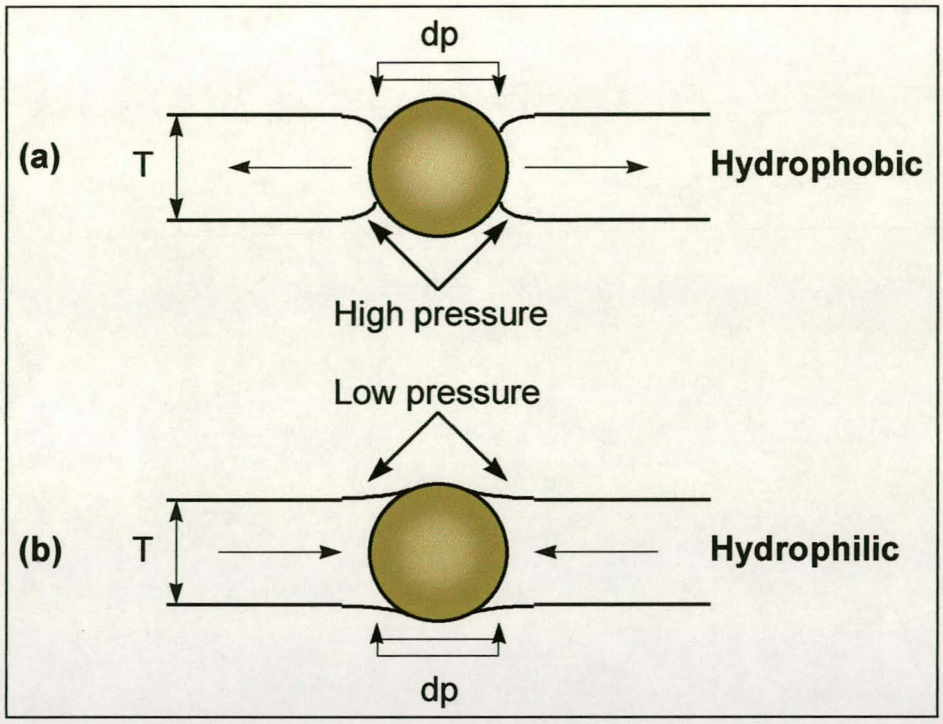

Figure 2-4: Spherical particle protruding through both sides of a bubble film and the capillary pressure-driven mechanism of bubble film rupture.

Frye and Berg[18] proposed a mechanism for particle-induced film rupture and performed a hydrodynamic analysis to determine criteria for effective antifoam action by solid particles. They assumed that the mechanism that causes bubble film thinning or stabilisation is driven by capillary pressure. As shown Figure 2-4, a coarse particle will bridge the film upon entering the froth, and curvature of the air-water interface will occur in order to satisfy the contact angle requirements at both interfaces. This curvature will result in local pressure variations, the magnitude of which is determined by the Young-Laplace equation:

$$\Delta P_c = \pm\sigma\left(\frac{1}{R_1} + \frac{1}{R_2}\right) \qquad \textbf{Equation 2-3}$$

where ΔP_c is the capillary pressure drop across the interface [N/m²], σ is the surface tension [N/m] and R_1 and R_2 are the principal radii of curvature of the surface [m]. The radius and the direction of the curvature determine the magnitude of the local pressure variations in the bubble film. ΔP_c would be positive should the curvature be convex going from the liquid to the solid phase. As shown in Figure 2-4(a), contact angles greater than 90° will result in a higher pressure adjacent to the particle than far from the particle (Frye & Berg[18]). This high pressure will cause a flow of liquid away from the particle, resulting in bubble film thinning and breakage. As the contact angle approaches 90°, the radius of curvature increases and the flow of liquid away from the particle decrease. The interface curvature will become concave if the contact angle is less than 90° (Figure 2-4(b)), resulting in a low-pressure region adjacent to the particle. Liquid will be pushed towards the particle followed by a film stabilising effect as the particle immerses itself in the film.

2.4 Particle Wettability and Contact Angle

Various references are made to particle wettability (or hydrophobicity) and contact angle in the previous sections. Since particle wettability is an important parameter in determining the probability and time of bubble film rupture in two-phase foams, it would therefore be appropriate to discuss these concepts in slightly more detail.

2.4.1 Background

As far back as 1930, Taggart et al[19] established that the contact angle is an important measure of floatability. This concept of wettability and contact angle is an integral part of the above mentioned theories on bubble film thinning and rupture as well. Rudimentary spoken, a solid surface can be seen as wettable when, on withdrawing the solid from a liquid, an unbroken film of liquid persists on the surface (Adamson[20]). On the other hand, separate droplets appear on the surface of the solid when the solid is said to be non-wettable. However, rough and heterogeneous surfaces are well known to exhibit hysteresis of the wetting phenomena and measured contact angle (Neumann and Good[21]). Therefore, separate droplets may form when the surface is dry, while a liquid film, absorbing any droplets placed on the surface, may be resident after immersion. A quantitative measure of the wettability is provided by contact angles.

The meeting place of the three phases in the flotation froth, i.e. solid, liquid and air, is characterised by the angle of contact, θ, of the liquid on the solid, as measured through the liquid phase. When a mass of liquid comes into contact with a solid surface, the liquid-vapour interface will adapt to a state of minimum area and constant surface curvature as dictated by the physical constraints of the system. Figure 2-5 shows the behaviour of a liquid drop when brought into contact with a flat hydrophilic ($\theta < 90°$) surface.

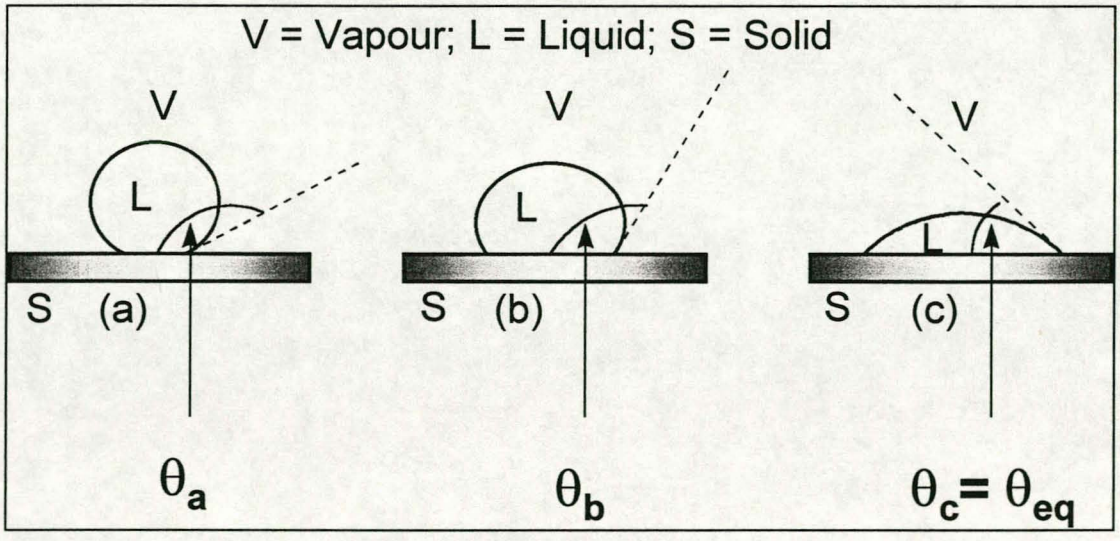

Figure 2-5: Liquid drop in contact with solid surface.

The contact angle, as shown in Figure 2-5, is dependent on the properties of all the phases. Figure 2-5(a) shows the situation when the liquid drop has very recently touched the solid surface. The contact angle, θ_a, is still almost 180°. After some time (Figure 2-5(b)) the liquid drop has begun to spread and the contact angle, θ_b, is approaching the equilibrium state. In Figure 2-5(c) the system has reached its equilibrium state. The liquid-vapour-solid interface has stopped moving and the contact angle, θ_c, has reached its equilibrium value (θ_{eq}). While the liquid-vapour-solid interface line is moving, the contact angles formed are called dynamic contact angles (θ_a and θ_b), for which the general symbol θ_d is used.

2.4.2 Measurement of contact angles

The accurate and reproducible measurement of contact angles is imperative in order to study the dynamic behaviour of particles of various degrees of wettability in two-phase foams. Several ways of measurement are reported in the literature. Huh[22] proposed a numerical regression method for the determination of the contact angle from the entire profile of the liquid drop. Electronic aids for the digitisation of photographic profiles of sessile drops and an iterative method of solution of the differential equations of the drop profile were used. In turn, the measurement of the contact angle of a liquid droplet on a transparent substrate by using a laser was investigated by Allain[23]. The beam is directed down through the droplet and diffraction at the droplet edge produces a circle on the screen below. The direct calculation of the average contact angle around the droplet perimeter is done on the basis of refractive index data and the geometry of the system.

Both the above methods suffer from the limitations of using delicate electronic and optical equipment, they are expensive and difficult to construct. A rugged, inexpensive and easy to build method was proposed by Fort[24], and it is based on the observation of the angle at which light from a point source is reflected from a liquid drop surface at its contact point with a solid. Drawbacks of this method are that it is restricted to measurement of angles less than 90°, and it must be operated in a darkened room.

When the solid has a flat surface available, its contact angle with a liquid drop can be measured by direct observation (sessile drop technique), preferably under a microscope so that a small drop, undistorted by its weight, may be used[25]. A gas bubble can also be confined beneath the sample (captive bubble technique). However, Guttierez-Rodriques[26] found consistently that values for the captive bubble contact angles differed from values for the sessile drop technique on the same substrate (the captive bubble results were always lower, i.e. more hydrophilic). Because the contact angle of importance is that between the liquid and solid, it was decided to use one of the sessile drop techniques in the experimental phase of this dissertation.

The most obvious measurement technique is to observe the drop profile, take a tangent to the drop surface at the three-phase interface, and measure the contact angle with a protractor. Various workers project an enlarged image of the drop onto a screen, or simply photograph the drop (Billett et al[27] & Hansen[28]). It is often difficult to draw an

accurate tangent unless a full circle is superimposed over the drop. Although inexperienced operators may get reproducible results, such results may be significantly displaced from the true value.

It was thus decided to measure the contact angles from the droplet dimensions[29]. According to this method, the distorting effect of gravity can be neglected if the droplets are very small and contact angles can be determined from the dimensions of the droplets. The contact angles were then calculated using the following equation:

$$\tan\frac{\theta}{2}=\frac{h}{r} \qquad \textbf{Equation 2-4}$$

where θ is the contact angle, *h* the drop height [μm] and *r* the radius at the base of the drop [μm].

2.4.3 Relevance of contact angles measured on flat surfaces

The contact angle measured on a flat surface by the sessile drop or captive bubble techniques is a measure of the floatability of the particle. However, the method suffers from many disadvantages:

- It is extremely difficult to obtain a truly representative surface of the particle of the required size (at least 0.5 cm^2). It is thus necessary to use larger particles for contact angle measurements.
- The particle surface may not be representative of the natural particle surface due to the intense polishing required to obtain a completely clean, flat surface.
- Some experimental techniques in this category employ equilibrium times of up to 10 minutes[28]. As the process of bubble film thinning and rupture occurs in a matter of a few milli-seconds, questions as to the validity of the measured contact angle can be raised.
- The sessile drop method is static, whereas the flotation process is dynamic. According to de Geddes[30], who reviewed the statics and dynamics of solid wetting by liquids (including water), the phenomenon of hysteresis of contact angles is caused by chemical heterogeneity and physical roughness. This phenomenon affects virtually all systems and realistic studies cannot therefore be conducted. Most surfaces are subject to microscopic roughness and the contact angle must therefore be qualified by specifying whether the surface is being drained from the liquid (receding angle) or being immersed into the liquid (advancing angle).

According to Hanning and Rutter[31] these difficulties have been acknowledged by a number of authors which led at least one group to conclude that contact angles measured on polished (coal) surfaces may have very little relevance to natural (coal) surfaces. It is recognised that the latter of the above mentioned difficulties could have the most profound influence on the performance data of the novel flotation technique, and a more detailed investigation into a method of wettability quantification was thus justified.

2.4.4 *Alternative methods of wettability quantification*

Jiang and Holtham[32] conducted a dynamic study of collision velocity and adhesion between particles and bubbles in flotation. In their work (Figure 2-6) they proposed the concept of a collision angle β, and assumed that there is some critical limiting value of the collision angle, β_a, the adhesion angle. The adhesion angle provides a description of the dynamic collision and adhesion process and is directly linked to the probability of adhesion. They also proved that the adhesion angle increases with collector concentration and it can therefore be assumed that the adhesion angle will increase with increasing hydrophobicity of the particle. The work, however, was performed on fine particle flotation with very small bubbles, but it can be assumed that similar behaviour would be observed with coarse particles and larger bubbles.

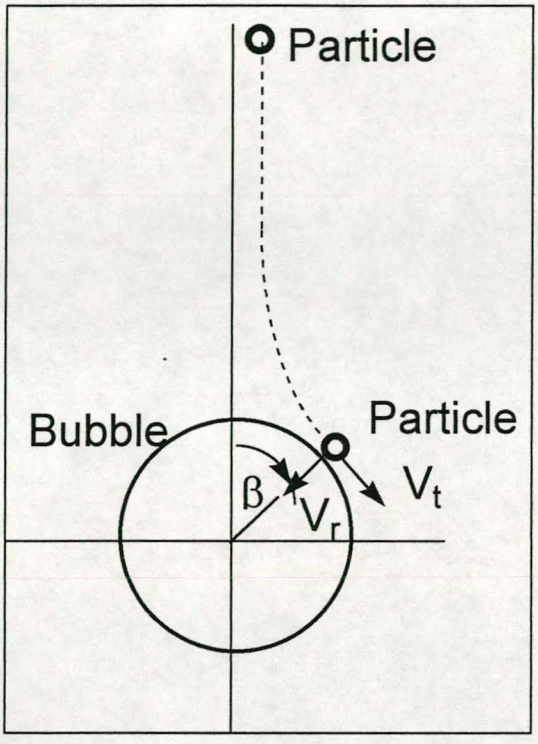

Figure 2-6: The bubble particle collision model after Jiang and Holtham[32].

Hanning and Rutter[31] described a novel bubble-particle attachment method for deriving dynamic contact angles at the air/water/solid interface. The method is based on work by Scheludko, Toshev & Bojadjiev[33] who defined the upper limit of floatability of an immersed sphere (in the absence of shear forces) as:

$$R_{max} = \sqrt{\frac{3\gamma_{LV}}{2\Delta\rho g}}.\sin\frac{\theta}{2} \qquad \textbf{Equation 2-5}$$

where R_{max} is the radius of the largest particle that can be raised against gravity [m], γ_{LV} is the liquid surface tension [N/m], $\Delta\rho$ is the density difference between the immersed solid and the liquid [kg/m^3], g is the acceleration due to gravity [m/s^2] and θ is the dynamic contact angle. The method therefore involves the determination of the

diameter of the largest particle, from a population of particles immersed in water, which can be raised against gravity by a captive air bubble.

The apparatus is shown in Figure 2-7. A small bubble is blown at the immersed end of the capillary by means of a micro syringe attached to a flexible tube. After contact with a particle, the capillary tube is carefully raised away from the bed by means of the lever. Attachment is said to have taken place if observation through a low powered microscope show that the bubble has lifted the particle clear from the particle bed.

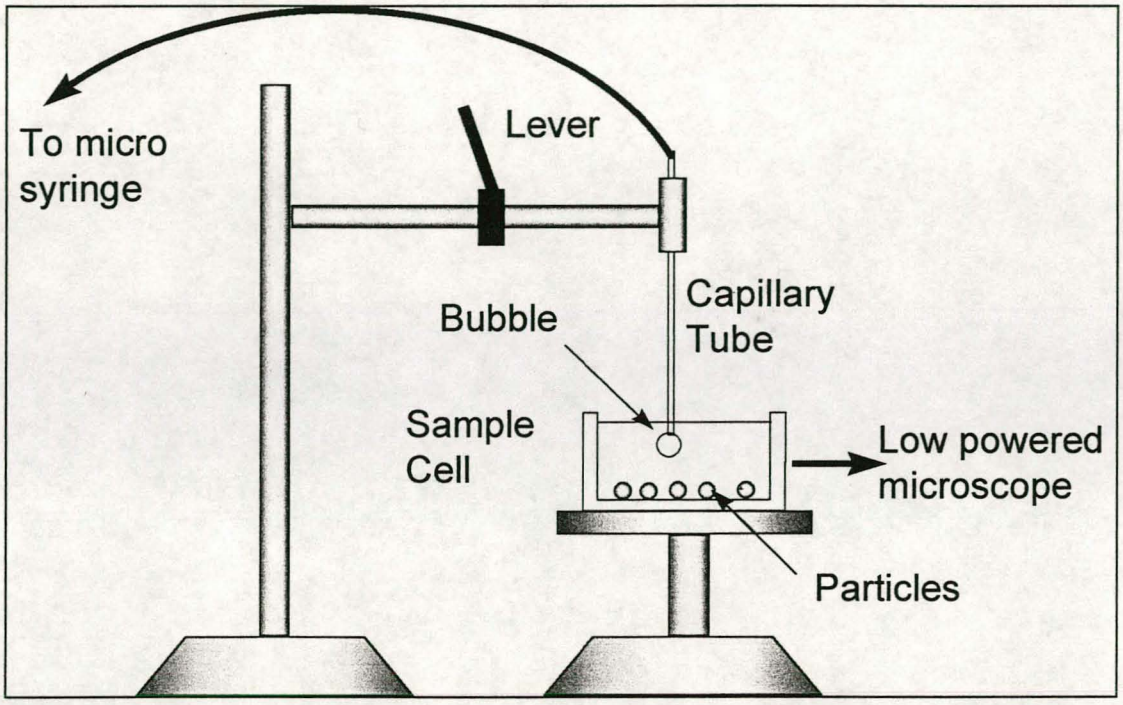

Figure 2-7: Bubble particle attachment apparatus after Hanning and Rutter[31]

Both these indirect contact angle measurement techniques were investigated in the search for a reproducible contact angle measurement technique. However, the drop profile technique (as discussed in section 2.4.2) yielded more reproducible results and was significantly easier to operate. The above mentioned techniques were therefore not used.

2.5 Summary and the Concept of Reverse Froth Flotation

When particles are introduced to a conventional flotation cell (as a pulp), the particle contact angle has to increase as the particle size increases to maintain the same level of recovery (Trahar[8] and Crawford and Ralston[12]). However, when these highly hydrophobic particles are present in the froth phase, Dippenaar[15], Hemmings[17] and Frye & Berg[18] has shown that they could act as very effective film breakers and therefore report back to the pulp phase. This film thinning action depends on the capillary pressure-driven flow, which in turn depends on the particle contact angle and the structure of the froth.

In a froth, the size of the bubbles increases with increasing height above the liquid/froth interface due to bubble coalescence, a decreased hydrostatic head, and froth drainage. The structure of the froth changes accordingly from (a) a bubble swarm at the liquid/froth interface to (b) a packed bubble bed in the intermediate region to (c) a polyhedral structure at the surface. The polyhedral bubble structure is characterised by the fact that the bubbles are separated by rigid liquid films rather than existing as individual mobile entities at the interface, and it is under these conditions that the mechanism of film thinning is most effective. This suggests that the coarse particles should therefore be introduced onto the froth surface to maximise the efficiency of the separation.

When introduced to the froth surface, a coarse particle will be surrounded by a number of bubbles. Although the particle is not immersed in the film to the same degree as assumed by Dippenaar[15], Hemmings[17] and Frye & Berg[18], the same principles of bubble film stability and film rupturing action would apply at each point where the film and the particle are in contact. Hydrophobic particles will therefore act as bubble film breakers and would settle through the froth under gravity to be recovered as an underflow (concentrate) product. Hydrophilic particles, however, will be supported by the bubble films and therefore be recovered as a float (tailings) product.

A flotation cell was therefore developed where particles are fed onto the froth surface. To prevent overcrowding of the froth, the froth had to be continually renewed, which pointed to a moving froth bed. Apart from these two requirements the cell had to be easy to operate and capable of yielding reproducible results. The following chapter details this development of the cell, from the first prototype to the final cell design. In addition, chapter 3 describes the various experimental procedures including the cell operational procedure, modifying the test particle surface and measuring the associated contact angle, measuring the particle density and measuring the bubble size distribution in the cell.

3. EXPERIMENTAL SET-UP AND PROCEDURES

The previous chapter focused on the work done by various researchers that laid the foundation to the development of the reverse froth flotation cell. In particular, the underlying principles of the technique, together with the need for a flotation cell where coarse particles could be fed directly onto a moving froth surface, was identified. The development of such a flotation cell is described in this chapter. In addition all experimental procedures as well as apparatus used are described in full.

3.1 Original Flotation Cell Design

The original cell was designed and patented by Dr. Victor Ross[1]. In order to develop the concept further, and to gather experimental results to quantify the mathematical model, a similar cell was manufactured at the University of Stellenbosch (US). The original cell design, together with the flowsheet for water and frother, is shown in Figure 3-1, with photographs of the original cell and set-up included in Appendix C.

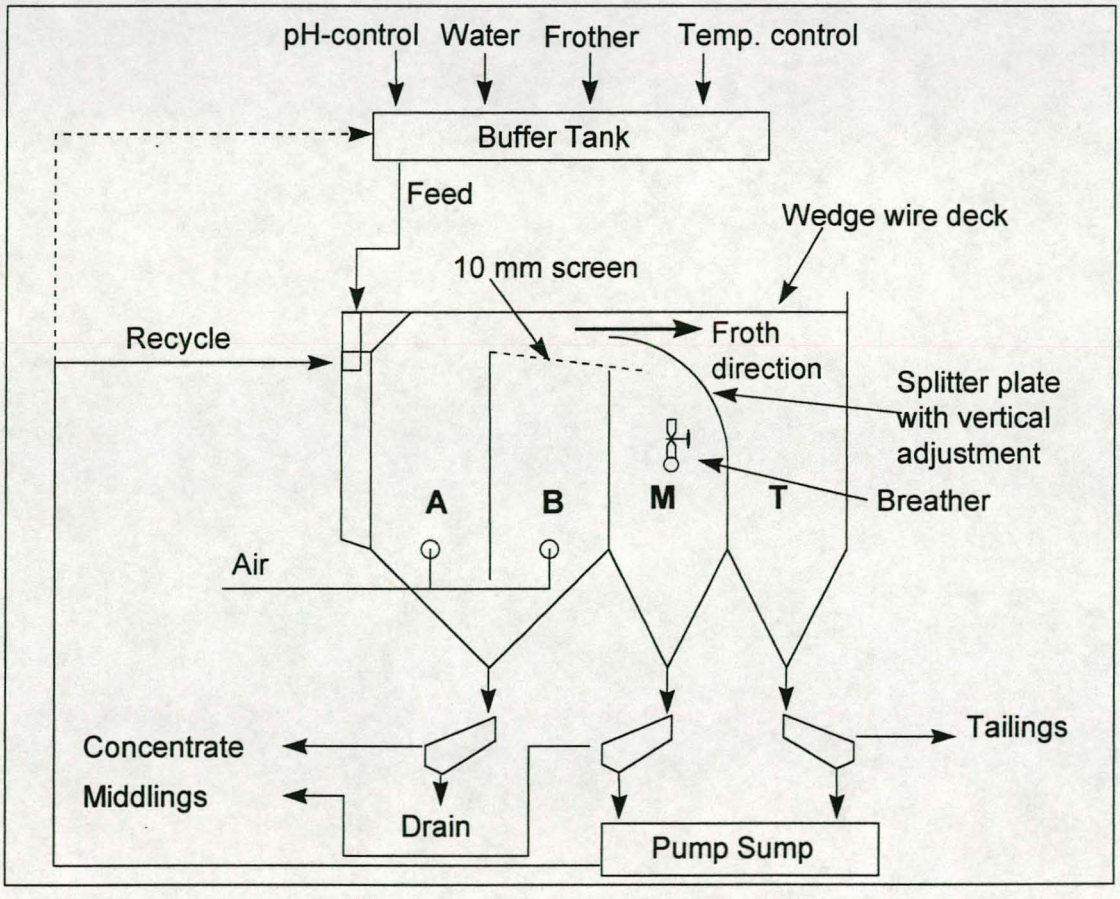

Figure 3-1: Original Ross[1] cell design together with aqueous phase flowsheet.

The following legend applies to Figure 3-1:

- **A** = sub-compartment A in concentrate compartment.

- **B** = sub-compartment B in concentrate compartment. These two sub-compartments (A and B) are inter-linked with a common outlet at the bottom and serve to collect the cell concentrate.
- **M** = middlings compartment – designed to collect the middlings fraction.
- **T** = tailings compartment to collect tailings.

Due to the confidential nature of the detail equipment design, detailed drawings together with cell dimensions are provided elsewhere (van Dyk[34]). Some of the features of the original cell design, however, include:

- The flotation cell is made of 5mm clear PVC sheeting. This provides the operator with essential visuals of the froth structure and phenomena in the cell.
- Air is blown into sub-compartments **A** and **B** through ceramic spargers with 100µm apertures.
- To enable the settling of a particle through the froth bed, the rate at which new bubble films arrive at a horizontal plane must be kept smaller than the rate of bubble film breakage by the particle. The vertical velocity component of the bubbles should therefore be kept as small as possible. A wedge wire deck of 2mm stainless steel rods spaced at 2mm intervals is therefore placed over the length of the cell to force the froth into moving largely in a horizontal direction instead of vertically upwards.
- A 10mm screen is placed over sub-compartment **B** at a 10° angle, to further restrict the vertical velocity component of the froth and to provide a froth support for the vertically moving froth bed from sub-compartment **A**.
- Particles are fed onto the horizontally flowing froth bed, and allowed to settle through the froth.
- The flotation cell is fitted with a splitter plate (see Figure 3-1) which is height adjustable in order to cut the froth at a predetermined height above the middlings compartment (**M**). The optimum particle recovery can therefore be controlled.
- The recycle compartment next to sub-compartment **A** is open to sub-compartment **A** through slots installed at the bottom. The recycle compartment serves as a receiving compartment for the recycled aqueous phase and therefore allows the recycled aqueous phase to report back to sub-compartments **A** and **B** without disturbing the froth phase.

The buffer tank serves as an initial conditioning tank for the water, frother addition, temperature control and pH control (see cell operation, section 3.4.1). From the buffer tank the aqueous phase is fed to the recycle compartment of the cell. The froth, and hydrophilic particles, are carried over into the middlings and tailings compartments (**M** and **T** respectively) where the froth breaks down. The particles are separated from the aqueous phase by 1mm screens from where the aqueous phase is pumped, via the pump sump, back into the recycle compartment in a closed loop. A 1mm screen recovers the hydrophobic particles from the concentrate compartment (**A** and **B**) when the cell is drained.

Although satisfactory preliminary results were achieved with this original cell design, reproducibility of results proved to be extremely difficult. Many alterations were therefore made during the course of the study to the cell, as well as the cell operational procedure. A detailed discussion, together with subsequent results of each modification, is provided elsewhere (van Dyk[34]). The main aims of these modification were twofold:

- To provide a "homogeneous" froth structure without localised disturbances, i.e.
  - large bubbles that rupture and thereby destroy the surrounding froth.
  - uneven bubble flux distribution across the width of the cell.
  - restrictions to bubble flow causing bubble rupture and subsequent large bubbles.
- To generate a horizontal froth belt from sub-compartment **A** without short-circuiting to other compartments.

A summary of these modifications is provided below, and will suffice for the purpose of this dissertation:

- If a rigid froth structure is present in the flotation cell, air hold-up occurs in the middlings compartment (**M**) due to the slow breakdown of froth. This resulted in air escaping at irregular intervals, between the splitter plate and the screen, into the froth phase. Apart from irregularly breaking down the horizontal flowing froth structure, the flow of froth into the middlings compartment (**M**) was hindered, resulting in skewed results. A breather pipe with adjustable valve was therefore installed in the middlings compartment (see Figure 3-1 and photographs, Appendix C) and the flow of froth into the middlings compartment could therefore be controlled.
- It was noted that relatively high air flowrates in sub-compartment **B** caused froth to overflow directly from sub-compartment **B** into the middlings compartment (**M**). This flow caused the horizontal froth belt from sub-compartment **A** to be lifted over the splitter plate, directly into the tailings compartment (**T**). Since the splitter plate could not "cut" the horizontal froth belt, the recovery of intermediate hydrophobic particles (contact angle close to 90°) to the tailings was distorted. The aeration rate in sub-compartment **B** was subsequently set to a point where the froth in that compartment would just reach the 10mm screen. The only function of the froth in sub-compartment **B** would thus be to provide a froth support, or froth "bearing", for the horizontal froth belt from sub-compartment **A**.
- Compressed air lines were connected to both sides of the spargers to improve the bubble flux distribution across the width of the cell.
- The regular and thorough cleaning of the cell prevented the adhesion of bubble films to the sides of the cell, and the subsequent creation of dead regions in the cell.

- The 10mm screen above sub-compartment **B** caused the restriction of free bubble flow. The screen was therefore replaced by a 0.5mm stainless steel rod deck in the direction of froth flow. Initially the deck had a 3.0mm spacing in-between rods. However, the narrow spacing prevented the free flow of bubbles through the deck, causing the bubbles to collapse and form air pockets that escaped through the deck. Increasing the spacing solved the problem of bubble coalescence, however, a strong down draught occurred at the beginning of sub-compartment **B** as froth from sub-compartment **A** passed over the plate dividing the two compartments. The deck was subsequently modified to create a "piano effect". Short rods (40 mm long) were inserted in every 6.5mm gap. The rod gap was therefore reduced to 3.0mm for the first 40mm, increasing to 6.5mm for the remainder of the deck.
- The "piano" rod deck solved many of the problems. However, at low aeration rates in sub-compartment **B** the froth would only reach the lower point of the inclined rod deck resulting in a bubble entrapped under the deck (see Figure 3-2). This bubble would escape through the deck at irregular intervals causing localised froth bed disturbances. In the case of higher aeration rates in sub-compartment **B**, the froth bed reached the top point of the inclined rod deck. However, the resulting bubble flux from sub-compartment **B** into the horizontal moving froth bed would cause a distorted flow pattern above sub-compartment **B** (see Figure 3-3) resulting in an increase in recovery of particles to the tailings. By changing the cell configuration to a horizontal piano rod deck, these problems were alleviated to a certain extent.

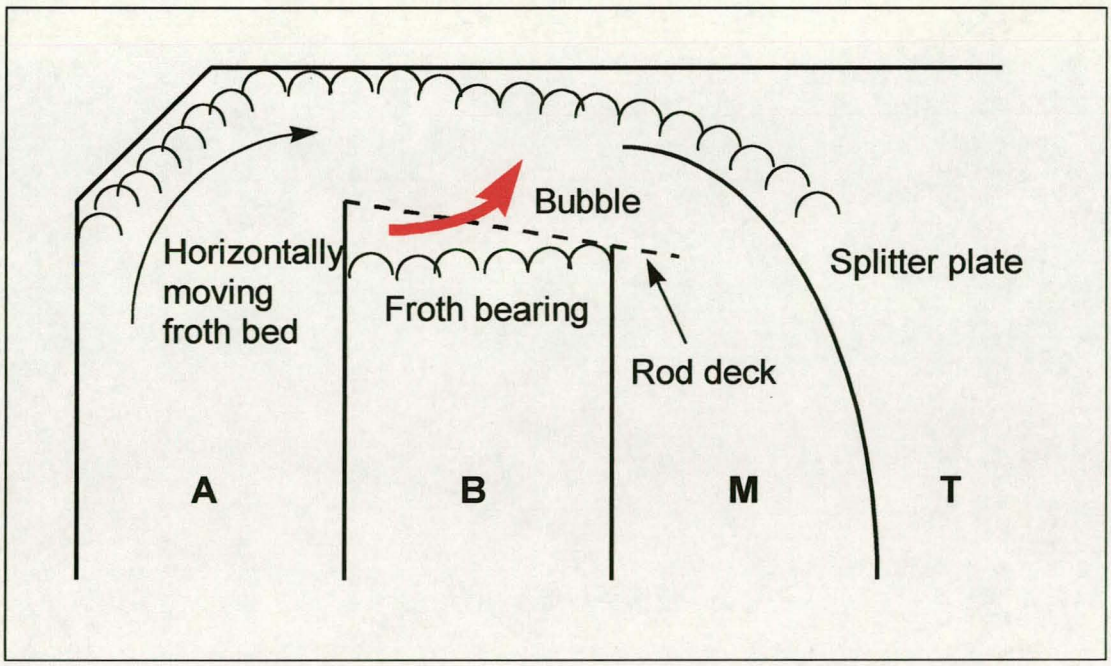

Figure 3-2: Entrapped air bubble above sub-compartment B resulting in localised froth disturbances.

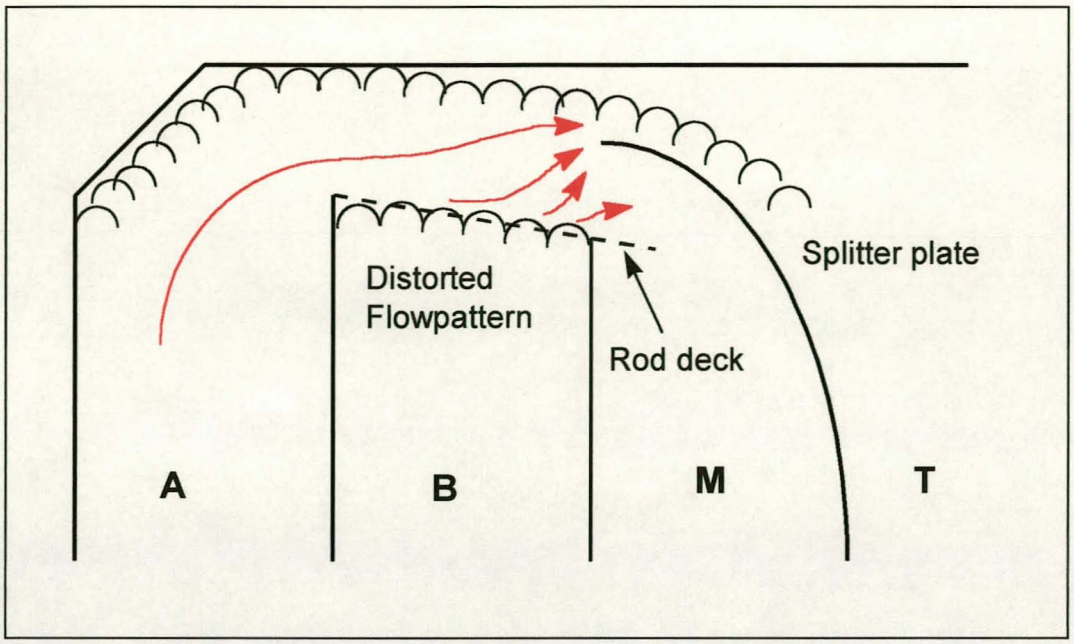

Figure 3-3: Distorted flowpattern above sub-compartment B.

3.2 Final Flotation Cell Design

Most of the localised froth disturbances were eliminated with the above modifications and alterations. However, once it was realised that the various alterations were mere solutions to symptoms of a flawed design, a major cell design review was conducted. The outcome of this review culminated in a final flotation cell design as depicted in Figure 3-4 with photographs included in Appendix C. Again, due to the confidential nature of the equipment development, design dimensions are given elsewhere[34]. Features of the final cell design include:

- The cell height was increased to improve the air distribution across the water/froth interface. A quiescent interface was subsequently attained, resulting in froth disturbances being minimised.
- All the straight inter-compartment separation weirs were replaced with bent weirs to force the froth in a horizontal direction and to minimise froth disturbances. The previous weir design caused bubble coalescence and bubble breakage, resulting in localised froth disturbances. An increase in the horizontal cross-sectional area of sub-compartments **A** and **B** would retard the flow of froth. The weirs were therefore bent at decreasing radii and at increasing depths from the top of the cell, when moving from left to right as in Figure 3-4.
- The "piano" rod deck above sub-compartment **B** was removed to minimise the localised froth disturbances as described in section 3.1.
- The adjustable breather valve in the middlings compartment was retained.
- The height adjustable splitter plate above the middlings compartment (**M**) was retained.

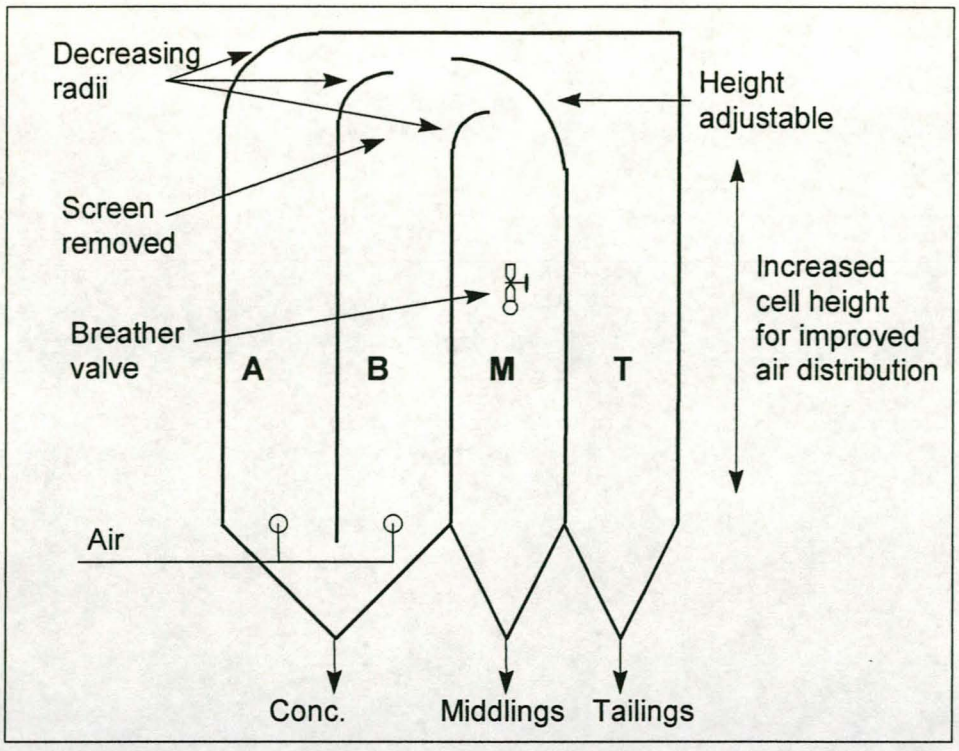

Figure 3-4: Final flotation cell design.

3.3 Test Particles

Density tracers of various sizes, specific gravities and shapes were used in the testwork. The surface area, volume, calculated mass and mass-to-surface-area ratio of each particle type is given in Table 3-1.

In addition to the tracer testwork, various tests were conducted with ores obtained from various mines. Two samples were received from the Orapa diamond mine in Botswana as final recovery tailings, and two samples were prepared from Harmony gold mine ROM ore. These samples are summarised in Table 3-2. The objective of using final diamond recovery tailings was to investigate whether the technique could replace grease belts in the final processing of fine (-3mm) diamondiferous gravels (see chapter 1). Gold ores were investigated to answer the need for a cost effective coarse particle flotation technique for the underground concentration of sulphur bearing gold ores by coarse milling and flotation[2].

3.4 Experimental Procedures

3.4.1 Cell operation

The following operational procedure for the flotation cell was established:

- The conditioning tank was filled with the desired amount of demineralized water and the thermostat was set to control the water temperature at 25°C.
- The desired amount and type of frother was then added to one (1) litre of demineralized water in a cylindrical flask and stirred at 700 rpm for a period of ±10min in order to disperse the frother throughout the water.
- The diluted frother mixture was then added to the conditioning tank.

Table 3-1: Applicable data of density tracers used in testwork.

	Dimensions [mm]			SG	Area	Volume	Mass
Shape	L	H	W		mm²	mm³	[mg]
Cube	3.05	3.05	3.05	3.5	55.81	28.37	99.30
				3.3			93.63
				3.1			87.96
				2.9			82.28
				2.7			76.61
				2.6			73.77
Cube	2.10	2.10	2.10	3.5	26.46	9.26	32.41
				3.3			30.56
				3.1			28.71
				2.9			26.86
				2.7			25.00
				2.6			24.08
Flat	3.05	1.52	3.05	3.5	37.15	14.14	49.49
				3.3			46.66
				3.1			43.83
				2.9			41.01
				2.7			38.18
				2.6			36.76
Flat	2.10	1.05	2.10	3.5	17.64	4.63	16.21
				3.3			15.28
				3.1			14.35
				2.9			13.43
				2.7			12.50
				2.6			12.04
Disc	Rd= 1.1mm	Rs= 0.65		3.1	33.54	12.51	38.77
				2.9			36.27
Cylinder	2.08 ∅	1.30		3.5	19.73	6.73	23.55
				3.1			20.86
				2.9			19.51
				2.7			18.17
Cylinder	2.08 ∅	3.38		3.5	28.88	11.49	40.20
				3.1			35.60
				2.9			33.31
				2.7			31.01
Sphere	2.50 ∅			3.63	19.63	8.18	29.70

Table 3-2: Size fractions and average SG's of industrial ores.

Source	Size fraction	Average SG
Orapa recovery tailings	-2+1mm (60% passing 1.72mm)	3.82
Orapa recovery tailings	-3+2mm (80% passing 2.36mm)	3.76
Harmony ROM	–2.8+1.7mm	2.82
Harmony ROM	–3.35+2.8mm	2.76

- Next, the pH was adjusted with either hydrochloric acid or a sodium hydroxide solution to the desired level (usually pH = 7), and the mixture was allowed to condition for a further 10 minutes.
- Following the conditioning of the aqueous phase, the recycle compartment of the cell was filled to approximately 70mm above the desired operational level. While filling the cell, the air flowrate in both sub-compartments **A** and **B** was set to a low level (in order to prevent the aqueous phase from entering the air lines).
- The air flowrate in sub-compartment **B** was then set to a level where a froth bearing was created for the horizontal froth belt from sub-compartment **A**.
- Once the froth bearing was created, the air flowrate in sub-compartment **A** was set to the desired level.
- As soon as the desired liquid level was reached in the cell, the recycle pump was switched on and the aqueous phase recycled.
- During the run, the aqueous phase reporting to the pump sump via the middlings and tailings compartments was either recycled to the conditioning tank or to the feed compartment (see Figure 3-1).
- The cell was run at these settings for a minimum period of 20 minutes in order to obtain a stable froth bed and operating conditions. The water level in both the cell and the pump sump was manually controlled via valves installed on the cell discharge and pump sump discharge. This inevitably resulted in the cell level oscillating during operation. However, the oscillations were small and did not cause localised froth bed disturbances.
- Once a stable froth bed was obtained the test run was commenced. One of two operating modes was followed:
  - Density tracers were manually fed onto the froth bed from a plate attached to the feed end of the cell.
  - Ores were fed onto the froth bed via a variable speed vibratory feeder, positioned so that the lip of the feeder is at the end of the bent cell wall of sub-compartment **A**.
- Tracers or ore reporting to the tailings or the middlings were separated from the aqueous phase by screens placed on these compartments' outlets, while particles reporting to the concentrate (sub-compartments A and B) were recovered at the completion of a run during the draining of the cell.
- In order to prevent liquid from entering the air lines, the air flowrate was turned down only after the cell was drained.

3.4.2 Preparation of ore particles

Both the density tracers and Orapa final recovery tailings required no prior size fraction preparation before testwork. However, the Harmony ROM ore was crushed in a cone crusher and screened into two size fractions, namely –2800+1700µm and –3350+2800µm. Al particles smaller than 1700µm were discarded for the purposes of the testwork.

3.4.3 Density estimation

Three methods were used to determine the average density of each size fraction of the density tracers as well as the industrial ores:

1. Density bottles were used to determine the average density of 10 particles at a time. Due to the inherent inaccuracy of the method and randomly sized ore particles, no reproducibility of the values could be obtained.
2. A helium pycnometer was used to determine the average density of a batch of particles. Due to the porosity of the density tracers, again no reproducibility of the density value could be obtained.
3. Each density and size fraction was split into five sub-fractions and the average density of each sub-fraction was determined by weighing the fraction and recording the volume of water displaced in a grade B burette. Good reproducibility of results was attained and the average density of each size and density fraction was taken as the average of the densities of the five split fractions.

3.4.4 Static contact angle measurement

As discussed in section 2.4.2, the accurate and reproducible measurement of the static contact angle of the test particles was essential for the study. Due to the limitations of the various methods reported in the literature, it was decided to calculate the static contact angle from sessile droplet dimensions (Equation 2-4, section 2.4.2). The accurate measurement of the droplet dimensions was therefore imperative.

The apparatus used is shown in Figure 3-5. A low powered travelling microscope, fitted with micrometers on its horizontal and vertical axis, allowed the drop height and radius and the base of the drop to be determined accurately. The experimental procedure was as follows:

- The surface of a glass plate was coated with the desired coating (see section 3.4.5), and the coated plate placed on the measurement table.
- A droplet of 0.001ml was then placed on the coated surface with a micro syringe.
- One (1) minute was allowed to enable the liquid to reach equilibrium.
- The drop height and radius was then measured at the drop base with the travelling microscope and the equilibrium contact angle calculated using Equation 2-4.
- The procedure was repeated a minimum of five (5) times in order to calculate the average equilibrium contact angle.

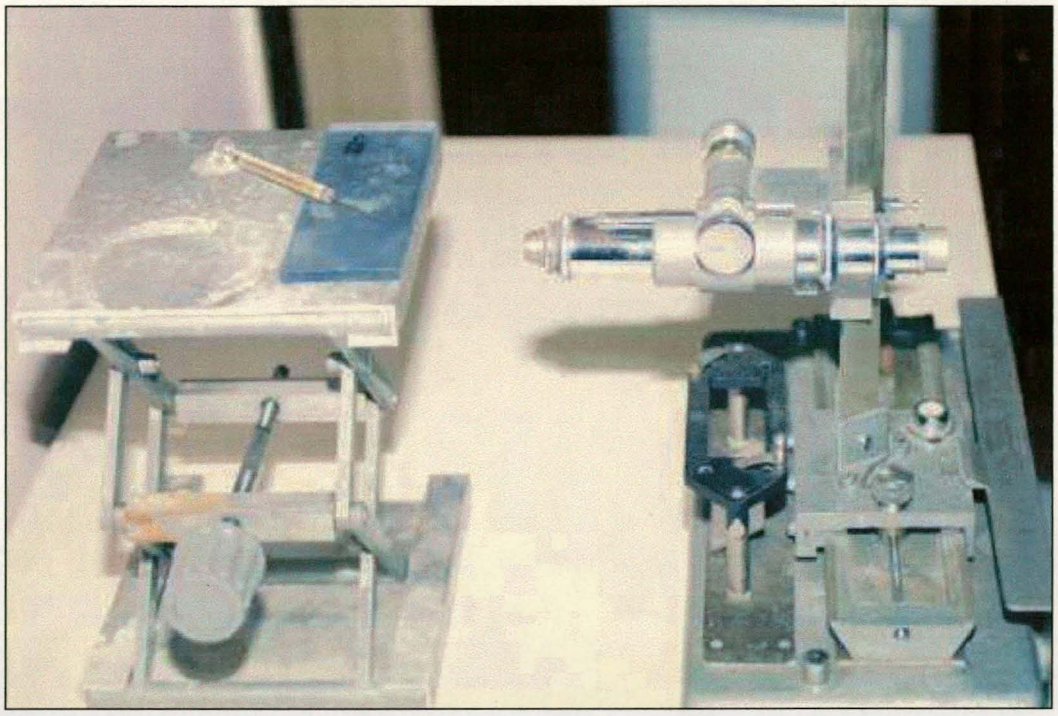

Figure 3-5: Apparatus for measurement of equilibrium contact angles.

The apparatus as described yielded static contact angles which were within the experimental error determined by other investigators using the sessile drop profile technique. Reproducibility was good, within plus or minus five (5) degrees. Table 3-3 gives a series of measured equilibrium contact angles for distilled water on a gold surface.

Table 3-3: Measure equilibrium contact angles of distilled water on gold.

Observation Number	Equilibrium Contact Angle [°]	Observation Number	Equilibrium Contact Angle [°]
1	71.28	6	69.80
2	61.53	7	64.07
3	66.49	8	67.74
4	63.95	9	68.29
5	66.43	10	67.38
Average measured equilibrium contact angle on gold surface = 66.7°			

The equilibrium contact angle of distilled water on a gold surface is reported in the literature as 66° (Huh & Reed[22]).

3.4.5 Modification of particle surface properties

To study the dynamic behaviour of particles with various degrees of wettability in the froth phase of the cell, it was necessary to modify the surface properties, or wettability, of the particles. Since the experimental work was based on both density tracers and industrial ores, the modification of surface properties will be discussed accordingly.

3.4.5.1 Density Tracers

The density tracers were obtained from either the De Beers Industrial Diamond Division or purchased from a United Kingdom based manufacturing facility of Van Eck and Lurie. All tracers were manufactured from a high-density plastic with inert surfaces. The modification of the particle wettability by the chemical attachment of hydrophilic or hydrophobic substrates to the surface of the particles was therefore impossible. A method, therefore, had to be devised whereby the density tracers could be coated with a stable coating, where different coatings (or substances) will yield different equilibrium contact angles in a water-frother mixture.

Various paints, waxes, lubricants and adhesives were initially tested as coatings. However, several of these initial coatings were discarded since the coatings were unstable in the water-frother mixture, or the coating substance contained a volatile component which destroyed the bubble films in the flotation froth. Eventually five suitable coatings were selected. A good spread of equilibrium contact angles in the water-frother mixture was attained, from as low as 44.2° to as high as 98.1°. The coatings with their respective equilibrium contact angles are given in Table 3-4.

Table 3-4: Density tracer coatings & corresponding equilibrium contact angles.

Coating substance	Equilibrium Contact Angle
Paint #1	98.1°
Candle wax	97.9°
Adhesive #1	77.3°
Paint #2	65.3°
Paint #3	44.2°

During repeated testwork it was found that hydrophobic coatings (equilibrium contact angles > 90°) become increasingly hydrophilic with time. This is in accordance with observations by Adam[35] who stated that prolonged soaking of organic materials in water (including varnished or painted surfaces and even paraffin wax) produces a greater or smaller decrease in the equilibrium contact angle. The predominant mechanism responsible for this hydrophilic ageing is the fact that water molecules become entrapped in the surface layers, thus increasing the adhesion of water to the surface of the particle.

A possible solution to the problem of ageing was the use of methylated quartz particles and glass beads, rather than coating the density tracers. The hydrophilic-hydrophobic character of silica surfaces has been extensively investigated[36, 37, 38]. Although used by various researchers[31, 39, 40] to help them in understanding flotation behaviour, the methylation technique suffers from various disadvantages such as laborious experimental procedures, the use of pure chemicals and inert atmospheres, and an increased wettability after prolonged exposure to water or moisture. This approach was therefore discarded.

The above drift in the wettability characteristics of the various coatings was seen as an opportunity to investigate a wide spectrum of equilibrium contact angles in the dynamic behaviour of particles in the froth phase. If the change in wettability is related to the time of exposure to the aqueous phase, the influence of wettability on the recovery of particles can be investigated by using one coating and monitoring the time of contact with the aqueous phase. The candle wax coating was the obvious choice for this line of experiments since:

- The candle wax coating is stable and easy to apply.
- The candle wax coating yielded the lowest standard deviation in reproducibility experiments.
- Fresh candle wax yields an equilibrium contact angle of ±98° (see Table 3-4), i.e. the coating is inherently hydrophobic.
- An increase in wettability was attained after prolonged soaking in water (see Figure 9-1).

3.4.5.2 Industrial ores

No modification to the surface properties of the Orapa tailings was attempted. However, gold is strongly associated with pyrite and arsenopyrite in the Harmony ROM ore containing 1.36% (by mass) of sulphur. In an attempt to investigate the possibility of utilising the technique for a pre-concentration treatment phase for gold ores, the ore was conditioned with Sodium Ethyl Xanthate. As per conventional flotation theory, the Xanthate renders the sulphides hydrophobic, while the gangue material is naturally hydrophilic. A separation on the basis of hydrophobicity could therefore be attempted.

3.4.6 Bubble size measurement

The bubble size is an integral part of the modelling of particle behaviour in the novel flotation cell (see sections 5.6 & 5.7). At first, the bubble size was determined by visual observations and was therefore very inaccurate. However, a technique for measuring the size of bubbles in two and three phase systems was developed by Randall *et al.*[41]. As this equipment would play a vital role in the verification of the mathematical model it was subsequently purchased.

The system works on a very simple basis. The bubbles are drawn up through a capillary tube by vacuum. A pair of optical detectors, situated in a brass block surrounding the capillary, measures their length and velocity. The data are stored in the memory of a microprocessor system. Up to 4000 bubbles may be collected for the determination of each bubble size distribution. A software package converts the data stored in the files into bubble size distributions

Figure 3-6 is a graphic illustration of the valve and piping configuration of the UCT bubble size analyser (Randall *et al.*[41]). The configuration allows the bubbles to be drawn through the capillary detector under vacuum and collected in the gas burette. The total volume of bubbles is recorded and used for the calculation of the bubble size distribution.

The experimental procedure for bubble size measurement was as follows:

- Before any measurements could be taken the lines were flushed from any bubbles. This was done by setting valve A to the *flush* position and valve B to the *sample* position. In addition, valve D was *closed* while valve E was in the *open* position. The vacuum was then turned on until all bubbles were flushed from the pipes.
- The bubble capturing burette was subsequently filled with water by keeping valve A in the *flush* position, but setting valve B to the *read* position. Valve C at the top of the burette was *opened* and valves D and E were kept in the *closed* and *open* positions respectively. The equalisation tank was then raised in order to fill the burette with water. Once filled, valve C was *closed*.
- To collect and measure the bubbles, valve A was at first kept in the *flush* position while valve B was turned to the *sample* position, valve C was *closed* and the vacuum was turned *on*. Water was now drawn through the system from the flush reservoir. When the operator was ready to start the measuring cycle the electronics for measuring were enabled. The start button on the micro processor unit was depressed, the stop/go switch was set to go and valve A was set to the *sample* position. At this stage the bubbles were drawn through the detectors and measurements were being recorded by the micro processor unit.
- To end the measuring cycle, stop was pressed on the micro processor unit and simultaneously, valve A was switched to the *flush* position.

The bubble size analyser is incapable of measuring the bubble size distribution in the froth phase. However, to obtain an indication of the average bubble size in the froth phase of the flotation cell (adjusted for the linear decrease in pressure – see section 5.6), the probe was positioned just beneath the liquid-froth interface. It was therefore assumed that the bubble size distribution at the liquid-froth interface is similar to that in the froth phase itself. This assumption was confirmed by recent work of Feng and Aldrich[42], where they showed that the bubble size distribution in the surface foam of water with a surfactant (such as soap) is very similar to the distribution in the bulk phase, especially when the bubbles are small.

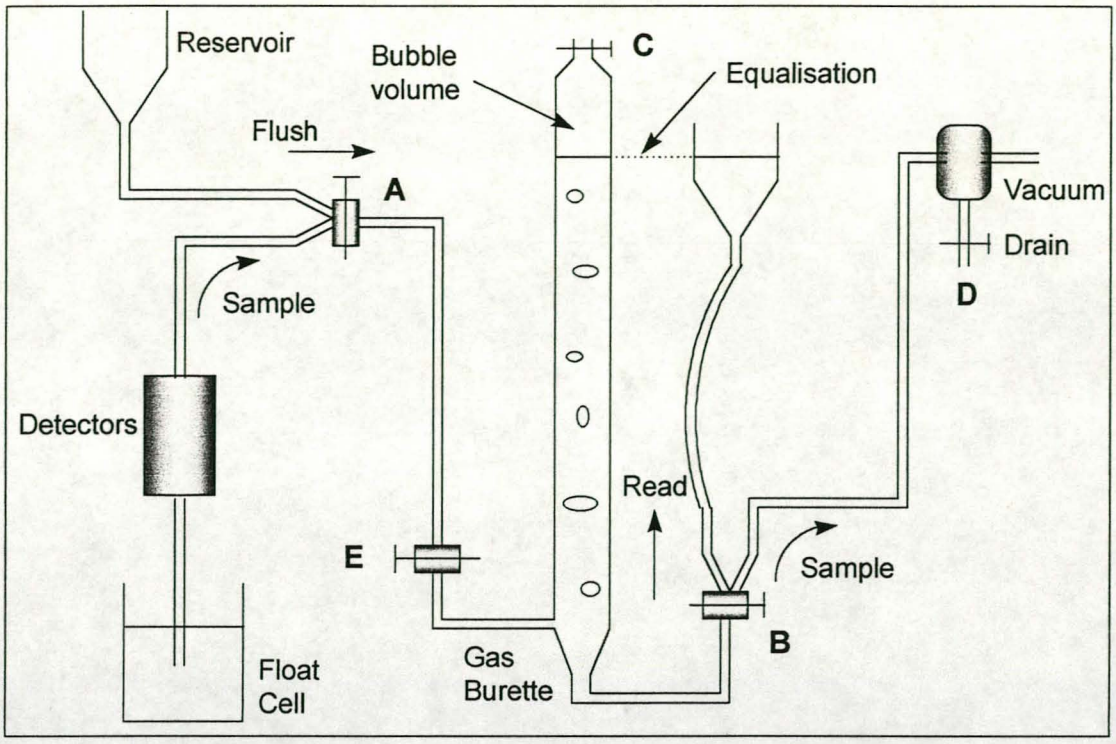

Figure 3-6: Configuration of the UCT bubble size analyser (Randall et al. [41]).

3.4.7 Measuring water concentration at {x,y} position in froth

The water concentration at a {x,y} position in the froth is used to calculate the air hold-up at that specific position (see section 5.5). In order to measure the water concentration, the apparatus (as shown in Figure 3-7) was used. It consists of a flexible tube attached to a large surgical syringe. The flexible tube is inserted in the froth phase of the reverse froth flotation cell at the required {x,y} measuring position. The plunger of the syringe is then rapidly pulled out in order to suck up both the air and liquid present at the {x,y} position in the froth. The water volumetric concentration is then determined from the total volume of air and water captured versus the volume of water captured (both accurately read off from the calibration on the surgical syringe).

To ensure good reproducibility, the syringe was always held at a lower position than the measuring position in the froth. Although this might seem as quite a crude method of determining the water concentration, remarkably good reproducibility of measurements was obtained.

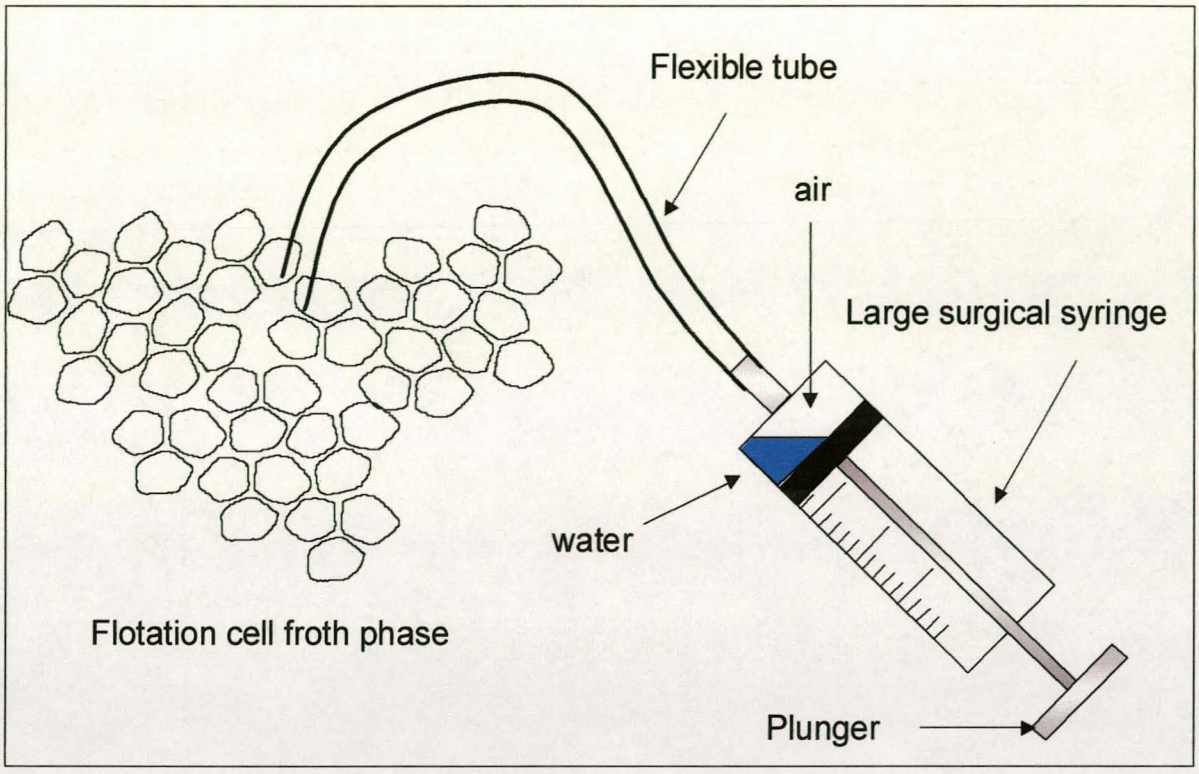

Figure 3-7: Apparatus for measuring water concentration in froth

3.5 Sulphur Analysis

All sulphur analyses on the Harmony ROM ore were done through an automatic LECO instrument at the University of Cape Town. Prior to analysis, the ore samples were ground to at least 90%-45µm in a ZiebTech pulveriser. The subsequent samples (±40 grams) were then sampled to obtain a representative sample of ±1 gram. The automatic LECO was selected, since a manual LECO coupled to a titrator is too inaccurate for the low %sulphur present.

3.6 Summary

In this chapter the experimental procedures, as well as the apparatus used during the experimental phase of this work, are described in full. All experiments were conducted with the apparatus described in this chapter. In addition, a brief summary of the development process behind the new flotation cell was given.

4. MODEL DEVELOPMENT

The previous three chapters discussed the development of the reverse froth flotation technique. In chapter 1 it was identified *why* the concept was developed while chapter 2 expanded on *how* previous work led up to the development of the concept. Chapter 3, in turn, described the "*what*" of the physical equipment, i.e. the development of the cell and its operational procedures.

In the three chapters that follow this chapter (chapters 5 to 7), the various segments of the dynamic model describing the behaviour of coarse particles in the reverse froth flotation cell are developed. This dynamic model was born out of observations of the behaviour of particles in the cell, as well as identifying shortcomings of initial phenomenological modelling attempts. This chapter will therefore first review commonly used terminology before moving on to providing the background to the dynamic model. Shortcomings of the initial modelling attempts are then identified together with the required components of a model capable of simulating the experimentally observed trends, and hence investigate the various mechanisms qualitatively.

4.1 Definitions of Commonly used Terminology

It is often assumed that the reader of a dissertation has a sufficient knowledge and understanding of the terms used in that dissertation. However, more often that not, there exists an array of definitions for the same terminology, even under the so-called experts in the area. In order to prevent unnecessary confusion and frustration under the readers of this dissertation, the following section will attempt to provide definitions for the most commonly used terminology.

4.1.1 Foam and Froth

The American Heritage® Concise Dictionary[43] defines a foam as a mass of bubbles in a matrix of liquid film, especially on the surface of a liquid. A foam can therefore be described as a dispersion of a gas in a liquid. This dispersion can occur via a number of methods, such as sparging the gas into the liquid or shaking the gas and liquid together. The geometry of the bubbles in a foam is determined by the gas phase volume. Once a critical gas phase volume has been reached, the bubbles distort to form polyhedral bubbles separated by thin films with Plateau Borders at the intersection of the films[44]. In some flotation literature, such a distorted foam is usually referred to as a froth, or metastable foam[45], but since a froth is a sub-class of a foam, many authors do not make the distinction. For the purpose of this dissertation, we will always refer to a flotation froth as a colloidal system of polyhedral bubbles characterised by thin films and Plateau Borders. Prior to the critical gas phase volume being reached, the resulting foam is referred to as wet or transient foams[45].

4.1.2 Hold-up

For the purpose of further discussions, the hold-up of any species is defined as the *volumetric* fraction of that species in either the froth or pulp phase.

4.1.3 Pulp-froth interface

The interface between the pulp and froth phases in the cell is defined as the horizontal level in the cell where:

$$\frac{\partial^2 \varepsilon}{\partial^2 z_j} = 0 \qquad \textbf{Equation 4-1}$$

where ε is the hold-up of air and z_j the height in the cell (measured from the position of the sparger upwards).

In other words, the pulp-froth interface is located at the horizontal level in the cell with the maximum differential change in the air hold-up.

4.1.4 Pulp phase

The reverse froth flotation concept is based on feeding coarse particles onto the top of a continuously renewed froth 'bed' (see section 3.4). Once the particles have passed through the pulp-froth interface into the pulp phase, it is assumed that due to the coarse nature of the test particles (see Table 3-1 & Table 3-2), the particles would not re-attach to rising bubbles and thereby report back to the froth phase. For the purposes of modelling, the pulp phase is therefore only seen as a bi-component system (air and liquid).

4.1.5 Particle Velocity

Once introduced into the froth phase, the particles will interact with the froth structures and either be carried towards the third compartment or break through the froth at a rate dictated by the physical properties of the liquid films and the particles. For the purpose of this dissertation, the **absolute velocity** of a particle in the froth is defined as the velocity relative to an arbitrarily chosen stagnant point outside of the flotation cell. The particle will also move relative to the surrounding froth structures. In order to describe such movement, the **settling velocity** of a particle is defined as its velocity *relative* to the surrounding froth structures.

4.2 Background to the Model

With the commonly used terminology defined, we will now look at how a froth is formed, how the froth structure can be expected to change inside a froth and how coarse particles behave as they settle through a froth. This information, although qualitative, will form the backbone of the dynamic model described in chapter 5 to 7.

4.2.1 The formation of a froth

A film of liquid is formed when a gas bubble, rising in the liquid phase, approaches another bubble (Figure 4-1, Step 1). The foam is described as a 'wet foam' and consists of spherical bubbles separated by thick liquid walls or lamellae. If a surface active agent (frother) is present, the flow in the liquid films will be retarded, and the bubble shapes will flatten (Figure 4-1, Step 2). This distortion continues until the critical gas phase volume is reached upon which the characteristic froth structure of thin liquid lamellae and Plateau borders arises (Figure 4-1, Step 3).

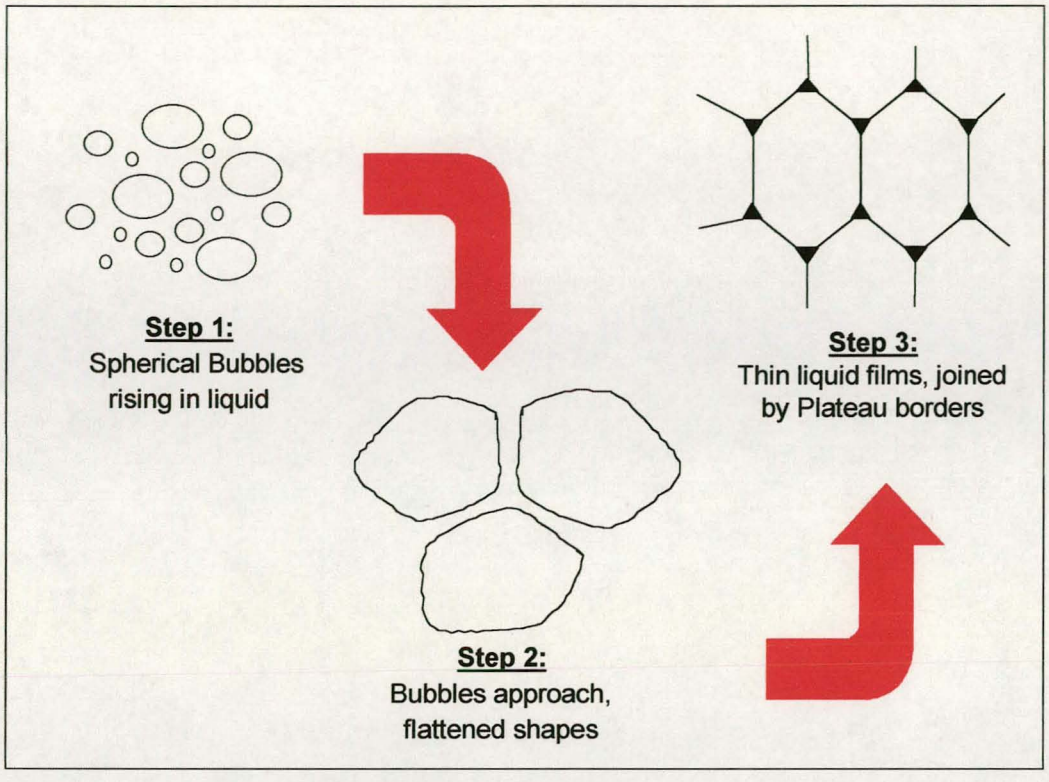

Figure 4-1: Steps during formation of a froth

The stability of a froth is directly related to the stability of these liquid lamellae. As the water drain from the froth with increasing height above the pulp-froth interface, the size of the bubbles increases due to coalescence and a decreased hydrostatic pressure. The froth therefore becomes more rigid but less stable with increasing height above the pulp-froth interface, which will affect the flotation of particles of various surface characteristics and sizes in the novel flotation cell.

4.2.2 The behaviour of particles in a froth

Visual observations of the behaviour of particles in the froth phase of the cell have shown that the particles are positioned in the froth at a level where they are best supported by the bubbles. For instance, while the 1mm flat density tracers are light enough to be floating on the surface of the froth, the 2mm cubic density tracers are floating at a lower level in the froth. This suggests that there is an optimum froth

condition, at a particular bubble size, for the flotation of a particle of a certain size, shape and surface characteristics.

This optimum froth condition can be explained intuitively. Figure 4-2 is a schematic representation of a particle in the froth phase of the cell. The particle is introduced onto the froth surface where the froth is well drained and the interstitial bubble films are relatively thin (Figure 4-2 (a)). At this position only a few thin liquid films support the particle. Although these films, or 'legs', are very rigid, they may not be strong enough to support the particle and the particle could slip down in the froth until it reaches a position near the middle of the froth as depicted in Figure 4-2 (b). At this position, the bubbles are smaller and the liquid hold-up is higher. The particle is now supported by a larger number of thicker 'legs', albeit that the 'legs' are less rigid. If the particle is too heavy, it will slip down even further into the froth (Figure 4-2 (c)). Although the 'legs' are thicker in this position in the froth, they are not rigid enough to support the particle, and the particle would settle from the froth phase into the liquid phase below. Using the same analogy, it follows that a flat particle with the same mass as a more spherical particle would be supported by more bubble films, and hence would float more easily in the froth.

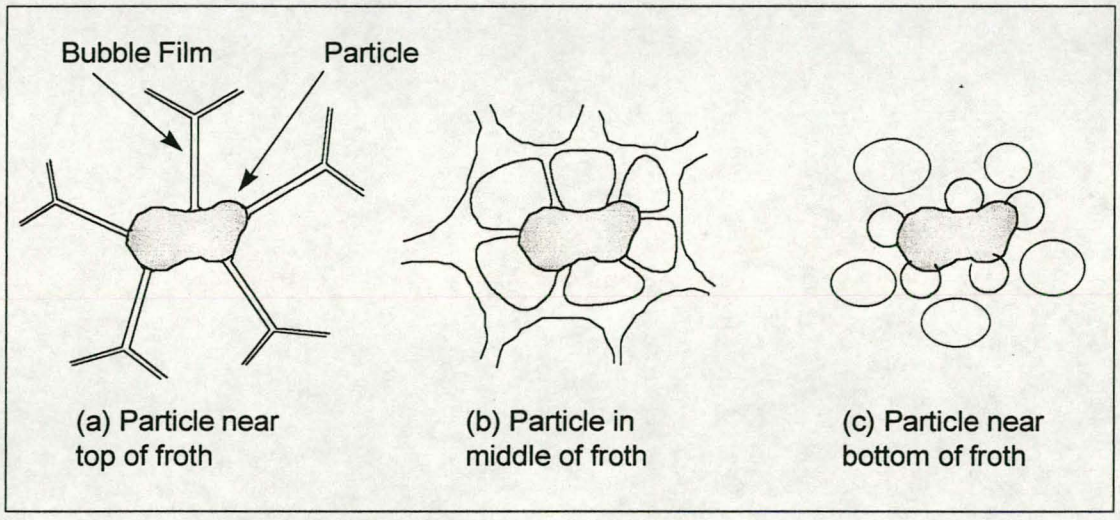

Figure 4-2: Schematic representation of a particle at various vertical positions in a froth

4.3 Initial Modelling Attempts

4.3.1 Bubble Swarm Model

As far as could be ascertained, no published data or models exist on the support of particles by a froth. It was therefore initially attempted to model the coarse particle/bubble interactions by modification of equations describing the settling of particles in a bubble swarm, such as those in an aerated liquid. However, this idea was not pursued further because of important differences between the mechanisms in a bubble swarm and the settling of particles through a froth. These included:

- While the air hold-up in a swarm of bubbles in a liquid is approximately 20 percent, it is much higher in a froth, normally in excess of 80 percent. This means that particle-bubble interaction (and in particular particle-liquid film interaction) would play a more significant role in the froth than in an aerated liquid.
- The surface characteristics of particles do not influence their settling velocity in a liquid, but, because of the bubble-particle interactions, it would certainly be affected in a froth. The relative hydrophobicity or hydrophilicity of the particles would determine the degree to which the settling would be affected.
- The equations for particles settling in a bubble swarm describe conditions where the particles are small in relation to the bubbles. In the reverse froth flotation process, the particles are of an equivalent size or larger than the bubbles. A number of bubbles would therefore surround a particle, compared to a number of particles surrounding a bubble in conventional flotation theory.

4.3.2 The Ross Model

A phenomenological model of the technique was developed by Ross[46] to investigate the effects of numerous parameters on the process in a theoretical manner. The model was based on the work by Dippenaar[15] and Hemmings[17].

As discussed in section 2.3, Dippenaar observed that a moderately hydrophobic particle can be turned into an effective film breaking particle if the particle is coated by a substrate that produces a contact angle of more than 90° on the particle. Hemmings, in turn, postulated a Protruding Particle Theory. Since both these authors' work was found to be analogous to the mechanisms in the reverse froth flotation cell, their respective theories were expanded to account for the various particle and froth properties. As stated above, a particle in the froth is surrounded by a number of bubble films. Although a particle is not immersed in the film to the same degree as assumed by Dippenaar and Hemmings, it was assumed that the same principles of bubble film stability and film rupturing action would apply at each point where the bubble films are in contact with the particle.

Particle characteristics such as size, shape, orientation and surface characteristics as well as froth characteristics such as thickness of bubble films, bubble size and residence time of bubbles in the cell, were incorporated. Due to the lack of published work on the field of particle support by bubble films, it was attempted to describe the behaviour of particles in terms of the *assumed* behaviour of a particle of a given size, shape and surface characteristics. It was assumed that such a reference particle was supported just strongly enough by the bubble films of a certain thickness and rigidity to float. The relative ease at which any other particle would float (or sink) in the froth was then described in terms of the constructive or destructive stresses caused on the bubble films by the particles (Hemmings[17]).

Two different mechanisms were considered by Ross[46] to account for the behaviour of hydrophobic and hydrophilic particles respectively, i.e:

- A highly hydrophobic particle would not tend to immerse itself in the bubble films. The dominant mechanisms for hydrophobic particles were therefore assumed to be the thinning and resultant rupture of the bubble films.
- A hydrophilic particle would tend to immerse itself in the bubble films. In addition to being supported by the bubble films below the particle, the films above the particle could exert an upward force on the particle if its contact angle is sufficiently low. In such a case the particle would try to establish an equilibrium contact angle with the liquid films and could even be lifted by the bubble films above the particle.

4.3.2.1 Modifications to the Ross Model

A detailed study of the Ross model[46] was conducted and a couple of minor changes were made to it. Ross assumed that because of the large d_p/T ratio (where d_p is the particle diameter and T is the bubble film thickness), the instantaneous contact angle, θ_i in all cases will be approximately 90°. The driving force for bubble thinning was therefore assumed to be equal to the equilibrium contact angle minus 90°. The decision whether a particle was hydrophobic or hydrophilic was therefore made on whether its equilibrium contact angle was greater or less than 90°. Hemmings[17], however, postulated that the condition that is required to produce a destructive compressive stress reaction in a bubble film is:

$$\cos\theta < \frac{T}{d_p} < \cos\frac{\theta}{2} \qquad \textbf{Equation 4-2}$$

where θ is the contact angle, T is the bubble film thickness and d_p is the diameter of the particle. The condition that is required to provide a supportive tensile stress reaction in the bubble film and thus allowing the particle to be carried along in the froth is:

$$0 < \frac{T}{d_p} < \cos\theta \qquad \textbf{Equation 4-3}$$

By calculating the T/d_p ratio, the criteria in Equations (4-2) and (4-3) can therefore be used to decide whether a particle would react as hydrophilic or hydrophobic. The equivalent diameter of a particle, D_e, was used as the relevant d_p value. It is defined as follows:

Let D_l be the second longest dimension of the particle and define a volume and area factor. If V_p is the volume of the particle, then:

$$V_p = \phi_v \frac{\pi}{6} D_l^3 \qquad \textbf{Equation 4-4}$$

where ϕ_v = volume factor (ϕ_v = 1 for sphere).

If A_p is the area of the particle, then:

$$A_p = \phi_a \pi D_l^2$$ **Equation 4-5**

where ϕ_a is the area factor (ϕ_a = 1 for sphere).

Then, define the shape factor, λ, as:

$$\lambda = \frac{\phi_a}{\phi_v}$$ **Equation 4-6**

The equivalent diameter, D_e, of any particle is therefore equal to the diameter of a sphere with the same area to volume ratio as that of the particle, i.e:

$$D_e = \frac{D_l}{\lambda}$$ **Equation 4-7**

These changes were incorporated into the model and a computer program was written to do the calculations. The computational procedure for the program is as follows:

1) ENTER:
   - equilibrium contact angle, aeration rate, water flowrate associated with bubbles and bubble diameter.
   - Particle shape (cube, cylinder, flat, sphere), and relevant particle dimensions.
2) CALCULATE:
   - Shape factor, λ, and equivalent particle diameter, D_e.
   - Bubble radius, bubble film thickness and critical contact angle (from Hemmings[17]).
3) If equilibrium contact angle > critical contact angle then particle is hydrophobic, else particle is hydrophilic.
4) HYDROPHOBIC PARTICLES:
   - ENTER: k_f value (film thinning constant).
   - CALCULATE: Time for film breakage, time to fall through bubble, settling velocity, critical settling velocity.
   - CHECK: Report particle to overflow or underflow ?
5) HYDROPHILIC PARTICLES:
   - ENTER: Reference particle contact angle, reference ratio, reference particle density, simulated particle density, value of proportionality constant, k_i, and orientation notation.
   - CALCULATE: Reference ratio, surface ratio.
   - CALCULATE: force acting on simulated particle in relation to reference particle (cube), incorporating effects of surface ratios and orientation.

4.3.2.2 Discussion on modified Ross model.

The proposed model suffered from various shortcomings, the worst being the lack of indication from the model as to the dynamic behaviour of coarse particles in the reverse froth flotation cell. One of the biggest shortcomings is the fact that the particle density is not incorporated in the hydrophobic section of the model (density has a pronounced influence on the behaviour of particles in the froth - see section 9). In conjunction with this, no provision is made for the change over from a film breaking particle to a film stabilising particle.

The interaction of a particle with a bubble film is also omitted and is replaced by a film thinning constant (k_f). However, since the froth characteristics change with froth depth it cannot be assumed that the value of k_f will stay constant through the depth of the froth phase (see section 4.2.2). In addition, the behaviour of particles is described in terms of the assumed behaviour of a particle of given properties. It was assumed that such a reference particle was supported just strongly enough by the bubble films of a certain thickness and rigidity to float. The relative ease with which any other particle would float (or sink) in the froth was then described in terms of the constructive or destructive stresses caused on the bubble films by the particles together with a proportionality constant, k_i.

Very few dynamic interactions are therefore investigated in the modified Ross model, and only a relative indication as to the behaviour of the particle can be obtained. It therefore seems as if a very complex model will be needed to predict the behaviour of particles in the froth, especially if various particle shapes have to be incorporated.

4.4 The Requirements of a Dynamic Model

In order to understand and interpret the various factors that affect the behaviour of coarse particles in the cell, a fundamental model of the various mechanisms in the froth is required. Since it was observed that there is an optimum froth condition per particle of specific shape, size and surface properties (see section 4.2), the model should be capable of predicting the trajectory of any particle in the froth over discrete time events. Various particle properties will therefore have to be taken into account. These include:

- The surface properties of the particle, i.e. contact angle
- The shape of the particles
- The size of the particles
- The density of particles

In order to predict the settling velocity of the particles accurately, bubble flow streamlines will have to be calculated. At any position on a streamline the froth structure will have an influence on the particle recovery. The froth structure will therefore have to be modelled at any position in the cell, including factors such as:

- Bubble size
- Thickness of bubble films

- Residence time of the bubbles in the reverse froth flotation cell
- Air hold-up
- Bubble velocity

Apart from the above froth structure and particle properties, the dynamic interaction between the particle and the bubble films must also be taken into account. In section 2.3 the particle induced film rupture mechanism proposed by Frye and Berg[18] was discussed. In summary, they assumed that capillary pressure-driven flow is the basis for the dynamics of film rupture by solid particles. This was found to be analogous to the mechanisms involved in the novel separation technique, and was seen as a way of improving the dynamic nature of the model. In addition, the Frye and Berg model incorporated all the particle properties as described above, except for particle shapes which are not volumes of revolution. (In order to simplify calculations they only considered particle shapes that are volumes of revolution). The Frye and Berg model will therefore have to be expanded to include particles of cubic and flat shape.

The Frye and Berg model integrates numerically along the particle/film contact line to determine the total time for bubble film rupture to occur. An essential parameter in this integration process is the thickness of the lamellae in contact with the particle. Since the dynamic model should be capable of predicting the trajectory of any particle in the froth over discrete time events, a model is required that can describe the froth structure at any position in the froth. This ruled out the possibility of modelling the froth structure as a structural foam. Although it is well know that the ability of closed cell foams to bear weight is related to the foam geometry, the foam density and the macro-dimensions of the foam[47], these models assume the foam to be homogeneous throughout, i.e. constant cell dimensions and interstitial film thickness.

Fortunately, many researchers have ventured into the field of describing the froth structure in a flotation cell. Moys[48], in his paper on a plug-flow model for flotation froth behaviour, gives an excellent summary of the various attempts up to 1978. However, since the froth model is simply a device used to describe the particle behaviour in the froth and not the main aim of this dissertation, a simple and fundamental model for a cellular foam (as developed by Hartland & Barber[49] and modified by Steiner, Hunkeler & Hartland[50]) was selected.

The Hartland froth models[49 & 50] predict the bubble film thickness at any height in the froth. Two essential parameters in this model are the bubble size and the air hold-up at a specific height in the froth. As described later (see section 5.5 and section 5.6) both these parameters were approximated with experimental measurements.

Once the film thickness in contact with the particle can be calculated, the interaction of the particle with the bubble films must be determined. In order to simplify the model, it was assumed that any one of three actions could take place:

1. The film thickness is greater than the particle size (typically near the pulp-froth interface). It is assumed that under this condition, the particle would be immersed into the bubble films and no bubble film thinning and rupture would take place. The particle will therefore be transported by the bubble films, along a streamline, to the next discrete time event.
2. The bubble film thickness is less than a critical bubble film thickness, which will cause the bubble films to rupture upon contact with a particle. A force balance therefore needs to be conducted on the particle to determine whether the particle will fall through the froth to a lower position in the froth. Alternately, the particle will be supported by surrounding liquid films and be carried along the relevant streamline to a new position in the froth.
3. The process of film thinning will take place. It is assumed that during the time of film thinning the particle will be carried along a streamline to a new position in the froth. Once the film breaks, however, a force balance needs to be conducted on the particle as in (2) above.

In all three these actions, streamlines of the flow profile of the froth will have to be calculated in order to predict the direction and speed of particle travel in the froth.

In summary, by combining all the above discrete events, the trajectory of any particle in the reverse flotation cell froth can be predicted. The aim of such a model is not to predict exactly the experimental observations, but rather to simulate the observed trends and hence be able to investigate variables in isolation, which is not always possible in experimental work.

The subsequent chapters will describe the development of the various sections of the dynamic model. Chapter 5 will concentrate on the development of the froth model, including streamlines, bubble size prediction, hold-up estimation and bubble film thickness calculation. Chapter 6, in turn, will concentrate on the particle/bubble film interactions including the prediction of the breakage time of a bubble film by particles of various shapes and properties (including cubes and flats). The force balance a particle is subjected to in the froth and the fall time of a particle once the bubble film has ruptured will also be developed. Lastly, chapter 7 will concentrate on the computational procedures for the dynamic model, and will give a description of the computer code written to incorporate the model.

5. MODELLING OF FROTH PHASE

The requirements for a fundamental model to describe the behaviour of coarse particles in the reverse froth flotation cell are given in section 4.4. This chapter will address the development of a fundamental model for the froth phase of the reverse froth flotation cell. In particular, it will concentrate on:

- describing the cell configuration mathematically,
- the mathematical description of the flow of bubbles in the cell (streamlines),
- determining the x,y-vector velocity components at any position on a streamline,
- calculating the bubble film thickness at any position on a streamline,
- calculating the bubble size at any position on a streamline,
- and estimating the air hold-up at any position on a streamline.

As described earlier, the froth model is merely a tool to predict the trajectory of any particle in the froth over discrete time. Therefore, some simplifying assumptions have been made. However, it is believed that these assumptions will not compromise the accuracy of any of the predictions.

5.1 Assumptions to Calculate Flow of Bubbles

By observing the flow of bubbles in the cell, it was found that the bubbles follow distinct flow patterns. By describing these flow patterns mathematically, it would therefore be possible to predict the x,y vector velocity components of any bubble in the cell. Figure 5-1 depicts the methodology followed in calculating the flow patterns of bubbles in the cell.

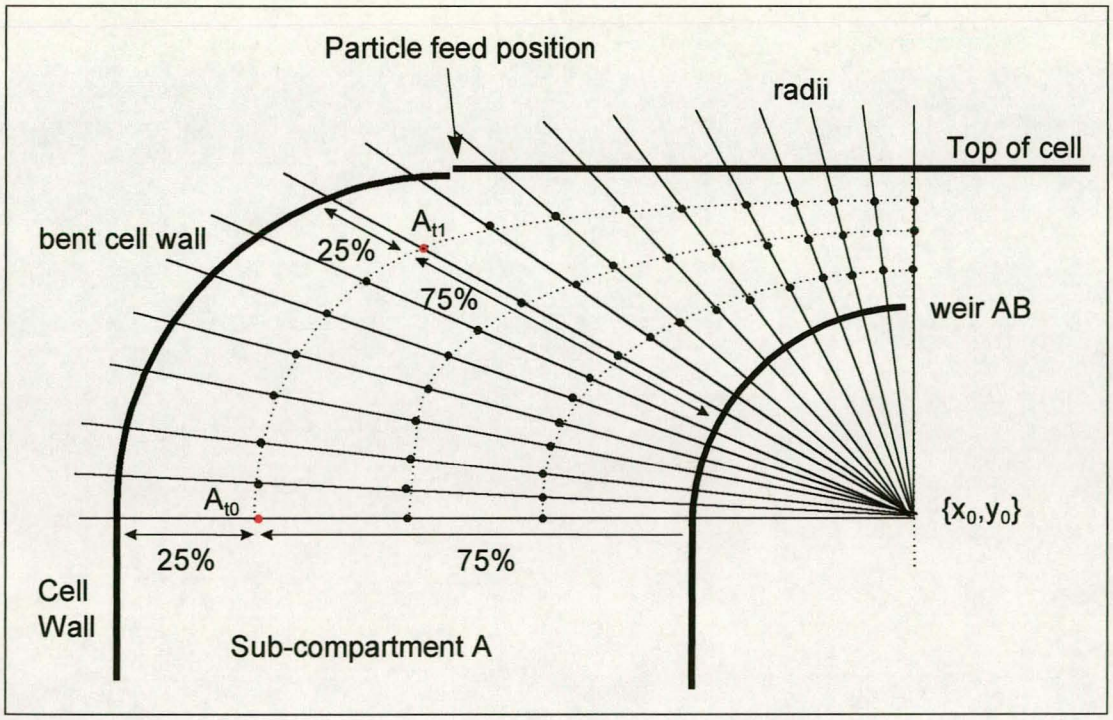

Figure 5-1: Graphical representation of bubble flow profiles

The methodology can be summarised as follows:

- Select an appropriate co-ordinate system with origin depicted as $\{x_0,y_0\}$.
- From the $\{x_0,y_0\}$ origin, draw radii to intersect the physical boundaries of the section of the cell being described. In Figure 5-1 the procedure is shown for sub-compartment A in the concentrate compartment (see section 3.2). The physical boundaries are therefore the bent cell wall, the weir between sub-compartment A and sub-compartment B (weir AB) and the top of the cell.
- Assume that a specific bubble will remain at the same relative distance from the physical boundaries of the system, along all radii. Consider the bubble marked as *A* in Figure 5-1. Upon entering the section of the cell being described (A_{t0}) the bubble is positioned 25% from the wall of the cell and 75% from weir AB on the first radius line. At time *t1* (A_{t1} in Figure 5-1) the bubble has moved up in the cell, but it remains at a relative position of 25% from the wall of the cell and 75% from weir #1 along the specific intercept length.
- By simply "connecting the dots" a flow line of a bubble can now be plotted.
- In order to adapt to different conditions in the cell, the origin of the co-ordinate system, $\{x_0,y_0\}$, can be moved, thereby plotting different flow patterns of bubbles.
- By following this methodology, the position of any bubble A_i at time *tj* can be predicted.

In order to use this methodology, the following mathematical descriptions are required:

- The physical boundaries of each section have to be described mathematically in terms of the chosen co-ordinate system.
- The distance between the physical boundaries (intercept length) of the cell, along a specific radius has to be calculated.
- The bubble position then has to be superimposed on this intercept length.
- The direction of movement of a bubble on an intercept length has to be calculated.

5.2 Mathematical Description of the Cell Configuration

Figure 5-2 is an illustration of the side view of the top section of the reverse froth flotation cell. Since we are only interested in the interaction of particles with the froth phase, we only need to declare variables around the froth section of the cell. The following variables are physical dimensions of the cell:

- r_1 = radius of the bent cell wall of sub-compartment A = 90 mm in the test cell
- r_2 = radius of the weir between sub-compartments A and B (weir AB) = 55 mm in the test cell
- r_3 = radius of the weir between sub-compartment B and the middlings compartment (M) = weir BM = 35 mm in the test cell
- h_1 = depth from the top of the cell to the top of weir AB = 40 mm in the test cell
- h_2 = depth from the top of the cell to the top of weir BM = 65 mm in the test cell
- l_1 = width of sub-compartment A = 150 mm in the test cell
- l_2 = width of sub-compartment B = 150 mm in the test cell

In addition to these physical dimensions, the depth from the top of the cell to the overflow height of the froth (h_3) needs to be specified.

To assist with the mathematical description, various constants for the cell configuration are defined. As shown in Figure 5-2, these include:

$$k_1 = h_2 + r_3 - r_1 \qquad \textbf{Equation 5-1}$$

$$k_2 = h_2 + r_3 - h_1 - r_2 \qquad \textbf{Equation 5-2}$$

$$k_3 = l_1 + l_2 + r_3 - r_1 \qquad \textbf{Equation 5-3}$$

$$k_4 = l_2 + r_3 - r_2 \qquad \textbf{Equation 5-4}$$

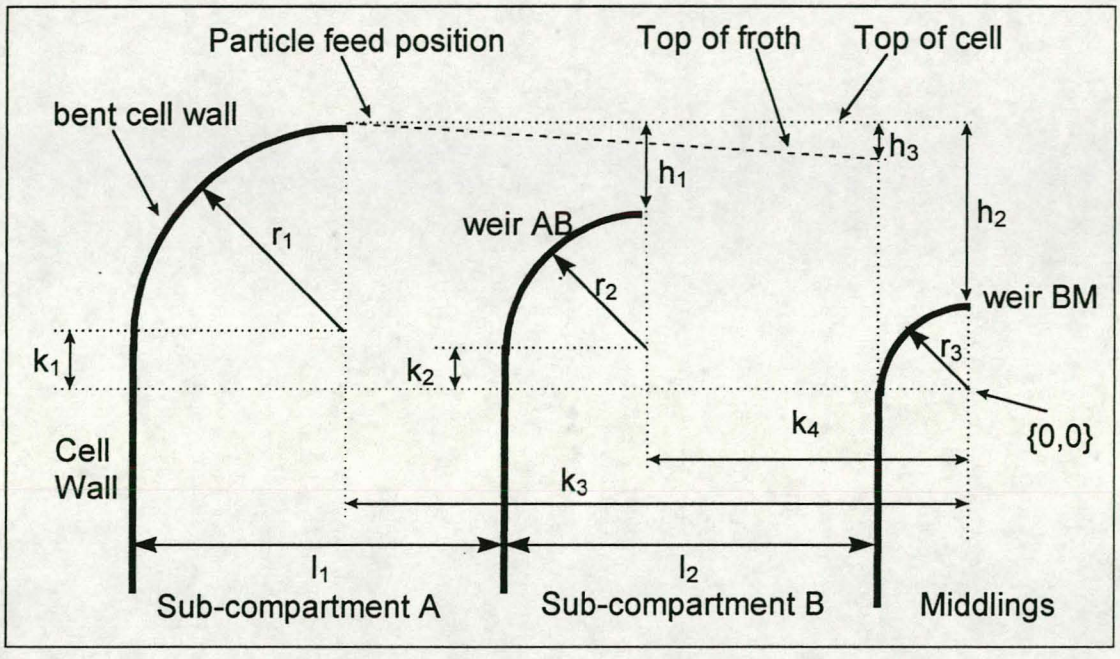

Figure 5-2: Descriptive explanation of variables for physical cell configuration

Using the above variables and constants, the cell boundaries can now be described in terms of a co-ordinate system, with the origin indicated as {0,0} in Figure 5-2:

➢ Equation for vertical part of cell wall:

$$\therefore x = -(k_3 + r_1)$$

$$\therefore y = x \times \tan(\theta) \qquad \textbf{Equation 5-5}$$

with θ = angle of radius drawn from {0,0}

➢ Equation for curved part of cell wall:

$$(x - k_3)^2 + (y - k_1)^2 = r_1^2 \qquad \textbf{Equation 5-6}$$

➢ Equation for weir AB:

$$(x-k_4)^2+(y-k_2)^2=r_2^{\,2}$$ **Equation 5-7**

➢ Equation for weir BM:

$$x^2+y^2=r_3^{\,2}$$ **Equation 5-8**

➢ Equation for top of cell:

$$\therefore y=(h_2+r_3)$$

$$\therefore x=\frac{y}{\tan(\theta)}$$ **Equation 5-9**

with θ = angle of radius drawn from {0,0}

5.3 Mathematical Description of Bubble Flow

The froth bed was subdivided into three areas in order to describe the flow of bubbles. These are depicted in Figure 5-3:

- Area #1 is the froth area bordered by the curved cell wall, the top of the froth and weir AB. In addition, the area is bordered by a line drawn from the co-ordinate origin, $\{x_0,y_0\}$, through the end of weir AB and perpendicular to the top of the froth.
- Area #3 is bounded by the top of the froth and a parallel line drawn from the end of weir AB. The remaining two borders are the perpendicular line segment described above and a vertical line from the top of the froth through the top of the splitter plate.
- Weir AB and weir BM, together with the parallel line drawn from the end of weir AB (as described above), border area #2. The horizontal line through the {0,0} origin and the vertical line from the top of weir BM to the splitter plate form the remaining boundaries.

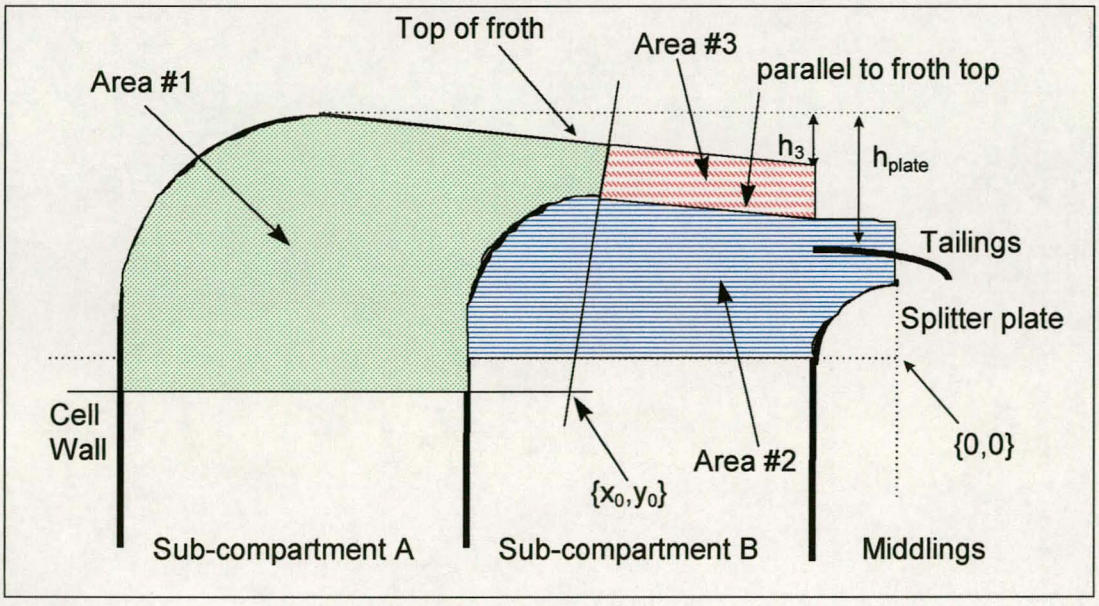

Figure 5-3: Froth areas used in froth model

The co-ordinate system with origin $\{x_0,y_0\}$ has been defined to assist with the calculation of flow lines in froth areas #1 and #3, as well as to have some flexibility to adjust the flow lines in these areas. Figure 5-4 shows how the origin of this reference co-ordinate system is derived:

- The user specifies y_0 in terms of the reference point indicated in Figure 5-4 (origin of circle superimposed on weir AB). The y_0 value in Figure 5-4, would therefore be negative.
- A line is constructed perpendicular to the straight line describing the top of the froth and intersecting the end-point of weir AB.
- By using standard geometry and with reference to the constants declared in Figure 5-2, it is possible to calculate the value of x_0 (with reference to the reference point) as:

$$x_0 = (r_2 - y_0) \cdot \frac{-h_3}{(l_1 + l_2 - r_1)}$$ **Equation 5-10**

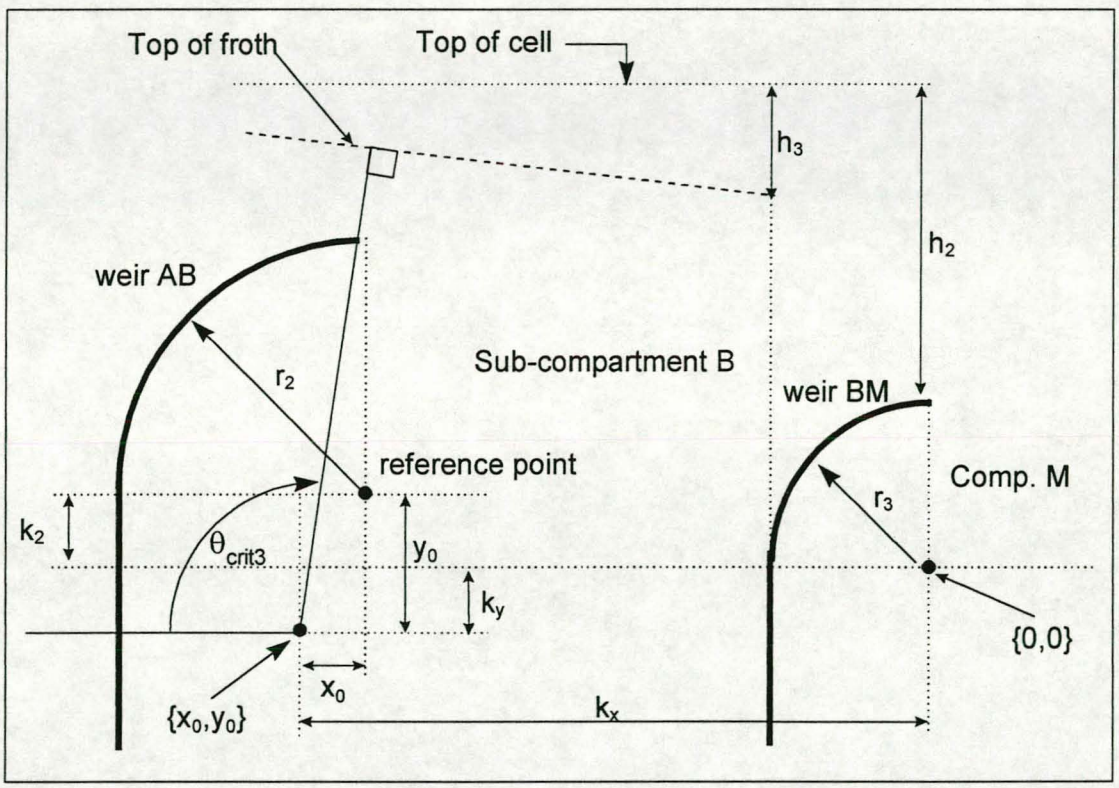

Figure 5-4: Definition of $\{x_0,y_0\}$ co-ordinate system

In order to convert between the $\{x_0,y_0\}$ and $\{0,0\}$ co-ordinate systems, two additional constants, k_x and k_y, are defined as:

$$k_x = k_4 - x_0$$ **Equation 5-11**

$$k_y = k_2 + y_0$$ **Equation 5-12**

In addition, to define the right-most boundary of froth area #1, the angle, θ_{crit3}, can be defined as:

$$\theta_{crit3} = \frac{\pi}{2} + \arctan\left(\frac{x_0}{r_2 - y_0}\right) \qquad \textbf{Equation 5-13}$$

However, should x_0 be positive as calculated by Equation 5-10 (if froth is very stable and top of froth extends above the top of the cell), the right-most boundary of froth area #1 is a vertical line from $\{x_0,y_0\}$ to the top of the cell.

5.3.1 Bubble flow calculation: Froth Area #1

The bubble flow lines for the froth area #1 are calculated in terms of the $\{x_0,y_0\}$ co-ordinate system. The area is subdivided according to the equations governing the physical boundaries of the area, as shown in Figure 5-5. Three sub-areas are defined based on the degrees of revolution around the $\{x_0,y_0\}$ origin of the co-ordinate system[2]. The three areas are:

- The area circumscribed by the bent cell wall, weir AB and radii (from $\{x_0,y_0\}$ origin) drawn at 0° and θ_{crit1}° respectively. θ_{crit1} is defined by the point $\{(l_1+l_2+r_3-k_x),(k_1-k_y)\}$ on the wall of the flotation cell, i.e:

$$\theta_{crit1} = \arctan\left(\frac{k_1 - k_y}{l_1 + l_2 + r_3 - k_x}\right) \qquad \textbf{Equation 5-14}$$

- The area circumscribed by the bent cell wall, weir AB and radii (from $\{x_0,y_0\}$ origin) drawn at θ_{crit1}° and θ_{crit2}° respectively with θ_{crit2} being defined by $\{(k_3-k_x),(r_1+k_1-k_y)\}$ on the end of the bent cell wall, i.e:

$$\theta_{crit2} = \arctan\left(\frac{r_1 + k_1 - k_y}{k_3 - k_x}\right) \qquad \textbf{Equation 5-15}$$

- The area circumscribed by the top of the froth, weir AB and radii corresponding to θ_{crit2}° and θ_{crit3}°, where θ_{crit3} is as defined in section 5.3, Equation 5-13 and shown in Figure 5-4.

The bubble flow profiles are described in terms of the angle of revolution around the $\{x_0,y_0\}$ origin, from zero degrees to θ_{crit3}. For each angle, θ (see Figure 5-5), the co-ordinates of the intercept with the physical boundaries of the sub-area are calculated. Once these co-ordinates, say (x_1,y_1) and (x_2,y_2), have been calculated (see Figure 5-5), the length of the intercept can be calculated from:

$$D = \sqrt{(x_1 - x_2)^2 + (y_1 - y_2)^2} \qquad \textbf{Equation 5-16}$$

where D = length between the two intercept points on the physical cell boundaries, as shown in Figure 5-5.

---

[2] For the purpose of this dissertation, the zero degree point is at the conventional 9 o'clock position, while the rotation around the $\{x_0,y_0\}$ origin is in the clockwise direction.

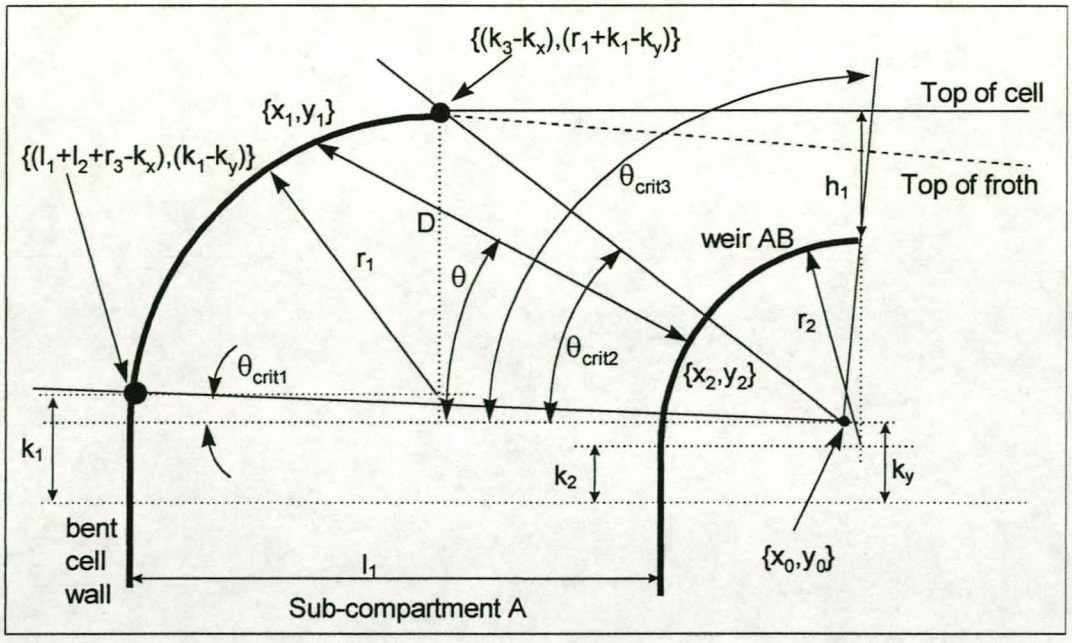

Figure 5-5: Definition of sub-areas for froth area #1 flow line calculation

5.3.1.1 Froth area #1, sub-area 1: angles from zero to θ_{crit1}

By using simple geometry, it can be shown that for all angles, θ, less that θ_{crit1}, the equations describing the co-ordinates of the intercept with the vertical cell wall will be:

$$x_1 = -\left(l_1 + l_2 + r_3 - k_x\right)$$
$$y_1 = -x_1 \times \tan(\theta)$$

Equation 5-17

The mathematical description of weir AB in terms of the $\{x_0,y_0\}$ co-ordinate system is:

$$\left(x_2 + x_0\right)^2 + \left(y_2 + y_0\right)^2 = r_2^{\,2}$$

Equation 5-18

However:

$$y_2 = -x_2 \times \tan(\theta)$$

Equation 5-19

By substituting equation 5-19 into equation 5-18, it can be shown that for the same angle, θ, in equation 5-17, the equation describing the co-ordinates of the intercept with weir AB will be:

$$\left(1 + \tan^2(\theta)\right) \cdot x_2^{\,2} + \left(2x_0 - 2y_0 \cdot \tan(\theta)\right) \cdot x_2 + \left(x_0^{\,2} + y_0^{\,2} - r_2^{\,2}\right) = 0$$

Equation 5-20

By solving for x_2 in equation 5-20 and substituting back into equation 5-19, the (x_2,y_2) co-ordinate can be determined.

By substituting (x_1,y_1) (from equation 5-17) and (x_2,y_2) into equation 5-16, the length between the intercepts, *D*, can be calculated. By following the procedure outlined in section 5.1, the bubble flow profiles of any bubble in this sub-area can now be calculated.

5.3.1.2 Froth area #1, sub-area 2: angles from θ_{crit1} to θ_{crit2}

Again by using simple geometry, the co-ordinates of the points of intercept of the radii with the sub-area boundaries can be determined as follows:

For all angles, θ, where $\theta > \theta_{crit1}$ and $\theta < \theta_{crit2}$, the equation describing the bent cell wall in terms of the $\{x_0,y_0\}$ co-ordinate system is:

$$\left(x_1 - \left(k_x - k_3\right)\right)^2 + \left(y_1 - \left(k_1 - k_y\right)\right)^2 = r_1^{\,2} \qquad \textbf{Equation 5-21}$$

However:

$$y_1 = -x_1 \times \tan(\theta) \qquad \textbf{Equation 5-22}$$

By substituting equation 5-22 into equation 5-21, it can be shown that the equation describing the co-ordinates of the intercept with the bent cell wall is:

$$\left(1 + \tan^2(\theta)\right) \cdot x_1^{\,2} + \left(-2\left(k_x - k_3\right) + 2\left(k_1 - k_y\right) \cdot \tan(\theta)\right) \cdot x_1 + \left(\left(k_x - k_3\right)^2 + \left(k_1 - k_y\right)^2 - r_1^{\,2}\right) = 0 \qquad \textbf{Equation 5-23}$$

By solving x_1 in equation 5-23, and substituting back into equation 5-22, the $\{x_1,y_1\}$ co-ordinate can be determined.

Since weir AB remains the other boundary of this sub-area, the $\{x_2,y_2\}$ co-ordinates are calculated as described in section 5.3.1.1 (using equations 5-18 to 5-20) for all angles, θ.

By substituting (x_1,y_1) (from equation 5-23) and (x_2,y_2) into equation 5-16, the length between the intercepts, *D*, can be calculated. By following the procedure outlined in section 5.1, the bubble flow profiles of any bubble in this sub-area can now be calculated.

5.3.1.3 Froth area #1, sub-area 3: angles from θ_{crit2} to θ_{crit3}

From equation 5-13 it can be shown that in terms of the $\{x_0,y_0\}$ co-ordinate system the gradient (*m*) of the right-most boundary line of froth area #1 is:

$$m = \frac{r_2 - y_0}{-x_0} \qquad \textbf{Equation 5-24}$$

Since this line is defined as perpendicular to the line describing the top of the froth in the new flotation cell (see section 5.3), the gradient of the top of the froth (*g*) in terms of the $\{x_0,y_0\}$ co-ordinate system is:

$$g = -m = \frac{x_0}{r_2 - y_0} \qquad \textbf{Equation 5-25}$$

In terms of the $\{x_0,y_0\}$ co-ordinate system, the co-ordinates of the point defining θ_{crit2} (end of bent cell wall) are $\{(k_x-k_3);(r_1+k_1-k_y)\}$. Since this point lies on the line describing the top of the froth, it can be shown that the equation describing the top of the froth in the novel flotation cell is:

$$y_1 = \frac{x_0}{r_2 - y_0} \cdot x_1 + \left[r_1 + k_1 - k_y - \frac{x_0}{r_2 - y_0}(k_x - k_3) \right] \qquad \textbf{Equation 5-26}$$

By substituting equation 5-22 into equation 5-26 for all angles, θ, where $\theta < \theta_{crit3}$ and $\theta > \theta_{crit2}$, it can be shown that:

$$x_1 = \frac{\left[r_1 + k_1 - k_y - \frac{x_0}{r_2 - y_0}(k_x - k_3) \right]}{-\left(\tan(\theta) + \frac{x_0}{r_2 - y_0} \right)} \qquad \textbf{Equation 5-27}$$

By solving x_1 in equation 5-27, and substituting back into equation 5-22, the $\{x_1,y_1\}$ co-ordinate can be determined.

As in section 5.3.1.2, weir AB remains the other boundary of this sub-area. The $\{x_2,y_2\}$ co-ordinates are therefore calculated as described in section 5.3.1.1 by using equation 5-18 to 5-20.

By substituting (x_1,y_1) (from equation 5-27) and (x_2,y_2) into equation 5-16, the length between the intercepts, *D*, can be calculated. By following the procedure outline in section 5.1, the bubble flow profiles of any bubble in this sub-area can now be calculated.

5.3.1.4 Froth area #1, extended sub-area 3: angles from θ_{crit3} to $\theta = 90°$

As described in section 5.3, a special case exists if the froth is very stable and the top of the froth expands to above the top of the cell. Under such conditions x_0 is calculated as a positive value (see equation 5-10), and the right-most boundary of froth area #1 is defined as a vertical line from $\{x_0,y_0\}$ to the top of the cell. The sub-area 3 of the froth area #1 is therefore extended, resulting in additional co-ordinates to be calculated.

For this extended area, the top of the froth remains the one boundary. The $\{x_1,y_1\}$ co-ordinates are therefore calculated by using equation 5-22 and equation 5-27 (as described in section 5.3.1.3).

The other boundary is described by a line drawn parallel to the line describing the top of the froth (see section 5.3). This boundary would therefore have the same gradient as the top of the froth, i.e.

$$g = -m = \frac{x_0}{r_2 - y_0} \qquad \textbf{Equation 5-28}$$

In terms of the $\{x_0,y_0\}$ co-ordinate system, the co-ordinates of the point defining the end of weir AB is $\{(-x_0);(r_2-y_0)\}$. Since this point lies on the line describing the bottom boundary of this extended sub-area, it can be shown that the equation describing this boundary is:

$$y_2 = \frac{x_0}{r_2 - y_0} \cdot x_2 + \left[r_2 - y_0 + \frac{{x_0}^2}{r_2 - y_0} \right] \qquad \textbf{Equation 5-29}$$

By substituting equation 5-19 into equation 5-29 for all angles, θ, where $\theta < 90°$ and $\theta > \theta_{crit3}$, it can be shown that:

$$x_2 = \frac{\left[r_2 - y_0 + \frac{{x_0}^2}{r_2 - y_0} \right]}{-\left(\tan(\theta) + \frac{x_0}{r_2 - y_0} \right)} \qquad \textbf{Equation 5-30}$$

By solving x_2 in equation 5-30, an substituting back into equation 5-19, the $\{x_2,y_2\}$ co-ordinate can be determined.

By substituting (x_1,y_1) (from equation 5-27) and (x_2,y_2) into equation 5-16, the length between the intercepts, *D*, can be calculated. By following the procedure outlined in section 5.1, the bubble flow profiles of any bubble in this sub-area can now be calculated.

5.3.2 Bubble flow calculation: Froth Area #2

The bubble flow lines for the froth area #2 are calculated in terms of the {0,0} co-ordinate system. The area is subdivided according to the equations governing the physical boundaries of the area, as shown in Figure 5-6. Three sub-areas are defined based on the degrees of revolution around the {0,0} origin of the co-ordinate system[3].

The three areas (as shown in Figure 5-6) are:

- The area circumscribed by weir AB, weir BM and the radii drawn (from the {0,0} origin) at 0° and θ_{crit1}° respectively, where θ_{crit1} is defined as point $\{-(l_2+r_3),(k_2)\}$ intersecting weir AB, i.e:

$$\theta_{crit1} = \arctan\left(\frac{k_2}{l_2 + r_3} \right) \qquad \textbf{Equation 5-31}$$

In the case where k_2 is negative $\theta_{crit1} = 0°$.

[3] The zero degree point is again defined at the conventional 9 o'clock position, while the rotation around the {0,0} origin is in the clockwise direction from 0° to 90°.

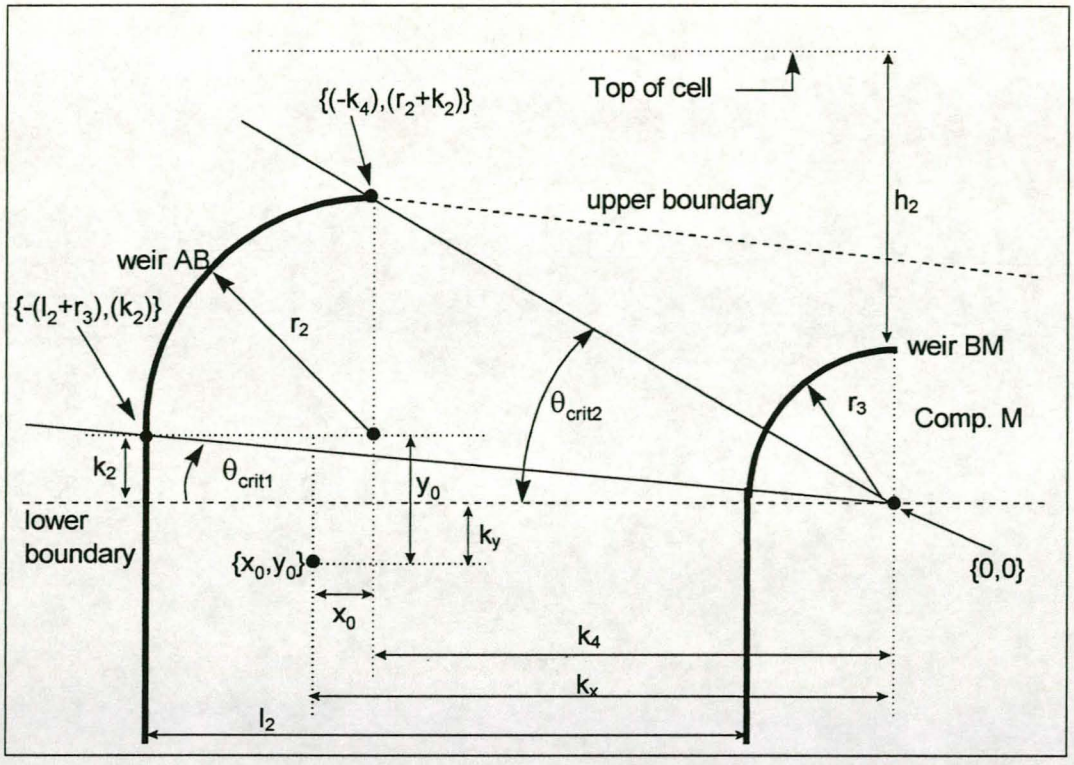

Figure 5-6: Definition of sub-areas for froth area #2 flow line calculation

- The area circumscribed by weir AB, weir BM and the radii drawn (from the {0,0} origin) at θ_{crit1}° and θ_{crit2}° respectively. θ_{crit2} is defined by the point $\{(-k_4),(r_2+k_2)\}$ intersecting weir AB, i.e:

$$\theta_{crit2} = \arctan\left(\frac{r_2 + k_2}{k_4}\right) \qquad \textbf{Equation 5-32}$$

- The area circumscribed by a line draw parallel to the top of the froth and going through the end of weir AB, weir BM and the respective radii drawn (from the {0,0} origin) at θ_{crit2}° and 90°.

As described in section 5.3.2, the bubble flow profiles are again calculated in terms of the angle of revolution around the {0,0} origin, from zero degrees to 90°. For each angle, θ (see Figure 5-6), the co-ordinates of the intercept with the physical boundaries of the sub-area are calculated. Once these co-ordinates, say (x_2,y_2) and (x_3,y_3), have been calculated the length of the intercept can be calculated from:

$$D = \sqrt{(x_2 - x_3)^2 + (y_2 - y_3)^2} \qquad \textbf{Equation 5-33}$$

where D = length between the two intercept points on the physical cell boundaries.

5.3.2.1 Froth area #2, sub-area 1: angles from zero to θ_{crit1}

Apart from the respective radii, the boundaries of this sub-area are a vertical section of weir AB and a section of weir BM (see Figure 5-6). Using simple geometry, it can be shown that the equations describing the vertical section of weir AB in terms of the {0,0} co-ordinate system are:

$$x_2 = -(l_2 + r_3)$$
$$y_2 = -x_2 \cdot \tan(\theta)$$

Equation 5-34

Since {0,0} is per definition the origin of the circle superimposed on weir BM with radius r_3, the co-ordinates of the radius intersection with weir BM can be determined from:

$$x_3 = -r_3 \cdot \cos(\theta)$$
$$y_3 = r_3 \cdot \sin(\theta)$$

Equation 5-35

In order to calculate the intercept length (*D*), the co-ordinates $\{x_2,y_2\}$ and $\{x_3,y_3\}$ (as calculated by equations 5-34 and 5-35) are substituted in equation 5-33. By following the methodology outlined in section 5.1, the bubble flow profiles of any bubble in this sub-area can now be calculated.

5.3.2.2 Froth area #2, sub-area 2: angles from θ_{crit1} to θ_{crit2}

The boundaries that have to be described mathematically for this sub-area are weir AB and weir BM (see Figure 5-6). Again by applying fundamental geometry, it can be shown that weir AB can be described in terms of the {0,0} co-ordinate system by:

$$(x_2 + k_4)^2 + (y_2 + k_2)^2 = r_2^2$$

Equation 5-36

However,

$$y_2 = x_2 \cdot \tan(\theta)$$

Equation 5-37

By substituting equation 5-37 into equation 5-36 it can be shown that:

$$(1 + \tan^2(\theta)) \cdot x_2^2 + (2k_4 + 2k_2 \cdot \tan(\theta)) \cdot x_2 + (k_2^2 + k_4^2 - r_2^2) = 0$$

Equation 5-38

By solving x_2 for equation 5-38 and substituting back into equation 5-37, $\{x_2,y_2\}$ can be determined for any angle, θ, where $\theta_{crit1} < \theta < \theta_{crit2}$.

As in section 5.3.2.1, equation 5-35 is used to determine $\{x_3,y_3\}$ any angle, θ, where $\theta_{crit1} < \theta < \theta_{crit2}$.

The co-ordinates $\{x_2,y_2\}$ and $\{x_3,y_3\}$ can now be substituted into equation 5-33 to calculate the intercept length, *D*.

5.3.2.3 Froth area #2, sub-area 3: angles from θ_{crit2} to θ = 90°

This sub-area is bound by a line drawn parallel to the top of the froth and going through the end of weir AB as well as weir BM. This parallel line is identical to the one described in section 5.3.1.4, although the line now has to be described in terms of the {0,0} co-ordinate system.

Since the gradient of the line will remain the same, equation 5-28 can still be used. However, in terms of the {0,0} co-ordinate system, the co-ordinates of the point defining the end of weir AB is $\{-(x_0+k_x);(r_2-y_0+k_y)\}$. Since this point lies on the line describing the bottom boundary of this extended sub-area, it can be shown that the equation describing this boundary is:

$$y_2 = \frac{x_0}{r_2 - y_0} \cdot x_2 + \left[r_2 - y_0 + \frac{x_0^{\,2}}{r_2 - y_0} + k_y + k_x \cdot \frac{x_0}{r_2 - y_0} \right] \qquad \textbf{Equation 5-39}$$

By substituting equation 5-37 into equation 5-39 for all angles, θ, where $\theta < 90°$ and $\theta > \theta_{crit2}$, it can be shown that:

$$x_2 = \frac{\left[r_2 - y_0 + \frac{x_0^{\,2}}{r_2 - y_0} + k_y + k_x \cdot \frac{x_0}{r_2 - y_0} \right]}{-\left[\tan(\theta) + \frac{x_0}{r_2 - y_0} \right]} \qquad \textbf{Equation 5-40}$$

By solving x_2 in equation 5-40, an substituting back into equation 5-37, the $\{x_2,y_2\}$ co-ordinate can be determined

As in section 5.3.2.1, equation 5-35 is used to determine $\{x_3,y_3\}$ any angle, θ, where $\theta_{crit2} < \theta < 90°$.

The co-ordinates $\{x_2,y_2\}$ and $\{x_3,y_3\}$ can now be substituted into equation 5-33 to calculate the intercept length, *D*.

5.3.3 Bubble flow calculation: Froth Area #3

The bubble flow lines for the froth area #3 are calculated in terms of the $\{x_0,y_0\}$ co-ordinate system. As shown in Figure 5-7, the area is subdivided into two sub-areas if x_0 is negative. However, in the case of x_0 being positive, only the second sub-area is applicable.

The froth area #3 is bounded by the line describing the top of the froth, and the line parallel to the top of the froth drawn through the end of weir AB. The remaining two borders are the line perpendicular to the top of the froth (as described in section 5.3.1.1) and a vertical line from the top of the froth through the top of the splitter plate. Due to the boundary configuration, the sub-areas are not described in terms of the degrees of revolution around the $\{x_0,y_0\}$ origin, but rather a linear co-ordinate system with $\{x_0,y_0\}$ as origin.

Once the co-ordinates of intersection, say (x_1,y_1) and (x_2,y_2), have been calculated the length of the intercept can be calculated from equation 5-16.

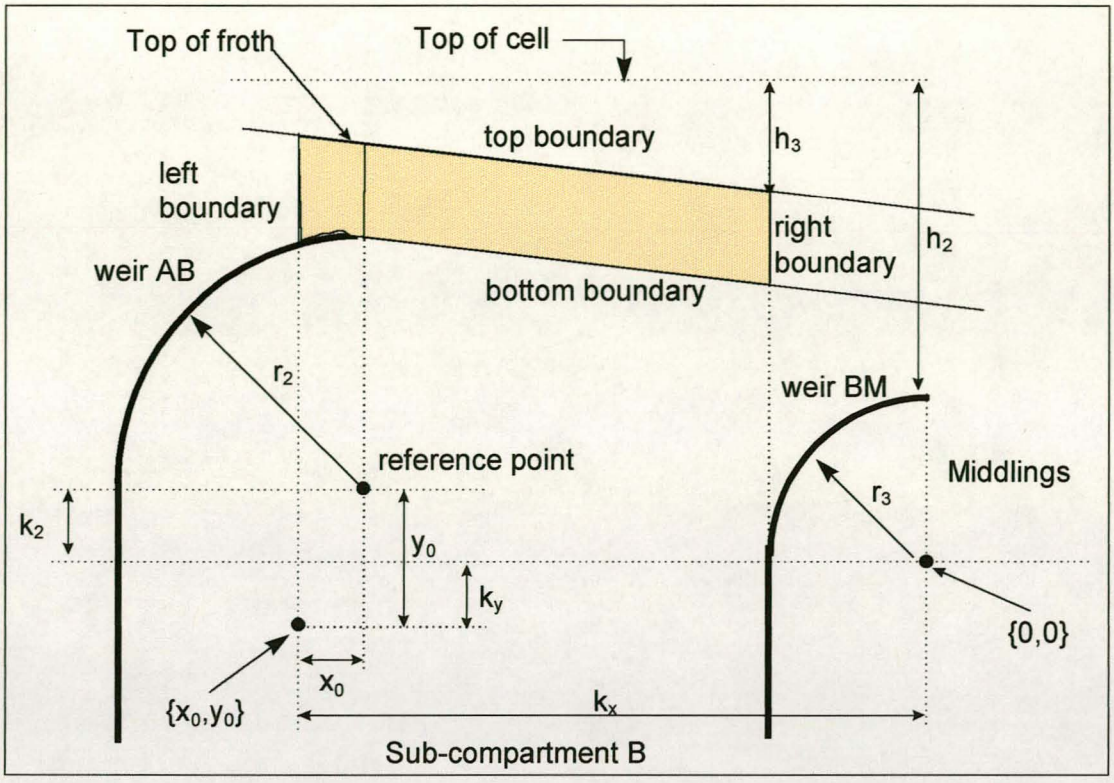

Figure 5-7: Definition of sub-areas for flow area #3 flow line calculation

5.3.3.1 Froth area #3, sub-area 1: all values of x_2 with $x_2 < 0$.

This area is only valid if x_0 is negative. In addition, the procedure to derive the equations that describe the top boundary is identical to the one described in section 5.3.1.3. The co-ordinates (x_1,y_1) can therefore be calculated by substituting x_2 for x_1 in equation 5-26.

In turn, the mathematical description of the section of weir AB in terms of the $\{x_0,y_0\}$ co-ordinate system is given by equation 5-18. The co-ordinate $\{x_2,y_2\}$ can therefore be calculated by substituting x_2 in equation 5-18.

5.3.3.2 Froth area #3, sub-area 2: all values of x_2 with $x_2 > 0$.

The top and bottom boundaries of this area are identical to those boundaries described under section 5.3.1.4. The $\{x_1,y_1\}$ co-ordinates are therefore calculated by substituting x_2 for x_1 in equations 5-26 (section 5.3.1.3), while the $\{x_2,y_2\}$ co-ordinates are calculated by substituting x_2 in equation 5-29.

5.4 Calculate Bubble Velocity Vector Components

As described in section 4.4, the model predicting the profile of a particle in the novel flotation cell could have one of three "states". The bubble film thickness could be greater than the particle size, the bubble film thickness could be less than a critical thickness or the action of bubble film thinning will take place. During all three these "states" the particle will be supported by the bubble films, or lamellae, and will be transported to a new position in the flotation cell over a discrete time period. In

order to calculate the "new" particle position in the froth, the x,y-vector components of the bubble velocity have to be determined.

If Vel_{xy} is the velocity of the bubble and θ_{dir} is the angle of direction of movement[4], then the x,y-velocity components can be determined from:

$$Vel_x = Vel_{xy} \times \cos(\theta_{dir})$$
$$Vel_y = Vel_{xy} \times \sin(\theta_{dir})$$

Equation 5-41

From equation 5-41, the angle of the direction of bubble movement, θ_{dir}, and the velocity of the bubble have to be estimated.

5.4.1 *Calculate angle of bubble movement, θ_{dir}*

In order to calculate the angle of bubble movement, θ_{dir}, consider a particle attached to a bubble at position {x,y} in the flotation cell, as shown in Figure 5-8. Per definition (see section 5.3), the bubble is situated in froth area #1. In addition, the angle of rotation, θ_{xy}, of the radius from the $\{x_0,y_0\}$ origin through the particle position is between θ_{crit1} and θ_{crit2}. The particle is therefore located in froth area #1, sub-area #2. By following the procedure as outlined in section 5.3.1.2, the $\{x_1,y_1\}$ and $\{x_2,y_2\}$ co-ordinates of the intersect points of the θ_{xy} radius with the bent cell wall and weir AB, can easily be determined.

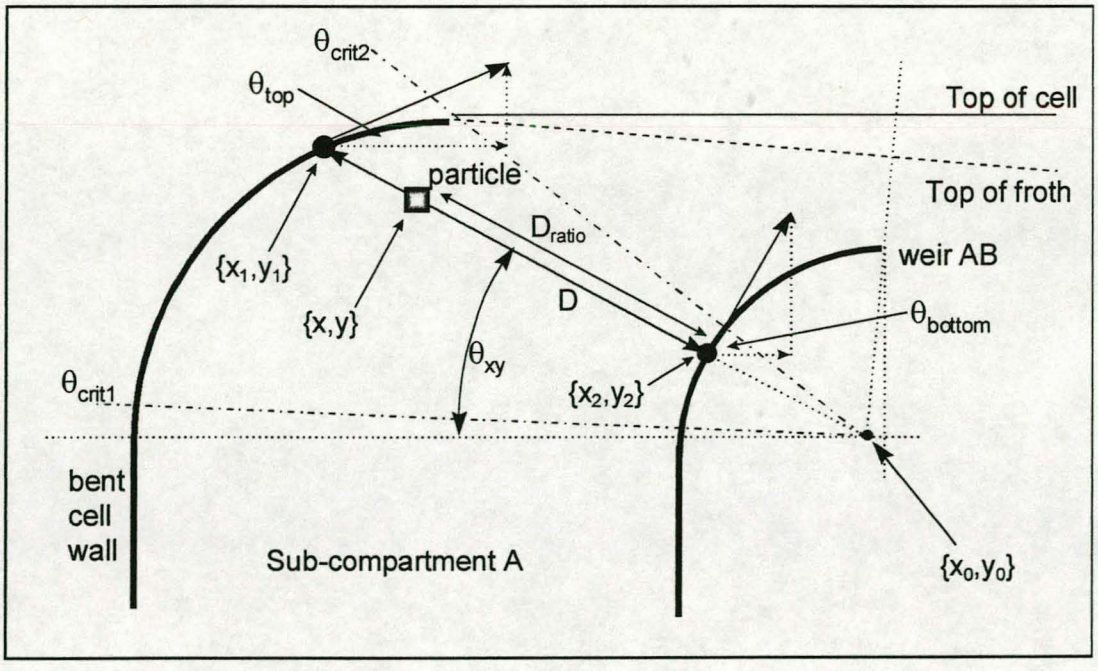

Figure 5-8: Calculation of angle of bubble movement, θ_{dir}

[4] To calculate the velocity components of the bubble, the angle of movement is defined in terms of a conventional co-ordinate system with 0° being at the three o'clock position and anti-clockwise rotation to 90° at the twelve o'clock position.

If the bubble was located close to the $\{x_1,y_1\}$ intersect (i.e. captured under the bent cell wall) the direction of movement can be described by a tangent constructed on the bent cell wall at $\{x_1,y_1\}$ (as shown in Figure 5-8). The angle of movement would then be equivalent to θ_{top}. In turn, if the bubble was located close to the $\{x_2,y_2\}$ intersect (i.e. moving along weir AB) the direction of movement would be given by a tangent constructed on weir AB at $\{x_2,y_2\}$, or θ_{bottom} as shown in Figure 5-8. Dependent on which physical sections define the top and bottom boundaries of the area in question, the two extremes in direction of movement will always be different. In order to calculate the direction of movement, θ_{dir}, at any position {x,y} in the cell, it is assumed that there is a linear relationship of the direction of movement along an intercept length, with θ_{top} and θ_{bottom} being the extremes values. This linear relationship depends on the relative position of the bubble/particle along an intercept length (D), i.e. D_{ratio}.

By using equation 5-16, the length of the intercept, D, can be calculated. Since the particle/bubble is located at the {x,y} position along this intercept, the relative particle position along the intercept, D_{ratio}, can be calculated from:

$$D_{ratio} = \frac{\sqrt{(x-x_2)^2+(y-y_2)^2}}{D} \qquad \textbf{Equation 5-42}$$

The direction of movement, θ_{dir} could therefore be calculated by:

$$\theta_{dir} = \theta_{top} \times D_{ratio} + \theta_{bottom} \times (1 - D_{ratio}) \qquad \textbf{Equation 5-43}$$

The direction of movement at the top and bottom boundary lines (θ_{top} and θ_{bottom} respectively) of each of the froth sub-areas, must therefore be determined.

5.4.1.1 Froth area #1, sub-area 1: angles from zero to θ_{crit1}

The equations governing the flow of bubbles in froth area #1, sub-area 1 are given in section 5.3.1.1. For this sub-area the top boundary is seen as the vertical section of the bent cell wall. Therefore:

$$\theta_{top} = \frac{\pi}{2} = 90° \qquad \textbf{Equation 5-44}$$

The bottom boundary is defined as weir AB, therefore:

$$\theta_{bottom} = \frac{\pi}{2} - \arctan\left(\frac{(y_2+y_0)}{-(x_2+x_0)}\right) \qquad \textbf{Equation 5-45}$$

5.4.1.2 Froth area #1, sub-area 2: angles from θ_{crit1} to θ_{crit2}

The bubble flow calculations for this sub-area are shown in section 5.3.1.2. If the bent cell wall is defined as the top boundary, then:

$$\theta_{top} = \frac{\pi}{2} - \arctan\left(\frac{\left(y_1 - \left(k_1 - k_y\right)\right)}{-\left(x_1 - \left(k_x - k_3\right)\right)}\right) \qquad \textbf{Equation 5-46}$$

Since the bottom boundary is again weir AB, equation 5-45 can be used to calculate θ_{bottom}.

5.4.1.3 Froth area #1, sub-area 3: angles from θ_{crit2} to θ_{crit3}

The equations that describe the flow of bubbles in this sub-area are derived in section 5.3.1.3. The line segment describing the top of the froth is the top boundary of this sub-area, therefore:

$$\theta_{top} = \arctan(g) \qquad \textbf{Equation 5-47}$$

with *g* being calculated from equation 5-25 in section 5.3.1.3.

Weir AB is again the bottom boundary of this sub-area. θ_{bottom} is therefore calculated from equation 5-45.

5.4.1.4 Froth area #1, extended sub-area 3: angles from θ_{crit3} to $\theta = 90°$

The bubble flow equations for the extended sub-area 3 of froth area #1 are given in section 5.3.1.4. The top boundary for this sub-area is the line describing the top of the froth, while the bottom boundary is the line, parallel to the froth top, but drawn through the end of weir AB. Since these lines are parallel, $\theta_{top} = \theta_{bottom}$ and both these values could therefore be calculated from equation 5-47.

5.4.1.5 Froth area #2, sub-area 1: angles from zero to θ_{crit1}

This froth sub-area is described by equation 5-34 and 5-35 in section 5.3.2.1. A vertical section of weir AB forms the top boundary of this sub-area. Equation 5-44 therefore describes θ_{top}. In turn, weir BM forms the bottom boundary, which leads to:

$$\theta_{bottom} = \frac{\pi}{2} - \theta \qquad \textbf{Equation 5-48}$$

where θ is the angle of revolution of the radius drawn from the {0,0} origin through the bubble position in the froth.

5.4.1.6 Froth area #2, sub-area 2: angles from θ_{crit1} to θ_{crit2}

Section 5.3.2.2 describes the equations to calculate the bubble flow profiles in froth area #2, sub-area 2. The top boundary of this area is weir AB, while the bottom boundary is weir BM. θ_{top} can therefore be calculated from:

$$\theta_{top} = \frac{\pi}{2} - \arctan\left(\frac{y_1 - k_2}{-(x_1 + k_4)}\right)$$ **Equation 5-49**

while equation 5-48 can be used to calculate θ_{bottom}.

5.4.1.7 Froth area #2, sub-area 3: angles from θ_{crit2} to θ = 90°

This sub-area is bound by the line drawn parallel to the top of the froth but going through the end of weir AB and weir BM (see section 5.3.2.3). Since this line is parallel to the froth top, θ_{top} could therefore be calculated from equation 5-47. Equation 5-48 can again be used to calculate θ_{bottom} since weir BM is the bottom boundary of this sub-area.

5.4.1.8 Froth area #3, sub-area 1: all values of x_2 with $x_2 < 0$.

Froth area #3, sub-area 1 is described in section 5.3.3.1. The top of the froth and weir AB bound the area. Equation 5-47 can therefore be used to calculate θ_{top}, while θ_{bottom} is given by:

$$\theta_{bottom} = \frac{\pi}{2} - \arctan\left(\frac{y_2 + y_0}{-(x_2 + x_0)}\right)$$ **Equation 5-50**

5.4.1.9 Froth area #3, sub-area 2: all values of x_2 with $x_2 > 0$.

The bubble flow equations for froth area #3, sub-area 2 are given in section 5.3.3.2. The top boundary for this sub-area is the line describing the top of the froth, while the bottom boundary is the line, parallel to the froth top, but drawn through the end of weir AB. Since these lines are parallel, $\theta_{top} = \theta_{bottom}$ and both these values could therefore be calculated from equation 5-47.

5.4.2 Calculate bubble velocity, Vel_XY

The bubble velocity at any {x,y} position in the froth, Vel_{xy}, is:

$$Vel_{xy} = \frac{G_{frotharea}}{A_D \cdot \varepsilon_{xy}}$$ **Equation 5-51**

where:

$G_{frotharea}$ = volumetric flowrate of air through the froth area in question.
A_D = the cross-sectional area of the flotation cell along an intercept length, D.
ε_{xy} = the estimated air hold-up at the {x,y} position.

In section 5.1, it was assumed that a bubble would remain on the same relative distance from the physical boundaries of the system, along all intercept radii. The cross-sectional are can therefore be determined by multiplying the intercept radii length, *D*, with the width of the flotation cell, which is 150 mm in the case of the experimental set-up.

In order to calculate $G_{frotharea}$, assume that air obeys the ideal gas law. Therefore:

$$P_{zj} \cdot V_{zj} = P_0 \cdot V_0 \qquad \textbf{Equation 5-52}$$

where:
P = absolute pressure
V = bubble volume

And the subscripts:
$_{zj}$ = denotes the height in the cell measured from the position of the air spargers.
$_0$ = denotes the conditions at the spargers in the cell.

Assume a hydrostatic linear decay of pressure with height in the cell,

$$P_{zj} = -\left(\frac{P_0 - P_{top}}{z_0 - z_{top}}\right) \cdot z_j + P_0 \qquad \textbf{Equation 5-53}$$

where:
P_{top} = pressure at the top of the cell
$(z_0 - z_{top})$ = height from the spargers to the top of the cell.

Since P_0 is equivalent to the absolute pressure at which air is introduced into the cell (400 kPa), the height from the spargers to the top of the cell is 0.75m and the pressure at the top of the cell is atmospheric ($P_{0.75}$ = 101.325 kPa), equation 5-53 reduces to:

$$P_{zj} = P_0 \cdot \left(1 - 0.99558 \cdot z_j\right) \qquad \textbf{Equation 5-54}$$

Substituting equation 5-54 into equation 5-52, V_{zj} can be determined as:

$$V_{zj} = \frac{V_0}{\left(1 - 0.99558 \cdot zj\right)} \qquad \textbf{Equation 5-55}$$

From the cell operation procedure, described in section 3.4.1, the air flowrate in sub-compartment B is set to a level where a froth bearing is created in froth area #2. It is therefore assumed that there is no transfer of air between froth area #2 and froth area #3. In addition it is assumed that no air escapes through the top of the froth. All the air introduced through the sparger in sub-compartment A (see Figure 3-4) therefore reports to froth area #1 and then to froth area #3, while the air introduced through the sparger in sub-compartment B reports to froth area #2.

Depending on the froth area in question, equations 5-55 and 5-51 can be transformed to:

$$Vel_{xy} = \frac{G_{frotharea}}{\left(D \times 150\right) \cdot \varepsilon_{xy} \cdot \left(1 - 0.99558 \cdot zj\right)} \qquad \textbf{Equation 5-56}$$

where:

$G_{frotharea}$ = volumetric flowrate of air through the sparger in sub-compartment A if dealing with froth area #1 and froth area #3, and volumetric flowrate of air through the sparger in sub-compartment B if dealing with froth area #2.

The only parameter that now has to be estimated is the fractional hold-up of air, ε_{xy} at any position {x,y} in the novel flotation cell.

5.5 Estimate Air Hold-up

The fractional air hold-up, ε_{xy}, at any position {x,y} in the froth is determined from the concentration of water in the froth at the {x,y} position, i.e.

$$\varepsilon_{xy} = 1 - \frac{C_q(x,y)}{\rho_q} \qquad \textbf{Equation 5-57}$$

where:

$C_q(x,y)$ = concentration of water at the position {x,y} in the froth [kg/m³]

ρ_q = density of water

The concentration of water at selected {x,y} positions in the froth was determined by the procedure as described in section 3.4.7 and shown in Figure 3-7. Since a particle could theoretically move to any {x,y} position in the froth phase, a vast amount of experimental data will have to be obtained to model the particle trajectories in the froth. It was therefore decided to use linear regression to fit a model to the experimental measurements, in order to predict the air hold-up at any position in the cell. Since the air-hold-up is dependent on the air flowrate into the various cell compartments, the frother used as well as the physical cell configuration, the regression model has to be fitted for each set of experimental conditions.

Since different air flowrates are used in the two cell compartments, a linear regression model was fitted to the air hold-up in each compartment. The equations used were:

$$\varepsilon_{\#1A} = aa \times zj + ab$$
$$\varepsilon_{\#1B} = ba \times zj + bb \qquad \textbf{Equation 5-58}$$

with:

aa, ab, ba and bb being the regression constants,

zj = depth in the cell measure from the position of the spargers

$\varepsilon_{\#1A}$ = air hold-up in sub-compartment A

$\varepsilon_{\#1B}$ = air hold-up in sub-compartment B

It was further found that remarkable R^2 values of up to 0.999 can be obtained by combining these equations into one, i.e.

$$\varepsilon_{xy} = \varepsilon_{\#1A} \times x_{lip} + \varepsilon_{\#1B} \qquad \textbf{Equation 5-59}$$

where:

x_{lip} is the vertical distance in the cell measured from the end of the bent cell wall.

The air hold-up at any position {x,y} in the cell can therefore be determined by calibrating equation 5-58 from experimental data (valid only for a specific set of experimental conditions) and substituting $\varepsilon_{\#1A}$ & $\varepsilon_{\#1B}$ into equation 5-59. The {x,y} co-ordinates can then be substituted for x_{lip} and zj respectively.

5.6 Calculate Bubble Size

The bubble size analyser (see section 3.4.6 and Figure 3-6) is incapable of measuring the bubble size distribution in the froth phase. However, to obtain an indication of the average bubble size in the froth phase of the flotation cell, the probe was positioned just beneath the liquid-froth interface. Since it is assumed that air obeys the ideal gas law, equation 5-52 and equation 5-54 must hold. Therefore:

$$P_{zj} \cdot V_{zj} = P_{h\_\text{int}} \cdot V_{h\_\text{int}} \qquad \textbf{Equation 5-60}$$

where:

h_int denotes the height at the pulp/froth interface (determined from equation 4-1).

By substituting equation 5-54 into equation 5-60 it can be shown that:

$$db_{zj} = db_{h\_\text{int}} \times \frac{(1 - 0.99558 \times h\_\text{int})}{(1 - 0.99558 \times zj)} \qquad \textbf{Equation 5-61}$$

where:

db = bubble diameter

h_int = height of pulp/froth interface (or where bubble size measurement was taken)

zj = height in froth (or y co-ordinate of {x,y} position).

5.7 Calculate Bubble Film Thickness

As described in section 4.4, the fundamental model of a cellular foam as developed by Hartland and Barber[49] and modified by Steiner, Hunkeler and Hartland[50] was selected to predict the bubble film thickness at any height in the froth. As in the Hartland and Barber model, the froth is assumed to be composed of dodecahedral bubbles. Although the dodecahedron does not tessellate accurately, the residual volume is only about 3%, making it an accurate enough assumption for the purpose of this dissertation. The properties of the dodecahedron (as quoted by Hartland and Barber[49]) are given in Table 5-1.

Table 5-1: Properties of a dodecahedral bubble[49]

Property	Value
Number of faces	12
Number of edges per face	5
Total number of edges	30
Number of bubbles sharing each face	2
Number of bubbles sharing each edge	3
In terms of a sphere of diameter, *db*, having the same volume:	
Length of edge	0.408.*db*
Area of face:	0.288.db^2

The volume of a spherical bubble of diameter *db* = ($\pi.db^3$)/6. It follows therefore that the number of bubbles per unit volume equals ($6\varepsilon/\pi db^3$), where ε is the air hold-up in the froth. By using the properties in Table 5-1, it can be shown[49] that the liquid hold-up in the films, ε_f can be estimated from:

$$\varepsilon_f = 3.295\varepsilon\frac{\delta}{db}$$ **Equation 5-62**

where:
δ = bubble film thickness
ε = air hold-up
db = bubble diameter

Similarly, the liquid hold-up in the borders, ε_b, can be expressed as[49]:

$$\varepsilon_b = 1.259\varepsilon\frac{r^2}{db^2}$$ **Equation 5-63**

where:
r = radius of curvature of the Plateau border.

The total liquid hold-up, $(1-\varepsilon)$ must be the sum of the ε_f and ε_b, therefore by combining equations 5-62 and 5-63:

$$\frac{(1-\varepsilon)}{\varepsilon} = 3.295\frac{\delta}{db} + 1.259\frac{r^2}{db^2}$$ **Equation 5-64**

From equation 5-64 it follows that:

$$r = \sqrt{\left(\frac{1-\varepsilon}{\varepsilon}\right)\frac{db^2}{1.259} - \frac{3.295\delta}{1.259}\cdot db}$$ **Equation 5-65**

In the steady state the height of the froth is determined by the coalescence of the bubbles or by the physical dimensions of the flotation cell[50]. Steiner, Hunkeler and Hartland[50] assumed that there will be no accumulation of liquid in any horizontal plane in the froth bed. The balance of liquid flow across any horizontal plane in the froth can therefore be written as:

$$q_u = q_d + q_t$$ **Equation 5-66**

where:
q_u = upflow of liquid per unit area into the horizontal plane.
q_d = downflow of liquid per unit area from the horizontal plane.
q_t = the flow of liquid removed from the top of the froth phase.

The flow of liquid removed from the froth phase, q_t, of the novel reverse froth flotation cell can physically be measured from either the middlings compartment or the tailings (see Figure 3-4). It is assumed for the purpose of the froth model that the flow of liquid measured from the middlings compartment is equal to the liquid removed from froth area #2. In turn, the flow of liquid reporting to the tailings is the flow of liquid removed from froth areas #1 and #3. There is therefore no liquid transfer between froth area #3 and froth area #2.

Steiner, Hunkeler and Hartland[50] proposed that because the walls of a border in the froth are not necessarily completely rigid, the downflow of liquid from a horizontal plane in the froth be expressed as:

$$q_d = 8.845\times10^{-3}\frac{\varepsilon^2\rho g r^4}{\mu k_v db^2} \qquad \textbf{Equation 5-67}$$

where:
ε = air hold-up at {x,y} position in froth
ρ = density of liquid phase, i.e. water
g = gravitational acceleration
r = radius of curvature of the Plateau border
μ = viscosity of liquid phase, i.e. water
k_v = velocity coefficient
db = diameter of bubble

In turn, from the properties of a dodecahedron given in Table 5-1, Hartland and Barber[49] derived the volume flowrate per unit area upwards as:

$$q_u = \frac{3.3v\delta}{db} \qquad \textbf{Equation 5-68}$$

where:
v = superficial gas velocity in the cell
δ = bubble film thickness
db = bubble diameter

By substituting equation 5-68 and equation 5-67 into equation 5-66 and rearranging the radius of the curvature of the Plateau border, r, can be expressed as:

$$r = \sqrt[4]{113.058\cdot\frac{\mu db^2 k_v}{\rho g\varepsilon^2}\cdot\left(3.3\frac{v\delta}{db}-q_t\right)} \qquad \textbf{Equation 5-69}$$

By combining equations 5-69 and 5-65 an equation can be derived that predicts the bubble film thickness at any position in the froth phase, i.e.

$$\delta^2 - \left(0.606 \cdot db \cdot \left(\frac{1-\varepsilon}{\varepsilon}\right) + 54.47 \frac{\mu \cdot v \cdot k_v}{\varepsilon^2 \rho \cdot db \cdot g}\right)\delta + 0.0918\left(\frac{1-\varepsilon}{\varepsilon}\right)^2 \cdot db^2 + 16.506 \frac{\mu \cdot q_t \cdot k_v}{\varepsilon^2 \cdot \rho \cdot g} = 0$$

Equation 5-70

By solving for δ in equation 5-70, the bubble film thickness any position {x,y} can be determined based on the air hold-up, bubble diameter, liquid density, liquid viscosity, velocity coefficient and liquid removed from the froth phase at that particular {x,y} position.

5.8 Summary

A fundamental model of the froth phase in the cell was developed in this chapter. The following procedure is made use of to calculate the air hold-up, bubble diameter and bubble film thickness at a position {x,y} in the cell:

- Determine in which froth area {x,y} is situated.
- Calculate superficial gas velocity, *v*, for that area by dividing the volumetric gas flowrate into the froth area by the horizontal cross sectional area of the cell.
- Use the measured values of q_t, $G_{frotharea}$, db_{h_int} for the froth area in question.
- Estimate the velocity coefficient k_v for the froth area in question.
- Estimate the air hold-up at {x,y} by equation 5-59.
- Calculate the bubble diameter at {x,y} from equation 5-61
- Calculate the bubble film thickness from equation 5-70.

As discussed in chapter 4, the next component of the model must describe the dynamic particle/bubble interactions at any position in the froth. Chapter 6 will address these interactions, while chapter 7 describes how the dynamic bubble/particle interactions are superimposed onto the froth structure at any position in the froth, as developed in this chapter.

6. MODELLING OF PARTICLE/FILM INTERACTION

As described in section 4.2.2, it was observed that each of the test particle species would float at a different "ideal" position in the froth. A fundamental model of the froth phase, capable of predicting the bubble size, bubble film thickness and air hold-up at any position in the froth, was developed in chapter 5. To predict the trajectory of a particle in the froth, the interaction of the particle with the bubble films at any froth position must now be determined. By "stepping through time" at discrete time events, the particle trajectory in the reverse froth flotation cell could then be predicted.

This chapter will therefore address the development of a fundamental model describing the particle/film interaction, taking into account the particle surface properties, particle shape, particle size and density. In particular, it will concentrate on:

- describing the general equations and procedures to calculate the time of bubble film rupture,
- describing the calculation of the film rupture time in particular for particles which have a volume of revolution shape,
- describing the model for selected particles which do not have a volume of revolution particle shape,
- deriving the force balance a particle of specific shape is subjected to while supported by the bubble films,
- and calculating the fall time of any particle in the froth, once film rupture has occurred.

6.1 Background to Calculating Bubble Film Rupture Time

In their paper on the antifoam action of solid particles, Frye and Berg[18] proposed a model to calculate the time of bubble film rupture by solid particles. According to these authors (and as described in section 2.3), the capillary pressure-driven flow is the basis for the dynamics of film rupture by solid particles, and is dictated by the Young-Laplace equation:

$$\Delta P_c = \pm\sigma_{AB}\left(\frac{1}{R_1}+\frac{1}{R_2}\right) \qquad \textbf{Equation 6-1}$$

where:

ΔP_c = capillary pressure drop across the interface
σ_{AB} = surface tension
R_1 & R_2 = principal radii of curvature of the meniscus at the particle/film contact

If the curvature of the interface (or meniscus formed at the particle/film contact point) is convex then the pressure at the contact point is higher than in the rest of the liquid film, resulting in liquid being pushed away from the contact point and subsequent film thinning. Conversely, if the curvature is concave, the low pressure zone will result in bubble film stabilisation.

Frye and Berg[18] further assumed that the mechanism of film thinning will only occur once the particle has bridged the liquid film. Due to the large particles being introduced into the reverse froth flotation cell, the particle will always bridge the bubble film. It is therefore assumed that the capillary pressure-driven mechanism of film thinning is applicable at each contact point of the bubble film with the particle.

To analyse the film breakage time, t_{th}, Frye and Berg[18] used a standard model of a circular film of radius R_{film} and a constant film thickness, δ, where the drainage rate of a film is controlled by a capillary pressure drop, ΔP_f, across the lamellae. Under these conditions, the resulting thinning rate is:

$$\frac{d\delta}{dt} = \frac{\Delta P_f \delta^3}{3\mu R_{film}^{\ 2}}$$ **Equation 6-2**

In addition, Frye and Berg[18] only considered particles shaped as volumes of revolution, and assumed that the particles would be axially centered upon bridging the liquid film. The parameters used in estimating the breakage time are shown in Figure 6-1.

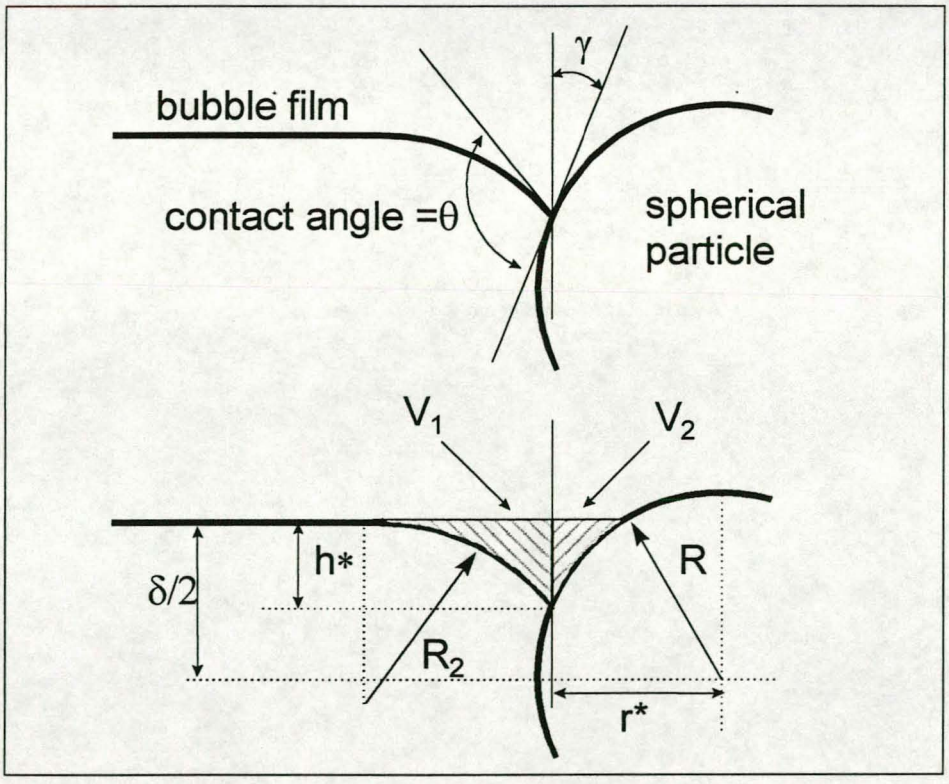

Figure 6-1: Parameter definition for breakage time calculation

The position of the contact point of the liquid film with the surface of the particle is given by h^*, while the steady state contact angle of the particle is θ and the second principal radius of curvature of the meniscus is shown as R_2. In order to estimate the breakage time, the movement of the contact point, h^*, along the surface of the particle is monitored until $h^* = \delta/2$ or reaches a critical film thickness.

The rate of movement of the contact point on the surface of the particle depends on the volumetric flowrate of liquid away from the particle (the meniscus is convex resulting in a positive pressure close to the point of contact - see above and equation 6-1). This flowrate, say Q, depends on the capillary pressure drop (ΔP_c), which in turn depends on the principal radius of curvature, R_2. The breakage time, t_{break}, can therefore be estimated as:

$$t_{break} = \frac{(V_1 + V_2)}{Q}$$ **Equation 6-3**

where:
V_1 and V_2 are the volumes of liquid that must be moved away from the particle as shown in Figure 6-1.

Due to the particle configuration (volumes of revolution), and the assumption of flat liquid films, the first principal radius of curvature (R_1 in equation 6-1) can be ignored[18]. From equation 6-1 and Figure 6-1, it can therefore be shown that:

$$\Delta P_c = \frac{\sigma}{R_2} = \sigma \frac{1 - \sin(\theta + \gamma)}{h^*}$$ **Equation 6-4**

where
γ = angle between the vertical at the point of film contact and a tangent to the particle surface.

The liquid flowrate, Q, can now be estimated by substituting ΔP_c of equation 6-4 into ΔP_f of the thinning rate (equation 6-2) and multiplying the thinning rate by the film area (πR_{film}^2). Therefore:

$$Q = \frac{\sigma \delta^3 \pi (1 - \sin(\theta + \gamma))}{3 \mu h^*}$$ **Equation 6-5**

Because of the complexity, and the various interrelationships of the parameters of these equations, the movement of the point of contact (h^*) along the particle surface has to be integrated numerically. Therefore, for each small integration step ($\Delta h^* = \delta/N$ where N = number of movement integration steps) along the surface:

$$\Delta t_{break} = \frac{\Delta(V_1 + V_2)}{Q(h^*)}$$ **Equation 6-6**

where:
$\Delta(V_1+V_2)$ = liquid volume removed for Δh^* interface movement along contact point.
$Q(h^*)$ = volumetric flowrate of liquid away from particle at h^* position of contact.

The total time for bubble film breakage can therefore be calculated from:

$$t_{break} = \sum_{h^*=0}^{h^*=\frac{\delta}{2}} \Delta t_{break}$$ **Equation 6-7**

6.2 Film Rupture Time: Particles with Volume of Revolution Shape

In order to calculate the breakage time for particles of different shapes, equation 6-5 and equation 6-6 will always hold as long as the particle is a volume of revolution and the particle is axially centred in the film. For each particle shape, however, the volume of liquid removed ($\Delta(V_1+V_2)$ per Δh^* integration step) has to be calculated. Due to the computational power of desktop computers, it was decided to numerically integrate these volumes per movement integration step, i.e. Δh^*. The volumes (V_1 and V_2) were therefore divided into discs, of thickness Δa, around the volume of revolution, where $\Delta a = h^*/M$ and M = number of volume integration steps.

6.2.1 Rod/Cylinder

The configuration of parameters for a rod/cylinder of radius R_{cyl} and height of L_{cyl} is shown in Figure 6-2. Compared to Figure 6-1, it is clear that:

$$V_2 = 0$$
$$\gamma = 0$$ **Equation 6-8**
$$r^* = R_{cyl}$$

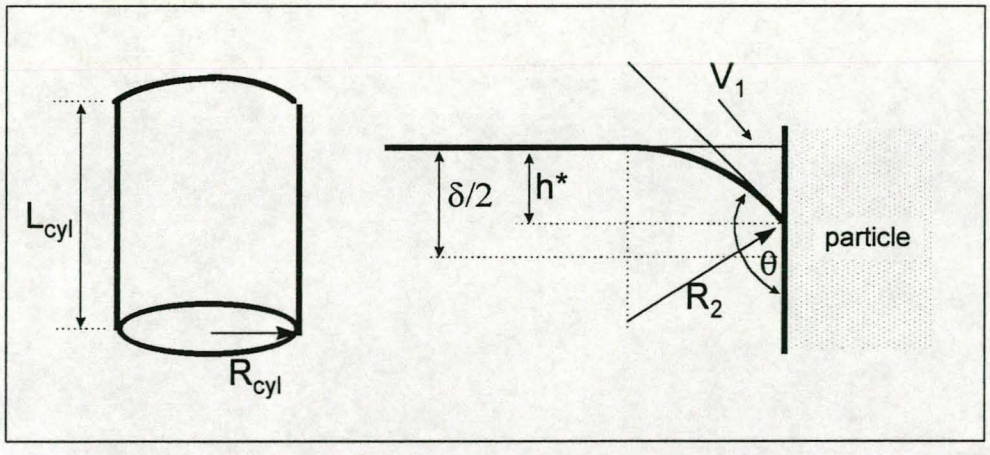

Figure 6-2: Parameter definition for rod/cylindrical particle

The additional parameters defined to calculate V_1 for a cylindrical particle are as shown in Figure 6-3. From Figure 6-3 it follows that:

$$b = R_2 \sin(\theta - 90°) - c$$
$$\therefore b = R_2 \sin(\theta - 90°) - \sqrt{2R_2 a - a^2}$$ **Equation 6-9**

where:

a = disk position = volume integration step length x counter = Δa x integration counter

b = outer disc radius - inner disk radius = width of annulus

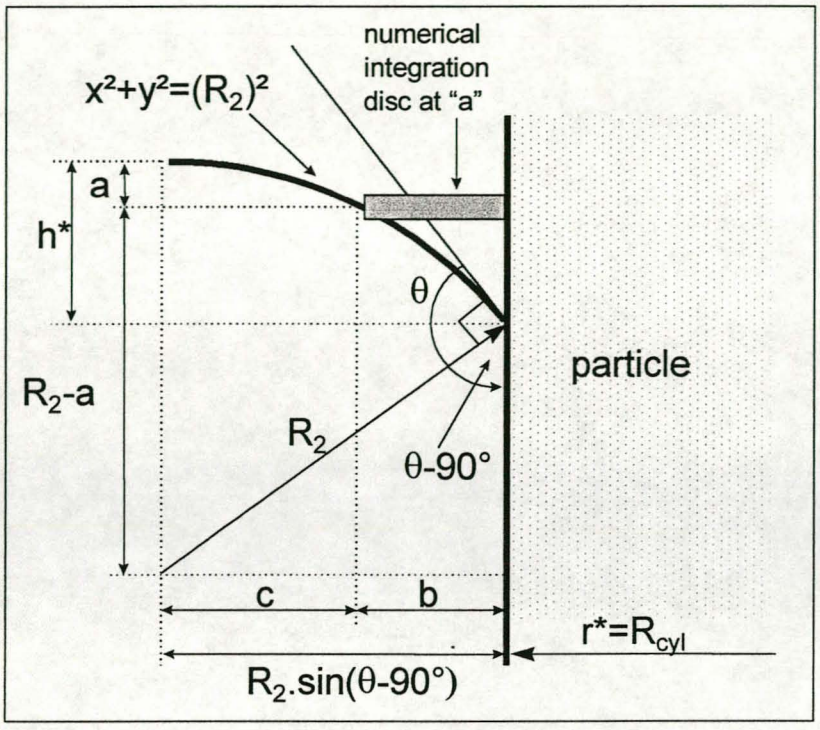

Figure 6-3: Calculation of V_1 for rod/cylindrical particle

It can therefore be shown that the volume of a disk at each volume integration position, *a*, is:

$$\text{disc volume} = \pi\left(\left(b + R_{cyl}\right)^2 - {R_{cyl}}^2\right)\cdot \text{disc thickness}$$

$$\therefore \text{disc volume} = \pi\left(\text{b}^2 + 2bR_{cyl}\right)\cdot \text{disc thickness} \qquad \textbf{Equation 6-10}$$

$$\therefore \text{disc volume} = \pi\left(b^2 + 2bR_{cyl}\right)\cdot \Delta a$$

Therefore:

$$V_1 = \sum_{a=0}^{h^*} \pi\left(b^2 + 2bR_{cyl}\right)\cdot \Delta a \qquad \textbf{Equation 6-11}$$

From equation 6-6, $\Delta(V_1+V_2)$ has to be estimated in order to calculate the incremental breakage time at position *h** along the particle surface. Therefore,

$$\Delta\left(V_1 + V_2\right) = \left(V_1\right)_{h^*} - \left(V_1\right)_{h^*-1}$$

where:

$(V_1)_{h^*}$ is calculated from equation 6-11

$(V_1)_{h^*-1}$ is V_1 as calculated from the previous integration step of h*.

6.2.2 *Cone*

The definition of bubble particle contact parameters for a conical volume of revolution of radius, x_c, and cone angle, β, is shown in Figure 6-4.

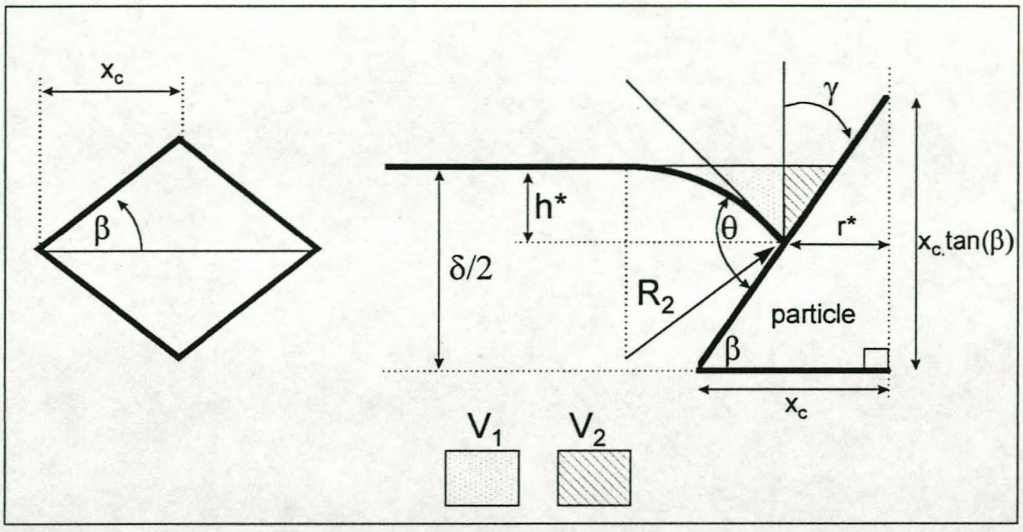

Figure 6-4: Parameter definition for conical particle

From Figure 6-4 it can be shown that:

$$\gamma = 90° - \beta$$ **Equation 6-12**

and

$$r^* = \frac{x_c \tan(\beta) - \frac{\delta}{2} + h^*}{\tan(\beta)}$$ **Equation 6-13**

In order to calculate the V_2 volume at any contact position along the conical particle, h^*, the parameters as shown in Figure 6-5 are defined:

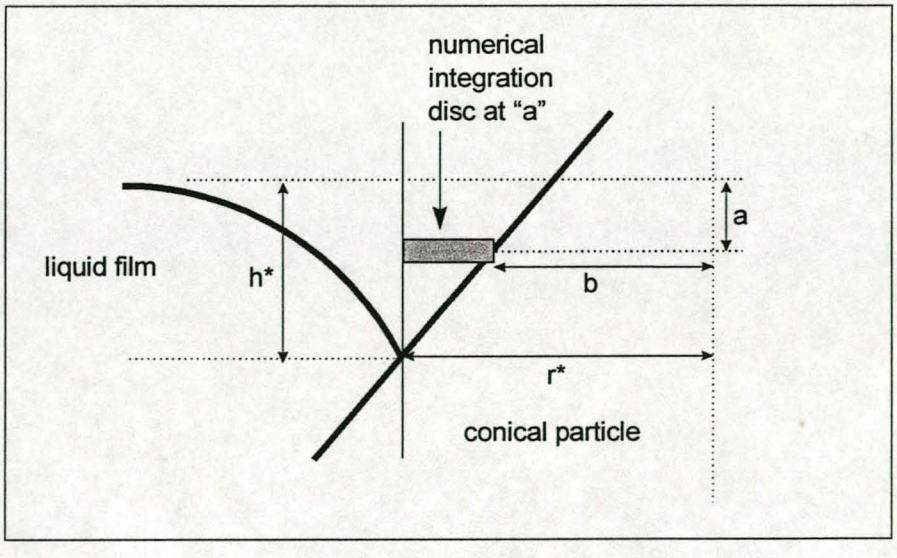

Figure 6-5: Calculation of V_2 for conical particle

For each volume integration position, a = Δa x integration counter, it follows that:

$$b = \frac{x_c \tan(\beta) - \frac{\delta}{2} + a}{\tan(\beta)}$$ **Equation 6-14**

The volume of the numerical integration disc at the integration position, a, can therefore be calculated from:

$$\text{disc volume} = \pi\left(r^{*2} - b^2\right) \cdot \text{disc thickness}$$

$$\therefore \text{disc volume} = \pi\left(r^{*2} - b^2\right) \cdot \Delta a$$ **Equation 6-15**

with b calculated from equation 6-14.

Therefore:

$$V_2 = \sum_{a=0}^{h^*} \pi\left(r^{*2} - b^2\right) \cdot \Delta a$$ **Equation 6-16**

To calculate the V_1 volume for a conical particle, the additional parameters, as shown in Figure 6-6, are defined.

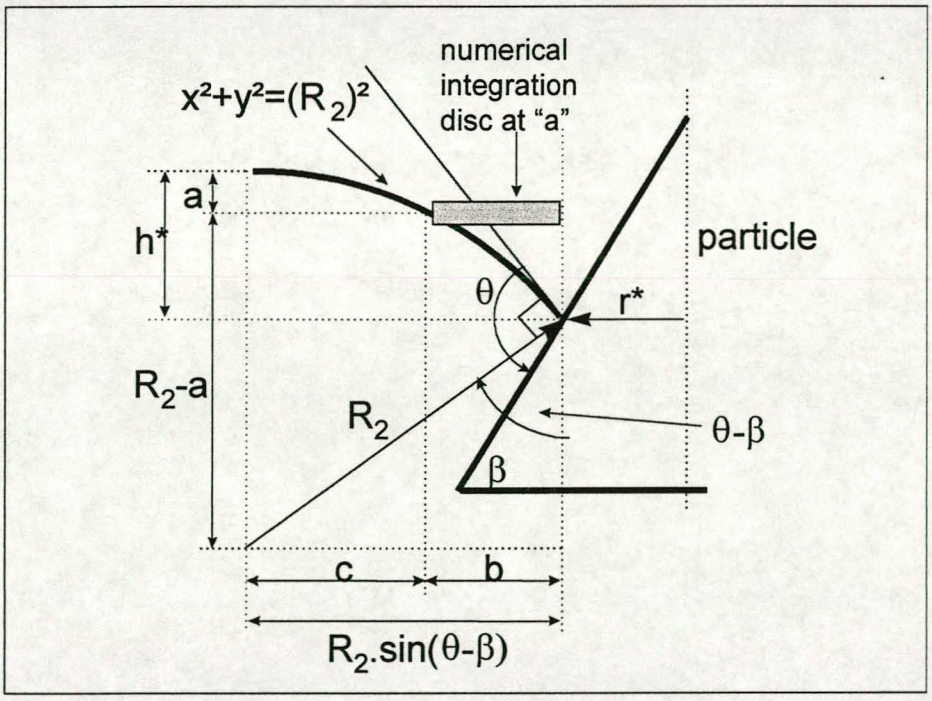

Figure 6-6: Calculation of V_1 for conical particle

From Figure 6-6 it follows that:

$$b = R_2 \sin(\theta - \beta) - c$$

$$\therefore b = R_2 \sin(\theta - \beta) - \sqrt{2R_2 a - a^2}$$ **Equation 6-17**

where:
a = disk position = volume integration step x counter = Δa x integration counter
b = outer disc radius - inner disk radius = width of annulus

The volume of the integration disc, as shown in Figure 6-6, can therefore be calculated as:

$$\text{disk volume} = \pi\left(b^2 + 2b\mathrm{r}^*\right)\cdot \Delta a \qquad \textbf{Equation 6-18}$$

with b calculated from equation 6-17.

Therefore:

$$V_1 = \sum_{a=0}^{h^*} \pi\left(b^2 + 2b\mathrm{r}^*\right)\cdot \Delta a \qquad \textbf{Equation 6-19}$$

From equation 6-6, $\Delta(V_1+V_2)$ has to be estimated in order to calculate the incremental breakage time at position h^* along the particle surface. Therefore, $\Delta(V_1+V_2) = (V_1+V_2)_{h^*} - (V_1+V_2)_{h^*-1}$

With:
V_1 calculated from equation 6-19
V_2 calculated from equation 6-16

6.2.3 Sphere

Figure 6-7 shows the parameters defined to calculate the breakage time of a sphere, of radius R_s, in contact with a bubble film. With the assistance of these parameters, it can be shown that:

$$\mathrm{r}^* = \sqrt{R_s^{\,2} - \left(\frac{\delta}{2} - h^*\right)^2} \qquad \textbf{Equation 6-20}$$

and

$$\gamma = \arccos\left(\frac{\mathrm{r}^*}{R_s}\right) \qquad \textbf{Equation 6-21}$$

In order to calculate V_2 for a spherical particle, the parameters in Figure 6-8 have been defined. From Figure 6-8 it can be shown that:

$$b = \sqrt{R_s^{\,2} - \left(\frac{\delta}{2} - a\right)^2} \qquad \textbf{Equation 6-22}$$

where:
a = disk position = volume integration step length x counter = Δa x integration counter

The volume of the integration disc at integration step "a" is therefore:

$$\text{disk volume} = \pi\left(r^{*2} - b^2\right)\cdot \Delta a \qquad \textbf{Equation 6-23}$$

Therefore:

$$V_2 = \sum_{a=0}^{h^*} \pi\left(r^{*2} - b^2\right)\cdot \Delta a \qquad \textbf{Equation 6-24}$$

with b calculated by using equation 6-22.

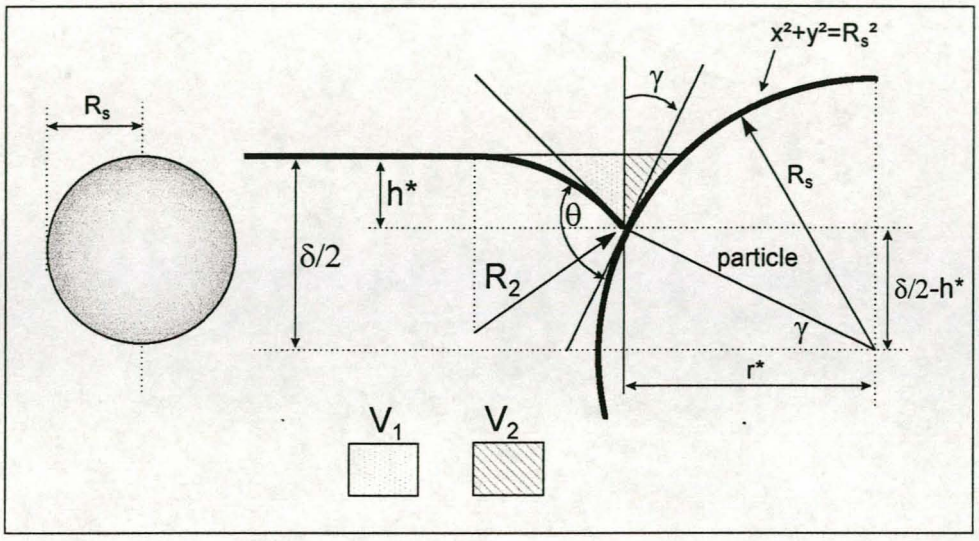

Figure 6-7: Parameter definition for spherical particle

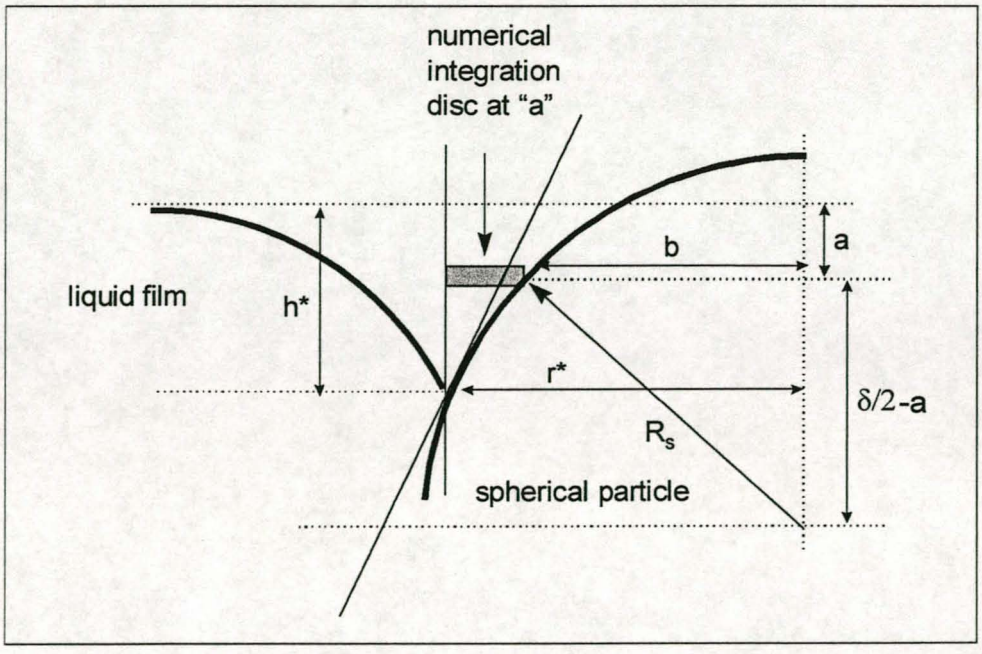

Figure 6-8: Calculation of V_2 for spherical particle

In order to calculate the breakage time of the bubble film by using equation 6-6, the V_1 has to be calculated as well. The parameters, as shown in Figure 6-9, were therefore defined. From Figure 6-9 it can be shown that:

$$b = R_2 \sin(\theta + \gamma - 90°) - c$$

$$\therefore = R_2 \sin(\theta + \gamma - 90°) - \sqrt{2R_2 a - a^2} \qquad \textbf{Equation 6-25}$$

Therefore, the volume of the integration disk (as shown in Figure 6-9) at integration position, a, is given by:

$$\text{disc volume} = \pi(b^2 + 2br^*) \cdot \Delta a \qquad \textbf{Equation 6-26}$$

By using equation 6-26, it can be shown that:

$$V_1 = \sum_{a=0}^{h^*} \pi(b^2 + 2br^*) \cdot \Delta a \qquad \textbf{Equation 6-27}$$

with b calculated from equation 6-25.

In order to calculate the incremental breakage time at position h^*, $\Delta(V_1+V_2)$ has to be estimated and substituted in equation 6-6. Therefore,

$\Delta(V_1+V_2) = (V_1+V_2)_{h^*} - (V_1+V_2)_{h^*-1}$

With:

V_1 calculated from equation 6-27

V_2 calculated from equation 6-24

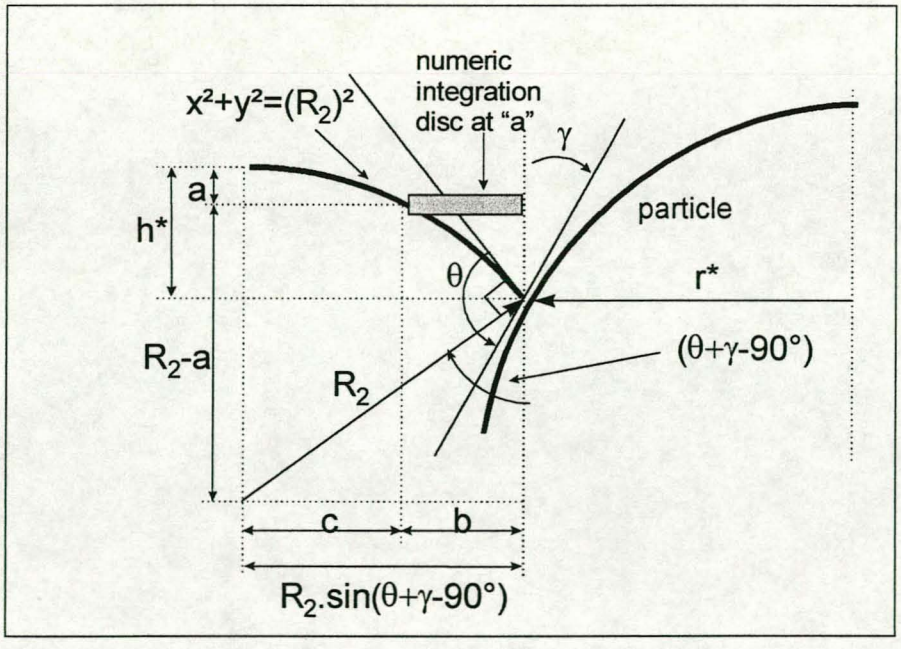

Figure 6-9: Calculation of V_1 for spherical particle

6.2.4 *Disc with rounded ends*

The physical particle parameters, as shown in Figure 6-10, are sufficient to describe a disc with rounded ends. Since the particle is centred in the bubble film upon bridging the film, the bubble film will be in contact with the rounded end of the particle. Therefore, in order to calculate V_1 and V_2, the same additional parameters are defined as for a spherical particle (see Figure 6-8 and Figure 6-9).

Equation 6-20 can therefore be used to calculate r* (with R_s as shown in Figure 6-10), while equation 6-21 can be used to calculate γ (with r* calculated by using equation 6-20).

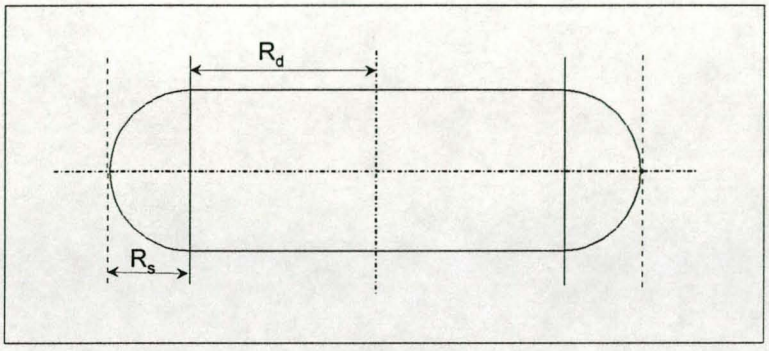

Figure 6-10: Parameter definition for disc with rounded ends

As described above, V_2 is calculated from Figure 6-8. Therefore, the integration parameter, *b*, can be calculated from equation 6-22. The volume of the integration disc at the position *a* along the particle surface is therefore:

$$\text{disc volume} = \pi\left(\left(\mathrm{r}^* + R_d\right)^2 - \left(b + R_d\right)^2\right)\cdot \Delta a \qquad \textbf{Equation 6-28}$$

Therefore:

$$V_2 = \sum_{a=0}^{h^*} \pi\left(\left(\mathrm{r}^* + R_d\right)^2 - \left(b + R_d\right)^2\right)\cdot \Delta a \qquad \textbf{Equation 6-29}$$

with *b* calculated from equation 6-22.

In turn, V_1 can be calculated from Figure 6-9. The integration parameter, *b*, for the calculation of V_1 can therefore be calculated from equation 6-25. The volume of the integration disc (as shown in Figure 6-9) at any position, *a*, along the particle boundary is therefore:

$$\text{disc volume} = \pi\left(\left(b + \mathrm{r}^* + R_d\right)^2 - \left(\mathrm{r}^* + R_d\right)^2\right)\cdot \Delta a \qquad \textbf{Equation 6-30}$$

with:
r* calculated from equation 6-20.
b calculated from equation 6-25.

Therefore:

$$V_1 = \sum_{a=0}^{h^*} \pi\left(\left(b + \mathrm{r}^* + R_d\right)^2 - \left(\mathrm{r}^* + R_d\right)^2\right) \cdot \Delta a \qquad \textbf{Equation 6-31}$$

In order to calculate the incremental breakage time at position h^*, $\Delta(V_1+V_2)$ has to be estimated and substituted in equation 6-6. Therefore,
$\Delta(V_1+V_2) = (V_1+V_2)_{h^*} - (V_1+V_2)_{h^*-1}$

With:
V_1 calculated from equation 6-31
V_2 calculated from equation 6-29

6.2.5 Ellipsoid

An ellipsoidal volume of revolution can be described by the parameters, as shown in Figure 6-11. From Figure 6-11 it can be shown that:

$$r^* = A\sqrt{\left(1 - \frac{\left(\frac{\delta}{2} - h^*\right)^2}{B^2}\right)} \qquad \textbf{Equation 6-32}$$

and

$$\gamma = Arc\tan\left(\frac{B\left(\frac{\delta}{2} - h^*\right)}{A\sqrt{B^2 - \left(\frac{\delta}{2} - h^*\right)^2}}\right) \qquad \textbf{Equation 6-33}$$

To calculate V_2, the numeric integration parameters, as shown in Figure 6-12, were defined. Based on those parameters it can be shown that at any position, a, along the surface of the particle:

$$b = A\sqrt{1 - \frac{\left(\frac{\delta}{2} - a\right)^2}{B^2}} \qquad \textbf{Equation 6-34}$$

Therefore, the volume of the numerical integration disc at position a is:

$$\text{disc volume} = \pi\left(\mathrm{r}^{*2} - b^2\right) \cdot \Delta a \qquad \textbf{Equation 6-35}$$

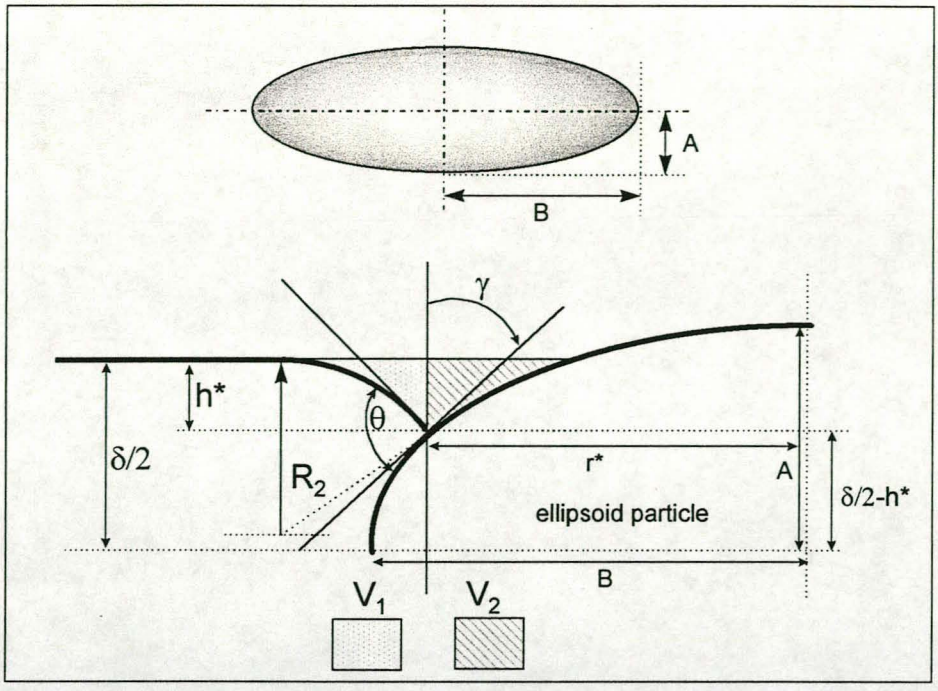

Figure 6-11: Parameter definition for ellipsoidal particle

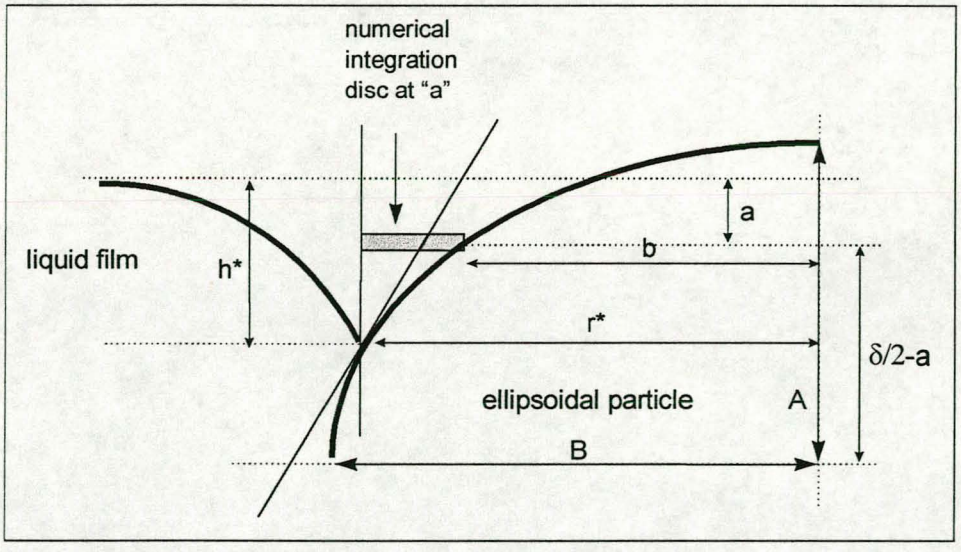

Figure 6-12: Calculation of V_2 for ellipsoidal particle

Therefore:

$$V_2 = \sum_{a=0}^{h^*} \pi\left(r^{*2} - b^2\right) \cdot \Delta a \qquad \textbf{Equation 6-36}$$

with parameter, b, calculated from equation 6-34.

In order to calculate the V_1 volume, the numerical integration parameters, as shown in Figure 6-13 were defined. To calculate the volume of the numerical integration disc, at any integration step, *a*, along the particle surface, it can be shown that:

$$b = R_2 \sin(\theta + \gamma - 90°) - \sqrt{2R_2 a - a^2} \qquad \textbf{Equation 6-37}$$

with γ calculated from equation 6-33.

Therefore, the volume of the integration disc at *a* is:

$$\text{disc volume} = \pi\left(b^2 + 2br^*\right)\cdot \Delta a \qquad \textbf{Equation 6-38}$$

with b calculated from equation 6-37.

Therefore:

$$V_1 = \sum_{a=0}^{h^*} \pi\left(b^2 + 2br^*\right)\cdot \Delta a \qquad \textbf{Equation 6-39}$$

In order to calculate the incremental breakage time at position h^*, $\Delta(V_1+V_2)$ has to be estimated and substituted in equation 6-6. Therefore,
$\Delta(V_1+V_2) = (V_1+V_2)_{h^*} - (V_1+V_2)_{h^*-1}$

With:
V_1 calculated from equation 6-39
V_2 calculated from equation 6-36

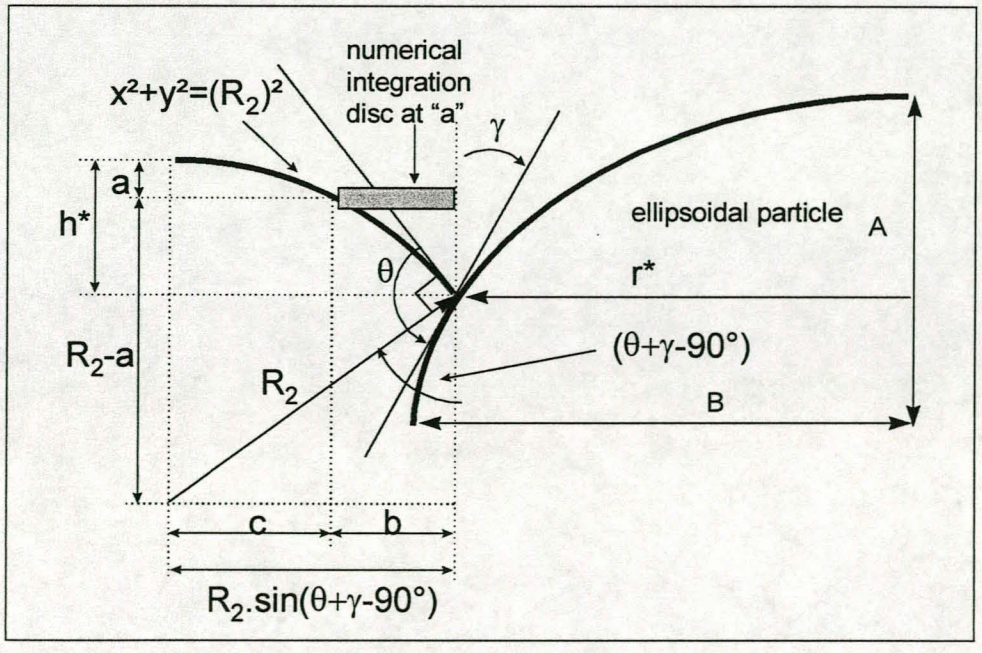

Figure 6-13: Calculation of V_1 for ellipsoidal particle

6.3 Film Rupture Time: Non-Volume of Revolution Particles

In the case of particles which have a volume of revolution shape, the meniscus in contact with the particle will be rotationally symmetrical. Since the R_1 principal radius of curvature can be ignored, this approach allowed authors, such as Frye and Berg[18], to reduce the Young-Laplace equation (see equation 6-1) to:

$$\Delta P_c = \sigma_{AB}\left(\frac{1}{R_2}\right) = (\rho_A - \rho_B)gz \qquad \textbf{Equation 6-40}$$

However, in the case of particle shapes which are not volumes of revolution, the menisci in contact with the particles will not possess rotational symmetry, and the R_1 radius of curvature cannot be ignored. These three dimensional menisci are still governed by the Young-Laplace equation, but the equation is unsolvable due to irregular boundaries and non-linear boundary conditions.

Various authors have therefore ventured into the field of numerically solving a three dimensional meniscus of an unsymmetrical configuration. Orr and Scriven[51] considered the problem of menisci between parallel vertical cylinders in a large array. This problem is nonlinear, second-order and an elliptic boundary-value problem with two space dimensions as independent variables. The authors used two numerical techniques, i.e. the finite difference method and the finite element method. Although good results were achieved, it did not provide solutions for menisci of unbounded extent and free liquid-solid contact lines. Orr, Brown and Scriven[52] therefore extended the finite element method to cater for these cases.

Orr and Scriven[53] then expanded the finite element approach to incorporate the singularity induced by a corner in the solid boundary (for instance at the edge of a cubic particle). At a corner, the meniscus may be unbounded if the liquid surface cannot simultaneously meet the contact angle boundary condition on the two solid surfaces that intersect there. The meniscus therefore appears to have a corner at the same place as the solid boundary. Although the finite element technique can be used to determine the shape of the meniscus in contact with a cubic particle (and thereby calculate the volume of liquid removed due to film thinning and subsequently the thinning rate), it was found to be very difficult to incorporate this technique into the discrete time model, as proposed in the previous sections.

Various other techniques in the literature were therefore investigated. Boruvka and Neumanm[54] found a special case of liquid in contact with a heterogeneous solid wall for which the Young-Laplace equation can be integrated analytically to obtain the shape of the liquid surface. In this case the wall consisted of alternating parallel strips of two different materials and the authors solved the problem based on conformal mapping. Although a solution was obtained, problems were experienced at the transition regions between strips[54] and the solution is only valid for this very special case. The approach was therefore not expanded to be included in the particle-film interaction model.

Wong et al.[55] used the augmented Young-Laplace equation to solve three-dimensional menisci in polygonal capillaries. They incorporated the disjoining thin-film forces in the Young-Laplace equation to eliminate the contact line, and thereby eliminating the free boundary problem. Although successful, this approach does not cater for the unbounded conditions (as assumed for all the other particle shapes in this dissertation) and only considers the shape of the menisci surface in a capillary. Kralchevsky et al.[56] used a energy balance and force approach to solve the shape of the menisci, however, they had to resort to volumes of rotation, and focused on the interaction between particles.

Based on this survey, it was decided to use a simplified approach to this highly complex problem. The approach is based on the Young-Laplace equation, and calculates the volume of liquid removed from the particle bubble contact point, as well as the pressure drop causing the movement of liquid, by numerical integration (similar to the approach of Frye & Berg[18]).

Consider the complete Young-Laplace equation (as given by Schulze[57] in his book on Physico-chemical Elementary Processes in Flotation):

$$\Delta P_c = \sigma_{AB}\left(\frac{1}{R_1}+\frac{1}{R_2}\right)=(\rho_A-\rho_B)gz \qquad \textbf{Equation 6-41}$$

with:

ΔP_c = the pressure difference between the inner and outer sides of the miniscus

R_1 & R_2 = principal radii of curvature of the meniscus. They occur in a plane perpendicular to each other and are both perpendicular to the tangent plane on the surface.

ρ_A & ρ_B = density of the liquid and air respectively

g = gravitational acceleration constant

z = height of the contact point measured from the flat section of the meniscus

Similar to the approach of Frye and Berg[18], the breakage time is calculated from:

$$\text{break time} = \sum_{h^*=0}^{\delta/2} \Delta t_{break} \qquad \textbf{Equation 6-42}$$

where:

Δt_{break} = given by equation 6-6 and

Δh^* = δ/N where N = number of movement integration steps along the surface

From equation 6-6, both Q (flow of liquid to or from particle) and $\Delta(V_1+V_2)$ (volume of liquid to be removed) have to be determined at the integration position h^*. Frye and Berg[18] showed that at any position, h^*, along the particle surface, Q can be calculated from:

$$Q = \frac{dV}{dt} = \frac{\pi h^{*3}\ \Delta P_c}{3\mu}$$ **Equation 6-43**

By substituting equation 6-41 into equation 6-43, the volumetric flow rate of liquid can be determined. However, from equation 6-41, it is necessary to calculate R_1 and R_2 at any position h^* along the particle surface.

Now, Frye and Berg[18] showed that (see Figure 6-1 for definition of parameters):

$$R_2 = \frac{h^*}{1-\sin(\theta+\gamma)}$$ **Equation 6-44**

By substituting equation 6-44 into equation 6-41, and substituting h^* for z, it can be shown that:

$$R_1 = \frac{\sigma_{AB}}{(\rho_A - \rho_B)gh^* - \frac{\sigma_{AB}(1-\sin(\theta+\gamma))}{h^*}}$$ **Equation 6-45**

As shown in Figure 6-14, R_1 is the principal radius of curvature describing the liquid-solid contact line. At the position h^* in Figure 6-14, equation 6-44 can be used to calculate the R_2 radius of curvature (perpendicular to the plane of the contact line). However, by moving along the contact line to a position, say Δd_p, it can be expected that R_2 will change. Nonetheless, by using simple geometry and by assuming that equation 6-44 will hold along the contact line, it can be shown that:

$$R_2' = \frac{h^{*'}}{1-\sin(\theta+\gamma)}$$ **Equation 6-46**

where:

$$h^{*'} = h^* - \left(R_1 - \sqrt{R_1^{\,2} - \Delta d_p^{\,2}}\right)$$ **Equation 6-47**

with R_2' and $h^{*'}$ as define in Figure 6-14.

Therefore, by choosing the integration parameter, h*, R_1 can be calculated from equation 6-45. Once R_1 is calculated, the contact line can be divided into discrete elements (say of width Δd_p) and $h^{*'}$, and the corresponding R_2', calculated at each discrete point along the contact line.

Once R_1 and R_2' are calculated at each point along the contact line, the corresponding values are substituted into equation 6-41 to calculate ΔP_c. The calculated value of ΔP_c is then substituted into equation 6-43 to calculate the volumetric flowrate of liquid away from the particle (at the contact point of the bubble film and the particle surface).

Only $\Delta(V_1+V_2)$ now needs to be estimated at each contact point, in order to use equation 6-6 to calculate the time of bubble film breakage time of a particle (of non-volume of revolution shape) in contact with a bubble film.

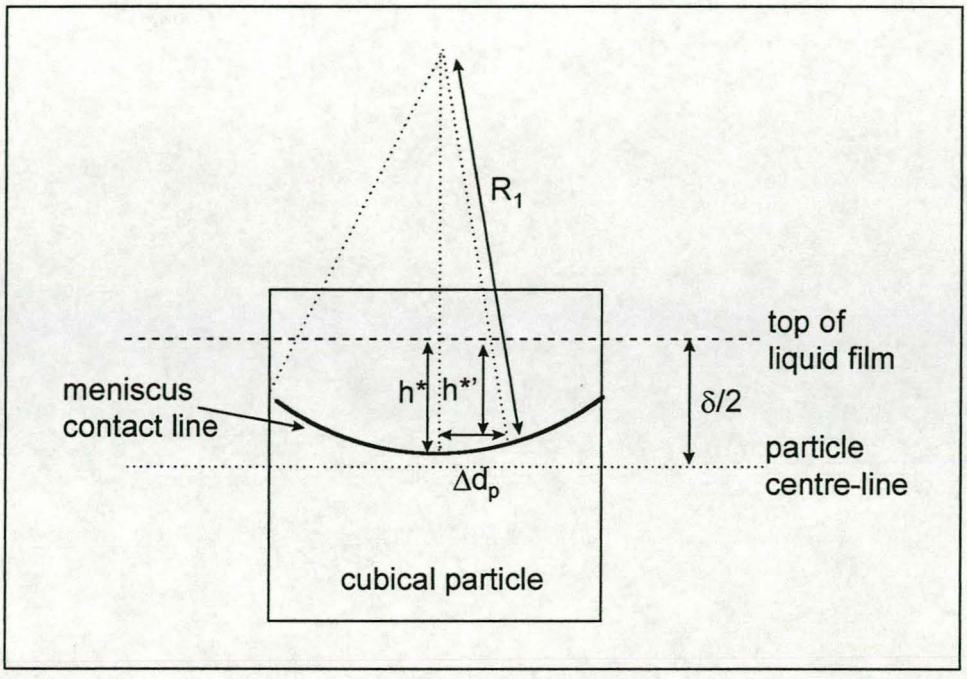

Figure 6-14: Definition of numerical integration parameters.

6.3.1 Cube

At any point, $h^{*'}$, on the meniscus contact line on the particle surface, it is assumed that the meniscus configuration is as shown in Figure 6-15. From Figure 6-15 it is clear that $V_2 = 0$ and $\gamma = 0$. Therefore, in order to calculate the volume of liquid to be removed from the bubble-particle contact, only V_1 has to be considered.

Therefore:

$$V_1 = Area(AEC) \cdot \text{thickness}$$
$$\therefore = \text{Area(AEC)} \cdot \Delta d_p$$

Equation 6-48

where:

Δd_p is the thickness of discrete element (as shown in Figure 6-14).

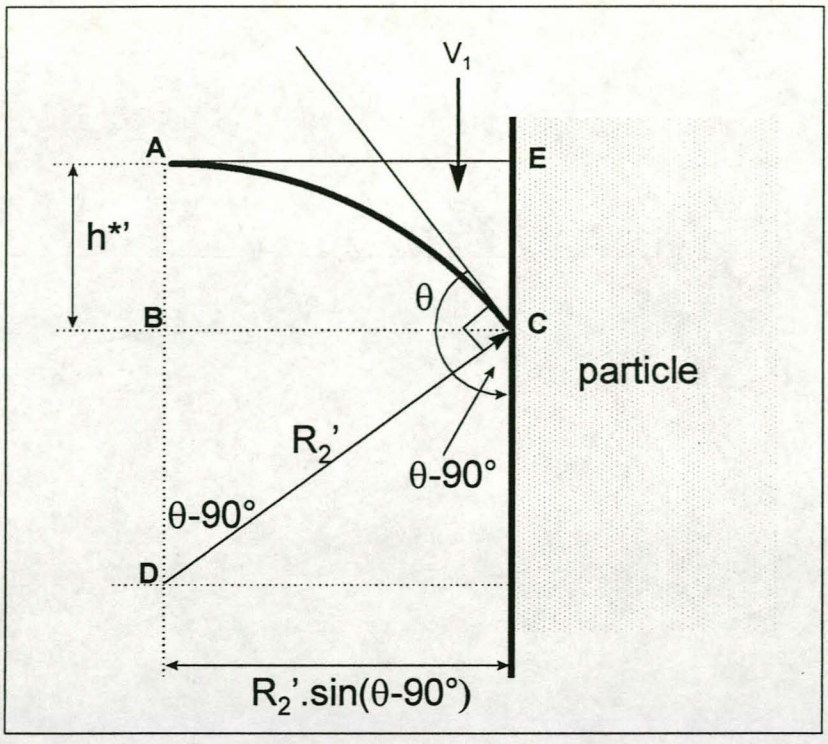

Figure 6-15: Calculation of V_1 for non-volume of revolution particle

Now:

$$Area(AEC) = Area(AECB) - Area(ACD) + Area(BCD)$$ **Equation 6-49**

where:

$$Area(AECB) = h^{*\prime} \cdot R_2' \sin(\theta - 90°)$$ **Equation 6-50**

$$Area(ACD) = \frac{\theta - 90°}{360°} \pi R_2'^2$$ **Equation 6-51**

$$Area(BCD) = 0.5(R_2' - h^{*\prime}) R_2' \sin(\theta - 90°)$$ **Equation 6-52**

with:

$h^{*\prime}$ and R_2' calculated from equation 6-47 and equation 6-46 respectively.

Therefore:

$$V_1 = 8 \cdot \left(\sum_{d_p=0}^{S_{cube}/2} Area(AEC) \cdot \Delta d_p \right) + V_{corners}$$ **Equation 6-53**

where S_{cube} = side length of cubic particle and the volume of liquid to be removed at the corners of the particle is approximated by:

$$V_{corners} = \pi \left(R_2^{corner} \cdot \frac{(h^{*corner})^2}{2} - \frac{(h^{*corner})^3}{3} \right)$$ **Equation 6-54**

To calculate the total pressure drop (ΔP_c) across the total liquid-air interface, the pressure drop at each discrete element (ΔP_c') is weighted by the volume of liquid to be removed from the liquid-solid interface at that discrete element. Therefore:

$$\Delta P_c = \sum_{h^*=0}^{\frac{\delta}{2}} \left(\frac{V_1^{h^*'}}{V_1^{total}} \cdot \Delta P_c' \right) \qquad \textbf{Equation 6-55}$$

6.3.2 *Flat*

The parameters describing a flat particle are shown in Figure 6-16. The same procedure as described in section 6.3 and section 6.3.1 is valid in calculating the bubble film breakage time of a flat particle supported by liquid lamellae. However, equations 6-53 and 6-54 are expanded to incorporate the different sizes of the various particle contact surfaces, i.e. contact surface #1 and contact surface #2 (as shown in Figure 6-16).

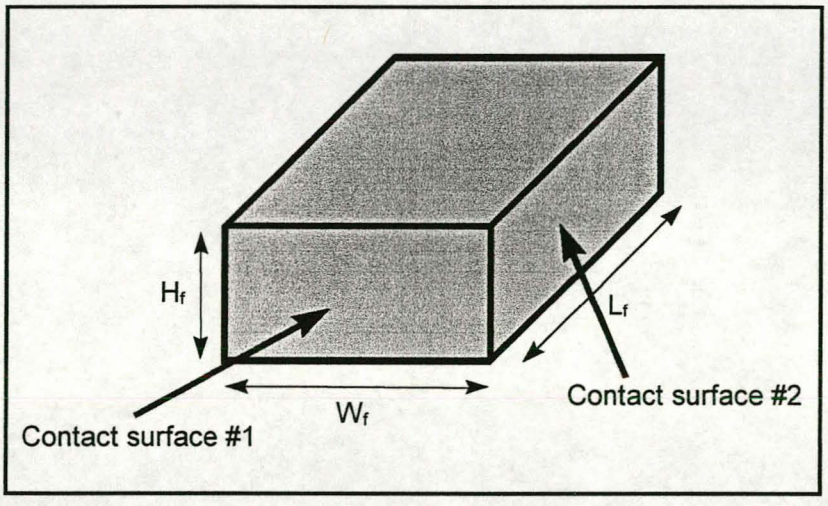

Figure 6-16: Parameters describing flat particle

6.4 Force Balance on Particles

This section derives the force balance a particle of specific shape is subjected to while supported by the bubble films. Rudimentary spoken, for any particle the net force acting on the particle in a vertical plane is:

$$F_{net} = F_{up} - F_{down} \qquad \textbf{Equation 6-56}$$

where:

F_{down} = down force = gravitational force down

F_{up} = up force = buoyancy force on particle + drag force exerted on particle

Although some attempts were made to calculate the force balance exerted on a particle suspended by a *liquid film*[57], no published literature exists describing the force balance exerted on a particle in a *froth bed*. In particular, no previous work has been done on the calculation of drag coefficients on particles moving through a froth bed, as well as describing the viscosity of a froth bed. Fundamentally, the

resistance offered by a froth to the movement of a particle is very different from that offered by a continuum of fluid. However, since this is a very complex field and justifies an entire study on its own, traditional fluid dynamic equations were used to describe the force balance on a particle in the froth.

Therefore:

$$F_{down} = V_p \rho_p g$$

$$F_{up} = V_p \rho_{froth} g + C_D A_0 \rho_{froth} \frac{v_y^2}{2} \qquad \textbf{Equation 6-57}$$

where:

V_p = volume of particle
ρ_p = density of particle
ρ_{froth} = density of froth = $((1-\varepsilon).\rho_{liquid} + \varepsilon.\rho_{air})$
g = gravitational acceleration constant
C_D = drag coefficient on particle
A_0 = projected area of particle (area on which drag forces will be exerted)
v_y = vertical velocity component in froth.

The drag coefficient on the particle, C_D, was estimated from standard fluid dynamic equations. The Reynolds number, R_{ep}, of the particle in the froth should thus be estimated, therefore:

$$R_{ep} = \frac{\rho_{froth} |v_y| D_p}{\mu_{froth}} \qquad \textbf{Equation 6-58}$$

where the viscosity of the froth, μ_{froth}, is assumed to be the viscosity of the liquid lamellae, μ, and D_p is the equivalent diameter of the particle. The equivalent particle diameter can be calculated by the same procedure as described in equation 4-4 to equation 4-7. However, the shape factor, λ, is calculated with reference to a *cubic* particle with the same volume and surface area of the particle in question. The equivalent particle diameter can then be calculated from:

$$D_p = \frac{D_e}{\lambda} \qquad \textbf{Equation 6-59}$$

where D_e is the second longest dimension of the particle in question.

Once the Reynolds number of the particle in the froth is calculated, C_D can be estimated from standard fluid dynamic equations, i.e:

$$\text{If } R_{ep} \le 0.5 \text{ Then } C_D = \frac{24}{R_{ep}}$$

$$\text{If } 0.5 < R_{ep} \le 1.0 \text{ Then } C_D = \frac{24}{R_{ep}} + 1.5$$

$$\text{If } 1.0 < R_{ep} \le 10 \text{ Then } C_D = \frac{24}{\exp\left(0.8 \ln\left(R_{ep}\right)\right)} + 0.4 \qquad \textbf{Equation 6-60}$$

$$\text{If } 10 < R_{ep} \le 500 \text{ Then } C_D = \frac{24}{R_{ep}}\left(1 + 0.15 \exp\left(0.687 \ln\left(R_{ep}\right)\right)\right)$$

$$\text{If } R_{ep} > 500 \text{ Then } C_D = 0.44$$

To calculate the net force interacting on a particle in the froth, the volume of the particle (V_p), the projected area of the particle (A_0), the second longest dimension (D_e) and the shape factor (λ) have to be calculated. The equivalent particle diameter is then calculated from equation 6-59, and substituted into equation 6-58 to obtain the Reynolds number. The Reynolds number is then used to calculate the drag coefficient on the particle from equation 6-60. All the respective parameters are then substituted into equation 6-57, which in turn is substituted into equation 6-56 to calculate the net force.

6.4.1 Rod/Cylinder

The parameters describing a rod/cylindrical particle are shown in Figure 6-2. Assuming that the cylinder orientates to stand upright in the froth, it can be shown that:

$$V_p = \pi\left(R_{cyl}\right)^2 L_{cyl}$$

$$D_e = 2R_{cyl}$$

$$A_0 = \pi\left(R_{cyl}\right)^2 \qquad \textbf{Equation 6-61}$$

$$\lambda = \frac{2\left(R_{cyl} + L_{cyl}\right)}{3L_{cyl}}$$

6.4.2 Cone

The physical parameters describing a cone are shown in Figure 6-4. By using simple geometry is can be shown that:

$$V_p = \frac{2}{3}\pi\left(x_c\right)^3 \tan\left(\beta\right)$$

$$D_e = 2\left(x_c\right)$$

$$A_0 = \pi\left(x_c\right)^2 \qquad \textbf{Equation 6-62}$$

$$\lambda = \frac{\sqrt{1 + \tan\left(\beta\right)}}{\tan\left(\beta\right)}$$

6.4.3 Sphere

Figure 6-7 shows the definition of parameters for a spherical particle. From Figure 6-7 the particle characteristics can be described as:

$$V_p = \frac{4}{3}(R_s)^3$$
$$D_e = 2(R_s)$$
$$A_0 = \pi(R_s)^2$$
$$\lambda = 1$$

Equation 6-63

6.4.4 Disc with rounded ends

The parameter definition for a disc with rounded ends is shown in Figure 6-10. Based on visual observations that the disc re-orientates upon breaking the films to "stand on its side", it can be shown that:

$$V_p = \pi R_d R_s \left(2R_d + \pi R_s + \frac{4(R_s)^2}{3R_d} \right)$$
$$D_e = 2(R_d + R_s)$$
$$A_0 = 4((R_d + R_s) \times R_s)$$
$$\lambda = \frac{\left(2(R_d)^2 + 4\pi R_d R_s \left(1 - \frac{R_d - R_s}{R_d + R_s} \right) \right) \cdot (R_d + R_s)}{3R_d R_s \left(2R_d + \pi R_s + \frac{4(R_s)^2}{3R_d} \right)}$$

Equation 6-64

6.4.5 Ellipsoid

The parameters defining an ellipsoidal particle are shown in Figure 6-11. Define the parameter, e_{ratio}, where e_{ratio} = A/B if B>A and e_{ratio} = B/A if A>B. Then, by using simple geometry, it can be shown that:

$$V_p = \frac{4}{3}\pi A^2 B$$
$$D_e = 2(A)$$
$$A_0 = \pi A^2$$
$$\lambda = \left(0.5 + \frac{B^2}{4A^2 e_{ratio}} \cdot \ln\left(\frac{1 + e_{ratio}}{1 - e_{ratio}} \right) \right) \cdot \left(\frac{A}{B} \right)$$

Equation 6-65

6.4.6 Cube

The equivalent particle diameter, D_p, from equation 6-59 is with reference to a cubic particle of side length S_{cube}. Therefore:

$$V_p = (S_{cube})^3$$
$$D_e = S_{cube}$$
$$A_0 = (S_{cube})^2$$
$$\lambda = 1$$

Equation 6-66

6.4.7 *Flat*

The parameters describing a flat particle are shown in Figure 6-16. From Figure 6-16 it is trivial to show that if L_f is the second longest dimension:

$$V_p = H_f \cdot W_f \cdot L_f$$
$$D_e = L_f$$
$$A_0 = H_f \cdot W_f$$
$$\lambda = \frac{H_f \cdot W_f + L_f \cdot W_f + H_f \cdot L_f}{3H_f \cdot L_f}$$

Equation 6-67

And similarly if W_f or H_f is the second longest dimension of the particle.

6.5 Calculate Particle Fall-time

The net force acting on a particle suspended in the froth of the novel flotation cell can be calculated from equation 6-56. Now, from basic physics:

$$F_{net} = M_p.a$$

Equation 6-68

where:
M_p = mass of particle
a = acceleration of particle at the moment that the bubble film breaks.

Therefore, by rearranging equation 6-68:

$$a = \frac{F_{net}}{V_p \rho_p}$$

Equation 6-69

with V_p and ρ_p as described for equation 6-57.

A particle trapped in a bubble film just before it is about to break the bubble film and fall to a deeper level in the froth, is shown in Figure 6-17.

From Figure 6-17, and by using elementary equations of motion:

$$s = ut + \tfrac{1}{2}at^2$$

Equation 6-70

where:
s = distance of fall = diameter of bubble = d_b
u = starting velocity = relative velocity of particle to bubble films = 0

t = time of fall = t_{fall}
a = acceleration on particle (calculated from equation 6-69)

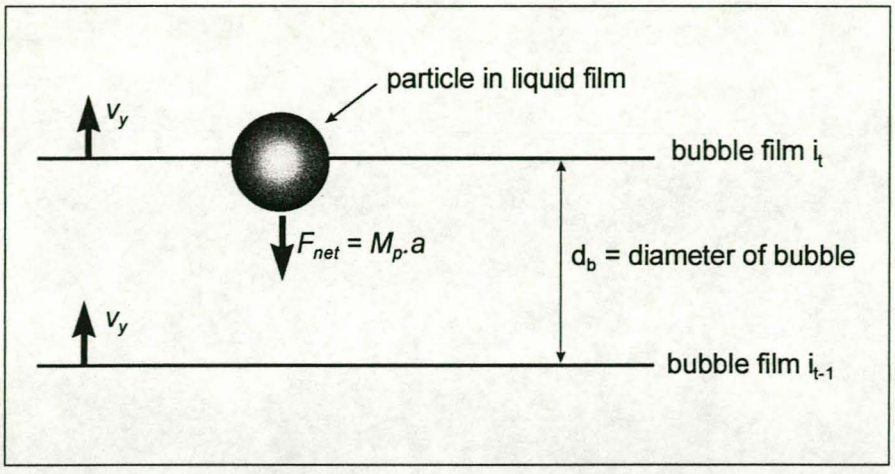

Figure 6-17: Simplified view of particle in bubble film & about to fall

Therefore:

$$t_{fall} = \sqrt{\frac{2V_p \rho_p d_b}{F_{net}}}$$

Assuming that the particle will not break the bubble film (i_{t-1}) upon impact, the particle will therefore move to a position in the cell given by:

$$y_{pos} = y_{pos(old)} - \left(d_b - t_{fall} \cdot v_y\right) \qquad \textbf{Equation 6-71}$$

6.6 Summary

In this chapter a fundamental model describing the particle/film interaction was developed. In particular the model is capable of predicting the film rupture time of any shaped particle, together with the force balance exerted on the particle by the bubble films. In addition, the model calculates the fall time of any particle in the froth, once film rupture has occurred.

In order to calculate the trajectory of any particle in the froth phase of the cell, these particle/film interaction characteristics needs to be superimposed onto the froth models (as developed in chapter 5) over discrete time periods. The associated computational procedures, together with a detailed description of the computer program written to do the calculations, are described in the following chapter.

7. COMPUTATIONAL PROCEDURES

This chapter describes the computational procedures used in the computer program written to calculate the trajectory of any particle in the froth phase of the cell. All the froth models (as derived in chapter 5) and particle/film interaction models (as derived in chapter 6) are incorporated in the computer program. The program was written in Borland Pascal, and the listing of the computer code is given in Appendix A. The program uses the TechnoJocks Turbo Toolkit v4.00, released in February 1988, as input/output devices. In addition, due to code length constraints, some of the calculations are contained in the Parti3.tpu Pascal Unit (listed in Appendix B). The program name is Lines11.pas and can be run from within the Command Prompt in Windows, or compiled in Borland Pascal v7.0.

Due to the length of the computer code, this section is divided into sub-sections, each describing a section of the source code. Where possible, references will be made to the equations derived in the model development sections of this dissertation, and each sub-section will be illustrated with appropriate flow-diagrams.

7.1 Program Initialisation and Cell Parameter Input

The flow diagram for this section of the code is shown in Figure 7-1. The Program starts by displaying the title and purpose of the program and waits until the user presses any key before it continues. The program then zeros all elements of the integration matrices. These matrices are used to store the co-ordinates of the flow profiles in the cell before displaying it in the DOS graphical window. Once all matrices are zeroed, the user is prompted to supply the parameters characterising the flotation cell (see section 5.3 and Figure 7-1). In order to simplify the use of the program, typical default values are supplied for each parameter. Once all parameters are entered, the program calculates the cell constants according to equations 5-1 to 5-4. The entire program can also be repeated, as shown by the repeat loop marked A in Figure 7-1.

7.2 Bubble Flow Profile Calculation and Display

The flow diagram for this section of the program is shown in Figure 7-2. The bubble flow profiles for the various froth areas (see Figure 5-3) are calculated, converted to the {0,0} co-ordinate system where applicable, and displayed in the DOS graphical window.

For Froth Area #1 the procedure ***Lines_Comp1*** is called. The equations, as derived in section 5.3.1 are used to calculate the co-ordinates of the bubble flow profiles, upon which the co-ordinates (in terms of the $\{x_0,y_0$ co-ordinate system) is stored in a matrix, **XY_Cor1**. Each sub-area (see Figure 5-5) of the froth is calculated in sequence according to the equations in Sections 5.3.1.1, 5.3.1.2, 5.3.1.3 and 5.3.1.4.

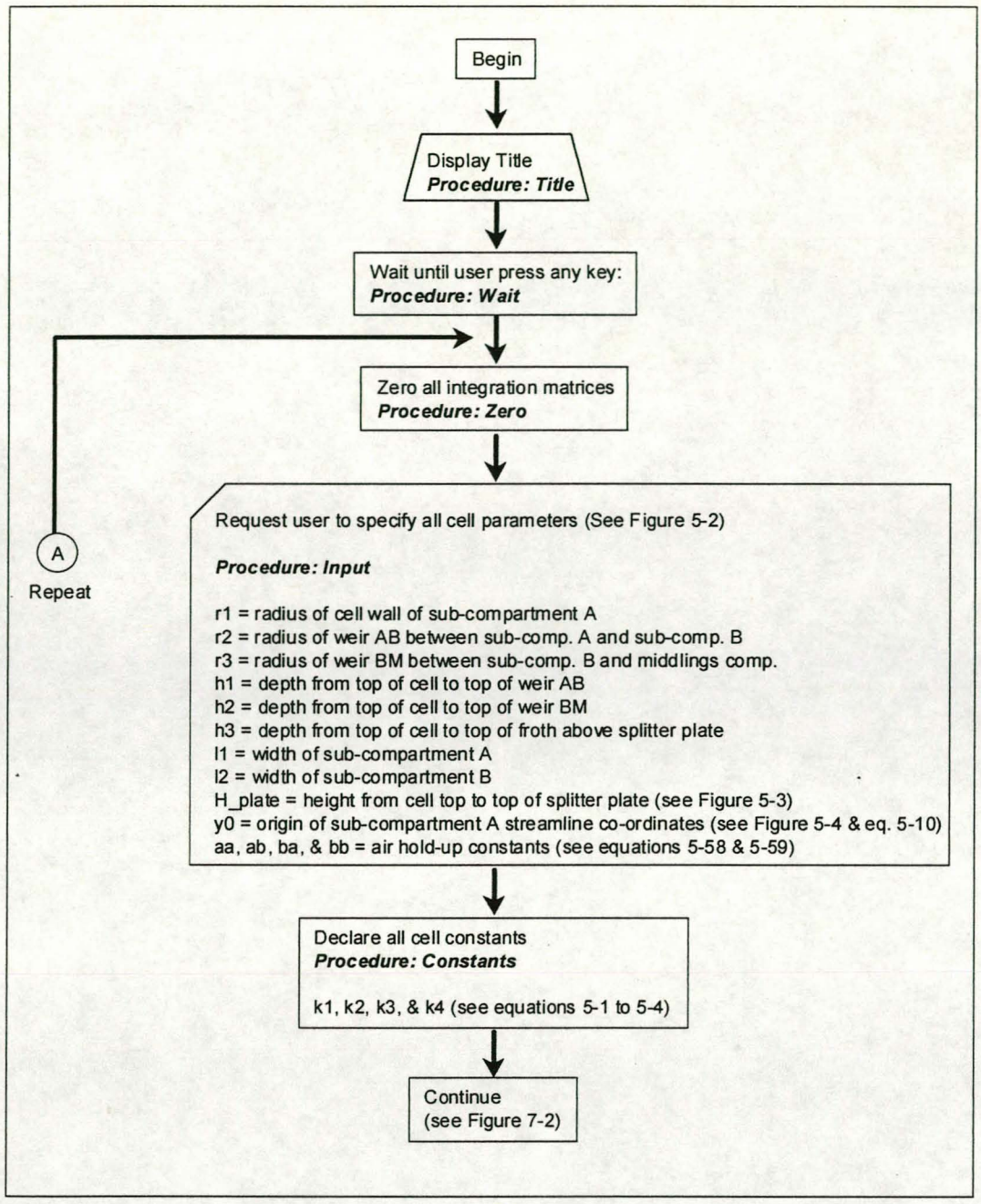

Figure 7-1: Flow diagram for Program Initialisation and Cell Parameter Input

For Froth Area #2, the procedure ***Lines_Comp2*** is called and the co-ordinates saved in a matrix **XY_Cor2**. The co-ordinates are calculated from the equations derived in section 5.3.2, with each froth sub-area (see Figure 5-6) calculated sequentially. For details of the equations used, see Sections 5.3.2.1, 5.3.2.2 and 5.3.2.3.

A similar strategy is used for the Froth Area #3. However, the procedure ***Lines_Comp3*** is called and the co-ordinates saved in a matrix called **XY_Cor3**. See Figure 5-7 for the definition of the various sub-area of the froth in this froth section. The equations, as described in section 5.3.3.1 and section 5.3.3.2 were used to calculate the co-ordinates for sub-areas #1 and #2 respectively.

Following the calculation of the various co-ordinates the $\{x_0,y_0\}$ co-ordinates are converted to the {0,0} co-ordinate system for Froth Area #1 and Froth Area #3 by calling the procedure ***Scale***. The profiles are then displayed in the DOS graph window by calling the ***DrawLines*** procedure (using the Borland graphics driver).

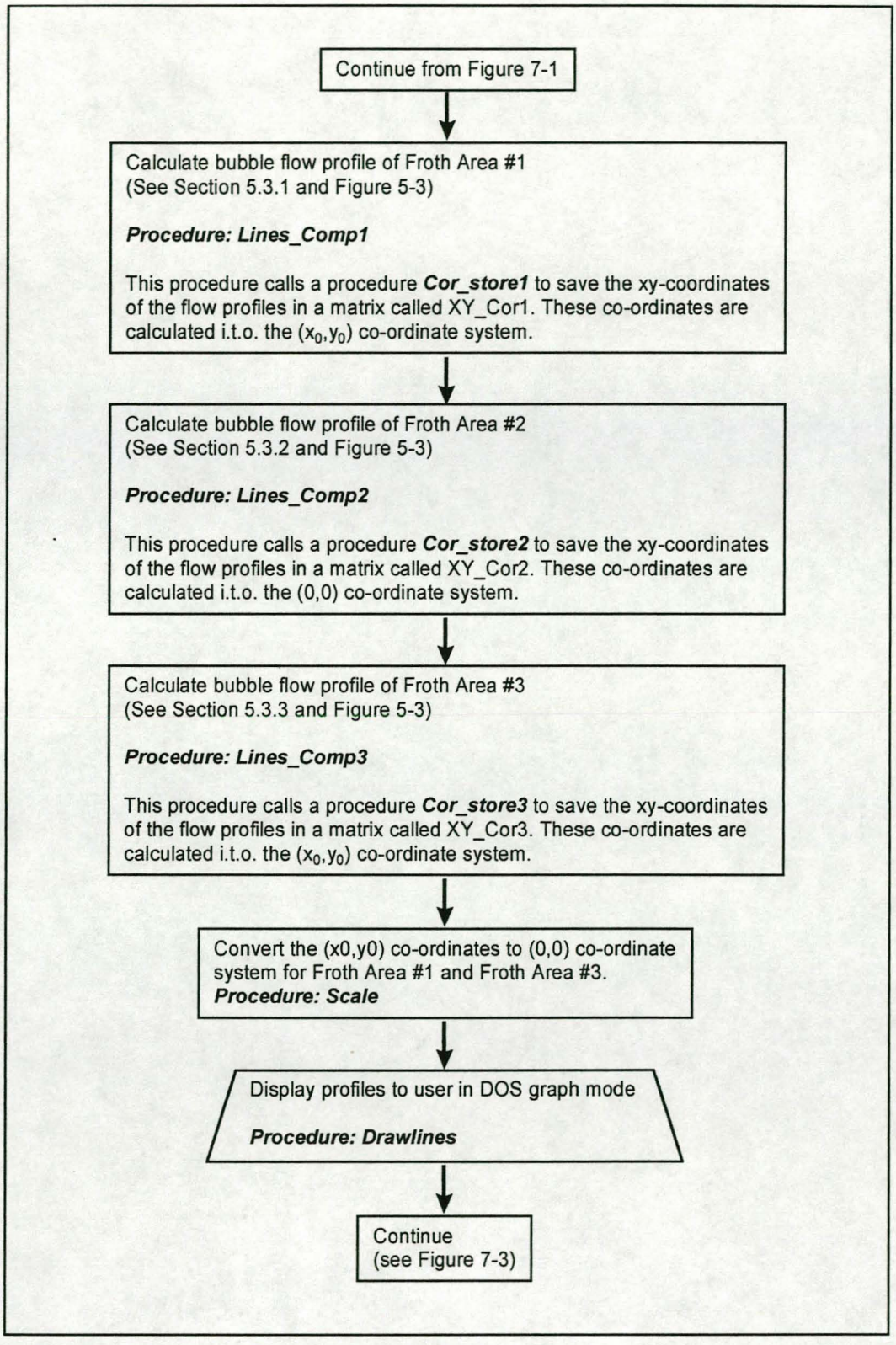

Figure 7-2: Flow diagram for bubble flow profile calculation & display

7.3 Input of operational and integration parameters

The flow diagram for this section of the computer code is given in Figure 7-3. Once the flow profiles in the reverse flotation cell has been displayed, the user is prompted to enter the parameters describing the experimental conditions in the cell (see section 5.5, 5.6 and 5.7). In addition the user has to specify the number of integration steps for the various numerical integration procedures (see Sections 6.1 and 6.2).

A second repeat loop starts at this point (see repeat loop "B"). This loop enables the user to maintain the same cell configuration, but investigates the dynamic behaviour of different particles at different experimental conditions in the cell. After supplying all the necessary experimental parameters, the user must press the "end" key to proceed to the next program section. The program then calculates the value of the air hold-up at the liquid froth interface for future use.

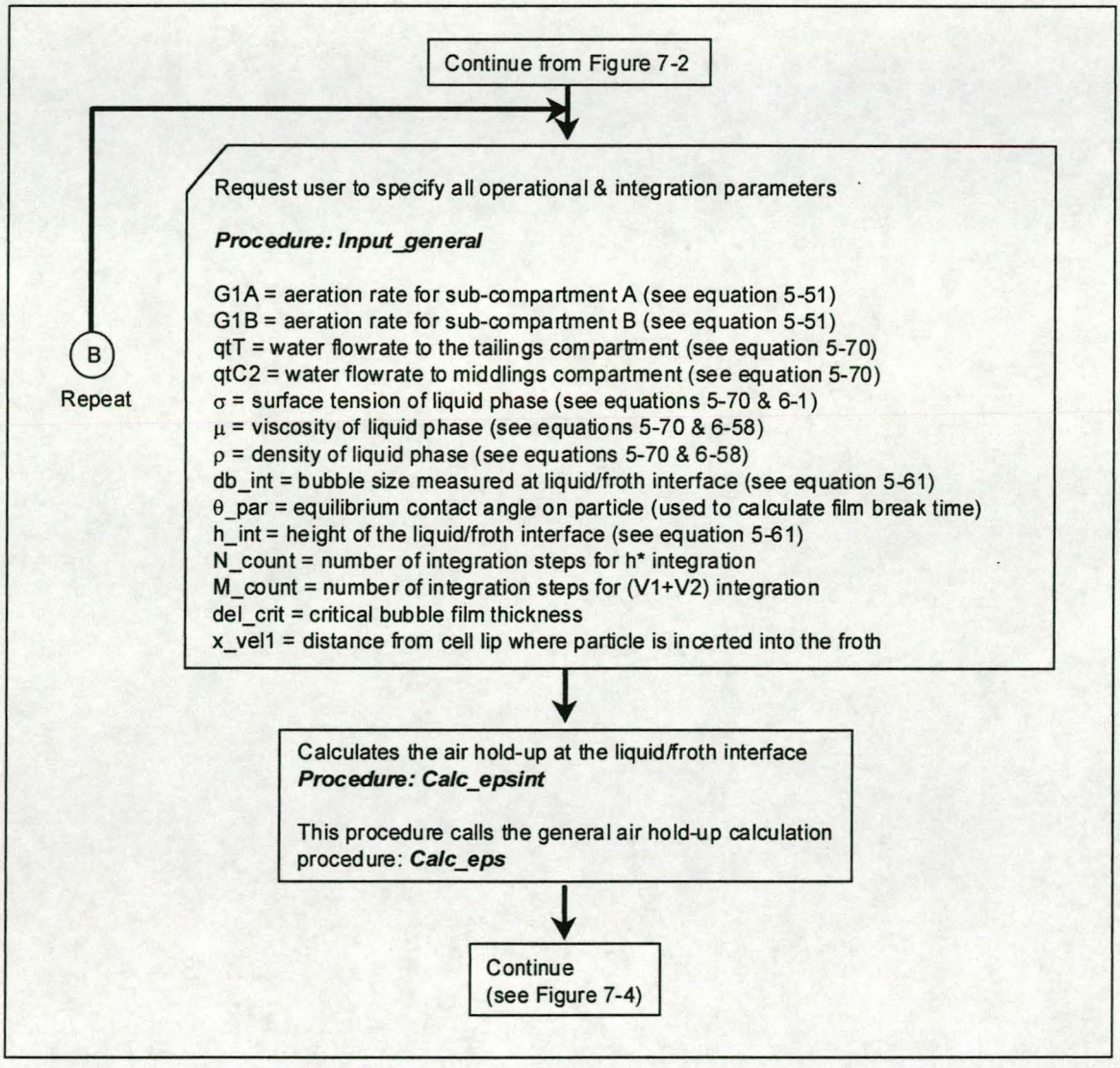

Figure 7-3: Flow diagram for input of operational and integration parameters

7.4 Particle shape selection

This section of the computer code allows the user to select the required particle shape for which the dynamic behaviour has to be simulated in the cell. Once a particle shape is selected, the program calculates the general force balance parameters applicable to the particle (see section 6.4). Figure 7-4 displays the flow diagram for this program section.

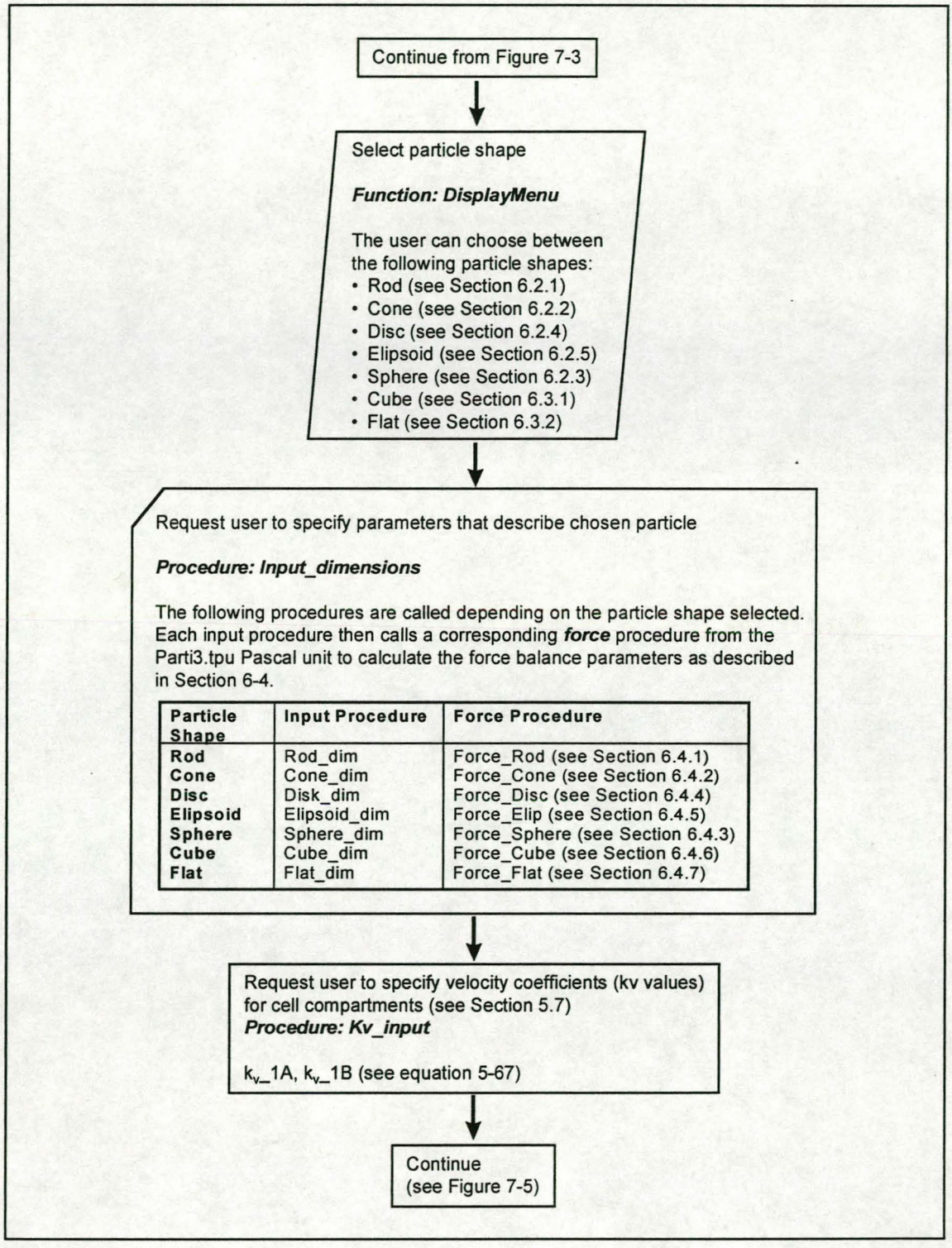

Figure 7-4: Flow diagram for particle parameter specification.

Since each particle shape is described by different size parameters, a corresponding size input procedure is called for each particle shape. Similarly, each particle shape is associated with a unique force balance calculation procedure (see section 6.4). Due to constraints being placed on the length of source code in Borland Pascal, the force calculation procedures are located in the Parti3.tpu Pascal Unit (see Appendix B).

Once the user has specified the required particle shape, and general particle size parameters, the program requests the user to specify the velocity coefficients (as discussed in section 5.7). The velocity coefficients are used in the calculation of the bubble film thickness at any position in the reverse froth flotation cell. The greater the velocity coefficient per froth area, the lower the downflow of liquid per unit area through a horizontal plane in the froth (see equation 5-67).

7.5 Particle Trajectory Calculation

Once the user has provided all the input information (as described in Sections 7.1 to 7.4), the program can now begin to calculate and plot the specified particle trajectory through the froth phase of the reverse froth flotation cell. The flow diagram for this calculation procedure is shown in Figure 7-5 and continued in Figure 7-6. The procedure is quite complex. The flow diagram has therefore been generalised around certain areas, with detailed discussions for each of these areas reserved for dedicated sub-sections.

As a start, the program plots the outline of the cell in the DOS graphical window. The trajectory of the particle is then plotted over this cell outline. The user can follow the particle trajectory throughout the calculation, and has the option of investigating different experimental conditions, and plotting the outcome of this on the same cell outline. A complete sensitivity analysis of the various particle and cell operational parameters can therefore be conducted with relative ease (see section 8).

Once the cell outline is plotted, the program calculates the {x,y} co-ordinates (in terms of the current computer screen display configuration) of the current particle position by using the ***Vel_Control*** procedure. For details on this procedure, see section 7.6 and Figure 7-7. The program then draws a line to this calculated {x,y} position, and calculates the bubble film thickness, δ, at this position by using equation 5-70 (contained in procedure ***Calc_Delta***).

As described in section 4.4, it is assumed that one of three actions can take place when a particle is supported by a matrix of bubble films, i.e.

1. The film thickness is greater than the particle size (typically near the pulp-froth interface). It is assumed that under this condition, the particle would be emerged into the bubble films and no bubble film thinning and rupture would take place. The particle will therefore be transported by the bubble films along a streamline to the next discrete time event.

2. The bubble film thickness is less than a critical bubble film thickness, which will cause the bubble films to rupture upon contact with the particle. A force balance therefore needs to be conducted on the particle to determine whether the particle will fall through the froth to lower position in the froth, or whether the particle will be supported by surrounding liquid films and be carried along the relevant streamline to a new position in the froth.
3. The process of film thinning will take place. It is assumed that during the time of film thinning the particle will be carried along a streamline to a new position in the froth. Once the film breaks, however, a force balance needs to be conducted on the particle as in (2) above.

The program therefore checks whether the particle is bridging the liquid. If bridging does not occur, it is assumed that the particle is supported by the bubble films, and carried to a new position in the froth. For the purpose of the model a transfer period of 1 millisecond is assumed. The new {x,y} position in the cell is therefore calculated by the procedure ***New_XY*** (see Figure 7-6).

If the particle bridges the liquid films, the program subsequently checks whether the bubble film thickness at the current {x,y} position is less than the critical bubble film thickness (as specified in section 7.3). If the bubble film thickness is less than the critical bubble film thickness, the bubble films will rupture upon contact with the particle. A force balance is therefore conducted on the particle (procedure: ***Calc_forces*** - see Figure 7-6).

If the bubble films, however, are thicker than the critical bubble film thickness, it is assumed that (for the period of bubble film thinning) the particle will be carried along a streamline to a new position in the froth (see Figure 7-5). The time of bubble film breakage must therefore be calculated. The program calls on the ***Break_time*** procedure to calculate this time of bubble film rupture (the procedure is described in detail in section 7.10 and Figure 7-11). The co-ordinates of the new position in the cell are then calculated by the procedure ***New_XY***, while the x and y velocity components of the particle at this new position are calculated by the ***Vel_Control*** procedure. For details on the ***Vel_Control*** procedure, see section 7.6 and Figure 7-7. A line is then drawn to the newly calculated {x,y} position in the cell.

As was the case above, a force balance must now be conducted on the particle at the new position in the cell. For this, the program calls the ***Calc_forces*** procedure (see Figure 7-6). If the downward forces acting on the particle are less than the upward forces, the particle will be supported by the bubble films, resulting in the particle being carried to a new position in the forth. It was found that any transfer period less than 0.04 seconds resulted in the same model predictions. A transfer period of 0.02 seconds was therefore assumed. The new {x,y} position in the cell is subsequently calculated by the procedure ***New_XY*** (see Figure 7-6).

However, if the down-forces acting on the particle are greater than the up-forces, the particle will not be supported by the bubble films. The particle will then fall through the froth onto the next bubble film. The fall time, as well as the new position of the particle in the forth, is estimated by the ***Fall*** procedure (the calculations is detailed in section 6.5).

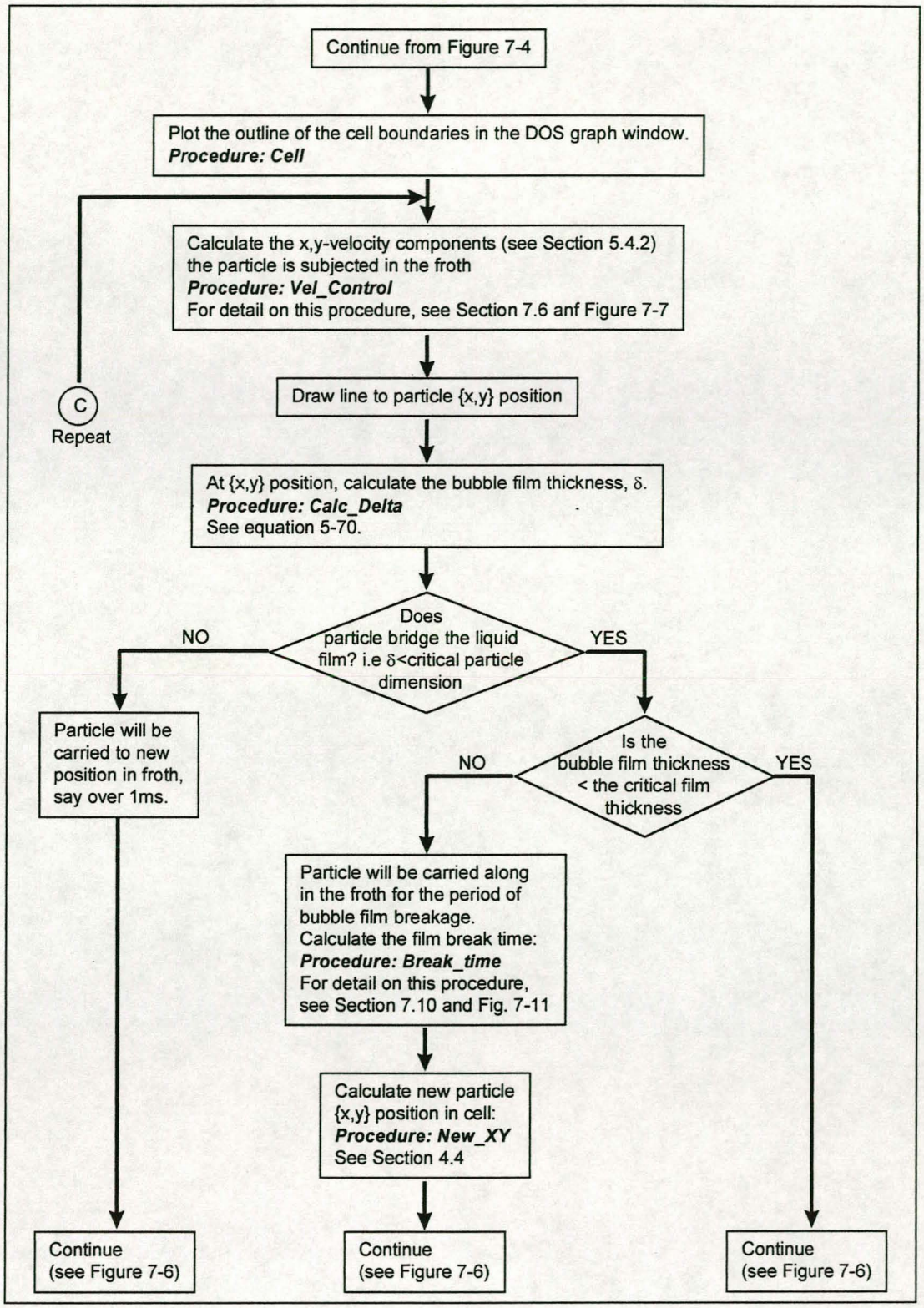

Figure 7-5: Flow diagram for particle trajectory calculation

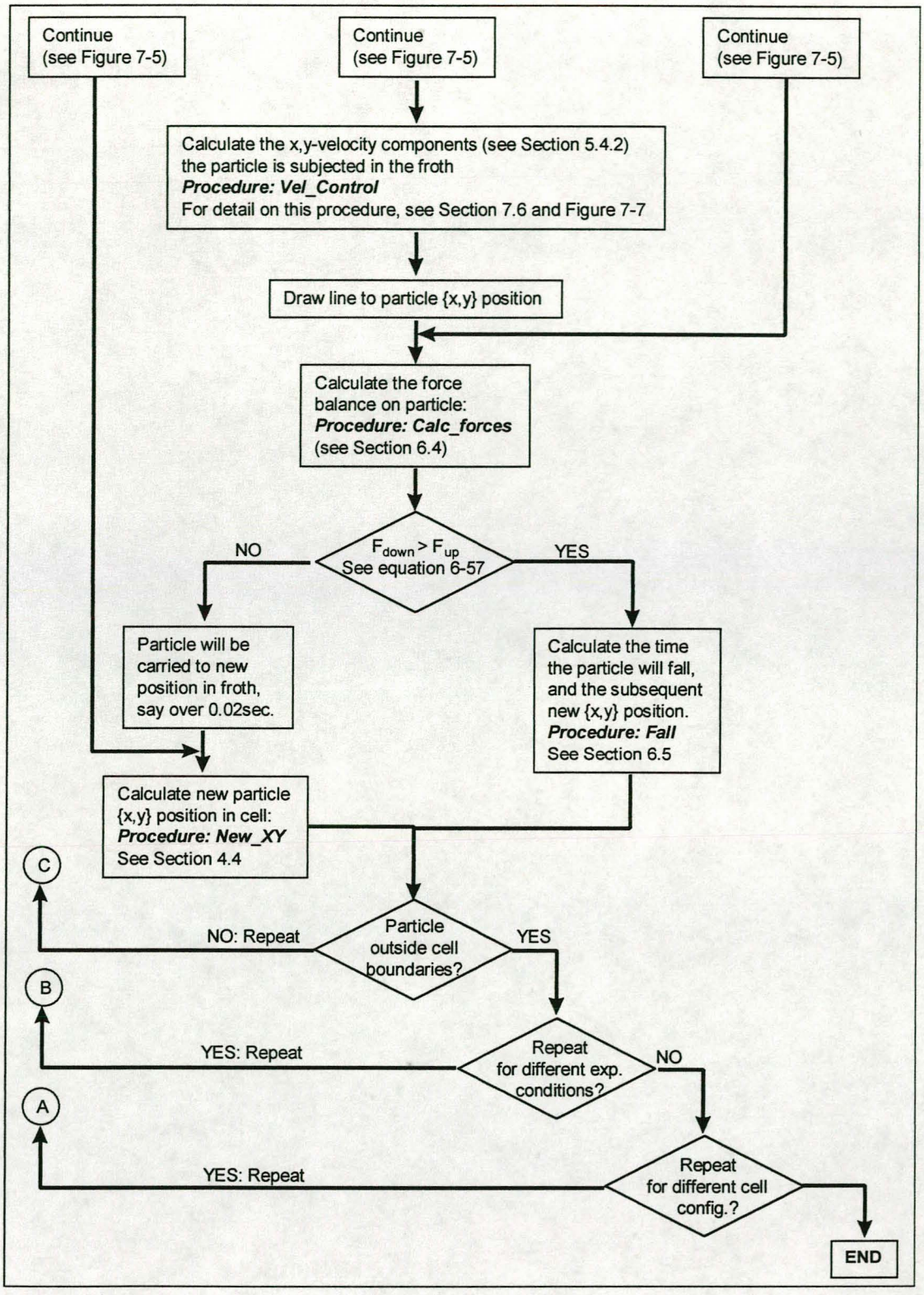

Figure 7-6: Continued flow diagram for particle trajectory calculation.

Following these calculations, the program will check whether the particle is still within the cell boundaries (i.e. not reported to either the tailings or any concentrate compartment - see Figure 3.1). If the particle is still within the calculation

boundaries the main program is repeated (marked as "C" in Figure 7-5). As soon as the particle leaves the calculation boundaries, the user is prompted whether he/she would like to repeat the program at the same cell configuration, but at different experimental conditions. If "yes" the program repeats to position "B" marked in Figure 7-3. If "no" the user is prompted whether he/she would like to repeat the entire program (i.e. at a different cell configuration. If "yes" the program repeats to "A" marked in Figure 7-1, otherwise the program will end.

7.6 Calculate particle velocity components

The flow diagram for calculating the x,y velocity components of a particle at any position in the reverse froth flotation cell is shown in Figure 7-7. As described in section 5.3 and section 5.4, the froth phase is divided into three main froth areas, each consisting of various sub-areas.

Each of these areas is governed by a unique set of equations describing the flow of bubbles, as well as the bubble velocity. The procedure ***Vel_Control*** therefore calls on the ***D_Cor_XY*** procedure to establish in which main froth area the particle is located. The ***D_Cor_XY*** procedure calculates the angle of rotation, θ_{xy}, of a radius drawn through the particle position and the $\{x_0,y_0\}$ origin (see section 5.4.1 and Figure 5.8). If θ_{xy} is less than 90° the particle is located in Froth Area #1 (as shown in Figure 5.3). However, if θ_{xy} is greater than 90°, the procedure ***Test_Y*** determines whether the particle is in Froth Area #2 or Froth Area #3.

If the particle is located in Froth Area #1, the particle velocity is calculated from the ***Velocity_XY1A*** procedure as described in section 7.7 and shown in Figure 7-8. Similarly, if the particle is located in Froth Area #3, the particle velocity is calculated from the ***Velocity_XYNext1A*** procedure as described in section 7.9 and shown in Figure 7-10. Both these procedures are with reference to the $\{x_0,y_0\}$ co-ordinate system.

However, all the calculations for Froth Area #2 are with reference to the {0,0} co-ordinate system (see section 5.3.2). Therefore, if the particle is located in Froth Area #2, the particle position is converted to the {0,0} co-ordinate system by the ***Scale_XY*** procedure. In addition, θ_{xy} is calculated in terms of the {0,0} co-ordinate system by the ***Calc_theta_vel1B*** procedure. The particle velocity is then calculated from the ***Velocity_XY1B*** procedure (as described in section 7.8 and shown in Figure 7-9).

A shown in Figure 7-7, dependent on the location of the particle, Vel_{xy}, θ_{top}, θ_{bottom} and D_{ratio} are calculated by either ***Velocity_XY1A***, ***Velocity_XY1B*** or ***Velocity_XYNext1A***. The direction of particle movement, θ_{dir}, and the x,y-velocity components of the particle (Vel_x & Vel_y) are then calculated from equations 5-43 and 5-41 respectively.

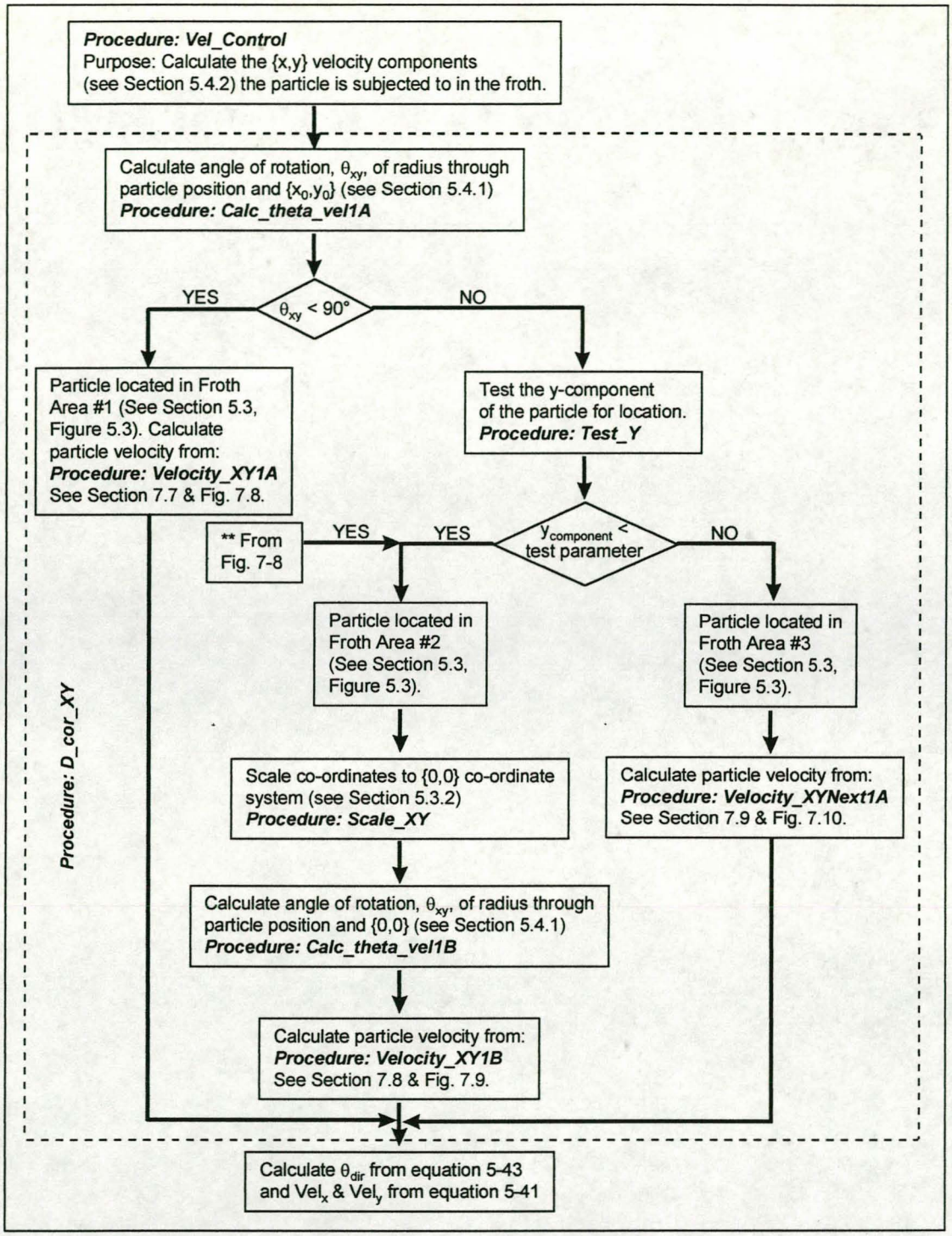

Figure 7-7: Flow diagram of particle velocity component calculation

7.7 Calculate particle velocity in Froth Area #1

The flow diagram for the calculation of Vel_{xy}, θ_{top}, θ_{bottom} and D_{ratio} if the particle is located in Froth Area #1, is shown in Figure 7-8.

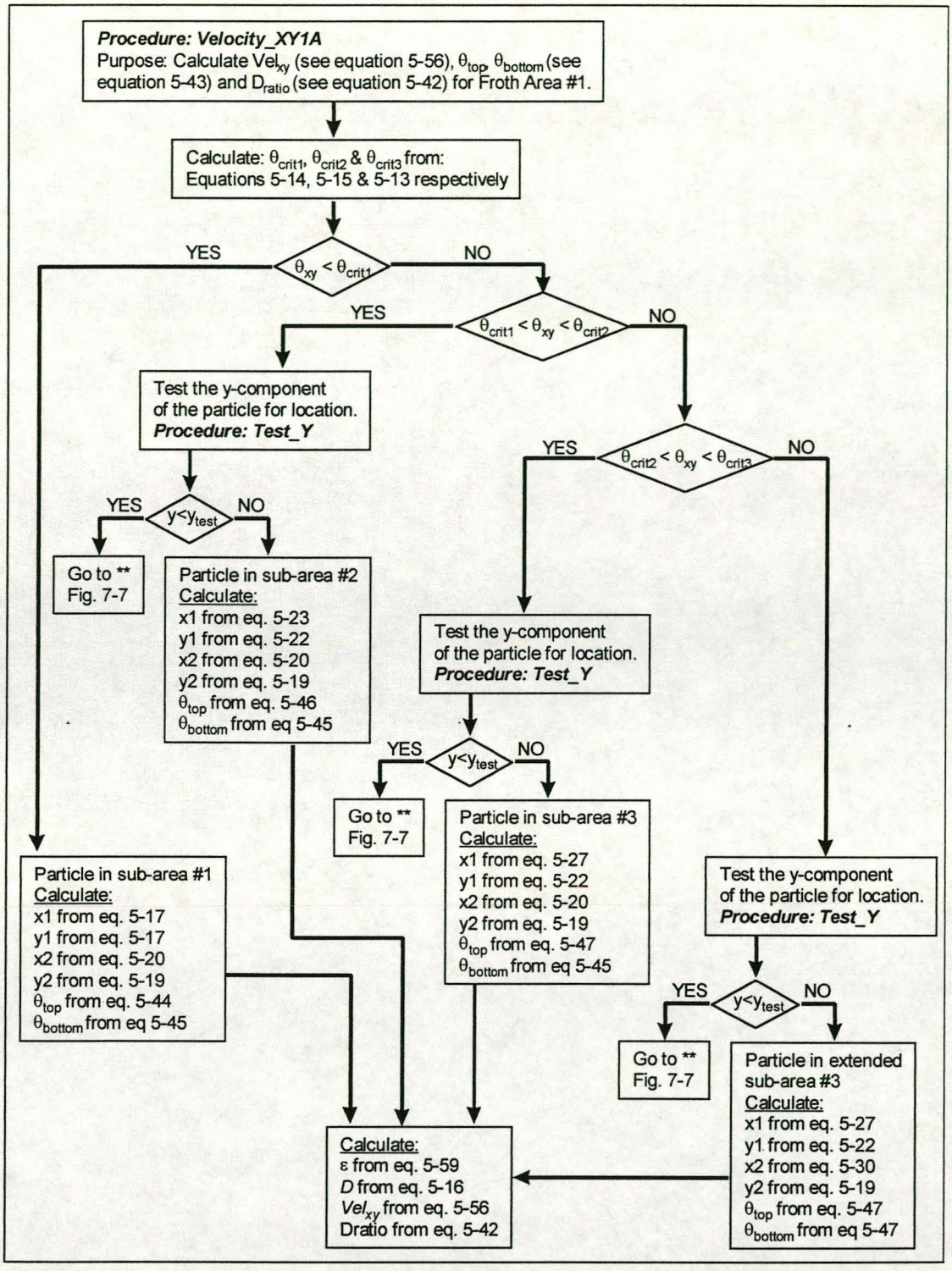

Figure 7-8: Flow diagram for particle velocity calculation in Froth Area #1

As described in section 5.3.1, the Froth Area #1 is divided into three sub-areas, with boundaries defined by specific angles of rotation around the $\{x_0,y_0\}$ origin (see Figure 5.4). The procedure (***Velocity_XY1A***) therefore commences by calculating θ_{crit1}, θ_{crit2} and θ_{crit3} from equation 5-14, 5-15 and 5-13 respectively. If the particle positional angle of rotation (θ_{xy}) is less than θ_{crit1}, the particle is located in the sub-area #1 (see section 5.3.1.1). Therefore (as described in section 5.3.1.1 and 5.4.1.1):

- x_1 is calculated from equation 5-17
- y_1 is calculated from equation 5-17
- x_2 is calculated from equation 5-20
- y_2 is calculated from equation 5-19
- θ_{top} is calculated from equation 5-44
- θ_{bottom} is calculated from equation 5-45

For each of the subsequent tests, the program has to check whether the particle might be located in Froth Area #2 all along. Therefore the program tests the y location of the particle by the ***Test_Y*** procedure. If the y-location of the particle is less than a test parameter, the particle is located in Froth Area #2, and the program continues at the "**" point as shown in Figure 7-7.

If θ_{xy} is greater than θ_{crit1}, the program proceeds to test whether the particle is located in the sub-area #2 (i.e. $\theta_{crit1} < \theta_{xy} < \theta_{crit2}$ - see section 5.3.1.2). If θ_{xy} is greater than θ_{crit1} but less than θ_{crit2}, and the y location is greater than the test parameter the particle is in Froth Area #1, sub-area #2. Therefore (as described in section 5.3.1.2 and 5.4.1.2):

- x_1 is calculated from equation 5-23
- y_1 is calculated from equation 5-22
- x_2 is calculated from equation 5-20
- y_2 is calculated from equation 5-19
- θ_{top} is calculated from equation 5-46
- θ_{bottom} is calculated from equation 5-45

If θ_{xy} is greater than θ_{crit2} but less than θ_{crit3}, and the y location is greater than the test parameter, the particle is located in Froth Area #1, sub-area #3 (see section 5.3.1.3). Therefore (as described in section 5.3.1.3 and 5.4.1.3):

- x_1 is calculated from equation 5-27
- y_1 is calculated from equation 5-22
- x_2 is calculated from equation 5-20
- y_2 is calculated from equation 5-19
- θ_{top} is calculated from equation 5-47
- θ_{bottom} is calculated from equation 5-45

If θ_{xy} is greater than θ_{crit3}, and the y_{test} parameter is less than the y location of the particle, the particle is located in Froth Area #1, extended sub-area #3 (see section 5.3.1.4). Therefore (as described in Sections 5.3.1.4 and 5.4.1.4):

- x_1 is calculated from equation 5-27
- y_1 is calculated from equation 5-22
- x_2 is calculated from equation 5-30
- y_2 is calculated from equation 5-19
- θ_{top} is calculated from equation 5-47
- θ_{bottom} is calculated from equation 5-47

Once the x_1, y_1, x_2, y_2, θ_{top}, and θ_{bottom} parameters have been calculated, the program proceeds to calculate the air hold-up, ε, from equation 5-59, the length of the intercept radius, D, from equation 5-16, the velocity of the particle in the froth, Vel_{xy}, from equation 5-56 and the relative position of the particle along the intercept, D_{ratio}, from equation 5-42.

7.8 Calculate particle velocity in Froth Area #2

The flow diagram for calculating the particle velocity in Froth Area #2, is shown in Figure 7-9.

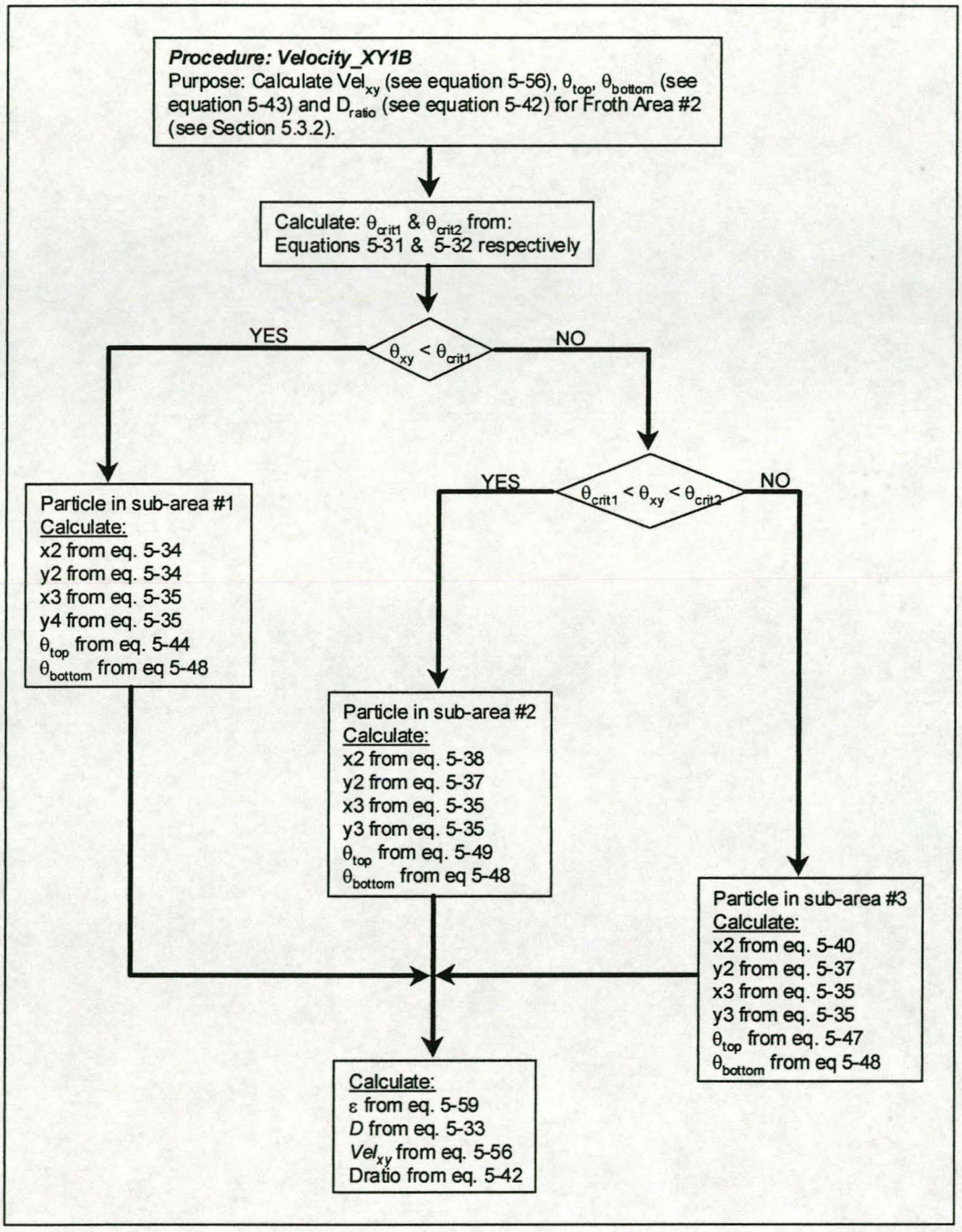

Figure 7-9: Flow diagram for particle velocity calculation in froth area #2

As described in section 5.3.2, the Froth Area #2 is sub-divided into three sub-areas. These sub-areas are bounded by the critical angles of rotation around the {0,0} origin, i.e. θ_{crit1} and θ_{crit2}. This procedure (***Velocity_XY1B***) therefore starts by calculating:

- θ_{crit1} from equation 5-31, and
- θ_{crit2} from equation 5-32

If the particle positional angle of rotation, θ_{xy}, is less than θ_{crit1}, the particle is located in the sub-area #1 (see section 5.3.2.1). Therefore (from section 5.3.2.1 and 5.4.1.5):

- x_1 is calculated from equation 5-34
- y_1 is calculated from equation 5-34
- x_2 is calculated from equation 5-35
- y_2 is calculated from equation 5-35
- θ_{top} is calculated from equation 5-44
- θ_{bottom} is calculated from equation 5-48

However, if the particle positional angle of rotation, θ_{xy}, is greater than θ_{crit1} but less than θ_{crit1}, the particle is located in the sub-area #2 (see section 5.3.2.2). Therefore (from section 5.3.2.2 and 5.4.1.6):

- x_1 is calculated from equation 5-38
- y_1 is calculated from equation 5-37
- x_2 is calculated from equation 5-35
- y_2 is calculated from equation 5-35
- θ_{top} is calculated from equation 5-49
- θ_{bottom} is calculated from equation 5-48

Finally, if the particle positional angle of rotation, θ_{xy}, is greater than θ_{crit2}, the particle is located in the sub-area #3 (see section 5.3.2.3). Therefore (from section 5.3.2.3 and 5.4.1.7):

- x_1 is calculated from equation 5-40
- y_1 is calculated from equation 5-37
- x_2 is calculated from equation 5-35
- y_2 is calculated from equation 5-35
- θ_{top} is calculated from equation 5-47
- θ_{bottom} is calculated from equation 5-48

Once the x_1, y_1, x_2, y_2, θ_{top}, and θ_{bottom} parameters have been calculated, the program proceeds to calculate the air hold-up, ε, from equation 5-59, the length of the intercept radius, D, from equation 5-33, the velocity of the particle in the froth, Vel_{xy}, from equation 5-56 and the relative position of the particle along the intercept, D_{ratio}, from equation 5-42.

7.9 Calculate particle velocity in Froth Area #3

The Froth Area #3 is described in section 5.3.3, with the flow diagram as shown in Figure 7-10.

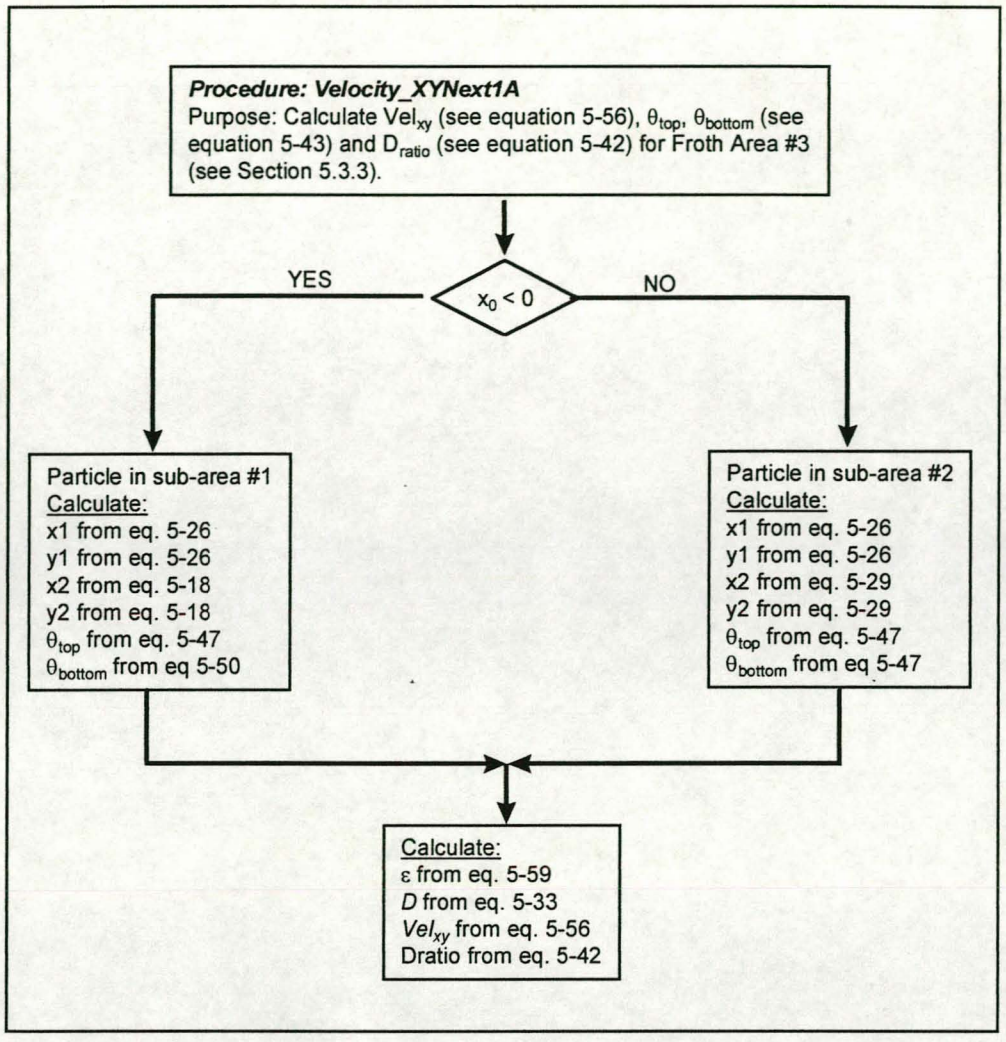

Figure 7-10: Flow diagram for particle velocity calculation in Froth Area #3

This area is sub-divided into two sub-areas, based on the position $\{x_0,y_0\}$ co-ordinates origin in the froth. Therefore, if x_0 is negative and the x-position of the particle is less than $-x_0$, the particle is located in the sub-area #1 (see section 5.3.3.1). Therefore (from section 5.3.3.1 and 5.4.1.8):

- x_1 is calculated from equation 5-26
- y_1 is calculated from equation 5-26
- x_2 is calculated from equation 5-18
- y_2 is calculated from equation 5-18
- θ_{top} is calculated from equation 5-47
- θ_{bottom} is calculated from equation 5-50

However, if the x-position of the particle is greater than $-x_0$, the particle is located in the sub-area #2 (see section 5.3.3.2). Therefore (from section 5.3.3.2 and 5.4.1.9):

- x_1 is calculated from equation 5-26
- y_1 is calculated from equation 5-26
- x_2 is calculated from equation 5-29
- y_2 is calculated from equation 5-29
- θ_{top} is calculated from equation 5-47
- θ_{bottom} is calculated from equation 5-47

As with the ***Velocity_XY1A*** procedure, once the x_1, y_1, x_2, y_2, θ_{top}, and θ_{bottom} parameters have been calculated, the program proceeds to calculate:

- the air hold-up, ε, from equation 5-59
- the length of the intercept radius, D, from equation 5-16
- the velocity of the particle in the froth, Vel_{xy}, from equation 5-56 and

the relative position of the particle along the intercept, D_{ratio}, from equation 5-42.

7.10 Calculate film breakage time by particle

This section described the ***Break_time*** procedure, as used to calculate the time of bubble film rupture by a particle of any shape. The flow diagram for this procedure is shown in Figure 7-11. This procedure is based on the discussion in section 6.1 of this dissertation.

As a start, the procedure calculates the integration step length of the movement of the contact line along the particle surface (Δh^*). Since the particle is assumed to be centrally arranged in the film, only the top half of the liquid film in contact with the particle is considered. The step length is determined by the number of integration steps, as specified by the user in the ***Input_general*** procedure (see Figure 7-3). In addition, the holding parameters (V_{hold}, t_{break}) are zeroed.

The procedure then moves into a repeat loop based on the value of the integration counter, i. On each repetition, the integration counter is incremented by one, while the length of h* is determined as step length of the movement of the contact line (Δh^*) multiplied by the integration counter.

The procedure then moves into particle shape specific procedures to calculate (V_1+V_2) and ΔP_c. These procedures are described in section 7.11 (see Figure 7-12) for particles of volume of revolution shape, and in section 7.12 (see Figure 7-13) for particles of non-volume of revolution shape. Once (V_1+V_2) and ΔP_c is calculated, the procedure calculates:

- Q from equation 6-5.
- $\Delta(V_1+V_2)$ as $(V_1+V_2) - V_{hold}$.
- Δt_{break} from equation 6-6, and
- t_{break} as $t_{break} + \Delta t_{break}$

The procedure will keep repeating until the integration counter, i, is greater than the number of integration steps, N.

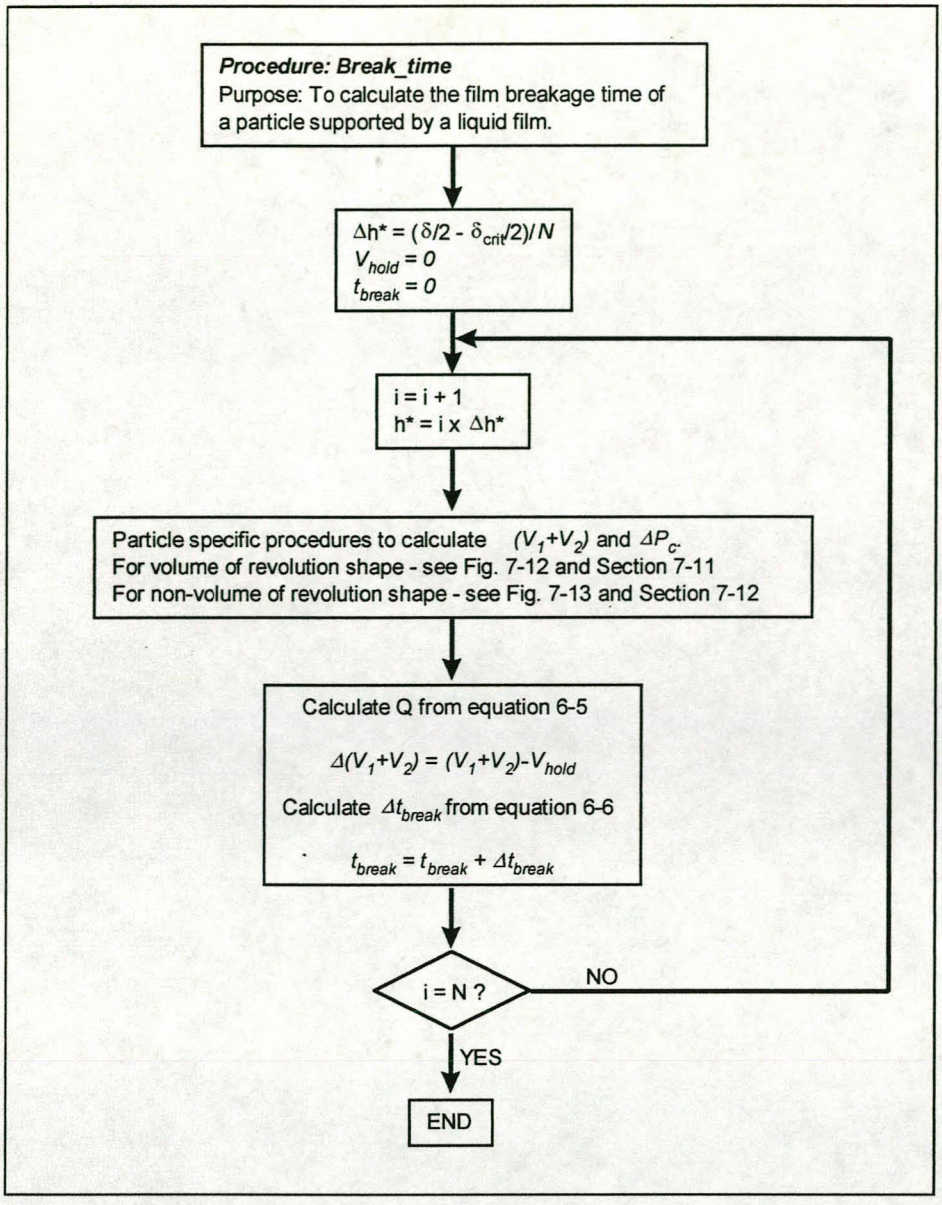

Figure 7-11: Flow diagram for particle film breakage time calculation

7.11 Volume of Revolution Particles

The procedure for calculating (V_1+V_2) and ΔP_c for particles of volume of revolution shape, is outlined in Figure 7-12. As described in section 6.2 of this dissertation, each particle shape is governed by a different set of equations in calculating (V_1+V_2) and ΔP_c. This flow diagram is therefore drawn up in a generic way, with the respective equations per particle shape indicated in tables where applicable.

The procedure starts by zeroing the integration counters, k & l, and the respective volumes (V_1 and V_2). In addition, it calculates the thickness of the volume integration discs (Δa) based on the current value of h* and the number of integration steps, M (as specified in the ***Input_general*** procedure by the user - see Figure 7-3).

The procedure then calculates γ and r* for the required particle shape under investigation. The equations describing this calculation are shown in Table 7-1.

Table 7-1: Equations used to calculate γ and r* per particle shape

Particle Shape	γ	r*
Rod	Equation 6-8	Equation 6-8
Cone	Equation 6-12	Equation 6-13
Sphere	Equation 6-21	Equation 6-20
Disc	Equation 6-21	Equation 6-20
Ellipsoid	Equation 6-33	Equation 6-32

Once γ and r* are calculated, the procedure calculates V_1 based on the values of the interim parameters *a* and *b*. The parameter a is calculated from the centre point of the integration counter time and the thickness of the volume integration discs (Δa). With each loop execution, the value of the integration counter, k, is incremented by one. The loop will terminate as soon as the value of the integration counter, k, is M (i.e. the number of numeric integration steps). The equations used to calculate b and V1 in this sub-loop are shown in Table 7-2 per particle shape.

Table 7-2: Equations used to calculate *b* and V_1 per particle shape.

Particle Shape	b	V_1
Rod	Equation 6-9	Equation 6-11
Cone	Equation 6-17	Equation 6-19
Sphere	Equation 6-25	Equation 6-27
Disc	Equation 6-25	Equation 6-31
Ellipsoid	Equation 6-37	Equation 6-39

Once V_1 has been calculated the procedure starts the sub-loop to numerically integrate V_2. With each execution of the sub-loop, the value of the integration counter, I, is incremented by one, and the loop will terminate if the I = M (number of integration steps specified by user). The value of V_2 is based on the value of the interim integration parameter, b. The equations used to calculate b and V2 per particle shape are shown in Table 7-3.

Table 7-3: Equation used to calculate *b* and V_2 per particle shape.

Particle Shape	b	V_2
Rod	N/A	V_2=0
Cone	Equation 6-14	Equation 6-16
Sphere	Equation 6-22	Equation 6-24
Disc	Equation 6-22	Equation 6-29
Ellipsoid	Equation 6-34	Equation 6-36

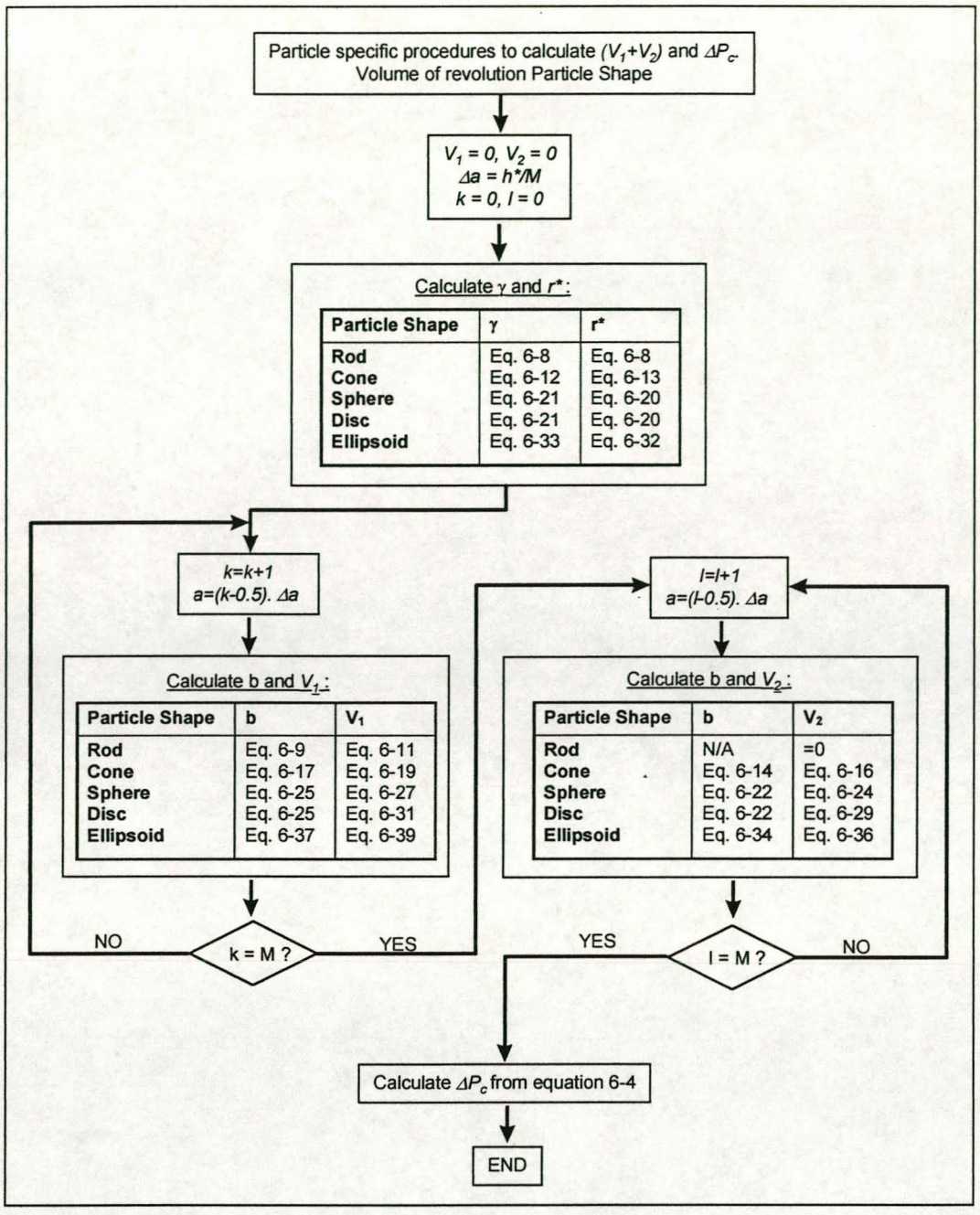

Figure 7-12: Flow diagram for volume of revolution particles

7.12 Cubic and Flat Particles

The procedure for calculating (V_1+V_2) and ΔP_c for cubic and flat particles, is outlined in Figure 7-13. As described in section 6.2 of this dissertation, each particle shape is governed by a different set of equations in calculating (V_1+V_2) and ΔP_c. This flow diagram is therefore drawn up in a generic way, with the respective equations per particle shape indicated in tables where applicable. In essence the diagram summarises the ***Cube*** and ***Flat*** procedures located in the Parti3.tpu Pascal Unit.

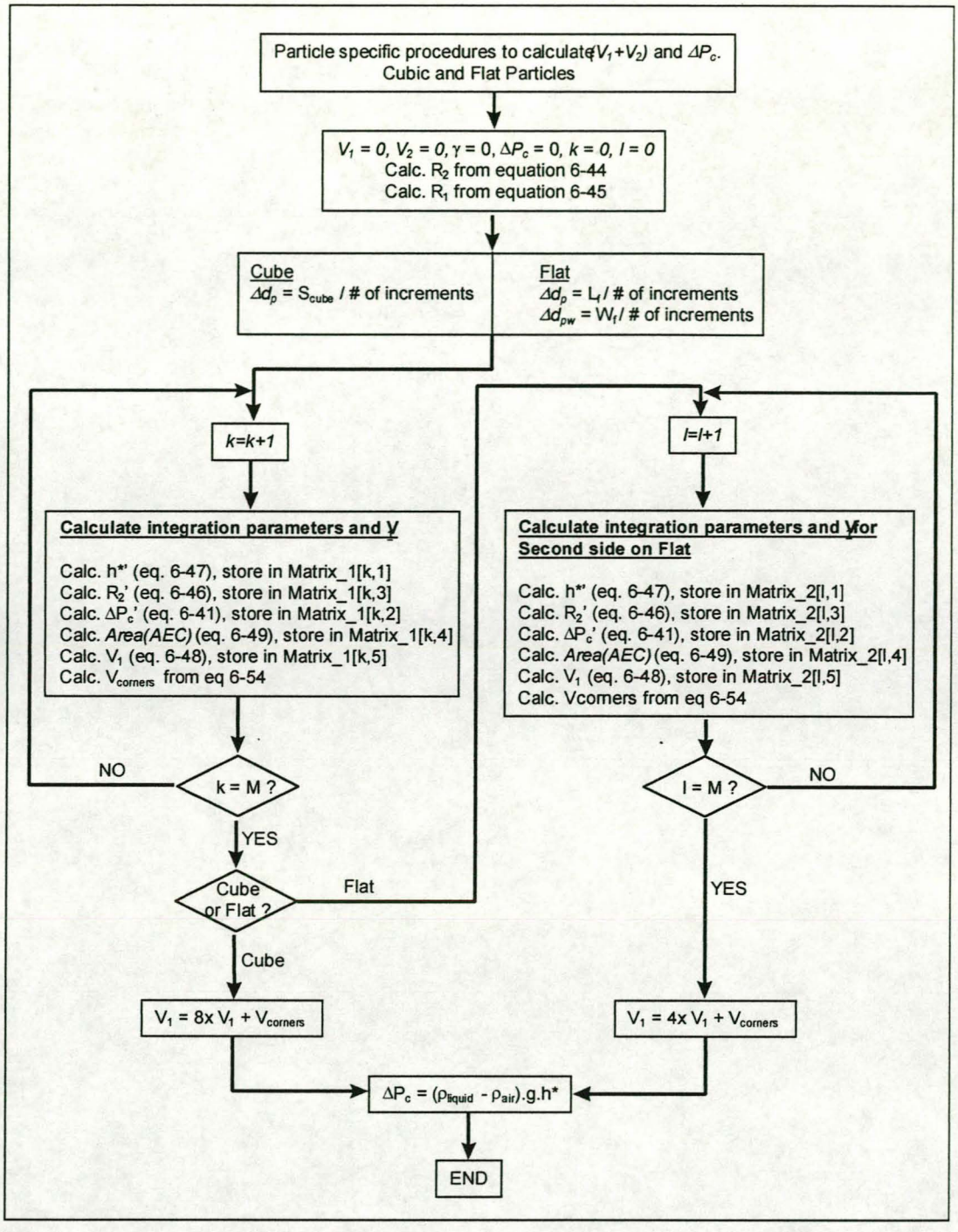

Figure 7-13: Flow diagram for cubic and flat particles

The procedure starts by zeroing the integration counters, k & l, as well as the respective volumes (V_1 and V_2), the pressure drop across the contact interface, ΔP_c, and γ. In addition, it calculates the principal radii of curvature (R_1 and R_2) of the meniscus from equations 6-44 and 6-55 respectively. Dependent on the particle shape, the procedure then calculates the step length along the contact line (see Figure 6-14). For a cube the step length, Δdp, is the side length of the cube divided by the number of integration steps along the contact line. For a flat, however, two faces could have different dimensions. Two step lengths are therefore calculated, i.e. Δd_p and Δd_{pw}.

The procedure now proceeds to calculate for each integration step, *k* or *l*, the V_1 volume to be removed from the contact line. The loops will continue until the number of integration steps, M (as specified in the ***Input_general*** procedure by the user - see Figure 7-3) is reached. For a cube, only one half of a face needs to be considered. The total volume to be removed will then be the eight times the volume per half face plus the volume of liquid at the corners. For a Flat, however, the faces could have different dimensions. Halves of two different faces are therefore considered, with the total volume equal to four times the sum of the volume per two faces plus the volume of the corners to be removed.

Therefore, for a cube the procedure is straightforward in that for each integration step, k:

- The value of $h^{*'}$ is calculated from equation 6-47 and stored in a calculation matrix in row k, column 1.
- The value of $h^{*'}$ is then substituted into equation 6-46 to calculate R_2'. The answer is stored in a calculation matrix in row k, column 3.
- The value of $\Delta P_c'$ can then be calculated by substituting R_2' and R_1 into equation 6-41. The answer is stored in a calculation matrix in row k, column 2.
- In order to calculate V_1, the *area(AEC)* has to be calculated as shown in Figure 6-15. The values of h*' and R2' are therefore substituted into equations 6-50, 6-51 and 6-52, which in turn are substituted into equation 6-49 to calculate the area. The answer is stored in a calculation matrix in row k, column 4.
- V1 is then calculated from equation 6-48 and stored in a calculation matrix in row k, column 5.
- In addition, the volume of the corners is calculated from equation 6-54.

The loop is repeated for the number of integration steps, M. The total volume, V_1, is then calculated from equation 6-53.

This same procedure is followed for a **Flat** shaped particle. The only difference is that the procedure is repeated for a second face (with integration counter l, and a different storage matrix) (see Figure 7-13). Following both the loops, the total volume is calculated from a modified equation 6-53 since two faces have already been considered. For both a Cube and a Flat, the pressure drop across the interface is then calculated from equation 6-41.

7.13 Summary

The respective computational procedures linking the froth models of chapter 5 with the particle/film interaction models of chapter 6 were described in this chapter. All the procedures are contained in a Borland Pascal program (Lines11.pas – Appendix A) and a Pascal Unit (Parti3.tpu – Appendix B). These computational procedures are extensively used in the following chapter that describes the sensitivity analysis conducted to analyse the effect of physical parameters on the rupture of bubble films (and subsequent particle trajectories) in the two phase froth of the flotation cell.

8. SENSITIVITY ANALYSIS

The development of a fundamental model to describe the behaviour of coarse particles in the flotation cell is described in chapters 5 and 6 of this dissertation. In turn, chapter 7 described how the various equations are utilised in the respective computational procedures. In order to analyse the effect of the various manipulative variables on the particle trajectory in the flotation cell, a sensitivity analysis was conducted. The results of the sensitivity analysis are displayed (in the form of graphical simulator output) and discussed in this chapter.

In order to predict the particle trajectory in the cell, bubble flow streamlines were calculated. Since the froth structure at each position in the cell will have an effect on the particle trajectory, the following froth variables were considered in the sensitivity analysis:

- Air flowrate through the spargers in the respective cell sub-compartments.
- Entrained water in the froth, i.e. water reporting to the middlings and tailings.
- Combined effect of various physical cell operating conditions.
- Bubble size at each operating condition.

In turn, various particle properties were investigated. These include:

- The effect of particle size at various operating conditions.
- The effect of particle density at various operating conditions.
- The effect of surface properties, i.e. contact angle, at various operating conditions.
- The effect of particle shape. Since the size, density and dimensions of each particle shape will influence the behaviour of particles in the froth, selected combinations of variables were kept constant and evaluated at various operating conditions. The combinations of variables included:
  - Particles with similar density and volume, i.e. mass.
  - Particles with similar mass and total surface area, i.e. Mass to Area Ratio.
  - Particles with similar density and Mass to Area Ratio.

8.1 Air Flowrate

The volumetric flowrate of air through the spargers directly affects the velocity of the bubbles in the reverse froth flotation cell (see equation 5-56). Intuitively though, it can be expected that the amount of entrained water in the froth, the air hold-up and subsequently the bubble film thickness will be affected as well. The proposed model, however, allows the manipulation of a single input variable while keeping all other variables constant. Figure 8-1 therefore shows the effect on the particle trajectory when manipulating the air flowrate through the sparger located in sub-compartment A. Figure 8-2, in turn, shows the effect of manipulating the air flowrate through the sparger in sub-compartment B.

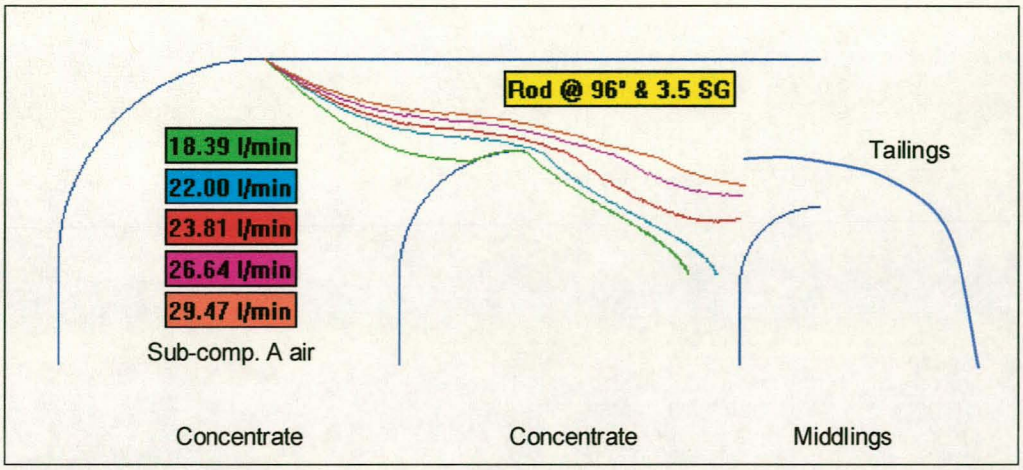

Figure 8-1: Effect of air flowrate through sub-compartment A.

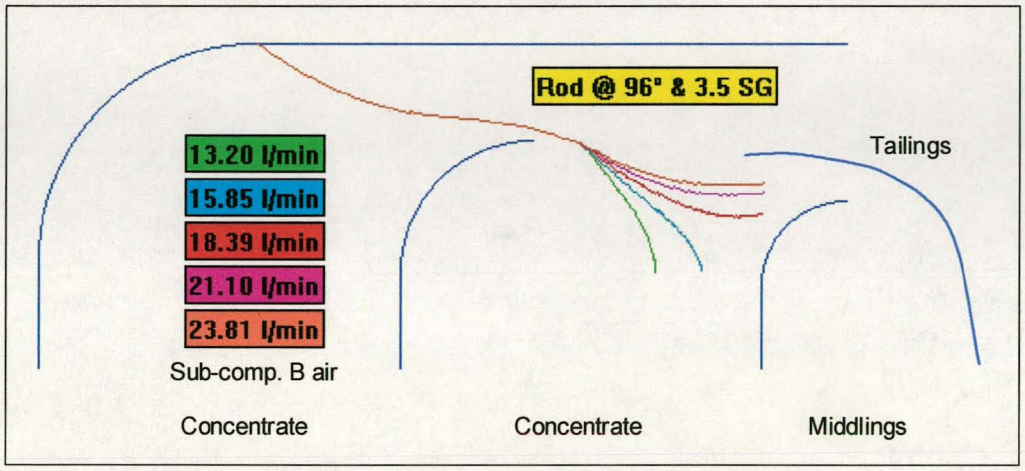

Figure 8-2: Effect of air flowrate through sub-compartment B.

The parameter settings for both Figure 8-1 and Figure 8-2 are shown in Table 8-1.

Table 8-1: Parameter settings for influence of air flowrate

Property	Value
Particle properties:	
➢ Shape	Rod / Cylindrical
➢ Size	3.38 mm long x 2.08 mm diameter
➢ Density	3500 kg/m³
➢ Contact Angle	96°
Operational Properties	
➢ Liquid Level (from top)	= 240 mm
➢ Splitter Plate (from top)	= 41 mm
➢ Bubble size at interface	= 1.09 mm diameter
➢ Water to tailings	= 31.6 cm³/sec
➢ Water to middlings	= 47.2 cm³/sec
➢ Froth height (from top)	= 10 mm

In Figure 8-1 the air through sub-compartment A was varied between 18.39 l/min and 29.47 l/min, while the air flowrate through sub-compartment B was kept at 18.39 l/min. As expected, an increase in air flowrate results in the particle profile to be lifted in the froth. Whereas at 18.39 l/min air the particle would report to the concentrate, the particle will report to the middlings compartment at an air flowrate of 29.47 l/min. The main reason for this is the increase in horizontal froth velocity, resulting in an increase in horizontal distance travelled by the particle for the same film breakage time (it is assumed that the particle is supported by the bubble films for the period of bubble film breakage).

Similarly, a classification of the same particle can occur if the air flowrate in sub-compartment B is manipulated. In Figure 8-2, the air flowrate in sub-compartment A is kept constant at 23.81 l/min, while the air flowrate in sub-compartment B is manipulated as shown. Although the particles now follow the same trajectory while in froth area #1, classification occurs when the particles enter froth area #2. Yet again this is due to an increase in the horizontal distance travelled for the same film rupture time.

In summary:

- Particles with identical properties will classify more to the tailings with an increase in air flowrate in sub-compartment A.
- A secondary classification can be obtained by manipulating the air flowrate through sub-compartment B.

8.2 Entrained Water

The entrained water in the froth affects the bubble film thickness (see equation 5-70). An indirect indication of the entrained water in the froth is the amount of water reporting to the middlings and the tailings compartments. Figure 8-3 and Figure 8-4 show the particle profile of a rod shaped particle with the manipulation of the liquid flow to the middlings and the tailings respectively.

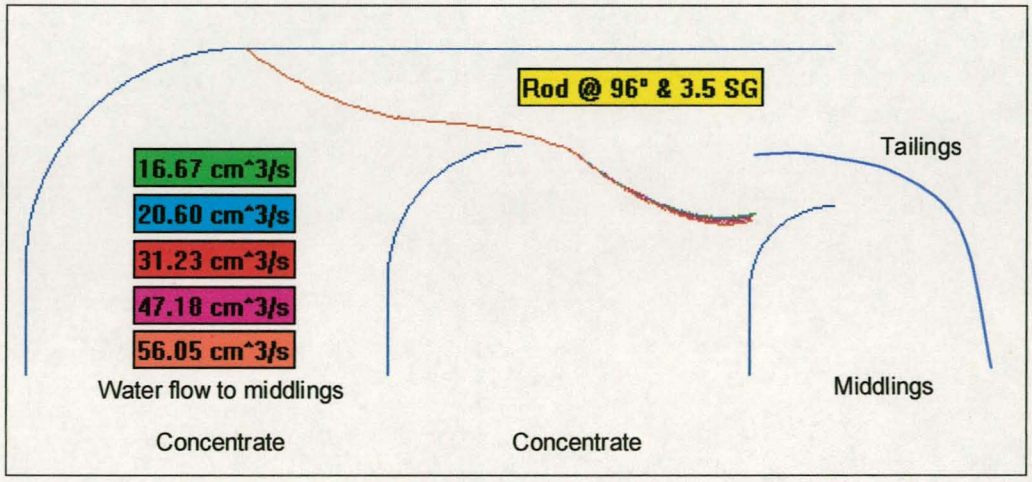

Figure 8-3: Effect of water flowrate to the middlings compartment

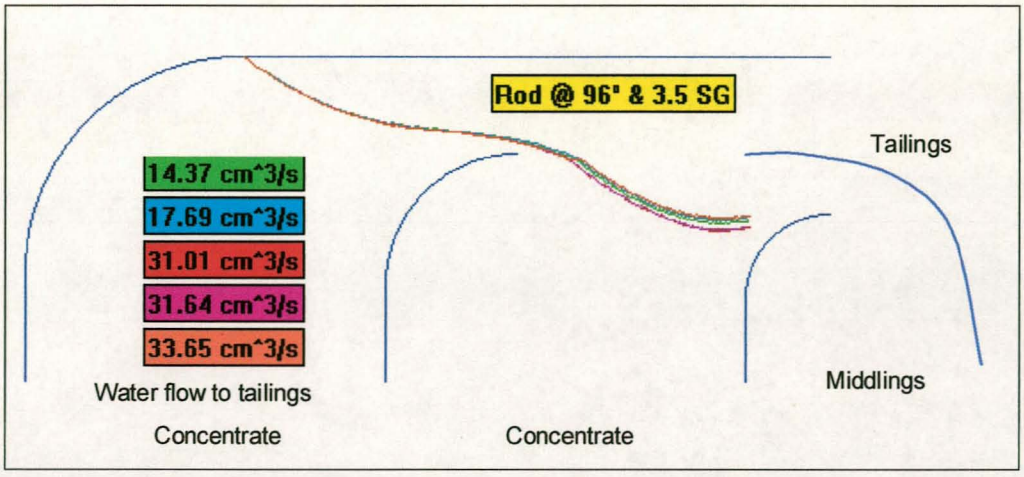

Figure 8-4: Effect of the water flowrate to the tailings compartment

The parameter settings for both Figure 8-3 and Figure 8-4 are shown in Table 8-2.

Table 8-2: Parameter settings for Figure 8-3 and Figure 8-4

Property	Value
Particle properties:	
➢ Shape	Rod / Cylindrical
➢ Size	3.38 mm long x 2.08 mm diameter
➢ Density	3500 kg/m³
➢ Contact Angle	96°
Operational Properties	
➢ Liquid Level (from top)	= 240 mm
➢ Splitter Plate (from top)	= 41 mm
➢ Bubble size at interface	= 1.09 mm diameter
➢ Air sub-comp. A	= 23.8 l/min
➢ Air sub-comp. B	= 18.4 l/min
➢ Froth height (from top)	= 10 mm

In Figure 8-3 the liquid flow to the tailings was kept constant at 31.6 cm³/sec, while the liquid flow to the middlings compartment was manipulated. As shown, only limited classification results. Nonetheless, an increase in water flow to the middlings results in a lower particle trajectory in the froth (albeit a very small influence). The limited effect is due to the combined effects of an increase in the bubble film thickness, the reduction in the air hold-up and the increase in bubble film rupture time.

Figure 8-4 shows the effect of manipulating the flow of liquid to the tailings while maintaining the flow of liquid to the middlings at a value of 47.2 cm³/sec. Although the classification of particles is slightly more pronounced, the effect is still negligible.

In summary:

- Manipulating the flow of liquid to the middlings and tailings compartments respectively, has a negligible effect on the trajectory of particles with identical properties.
- The manipulation of water flows is an artificial constraint on the process. Due to the interaction of various parameters, more value and insight will be gained in evaluating the particle trajectories under actual operating conditions (i.e. with parameters as measured during the experimental campaign).

8.3 Operating Conditions

Five operating conditions were selected in order to evaluate the effect of various operating and particle parameters on the trajectory of particles in the cell. These selected conditions were actual operating conditions for the cell (see section 9). The bubble flow streamlines of the respective operating conditions are shown in Figure 8-5 through to Figure 8-9. For each operating condition, the following common parameters were measured and/or determined:

- liquid density = 1000 kg/m^3
- liquid viscosity = 1.026x10^{-3} Pa.s
- liquid surface tension = 6.37 x 10^{-2} N/m
- velocity constant, froth area #1 = k_{v1A} = 3.5
- velocity constant, froth area #2 = k_{v1B} = 8.0

8.3.1 Operating condition #1

The bubble flow profile for the operation condition #1 is shown in Figure 8-5, with the measured parameters shown in Table 8-3.

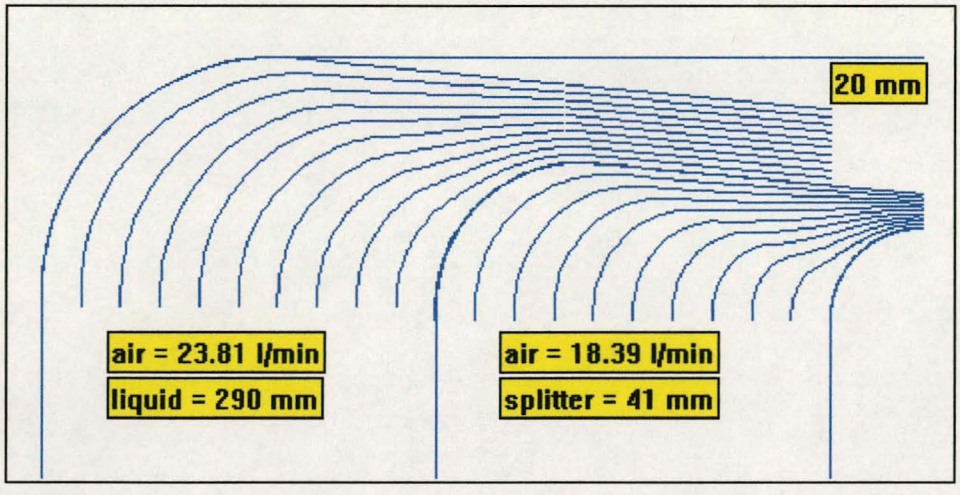

Figure 8-5: Bubble flow profiles for operating condition #1

As shown in Figure 8-5, the flow profiles are calculated only for selected regions of the cell above the liquid froth interface. It is assumed that if the particle reports to any region outside those shown, it will report to the concentrate, middlings or tailings sections. This assumption is valid due to the size of the particles considered. Once the particle has reported to the liquid phase (in the concentrate

compartment), the particle will not be able to reattach to a bubble and be carried into the froth phase. Similarly, once the particle has reported to either the tailings or middlings, it cannot move back into the froth phase.

Table 8-3: Measured parameters for operating condition #1

Parameter	Value
Air flowrate sub-compartment A	= 23.8 l/min
Air flowrate sub-compartment B	= 18.4 l/min
Liquid level (measured from cell top)	= 290 mm
Splitter plate (measure from cell top)	= 41 mm
Froth height over splitter (from top)	= 20 mm
Bubble diameter at interface	= 1.07 mm
Liquid flow to middlings	= 16.7 cm^3/sec
Liquid flow to tailings	= 14.4 cm^3/sec
Air hold-up aa coefficient (eq 5-58)	= 0.452
Air hold-up ab constant (eq 5-58)	= -0.186
Air hold-up ba coefficient (eq 5-58)	= 1.046
Air hold-up bb constant (eq 5-58)	= 0.176

8.3.2 Operating condition #2

The bubble flow profiles for the operating condition #2 are shown in Figure 8-6 with the measured parameters shown in Table 8-4. This condition has identical manipulated parameters to operating condition #1 except for a higher liquid-froth interface. Due to the increase in the liquid-froth interface the measured bubble diameter at the interface, air hold-up parameters, height of froth over the splitter plate and entrained liquid have changed (see Table 8-4).

Table 8-4: Measured parameters for operating condition #2

Parameter	Value
Air flowrate sub-compartment A	= 23.8 l/min
Air flowrate sub-compartment B	= 18.4 l/min
Liquid level (measured from cell top)	= 265 mm
Splitter plate (measure from cell top)	= 41 mm
Froth height over splitter (from top)	= 15 mm
Bubble diameter at interface	= 1.08 mm
Liquid flow to middlings	= 20.6 cm^3/sec
Liquid flow to tailings	= 17.7 cm^3/sec
Air hold-up aa coefficient (eq 5-58)	= 0.268
Air hold-up ab constant (eq 5-58)	= -0.047
Air hold-up ba coefficient (eq 5-58)	= 1.019
Air hold-up bb constant (eq 5-58)	= 0.198

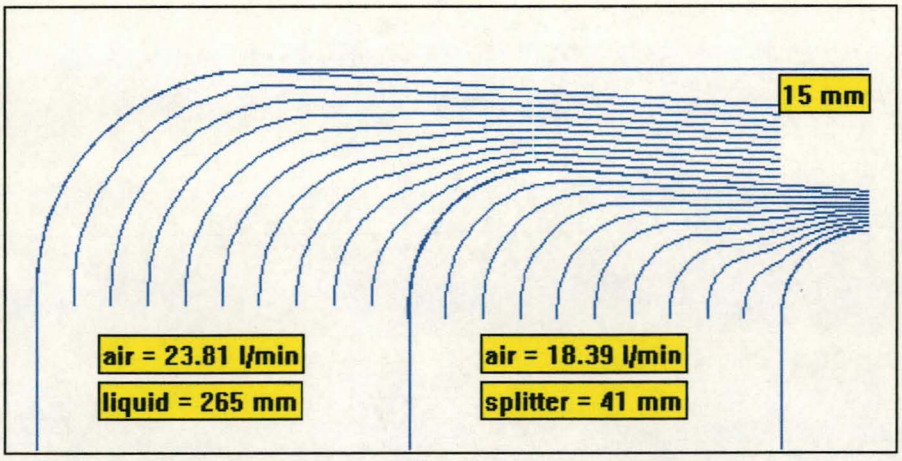

Figure 8-6: Bubble flow profiles for operating condition #2

8.3.3 Operating condition #3

The bubble flow profiles for the operating condition #3 are shown in Figure 8-7 with the measured parameters shown in Table 8-5. For this operating condition, the liquid-froth interface was increased yet again, with all other manipulative variables remaining as for operating conditions #1 and #2. Due to the increase in the liquid-froth interface the measured bubble diameter at the interface, air hold-up parameters, height of froth over the splitter plate and entrained liquid have again changed (see Table 8-5).

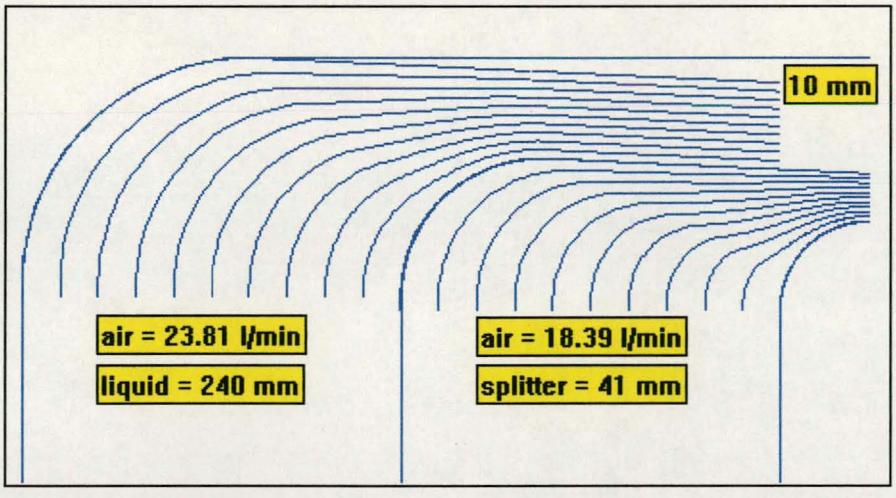

Figure 8-7: Bubble flow profiles for operating condition #3

Operating conditions #1 to #3 were designed to investigate the effect of liquid level on the particle trajectory in the cell. As expected (see Tables 8-3 to 8-5) the entrained liquid increases as the liquid-froth interface increases. This is mainly due to the liquid having less time to drain from the bubble film and Plataeu borders. In addition, the height of the froth over the splitter plate increases due to the more stable froth being generated and the bubble size increases due to the decreased hydrostatic pressure on the bubbles.

Table 8-5: Measured parameters for operating condition #3

Parameter	Value
Air flowrate sub-compartment A	= 23.8 l/min
Air flowrate sub-compartment B	= 18.4 l/min
Liquid level (measured from cell top)	= 240 mm
Splitter plate (measured from cell top)	= 41 mm
Froth height over splitter (from top)	= 10 mm
Bubble diameter at interface	= 1.09 mm
Liquid flow to middlings	= 47.2 cm^3/sec
Liquid flow to tailings	= 31.6 cm^3/sec
Air hold-up aa coefficient (eq 5-58)	= -0.421
Air hold-up ab constant (eq 5-58)	= 0.461
Air hold-up ba coefficient (eq 5-58)	= 1.145
Air hold-up bb constant (eq 5-58)	= 0.111

8.3.4 Operating condition #4

Operating conditions #4 and #5 were designed to investigate the effect of air flowrate on the trajectory of particles in the cell. For operating condition #4 the air flowrate in sub-compartment B was increased while all other manipulative variables were kept the same as for operating condition #3. The bubble flow profiles for this operating condition are shown in Figure 8-8 with the measured parameters shown in Table 8-6.

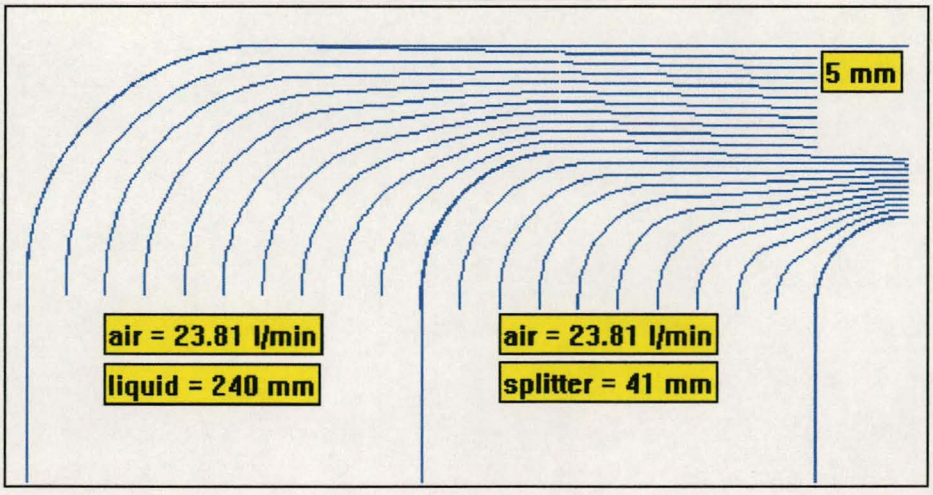

Figure 8-8: Bubble flow profiles for operating condition #4

Table 8-6: Measured parameters for operating condition #4

Parameter	Value
Air flowrate sub-compartment A	= 23.8 l/min
Air flowrate sub-compartment B	= 23.8 l/min
Liquid level (measured from cell top)	= 240 mm
Splitter plate (measured from cell top)	= 41 mm
Froth height over splitter (from top)	= 5 mm
Bubble diameter at interface	= 1.17 mm
Liquid flow to middlings	= 31.2 cm^3/sec
Liquid flow to tailings	= 31.0 cm^3/sec
Air hold-up aa coefficient (eq 5-58)	= -0.104
Air hold-up ab constant (eq 5-58)	= 0.302
Air hold-up ba coefficient (eq 5-58)	= 1.242
Air hold-up bb constant (eq 5-58)	= 0.012

8.3.5 Operating condition #5

For operating condition #5 the air flowrate in sub-compartment A was increased while all other manipulative variable were kept the same as for operating condition #3. The bubble flow profiles for this operating condition are shown in Figure 8-9 with the measured parameters shown in Table 8-7.

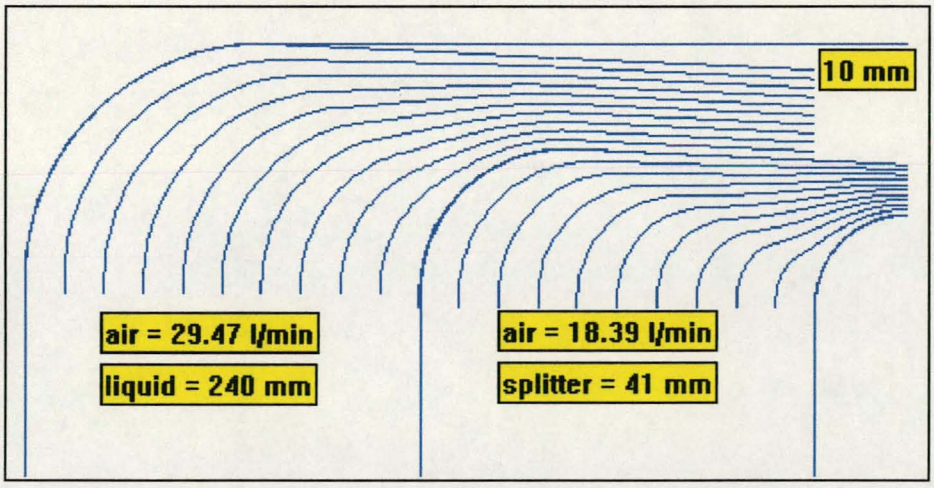

Figure 8-9: Bubble flow profiles for operating condition #5

Table 8-7: Measured parameters for operating condition #5

Parameter	Value
Air flowrate sub-compartment A	= 29.5 l/min
Air flowrate sub-compartment B	= 18.4 l/min
Liquid level (measured from cell top)	= 240 mm
Splitter plate (measure from cell top)	= 41 mm
Froth height over splitter (from top)	= 10 mm
Bubble diameter at interface	= 1.01 mm
Liquid flow to middlings	= 56.1 cm^3/sec

Liquid flow to tailings	= 33.7 cm³/sec
Air hold-up aa coefficient (eq 5-58)	= -1.002
Air hold-up ab constant (eq 5-58)	= 0.949
Air hold-up ba coefficient (eq 5-58)	= 1.386
Air hold-up bb constant (eq 5-58)	= -0.094

8.3.6 Summary of operating conditions

From Tables 8-3 to 8-7 it is clear that:

- An increase in the liquid-froth interface level, with all other manipulative parameters remaining constant, results in:
  - a smaller bubble size at the liquid froth interface;
  - the height of the froth overflow over the splitter plate to increase;
  - a less drained froth, i.e. the liquid flow to the middlings and tailings will increase;
  - the air hold-up throughout the cell to decrease.
- The opposite effects are the result of a decrease in the liquid-froth interface.
- An increase in the air flowrate through the sparger in sub-compartment A results in:
  - a decrease in the air hold-up in froth areas #1 and #3;
  - a decrease in the bubble size at the liquid froth interface;
  - the height of the froth overflow over the splitter plate to increase;
  - a less drained froth, i.e. the liquid flow to the middlings and tailings will increase.
- An increase in the air flowrate through the sparger in sub-compartment B results in:
  - a decrease in the air hold-up in froth areas #2 and #3;
  - an increase in the bubble size at the liquid froth interface;
  - the height of the froth overflow over the splitter plate to increase;
  - a less drained froth in froth area #2, i.e. the liquid flow to the middlings will increase.

8.4 Bubble Size

The effect of bubble size on the trajectory of particles of identical properties in the cell was investigated under each of the above five operating conditions. A particle with properties as shown in Table 8-8, was used in the simulations. Furthermore, the bubble size at the liquid-froth interface was set at:

- measured bubble size for specific operating condition *plus* one measured standard deviation
- measured bubble size for specific operating condition *plus* half the measured standard deviation
- measured bubble size for specific operating condition
- measured bubble size for specific operating condition *minus* half the measured standard deviation
- measured bubble size for specific operating condition *minus* one measured standard deviation

Table 8-8: Particle properties to investigate influence of bubble size

Property	Value
Particle properties:	
➢ Shape	Rod / Cylindrical
➢ Size	3.38 mm long x 2.08 mm diameter
➢ Density	3500 kg/m³
➢ Contact Angle	96°

The effect of the bubble size at the liquid-froth interface under the operating condition #1 is shown in Figure 8-10. Each particle profile is colour coded with the corresponding bubble size shown on the figure. For the purpose of black and white copies of this dissertation, the bubble size shown at the top of the list corresponds with the highest (flattest) particle profile in the cell, and vice versa.

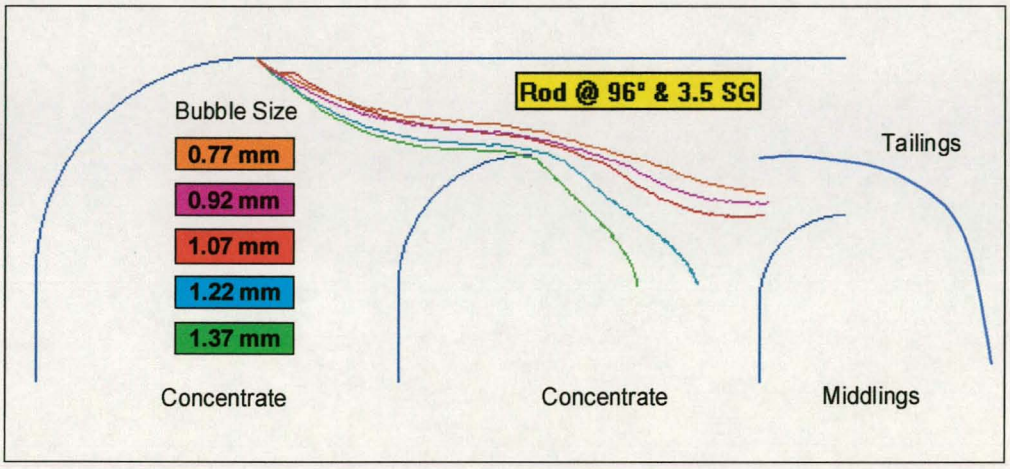

Figure 8-10: Effect of interface bubble size under operating condition #1

From Figure 8-10 it is clear that the interface bubble size has a pronounced effect on the particle trajectory under deep liquid-froth interface conditions (operating condition #1). Particle trajectories vary from comfortably reporting to the concentrate to reporting to the middlings fraction. At fine bubble sizes (0.7737 mm) particles could even report to the tailings, depending on the setting of the splitter plate.

Figure 8-11 shows the same profiles, but under operating condition #2, i.e. a slightly increased liquid-froth interface level. Again a significant spread of particle profiles is obtained, however, the profiles for the plus one standard deviation and plus half standard deviation conditions have lifted. The profiles for the smaller bubble size stay virtually the same.

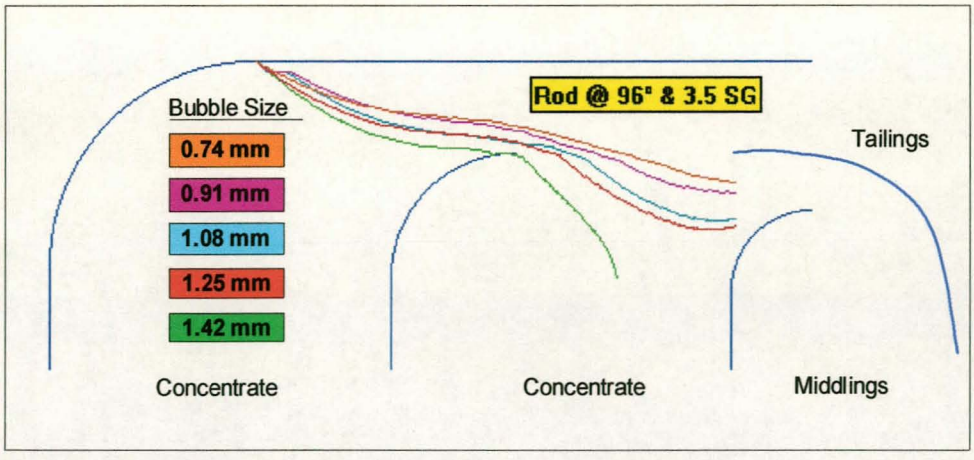

Figure 8-11: Effect of interface bubble size under operating condition #2

The particle trajectories for operating condition #3, i.e. a liquid-froth interface height of 240 mm, are shown in Figure 8-12. Again there is a pronounced influence on the particle trajectory, with the trajectory being lifted towards the tailings compartment with small bubbles and a steep trajectory to the concentrate for large bubbles. The bubble size at the liquid-froth interface is therefore critical in determining the trajectory of a particle in the froth.

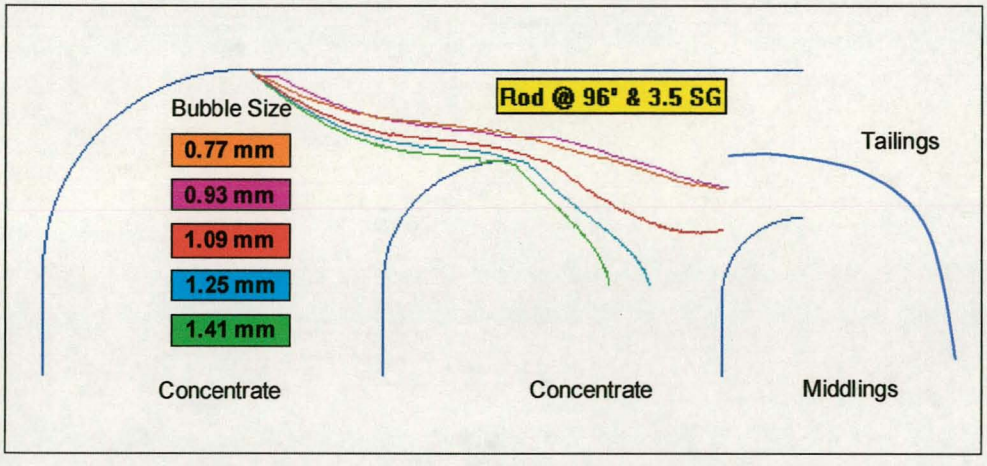

Figure 8-12: Effect of interface bubble size under operating condition #3

The same particle trajectories are shown for operating condition #4 in Figure 8-13. Since the air-flowrate through the froth area #1 is similar to the conditions for the operating condition #3, the particle trajectories show the same form in froth area #1 as in Figure 8-12. However, the air flowrate through sub-compartment B has increased resulting in the particle profiles in froth area #2 to be lifted due to the actions as described in section 8.1 caused by the influence of air flowrate. The spread in particle profiles for different bubble sizes therefore still occurs, however, to a lesser extent for froth areas #2 and #3.

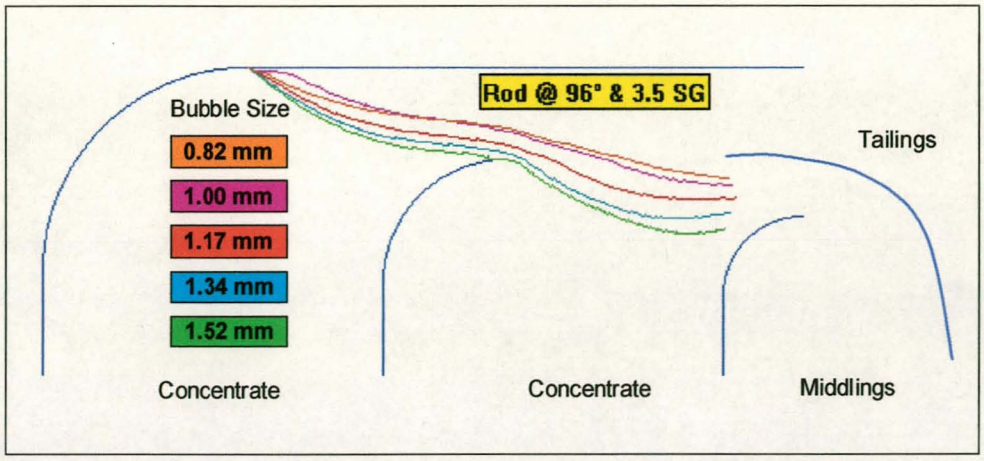

Figure 8-13: Effect of interface bubble size under operating condition #4

A similar exercise was conducted for the operating condition #5, i.e. increased air flowrate through the sparger located in sub-compartment A. The results of this exercise are shown in Figure 8-14. Again a spread in particle profiles is predicted, with a small interface bubble size resulting in a higher trajectory than large bubble sizes. However, compared with Figure 8-12 for operating condition #3, the classification (or spread) is much less. This can again be attributed to the effects discussed under the sensitivity analysis on air flowrate through the sparger located in sub-compartment A (see section 8.1), i.e. the increase in horizontal froth velocity. Particles have therefore less time to classify to the degree as shown in Figure 8-12.

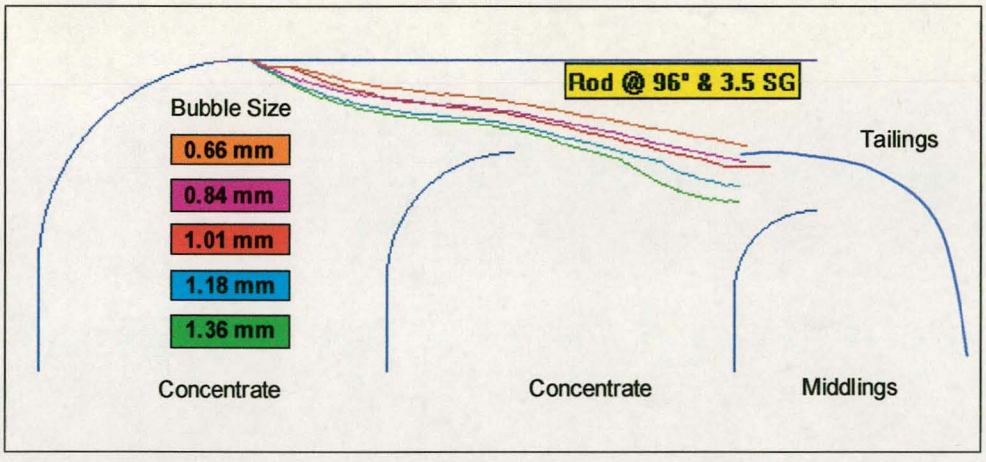

Figure 8-14: Effect of interface bubble size under operating condition #5

The spread in particle trajectory with varying interface bubble size can be attributed to two main reasons:

- From equation 5-70 it is clear that the bubble film thickness will reduce as the bubble size increases. Based on equations 6-5, 6-6 and the equations used for the calculation of V_1 and V_2 per particle size, the time of film rupture will decrease with a decrease in film thickness. The particle would therefore fall through the froth at an increased rate resulting in a lower trajectory.

- From equation 6-71 the particle fall time will increase with an increase in bubble size. Since the predominant movement during fall is in the vertical direction, it can be expected that the particle will travel at a steeper trajectory in the froth.

However, it is clear that the operating condition of the cell can either accentuate the spread, or reduce the effect.

In summary:

- An increase in interface bubble size results in a lower particle trajectory, and vice versa.
- By increasing the interface height, the spread becomes more accentuated, but the trajectories as a whole move downwards, i.e. towards the concentrate compartment. This is mainly due to more entrained water present in the froth, and an increase in bubble size at the liquid-froth interface.
- An increase in the air flowrate through the sparger located in sub-compartment B does not influence the classification in froth area #1. However, due to an increase in the horizontal froth velocity, the classification effect in froth area #2 is reduced.
- An increase in the air flowrate through the sparger located in sub-compartment A results in an overall increase in horizontal froth velocity. This increase causes the influence of bubble size to be less pronounced.

8.5 Particle Size

The effect of the particle size on the trajectory of a particle in the flotation cell was investigated under the five operating conditions outlined in section 8.3. Since a spherical particle can be described by a single dimensional parameter, a spherical particle was selected for the purpose of this exercise. In addition a particle density of 3500 kg/m^3 and an equilibrium contact angle of 98° (the equilibrium contact angle of the wax particle coating – see section 3.4.5) were selected. Five particle radii were investigated. The properties of the various particles are shown in Table 8-9.

Table 8-9: Spherical particle properties for size sensitivity analysis

Radius [mm]	Area [mm^2]	Volume [mm^3]	Mass [mg]	Mass/Area ratio
0.50	3.14	0.52	1.62	0.52
0.75	7.07	1.11	5.48	0.78
1.00	12.57	4.19	12.99	1.03
1.25	19.63	8.18	25.36	1.29
1.50	28.27	14.14	43.83	1.55

The particle trajectories under operating conditions #1, #2 and #3 are shown in Figure 8-15, Figure 8-16 and Figure 8-17, respectively. The corresponding trajectories are colour coded as shown. For the benefit of black and white copies of this dissertation, the highest trajectory in the cell corresponds to the first particle radius in the list, i.e. 0.5 mm.

From Figures 8-15 to 8-17 it is clear that a spread of particle trajectories occurs with increase in particle size. In addition, the higher the liquid level in the froth, i.e. more entrained water in the froth together with a larger bubble size, the more pronounced the spread of particle trajectories. With an increase in the liquid-froth interface, the lighter particles will float at a higher level in the froth, while the heavier particles will have increasingly steeper trajectories.

According to equations 6-24 and 6-27, the volume of liquid to be removed from the liquid-particle contact line increases with increasing particle size. According to equation 6-3 the time for bubble film rupture alone would therefore increase with increasing particle size. If only the time of bubble film rupture were considered, one would expect the larger particles to have a higher trajectory in the froth than the smaller particles. However, the effect of the force balance on the particle in the froth should be considered as well (see section 6.4). The mass of the particle, and thereby the downward force (see equation 6-68) of the particle on the supporting bubble films increases to the power of three as the particle size increases.

As shown in Figure 8-15, Figure 8-16 and Figure 8-17, the 0.5 mm and 0.75 mm particles have similar trajectories for all three operating conditions (although the trajectories are higher with an increase in liquid-froth interface). The reason for this phenomenon is that the effects of increasing bubble rupture time and increasing particle mass are counteracting each other. However, once the particles are larger than a critical size, the effect of the particle mass starts to dominate and the particle floats at increasingly steeper trajectories in the froth. The drop in particle trajectory as the liquid interface increases is mainly due to the increase in bubble size and the subsequent effect (as described in section 8.4) of bubble size on the trajectory of particles in the froth.

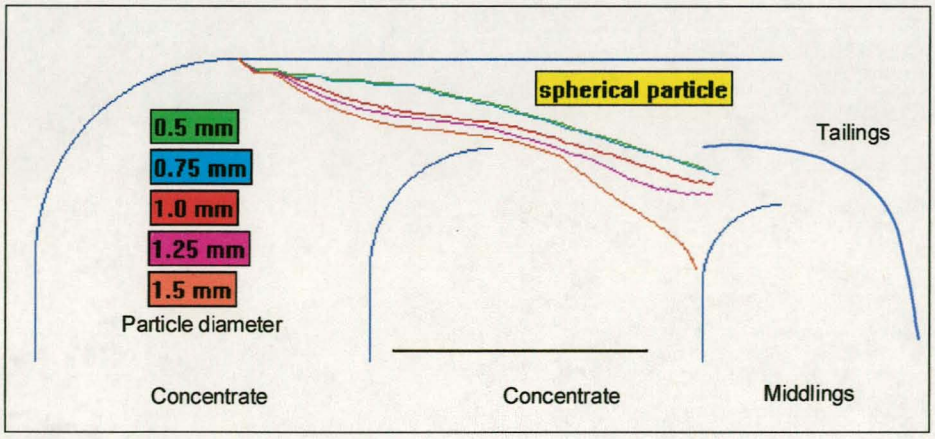

Figure 8-15: Effect of particle size under operating condition #1

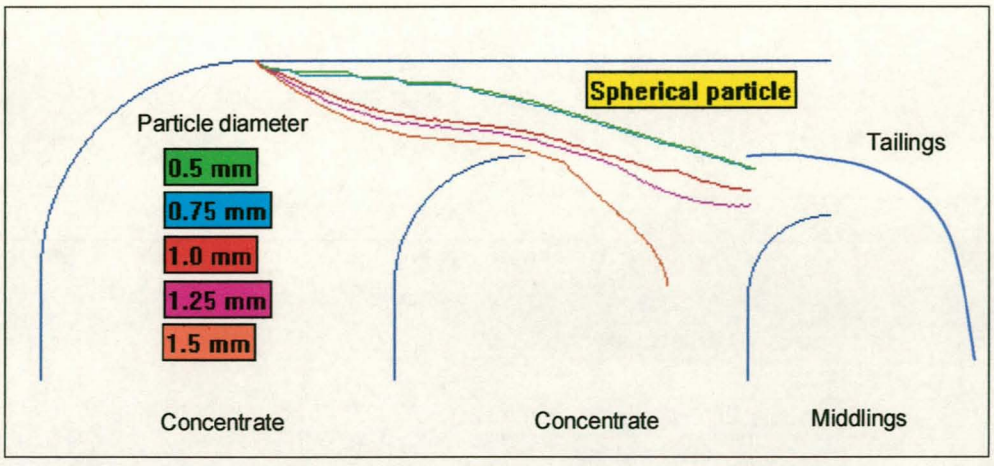

Figure 8-16: Effect of particle size under operating condition #2

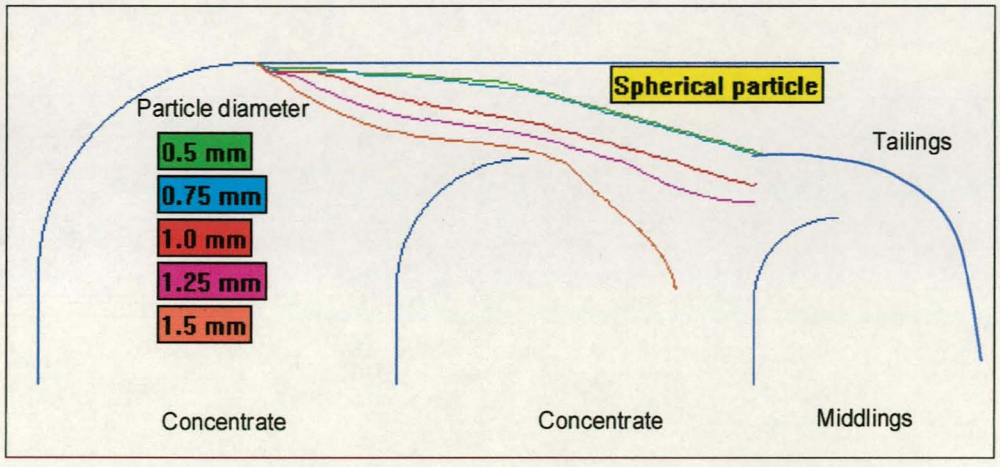

Figure 8-17: Effect of particle size under operating condition #3

Figure 8-18 shows the particle trajectories in the froth for an increase in the air flowrate through the sparger located in sub-compartment B (operating condition #4). Compared with the base case (operating condition #3 and Figure 8-17) the spread in particle trajectories still occurs, however, the particles float at significantly higher positions in the froth. This is to be expected due to the increase of the upward force exerted on the particles once the particles are in the froth areas #2 and #3. This phenomenon is described in section 8.1 of this dissertation (sensitivity analysis on the influence of air flowrate).

Figure 8-19 shows the trajectories for operating condition #5 (i.e. increase in the air flowrate through the sparger located in sub-compartment A). Compared to the base case (operating condition #3 and Figure 8-17) the spread in particle trajectory still occurs, but to a far lesser extent. This is mainly attributed to the increase in horizontal froth velocity in the forth area #1, as discussed under section 8.1.

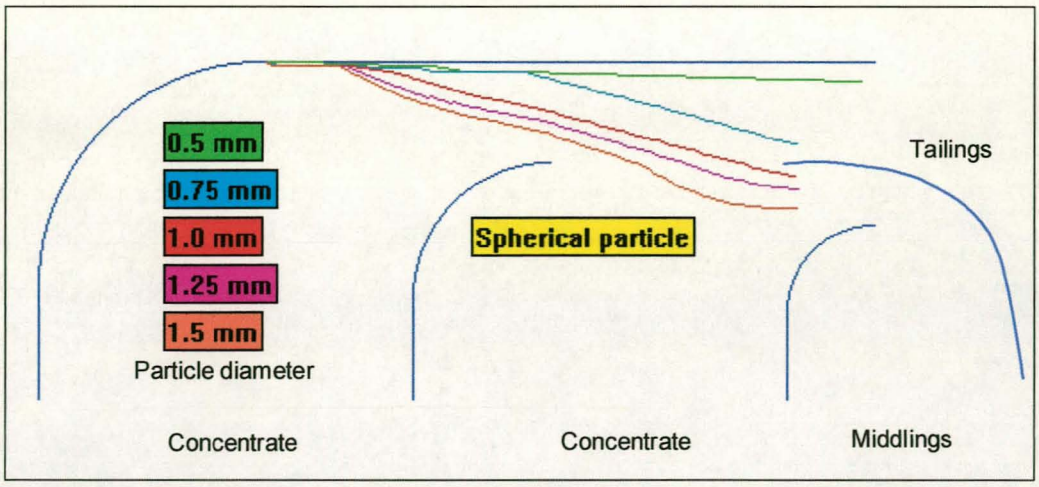

Figure 8-18: Effect of particle size under operating condition #4

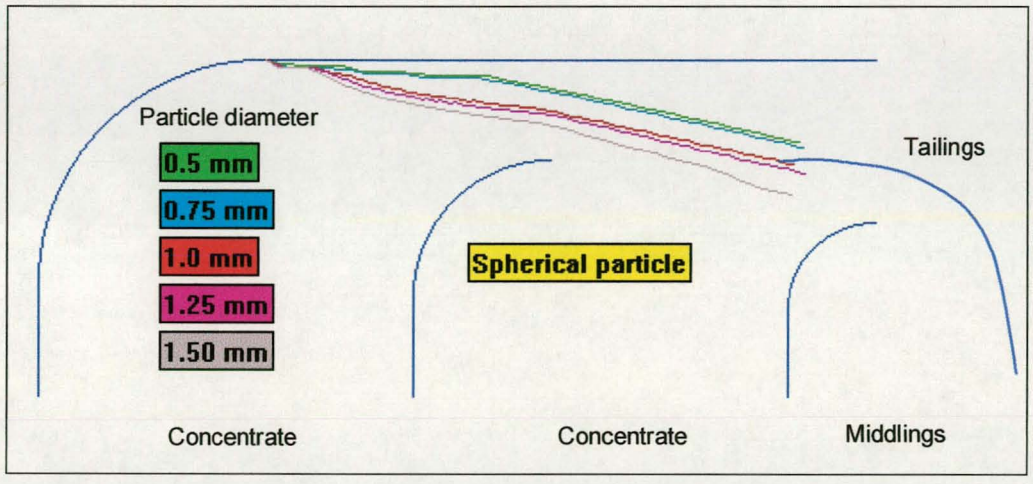

Figure 8-19: Effect of particle size under operating condition #5

In summary:

- Particles classify on the basis of particle size in the reverse froth flotation cell.
- The extent of classification is dependent on:
  - the actual particle size,
  - the liquid level in the froth, i.e. bubble size and entrained water,
  - the air flowrate through the various spargers, i.e. the upward force exerted on the particles and the horizontal velocity of the bubbles in the froth.
- The increase in particle size results in an increase in the film rupture time and an increase in the downward force exerted by the particle on the supporting bubble films. These effects can counteract each other at small particle sizes, however, with large particles the effect of the particle mass, and subsequent downward force, will dominate.

8.6 Particle Density

The effect of the particle density on the trajectory of a particle in the reverse froth flotation cell was investigated. The outcome of the various simulations under the operating conditions, as specified in section 8.3, are shown in Figure 8-20 through to Figure 8-24. For the purpose of this investigation, all manipulated variables were kept constant per operating condition, and the density of the particle varied. A rod shaped particle, 3.38mm in length and a radius of 1.04mm, with properties as shown in Table 8-10 was used. In addition, an equilibrium contact angle of 98° on the particle was selected.

Table 8-10: Rod shaped particle properties for density sensitivity analysis

Density [kg/m³]	Mass [mg]	Mass/Area Ratio
2700	31.01	1.07
2900	33.31	1.15
3100	35.60	1.23
3300	37.90	1.31
3500	40.20	1.39

The particle trajectories under operating conditions #1, #2 and #3 are shown in Figure 8-20, Figure 8-21 and Figure 8-22 respectively. The corresponding trajectories are colour coded as shown. For the benefit of black and white copies of this dissertation, the highest trajectory in the cell corresponds to the first particle density in the list, i.e. a SG of 2.7.

From Figures 8-20 to 8-22 it is clear that a separation in the particle trajectories occurs with an increase in particle density. The higher the particle density, the steeper are the particle trajectories in the froth. In addition, the higher the liquid level in the froth, i.e. more entrained water in the froth together with a larger bubble size, the steeper is the overall trajectory of particles in the froth (see the trajectory of the 3.3 SG particle for example).

This spread in particle trajectories can be attributed to the force balance on the particle supported by the liquid film in the froth. Based on equation 6-57, it is clear that the higher the particle density, the higher the downward force component on the particle. The net force (downward) on the particle would therefore increase, resulting in steeper particle trajectory. Similarly, as the liquid-froth interface increases, the bubble size increases together with the entrained liquid in the froth. However, the increase in bubble size dominates the increase in entrained liquid, resulting in the air hold-up fraction increasing. The higher the air hold-up fraction in the froth, the lower the froth density (see equation 6-57) resulting in the upward force component to reduce. The net force (downward) on the particle would therefore increase with increasing liquid-froth interface, resulting in a steeper particle trajectory.

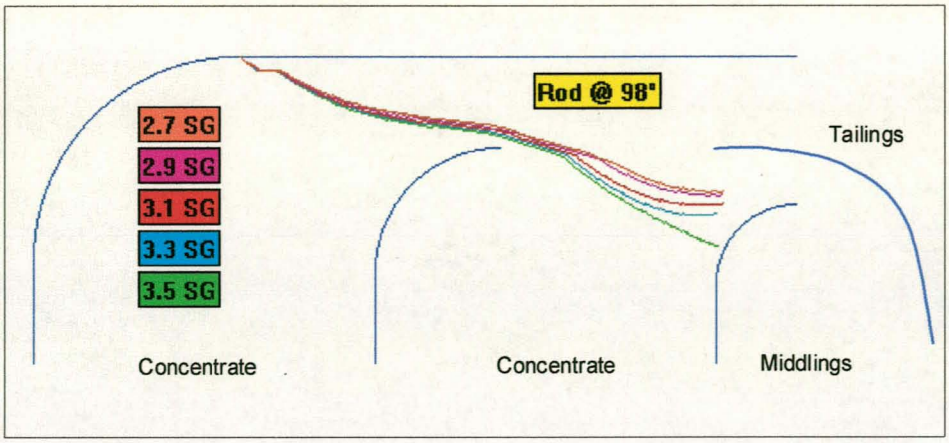

Figure 8-20: Effect of particle density under operating condition #1

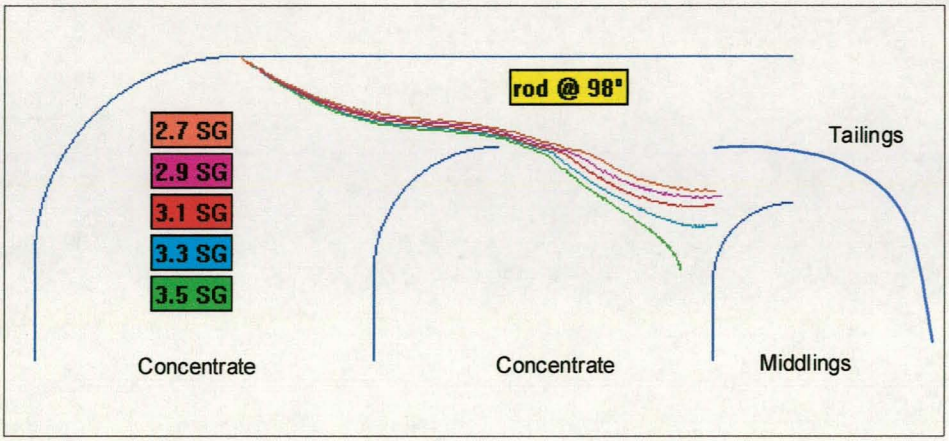

Figure 8-21: Effect of particle density under operating condition #2

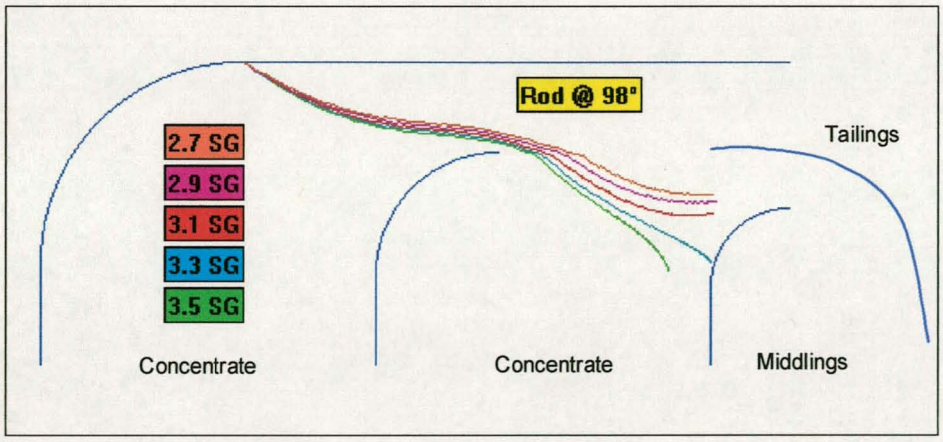

Figure 8-22: Effect of particle density under operating condition #3

Figure 8-23 shows the trajectories of particles of varying densities in the froth for an increase in the air flowrate through the sparger located in sub-compartment B (operating condition #4). Compared with the base case (operating condition #3 and Figure 8-22) the spread in particle trajectories still occurs, however, the particles are floated at significantly higher positions in the froth. In addition the spread of

trajectories is to a lesser extent. This is to be expected due to the increase of the upward force exerted on the particles and the increase in the horizontal froth velocity once the particles are in froth areas #2 and #3. This phenomenon is described in section 8.1 of this dissertation (sensitivity analysis on the influence of air flowrate).

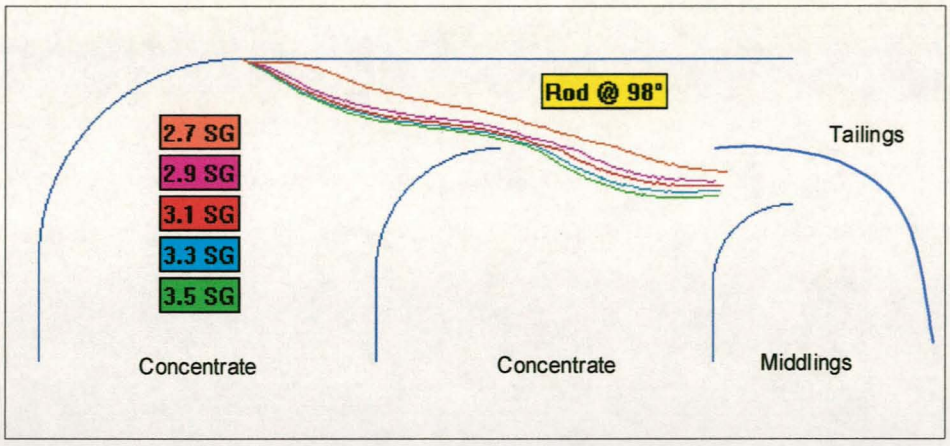

Figure 8-23: Effect of particle density under operating condition #4

The effect of increasing the air flowrate through the sparger located in sub-compartment A on the trajectories of particles of various densities is shown in Figure 8-24. Surprisingly, hardly any classification of particles occurs. However, the small spread still follows the general rule, i.e. lower density particles float at a higher position in the froth than higher density particles. The small extent of classification can be attributed to the large horizontal froth velocity component in froth area #1. The particles therefore spend far less time in the froth bed, resulting in less opportunity for classification.

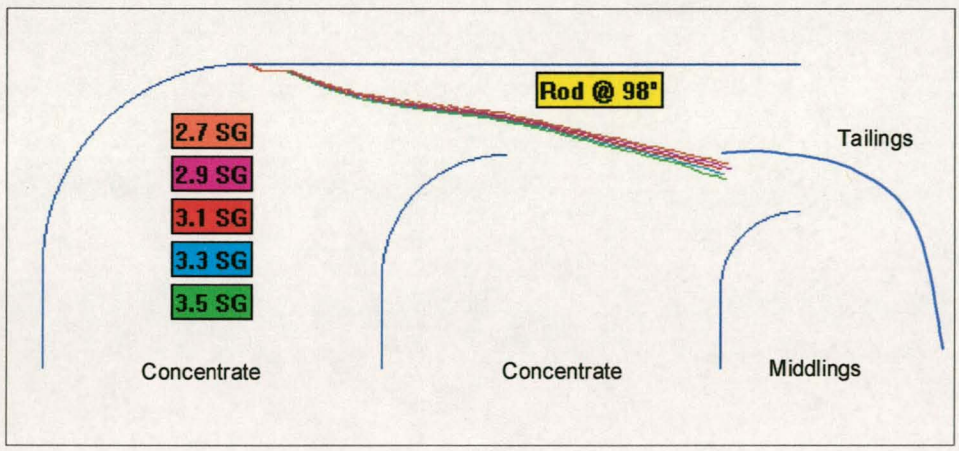

Figure 8-24: Effect of particle density under operating condition #5

In summary:

- The steepness of the particle trajectory in the froth will increase with an increase in particle density.

- The extent of the spread in trajectories is dependent on:
  - the actual particle density,
  - the level of the liquid-froth interface, i.e. the air hold-up fraction in the froth,
  - the horizontal froth velocity in the various froth areas, i.e. the air flowrate in the various sub-compartments.
- The predicted classification based on particle density is dependent on the force balance the particle is subjected to while supported by the bubble films in the froth. An increase in particle mass results in the particle floating at a lower position in the froth, while an increase in the froth density has the opposite effect. These phenomena can be explained with equations 5-56 and 5-57.

8.7 Contact Angle

The work of Dippenaar[15], Hemmings[17] and Frye and Berg[18] (see Literature Survey, chapter 2) has shown that the equilibrium contact angle on the surface of a particle determines the time of bubble film rupture. The effect of bubble film rupture time on the trajectory of a particle in the froth was therefore investigated under the five operating conditions outlined in section 8.3. For the purpose of this investigation, all manipulated variables in the cell were kept constant per operating condition, and the contact angle of the particle varied. A rod shaped particle of 3.38mm in length and a radius of 1.04mm was used. In addition, the particle density was set at 3500 kg/m^3.

Five equilibrium contact angles were investigated, i.e. 92°, 94°, 96°, 98° and 100°, as shown on the respective Figures 8-25 through to 8-29 (corresponding with the respective operating conditions, as described in section 8.3). The corresponding trajectories are colour coded as shown. For the benefit of black and white copies of this dissertation, the highest trajectory in the cell corresponds to the first particle contact angle in the list, i.e. 92°.

From Figures 8-25 to 8-27 it is clear that a spread in particle trajectories occurs with an increase in the equilibrium particle contact angle. The higher the equilibrium contact angle, the steeper the particle trajectory in the froth. This is mainly due to the decrease in the second principal radius of curvature (R_2 equation 6-1) as calculated from equation 6-4, and therefore the increase in the pressure drop across the contact interface (ΔP_c). As the pressure drop across the contact interface increases, the time of bubble film rupture will decrease (see equations 6-5 and 6-6). In addition, as the contact angle increases above 90°, the pressure drop will increase more rapidly due to the sinusoidal relationship (see equation 6-4). As shown, the particle trajectory in the froth will therefore become steeper with an increase contact angle.

Figures 8-25 to 8-27 further show that increasing the liquid-froth interface has very little effect on the overall position of the respective trajectories. However, the particle do float at a slightly lower level in the froth with increasing liquid-froth interface. As discussed in section 8.6, the air hold-up fraction increases with an

increase in the liquid-froth interface height. The higher the air hold-up fraction in the froth, the lower the froth density (see equation 6-57) resulting in the upward force component to reduce. The net force (downward) on the particle would therefore increase with increasing liquid-froth interface, resulting in a steeper particle trajectory.

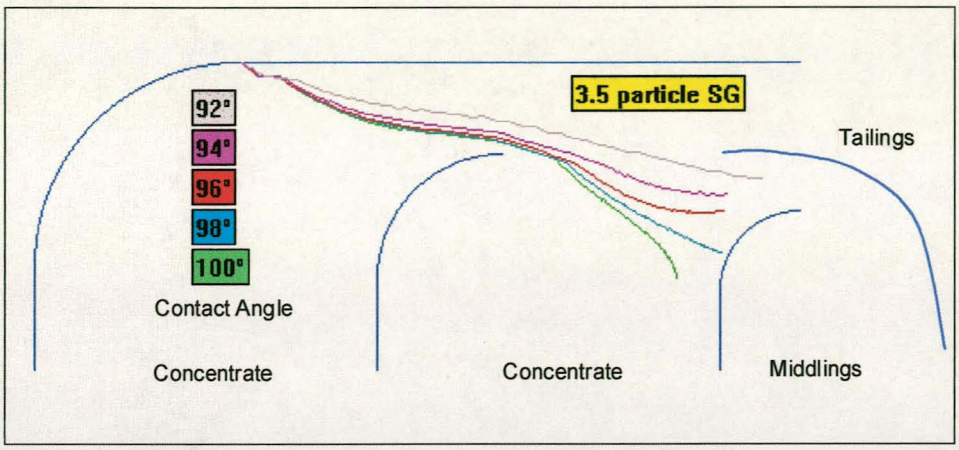

Figure 8-25: Effect of particle contact angle under operating condition #1

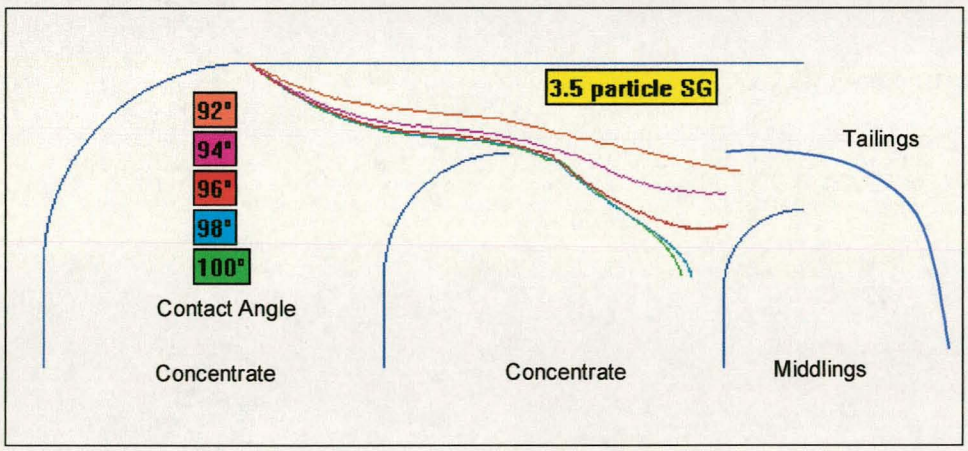

Figure 8-26: Effect of particle contact angle under operating condition #2

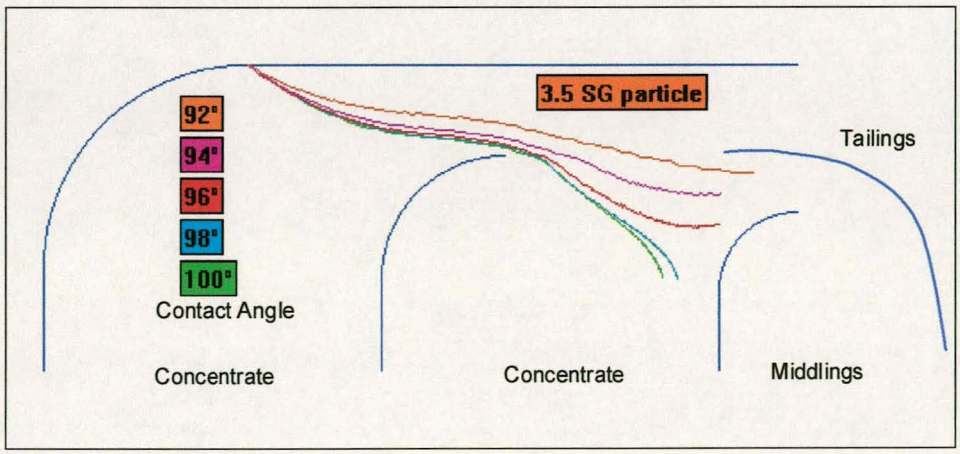

Figure 8-27: Effect of particle contact angle under operating condition #3

Figure 8-28 shows the particle trajectories at various contact angles for an increase in the air flowrate through the sparger located in sub-compartment B (operating condition #4). Compared to the base case (operating condition #3 and Figure 8-27) the spread in particle trajectories still occurs, however, the particles with high contact angles (above 96°) are floating at significantly higher positions in the froth, while the particles with low contact angles are floating at virtually the same position. The spread of trajectories occurs therefore to a lesser extent. This is to be expected due to the increase in the horizontal froth velocity once the particles are in the froth area #2. The low contact angle particles do not reach this froth area, resulting in a limited influence on their trajectory. However, the high contact angle particles reported to the froth area #2 in the base case (see Figure 8-27) resulting in their trajectories being lifted (see Figure 8-28). This phenomenon is described in section 8.1 of this dissertation (sensitivity analysis on the influence of air flowrate).

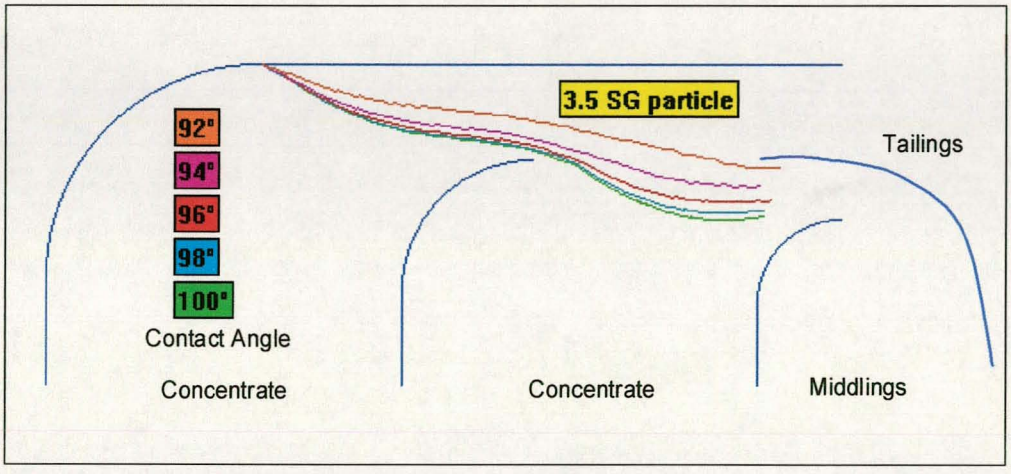

Figure 8-28: Effect of particle contact angle under operating condition #4

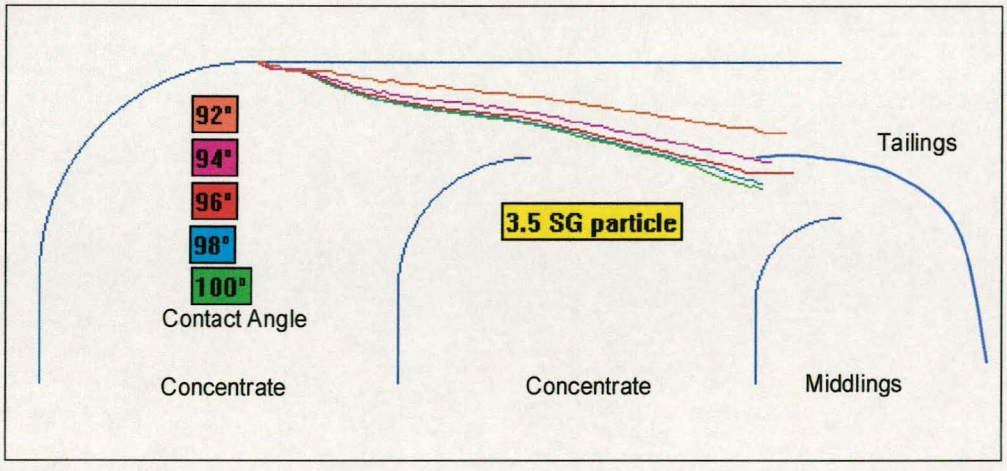

Figure 8-29: Effect of particle contact angle under operating condition #5

The effect of increasing the air flowrate through the sparger located in sub-compartment A on the trajectories of particles of various equilibrium contact angles, is shown in Figure 8-29. The spread in particle trajectories is reduced significantly. However, the spread still follows the general rule, i.e. particles with lower contact angles float at a higher position in the froth than particles with high contact angles. The reduction in the spread of the classification can be attributed to the large horizontal froth velocity component in froth area #1. The particles therefore spend far less time in the froth bed, resulting in less opportunity for classification.

In summary:

- The particle trajectory will become steeper as the equilibrium contact angle on the particle surface increases.
- The extent of the spread in trajectories is dependent on:
  - the actual equilibrium contact angle,
  - the level of the liquid-froth interface, i.e. the air hold-up fraction in the froth,
  - and the horizontal froth velocity in the various froth areas, i.e. the air flowrate in the various compartments.

8.8 Particle shape

In order to investigate the effect of the particle shape on the trajectory of particles in the froth, all parameters affecting the trajectory of a particle in the froth have to be constant while changing the particle shape. Two main driving forces determine the trajectory of a particle in the froth:

- The film rupture time, which is predominantly a function of the particle shape and the equilibrium contact angle on the particle.
- The force balance a particle is subjected to while supported by the bubble films in the froth (see equation 6-57).

By keeping the contact angle constant, the effect of particle shape can therefore be investigated. However, by manipulating the particle shape, the force balance on the particle will be altered. In order to keep the downward component of the force balance constant, the various particle shapes must have the same mass. Similarly, the cross sectional surface area (A_0) has the most pronounced influence on the upward component in the force balance, and should be kept constant. The particle shapes investigated (at a contact angle of 96°), together with their dimensional parameters and properties, are shown in Table 8-11 (see section 6.2 of this dissertation for definition of dimensional parameters per particle shape).

Each of the particles as shown in Table 8-11, has a mass of 28.71 mg and a cross sectional surface area of 4.41mm².

Table 8-11: Particle properties for shape sensitivity analysis

Shape	Dimensions [mm]	Density [kg/m³]	Volume [mm³]	Area [mm²]
Rod	R_{cyl} = 1.1848, L_{cyl} = 3.38	1926	14.91	33.98
Disc	R_s = 0.65, R_d = 0.5348	6312	4.55	16.85
Flat	L_f = 2.1, W_f = 2.1, H_f = 1.05	6200	1.63	17.64
Cube	S_{cube} = 2.1	3100	9.26	26.46
Sphere	R_s = 1.1848	4121	6.97	17.64
Cone	xc = 1.1848, β = 45°	8242	3.48	12.47

Figures 8-25 through to 8-29, correspond with the respective operating conditions #1 to #3, as described in section 8.3. The various particle trajectories are colour coded as shown. For the benefit of black and white copies of this dissertation, the highest trajectory in the cell corresponds to the first particle shape in the list, i.e. a rod shaped particle. Since the force balances on the particles are virtually identical, the spread in particle trajectories must be attributed to the influence of particle shape on the bubble film rupture time. This corresponds with the results as obtained by Frye and Berg[18].

As the liquid-froth interface level is increased the particles float at a higher level in the froth. This effect is more pronounced for cubic, flat and cone shaped particles. The effect of a reduction in the downward force component in the froth due to an increase in the air hold-up (with an increase in the liquid-froth interface level) must therefore be counteracted.

This counteraction is mainly due to the interaction of opposing effects as the bubble film thickness is reduced (larger bubbles are overriding the effect of more entrained water). From equation 6-5 it is clear that liquid flowrate away from the particle (Q) is directly proportional to the cube of the bubble film thickness (δ^3) but indirectly proportional to the integration position along the particle surface (h^*). Therefore, it is easy to show that:

$$Q \propto \delta^2 \qquad \textbf{Equation 8-1}$$

However, from the respective equations used to calculate the volume of liquid to be removed from the contact line per particle shape, it can be shown that:

$$(V_1 + V_2) \propto \delta^2 \qquad \textbf{Equation 8-2}$$

Based on equation 6-6, the rupture time is proportional to $(V_1+V_2)/Q$. It is easy to show that the two thickness effects therefore almost cancel out in calculating the rupture time for particles with rounded surfaces (sphere, rod, disc). However, for angular particles (cubic, flat and conical particles) the reduction in bubble film thickness results in the reduction in bubble film rupture time. This reduction in film

rupture time therefore counteracts the reduction in the downward force component, resulting in the steeper particle trajectory in the froth.

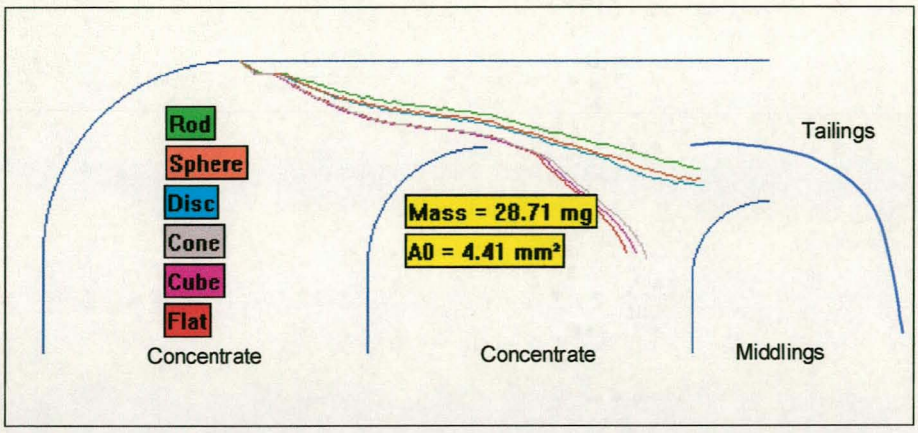

Figure 8-30: Effect of particle shape under operating condition #1

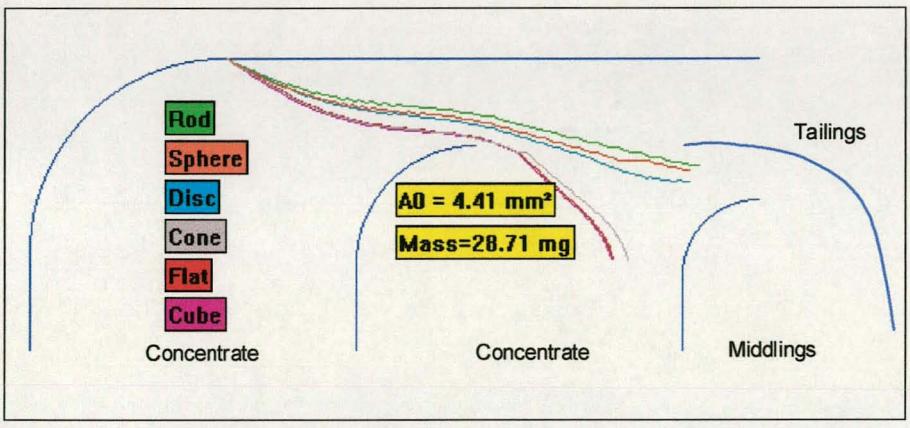

Figure 8-31: Effect of particle shape under operating condition #2

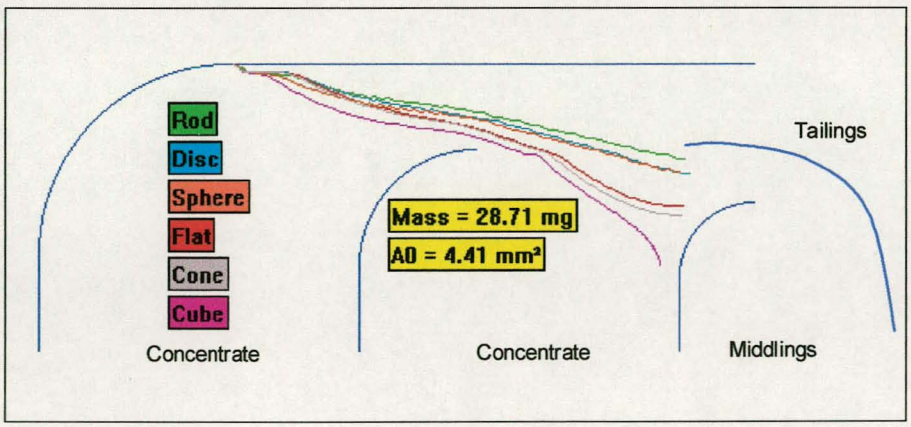

Figure 8-32: Effect of particle shape under operating condition #3

Figure 8-33 shows the particle trajectories (various shaped particles) for an increase in the air flowrate through the sparger located in sub-compartment B (operating condition #4). Compared with the base case (operating condition #3 and Figure 8-

32) the spread in particle trajectories still occurs, however, the particles are floating at significantly higher positions in the froth. In addition, the spread of trajectories occurs to a lesser extent. This is to be expected due to the increase in the horizontal froth velocity once the particles are in the froth area #2. The cylindrical, disc and spherical particles do not reach this froth area, resulting in a limited influence on their trajectory. However, the cubic, flat and conical particles reported to the froth area #2 in the base case (see Figure 8-32) resulting in their trajectories being lifted (see Figure 8-33). This phenomenon is described in section 8.1 of this dissertation (sensitivity analysis on the effect of air flowrate).

The effect of increasing the air flowrate through the sparger located in sub-compartment A on the trajectories of particles of the various shapes is shown in Figure 8-34. The spread in particle trajectories is reduced significantly. The reduction in the spread of the classification can be attributed to the large horizontal froth velocity component in froth area #1. The particles therefore spend far less time in the froth bed, resulting in less opportunity for settling through the froth bed and subsequent classification.

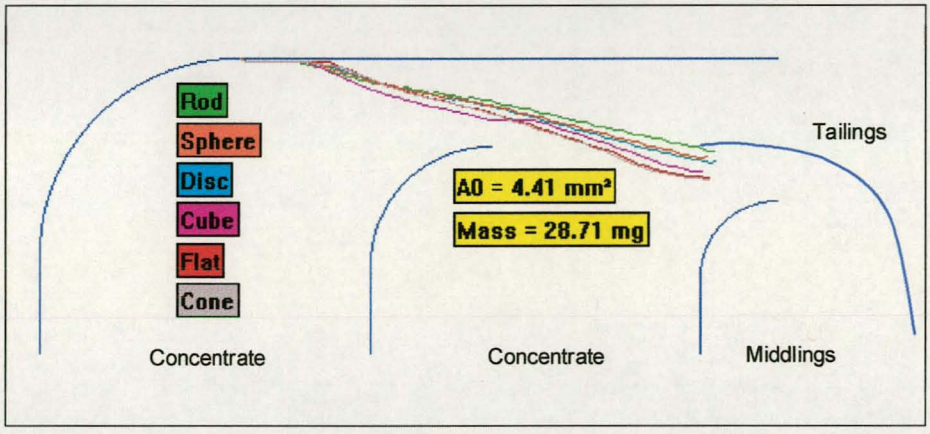

Figure 8-33: Effect of particle shape under operating condition #4

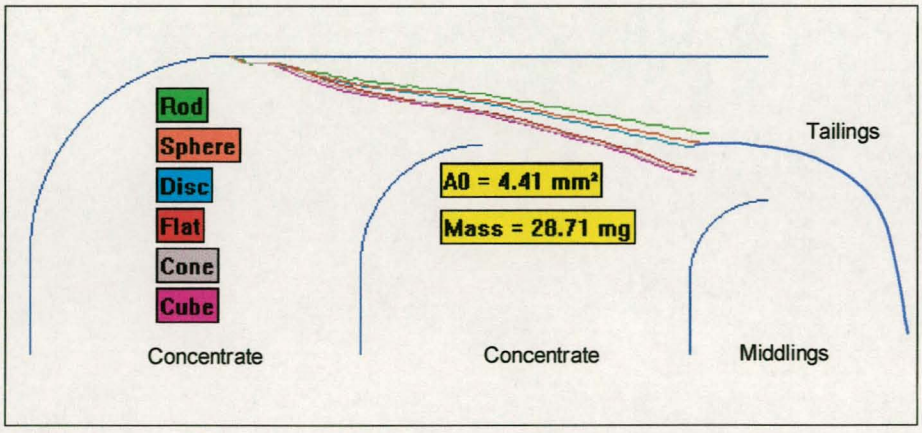

Figure 8-34: Effect of particle shape under operating condition #5

In summary:

- The particle shape has a pronounced effect on the trajectory of particles in the froth phase of the reverse froth flotation cell.
- Angular particles (cube, flat & cone) will have a steeper trajectory in the froth while rounded particles will float at higher trajectories.
- The extent of the spread in trajectories is dependent on:
  - the actual particle shape,
  - the level of the liquid-froth interface, i.e. the air hold-up fraction in the froth,
  - and the horizontal froth velocity in the various froth areas, i.e. the air flowrate in the various compartments.

8.9 Summary

In this chapter a sensitivity analysis was conducted on the major froth, as well as particle, manipulative variables. In practice, froth parameters such as entrained water and bubble film thickness, can only be varied independently to a limited degree. The effect of particle size, density, contact angle and shape was therefore investigated under 5 pre-selected operating conditions. At each of these operating conditions, actual measured froth parameters were used as input variables to the model. By following this route, artificial operating regimes were eliminated from the sensitivity analysis.

This sensitivity analysis proved to be valuable in investigating variables in isolation, which is not always possible in experimental work. However, for the model to be practically useful it has to be linked to actual operating data. The following chapter, therefore, compares the results of the testwork to the model output.

9. RESULTS OF TESTWORK AND MODEL COMPARISON

As discussed in the chapter 8 summary, the sensitivity analysis conducted with the dynamic model providing a good insight into the interrelationship of the various parameters affecting the behaviour of particles in the flotation cell. However, the dynamic model (as outlined in chapter 5, 6 and 7) must be linked to experimental results to test its validity.

This chapter therefore starts by describing the results obtained during wettability experiments conducted on the wax particle coatings (see section 3.4.5). These results are followed by extensive results on the behaviour of particles of various shapes, densities and contact angles under the various operating conditions. The results are presented in the form of bar charts divided into three regions, corresponding with the % recovery to the concentrate, middlings and tailings respectively. The x-axis of these charts corresponds with the particle SG's investigated, while the various bars per SG fraction correspond to the spread in contact angles investigated. The results are based on the recovery of 50 particles per density fraction, i.e. up to 300 particles per size class (dependent on the number of density fractions available).

Apart from these results, the section also contains selected particle trajectory plots, as predicted by the model. The purpose of these plots is to compare the model output to the actual experimental results. In order to prevent the unnecessary clutter of pertinent issues, only selected trajectories are plotted. Conclusions as to the validity of the dynamic model are then drawn based on these trajectories and the results of the sensitivity analysis, as described in section 8 of this dissertation.

The evolution of the flotation cell to its current design is briefly described in sections 3.1 and 3.2 of this dissertation. During this evolutionary process, various experimental results were obtained, and are described elsewhere[34]. This chapter, therefore, primarily describes the experimental results obtained in the final design of the reverse froth flotation cell under the controlled operating conditions as outlined in section 8.3. The final experimental set-up and procedures utilised in obtaining these results, are described in section 3.4.

9.1 Wettability Characteristics of Candle Wax Particle Coating

Adam[35] found that prolonged soaking of organic materials in water resulted in the decrease of the equilibrium contact angle of water on the surface of the organic material. Adam[35] further postulated that the predominant mechanism responsible for this hydrophilic ageing is the fact that water molecules become entrapped in the surface layers, thus increasing the adhesion of water to the surface of the organic material. This hydrophilic ageing was seen as an opportunity to investigate the behaviour of particles in the cell under various equilibrium contact angles.

Particles were therefore coated with candle wax, and stored under water for various periods of time. Figure 9.1 shows the results of contact angle measurements (see section 3.4.4) obtained on a clean candle wax surface at various soaking times. The results displayed are the average of thirty (30) measurement campaigns.

The maximum range obtained was 8.38° at around 300 and 330 minutes of soaking time. These points also showed the greatest standard deviation of 2.16 and 2.41° respectively. The range and standard deviation of all other soaking time measurements was below 5° and 1.44° respectively. These results provided not only confidence in the measurement technique (see section 3.4.4), but also in the ability of using the decay in hydrophobicity with soaking time in the experimental design.

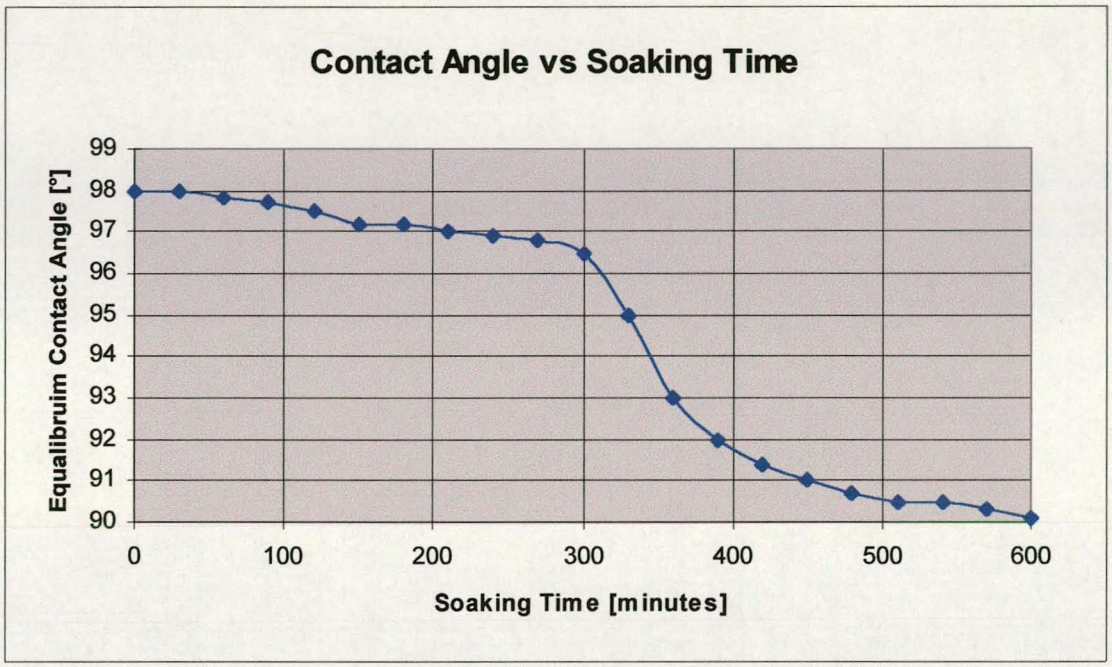

Figure 9-1: Decay in particle hydrophobicity with soaking time

The various contact angles quoted in the subsequent sections are the average of 10 measurements taken on sample particles soaked to the same time as the experimental density tracers.

9.2 The Effect of Operating Conditions on Particle Recovery

In order to investigate the effect of the various operating conditions on the particle trajectories in the cell, the behaviour of cubic density tracers of 2.1mm side length, under the five operational conditions (see section 8.3), was investigated. Various density fractions were available, the properties of which are given in Table 9-1 below.

Table 9-1: Properties of 2.1mm cubic particles

Density [kg/m³]	Mass [mg]
3500	32.41
3300	30.56
3100	28.71
2900	26.86
2700	25.00
2600	24.08

The behaviour of the 2.1mm cubes under operating condition #1 is shown in Figure 9-2, from which it can be seen that an increase in the particle contact angle will result in an increase in recovery to the concentrate for high SG particles. In addition, a decrease in the particle density results in the particle floating at a higher position in the froth (i.e. more particles reporting to the middlings and tailings). However, at low particle contact angles, the particles predominantly reports to the tailings, irrespective of the particle SG. This effect is mainly due to the decrease in film rupture time, resulting in the particle being supported by the bubble films, instead of an immediate rupture of the films. This effect can clearly be seen from the selected simulator output, as displayed in Figure 9-3.

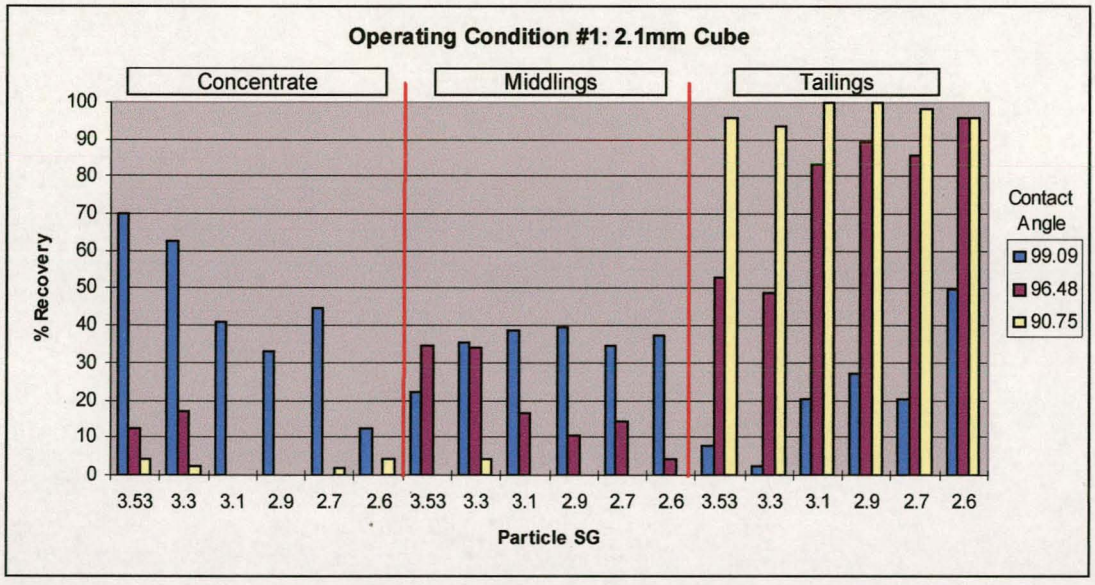

Figure 9-2: Behaviour of 2.1 mm cubes under operating condition #1

For the benefit of black and white copies of this dissertation, the particle conditions displayed in Figure 9-3 corresponds with the floating level of the particle in the cell, i.e. the 2.6 SG particle with a contact angle of 90.75° has the highest trajectory, while the 3.5 SG particle with the 99.09° contact angle has the steepest trajectory in the cell.

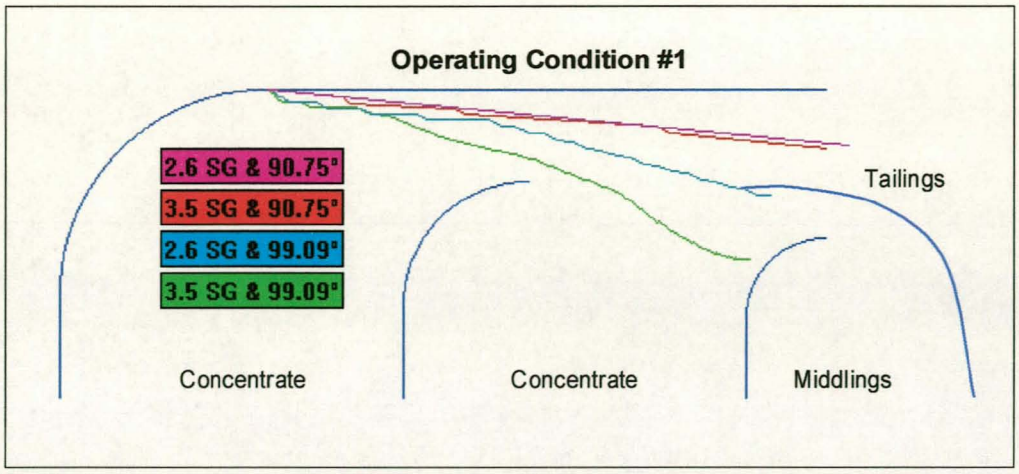

Figure 9-3: Particle trajectories for 2.1mm cubes - operating condition #1

The simulator output (Figure 9-3) clearly shows that for low contact angles, the particle density has very little effect on the trajectories of 2.1mm cubes in the cell. However, at high contact angles, the particle density has a marked effect on the particle trajectory. This is mainly due to the driving force for the particle trajectory shifting from the film rupture effect, to the force balance exerted on the particles. The simulator output therefore compares well with the experimental results. However, it is recognised that the simulator output predicts the particle trajectory under ideal operating conditions. In practice, a distribution in both the particle contact angle and the bubble size at the liquid-froth interface exists. The sensitivity analysis (Sections 8.4 and 8.7) has shown that both these factors could influence the trajectory of the particles significantly. The spread in recoveries can therefore be attributed to the distributions in bubble size, and contact angle that exist in practice.

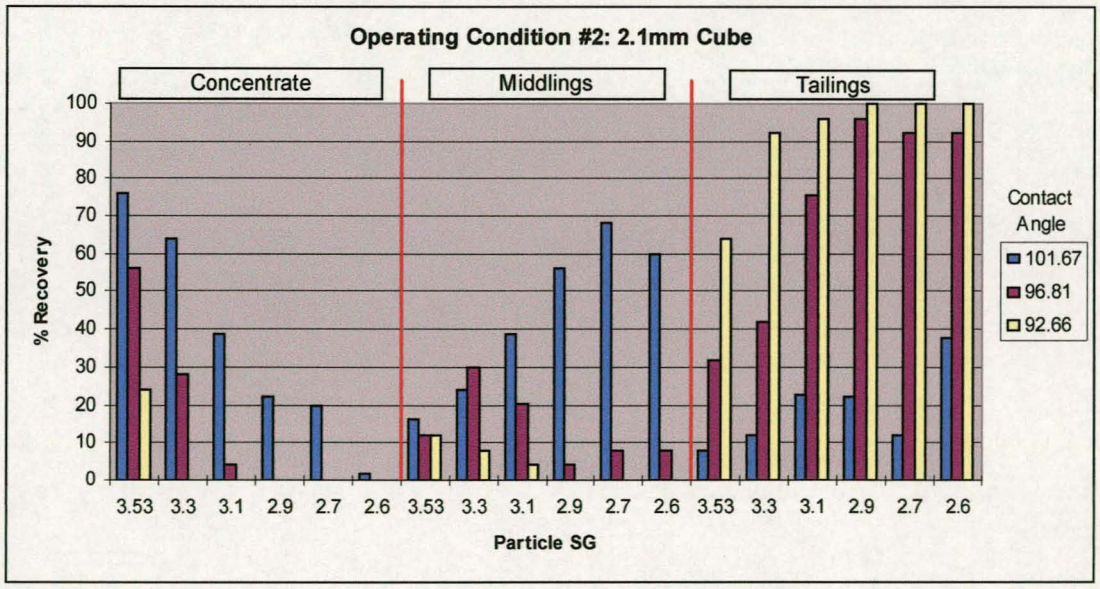

Figure 9-4: Behaviour of 2.1 mm cubes under operating condition #2

The effect of increasing the liquid-froth interface on the recovery of 2.1mm cubes is shown in Figure 9-4 and Figure 9-5. These two bar charts show the behaviour of 2.1mm cubes under operating conditions #2 and #3. As repeatedly shown in the sensitivity analysis (section 8), an increase in the liquid-froth interface results in a less particles reporting to the tailings. As predicted, this effect is more pronounced for particles with high contact angles and densities.

The 2.1mm cubes also follow the trends as predicted in the sensitivity analysis, when the air flowrate in sub-compartment B of the concentrate compartment is increased (operating condition #4). As shown in Figure 9-6, the increase in the froth horizontal velocity as well as the increase in the upward force component exerted on the particles, results in a decrease in the recovery to the concentrate, while more particles report to the middlings and tailings (compare Figures 9-6 and 9-5).

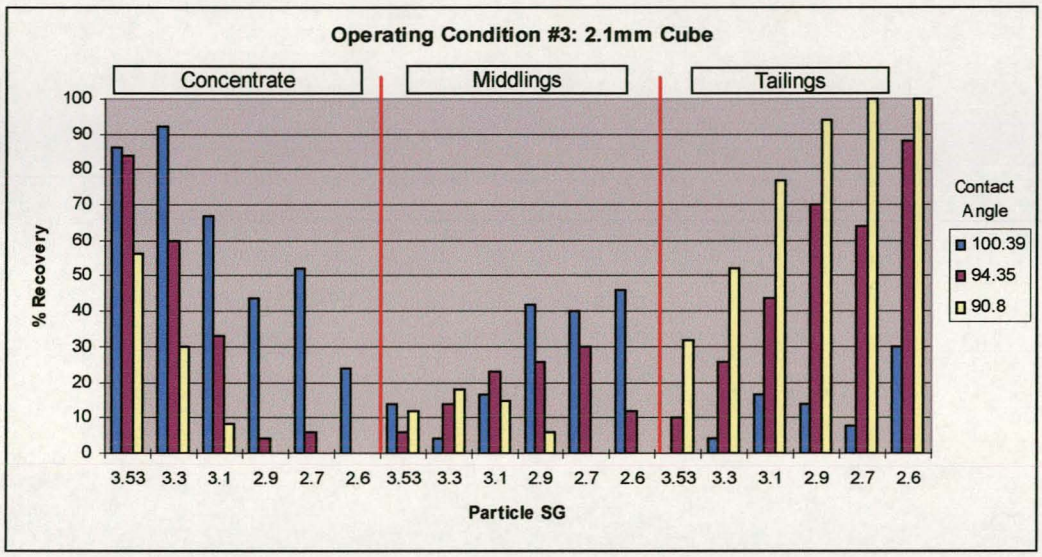

Figure 9-5: Behaviour of 2.1 mm cubes under operating condition #3

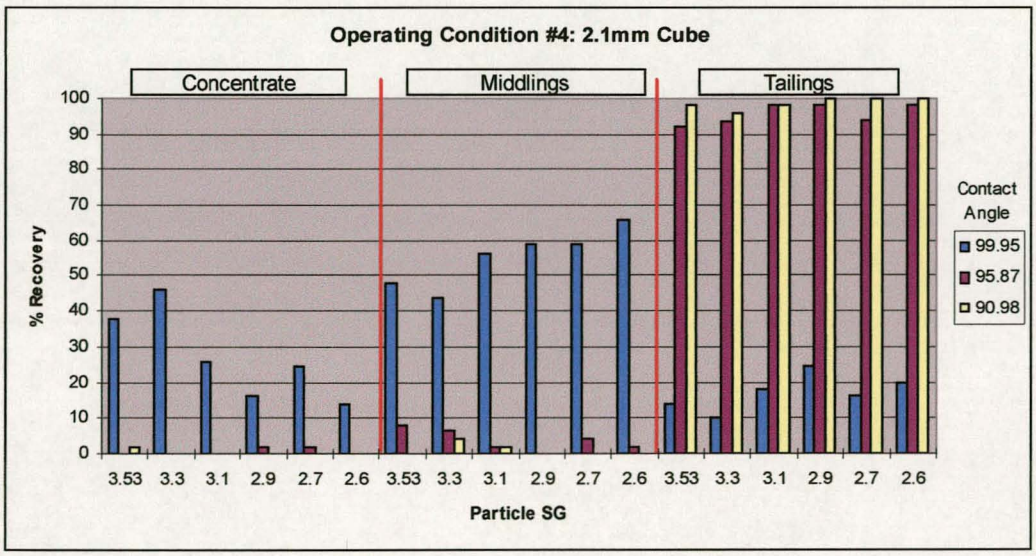

Figure 9-6: Behaviour of 2.1 mm cubes under operating condition #4

Increasing the air flowrate in sub-compartment A (operating condition #5), results in virtually all particles are reporting to the tailings, except for the high contact angle particles (see Figure 9-7). The high contact angle particles are still breaking the bubble films, but the increase in horizontal froth velocity results in a shift in recovery from the concentrate to the middlings. This effect is clearly demonstrated by the output from the model, as displayed in Figure 9-8. For the benefit of black and white copies of this dissertation, the particle conditions displayed in Figure 9-8 correspond to the floating level of the particle in the cell, i.e. the 2.6 SG particle with a contact angle of 90.75° has the highest trajectory, while the 3.5 SG particle with the 99.76° contact angle has the steepest trajectory in the cell.

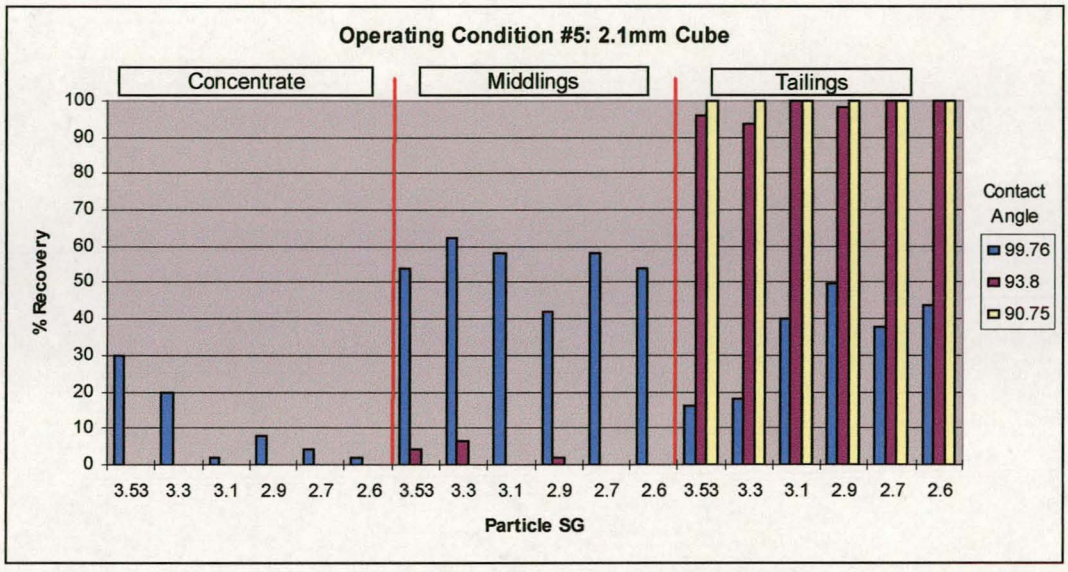

Figure 9-7: Behaviour of 2.1 mm cubes under operating condition #5

By comparing the simulator output (Figures 9-3 and 9-8) it is clear that all the particle trajectories have lifted. In addition, the high density, high contact angle particles are now reporting predominantly to the middlings fraction. All other trajectories end up above the splitter plate level, i.e. reporting to the tailings.

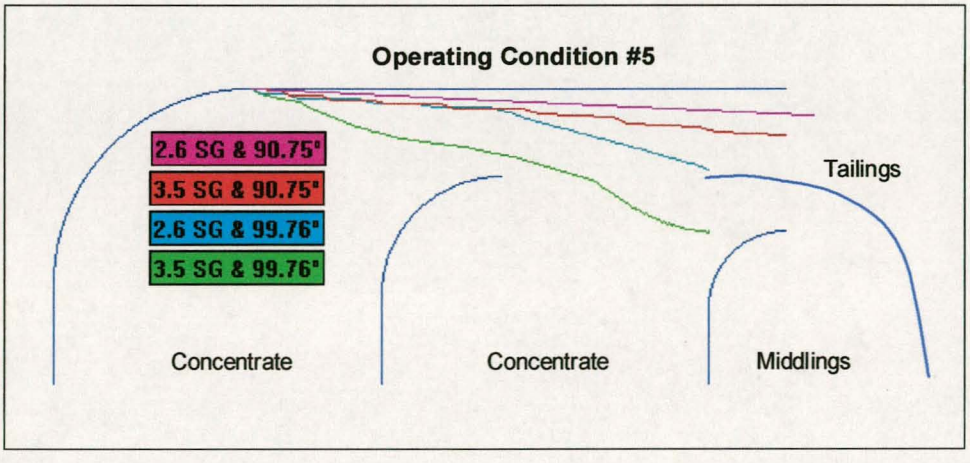

Figure 9-8 Particle trajectories for 2.1mm cubes - operating condition #5

9.3 The Effect of Particle Size on Particle Recovery

In order to determine the effect of particle size on the behaviour of coarse particles in the cell, two different particle shapes, each with two different particle sizes were investigated under operating condition #3. These were:

- Cubic particles of:
  - 3.05mm side length
  - 2.1mm side length
- Rod shaped particles of:
  - 3.38mm in length and 1.04mm radius
  - 1.98mm in length and 1.04mm radius

9.3.1 Cubic Particles

Figure 9-5 in section 9.2 above shows the experimental results for cubic particles of 2.1mm in side length under operating condition #3. The experimental results for cubic particles with a side length of 3.05mm under operating condition #3 are shown in Figure 9-9. The properties of the 3.05mm particles are given in Table 9-2 while the properties of the 2.1mm particles are given in Table 9-1, section 9.2.

Table 9-2: Properties of 3.05mm cubic particle properties

Density [kg/m^3]	Mass [mg]
3500	99.30
3300	93.63
3100	87.96
2900	82.28
2700	76.61
2600	73.77

From Figure 9-9 it is clear that, even at the highest liquid-froth interface, all the particles report to the concentrate, irrespective of density and contact angle. It seems that the particle mass of the 3.05mm cubes has thus exceeded a critical particle mass. The downward force component acting on the particle subsequently dominates the upward force components acting on the particle. The bubble films are therefore not strong enough to support the particles and the particles all fall through the froth and report to the concentrate. Looking at the properties of these particles (Tables 9-1 and 9-2), it is clear that the lightest 3.05mm cube (2.6 SG) is 227% more heavy as the heaviest 2.1mm cube (3.5 SG).

Based purely on these experimental results, no insight is gained into the influence of particle size on the trajectories of particles in the froth. The simulation model was therefore again utilised. Figure 9-10 shows the particle trajectories for 3.05mm Cubes, as predicted under operating condition #3. It is clear that virtually no classification of particles occurs, corresponding to the experimental results of Figure 9-9.

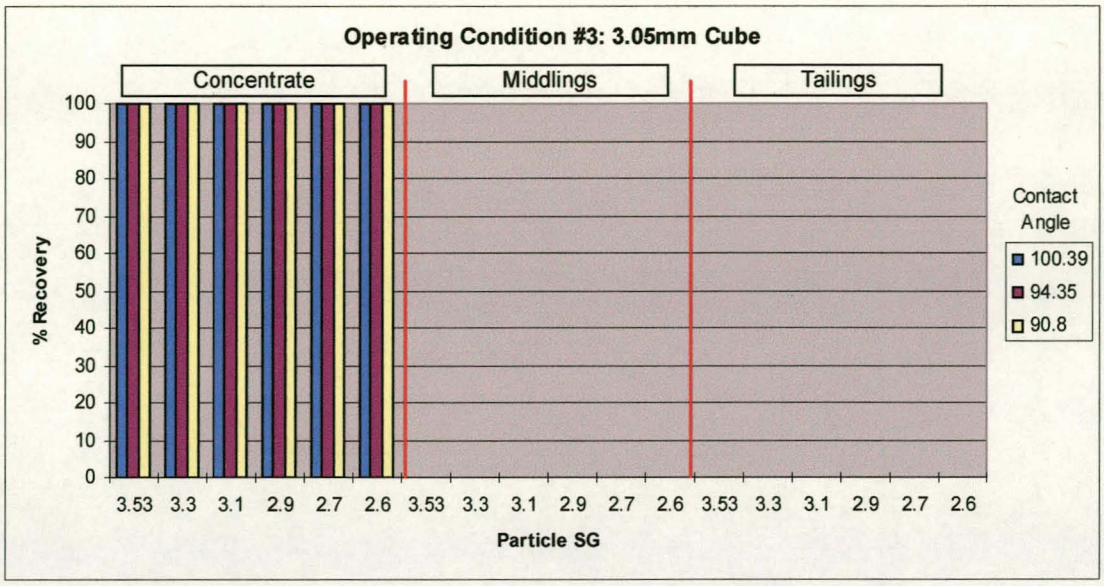

Figure 9-9: Behaviour of 3.05mm cubes under Operating Condition #3

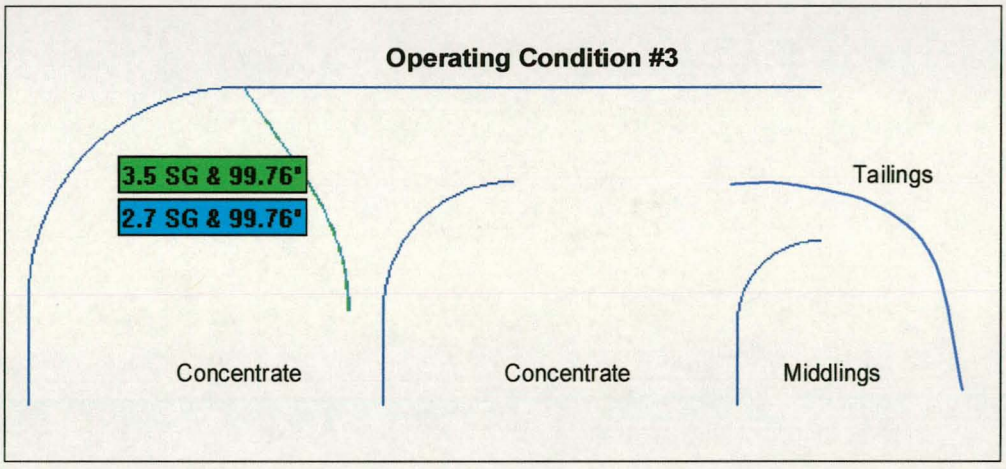

Figure 9-10: Particle trajectories for 3.05mm cubes - operating condition #3

The sensitivity analysis (see section 8) has repeatedly shown that by increasing the air flowrate through the sparger located in sub-compartment A, the horizontal velocity component, together with the upward force component, increases in the froth. It would therefore be expected that under operating condition #5, the 2.6SG 3.05mm cubes could be supported by the bubble films to a certain extent. The particle trajectories, as predicted by the model, under operating condition #5 (see Figure 9-11) confirm this. (For the benefit of black-and-white copies of this dissertation, the 3.5 SG & 99.76° particle have the steepest trajectory in the froth, while the 2.6 SG & 90.75° particle have the flattest trajectory).

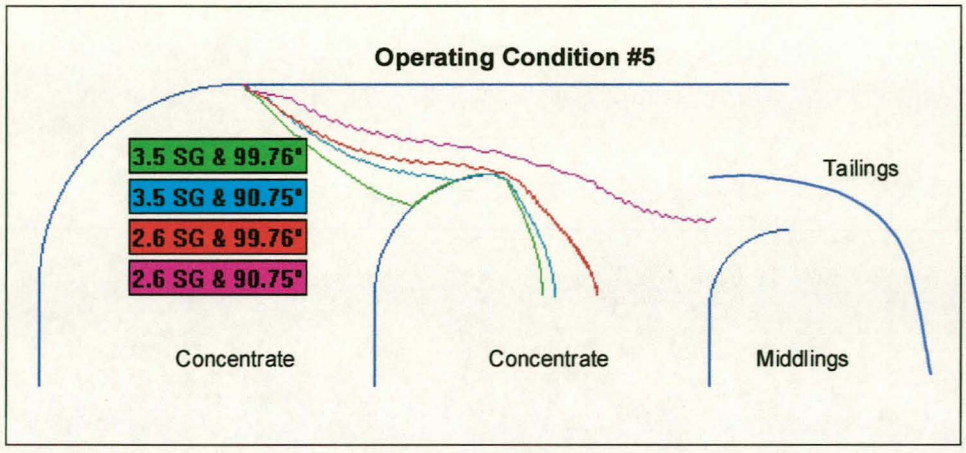

Figure 9-11: Particle trajectories for 3.05mm cubes - operating condition #5

Figure 9-11 predicts a shift in particle trajectories under operating condition #5. Particles with low contact angles increasingly reports to the middlings fraction and the tailings, with a decrease in particle density. The results of this experiment are shown in Figure 9-12, and confirm this prediction.

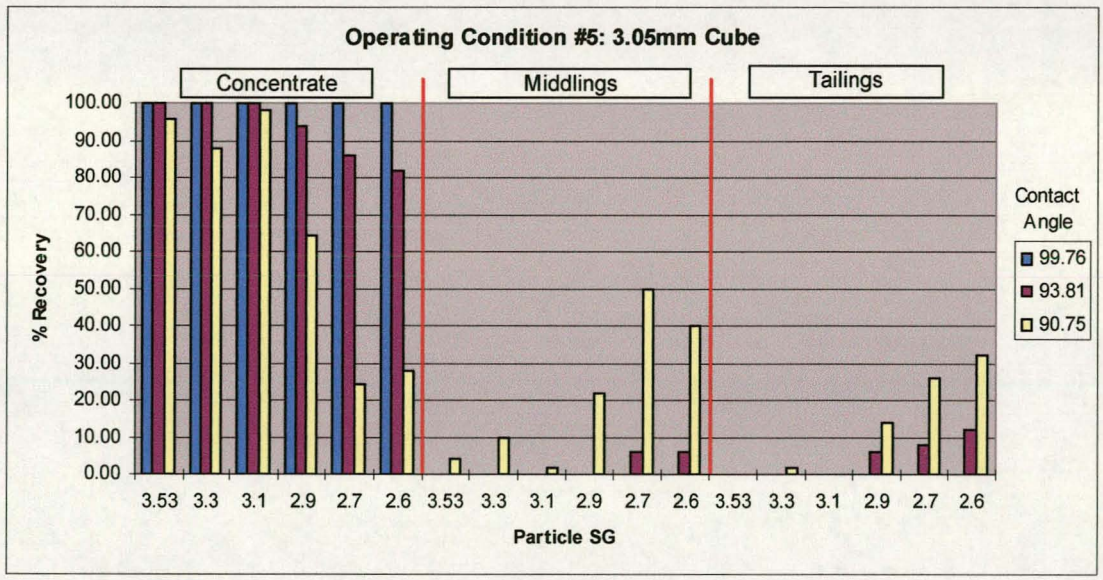

Figure 9-12: Behaviour of 3.05mm cubes under operating condition #5

By comparing Figure 9-7 with Figure 9-12, it is now clear that the smaller the particles (of similar shape and contact angle), the higher the particle trajectory in the froth. This trend is confirmed by comparing the model outputs under operating condition #5 (see Figures 9-8 and 9-11). The particle contact angle has very little influence on the behaviour of large, high density particles, as well as small, low density particles. This seems to indicate that particles will only separate on the basis of contact angle as long as the particle mass is between an upper and lower critical value. Any particle with mass greater that the upper critical value will be too heavy and will fall through the froth irrespective of the contact angle. Similarly, the upward force component acting on a particle with mass less than the lower critical

value will overshadow the downward force component. The particle will therefore remain supported by the froth, irrespective of the particle contact angle and bubble film rupture time.

9.3.2 Cylindrical/Rod shaped particles

Similar trends were noticed with cylindrical particles of the same diameter, but different lengths. Two cylindrical particle sizes were investigated:

- 3.38mm in length with a diameter of 1.04 mm, the particle properties of which are given in Table 9-3.
- 1.98mm in length with a diameter of 1.04 mm, the particle properties of which are given in Table 9-4.

The experiments were yet again conducted under operating condition #3, with various equilibrium contact angles being investigated. The results of this testwork are given in Figure 9-13 and Figure 9-14, respectively.

Table 9-3: Particle properties for rod with Rcyl=1.04mm and Lcyl=3.38mm

Density [kg/m³]	Mass [mg]
3500	40.20
3100	37.90
2900	33.31
2700	31.00

Table 9-4: Particle properties for rod with Rcyl=1.04mm and Lcyl=1.98mm

Density [kg/m³]	Mass [mg]
3500	23.55
3100	22.20
2900	19.51
2700	18.17

From Figure 9-13 it is clear that the influence of the particle density on the trajectory of the 3.38x1.04mm cylindrical particles increases as the equilibrium contact angle decreases. However, the majority of particles report to the concentrate. Figure 9-14 (1.98x1.04 cylindrical particles) shows that this effect is amplified for the smaller particles (of similar shape) to the extent that all the low SG particles report to the tailings, virtually irrespective of the particle contact angle.

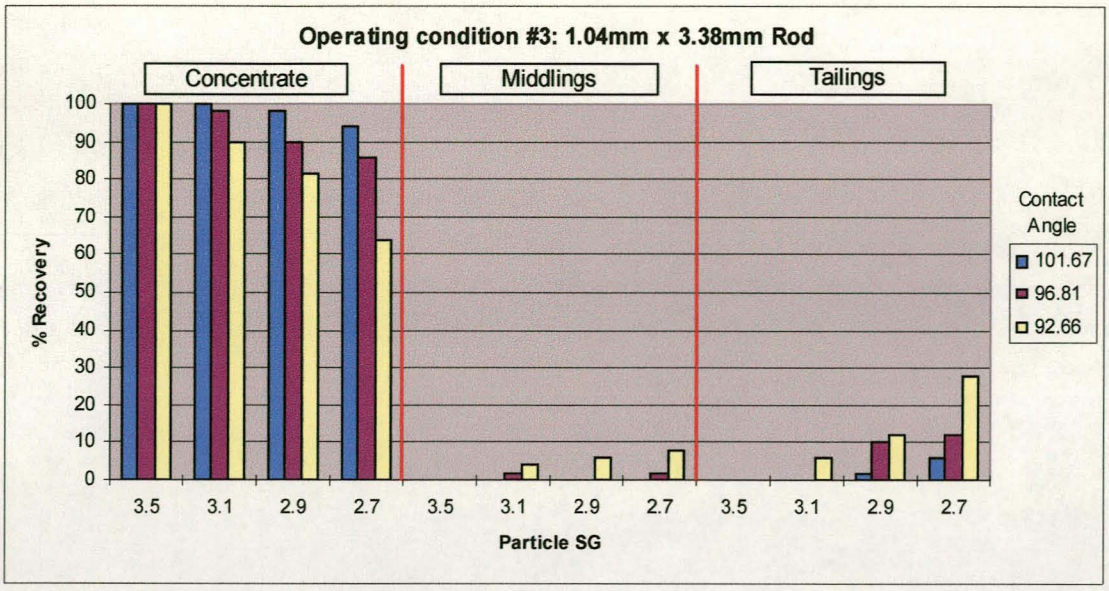

Figure 9-13: Behaviour of 3.38x1.04mm rods under operating condition #3

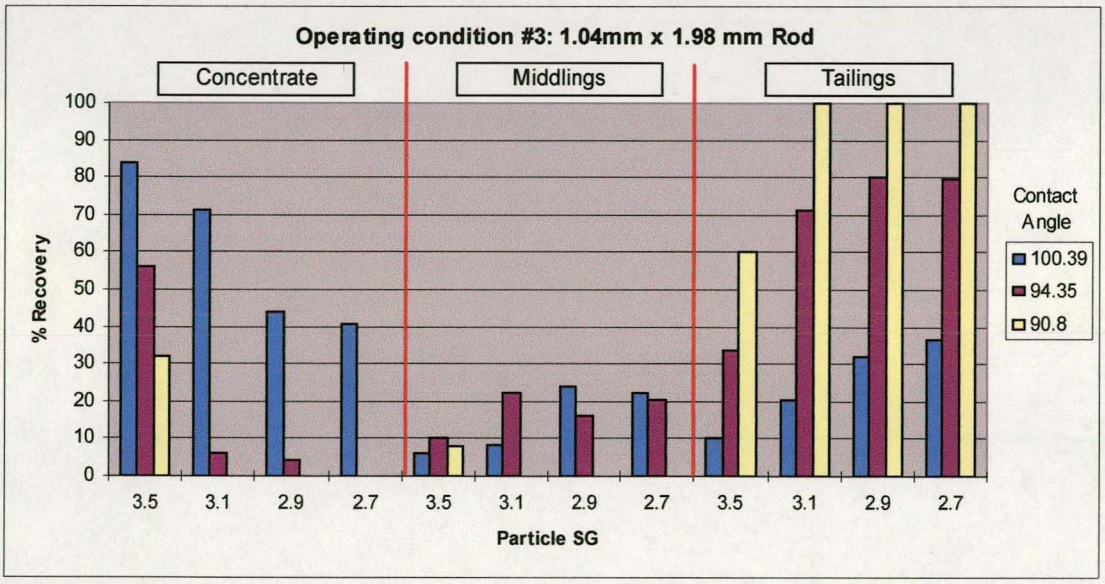

Figure 9-14: Behaviour of 1.98x1.04mm rods under operating condition #3

This again indicates that particles will only separate on the basis of contact angle as long as the particle mass is between an upper and lower critical value. Any particle with mass greater that the upper critical value will be too heavy and will fall through the froth irrespective of the contact angle. Similarly, the upward force component acting on a particle with mass less than the lower critical value, will be overshadowed by the downward force component. The particle will therefore remain supported by the froth, irrespective of the particle contact angle and bubble film rupture time. However, the upper and lower critical particle masses are particle shape specific. For cubic particles the limits were approximately between 25mg and 76mg. For cylindrical particles, however, these limits are approximately 19mg and 37mg respectively. It is therefore recognised that the mass limits are dependent on:

- Operating conditions, i.e
  - Bubble film thickness
  - Surface tension
  - Aeration rates
  - Bubble size
- Particle shape
- Particle size

The particle trajectories, as predicted by the dynamic models and corresponding to the experimental conditions of Figures 9-13 and 9-14 respectively, are given in Figures 9-15 and 9-16. For the benefit of black-and-white copies of this dissertation, the trajectories are again labelled in the order of trajectory height in the cell.

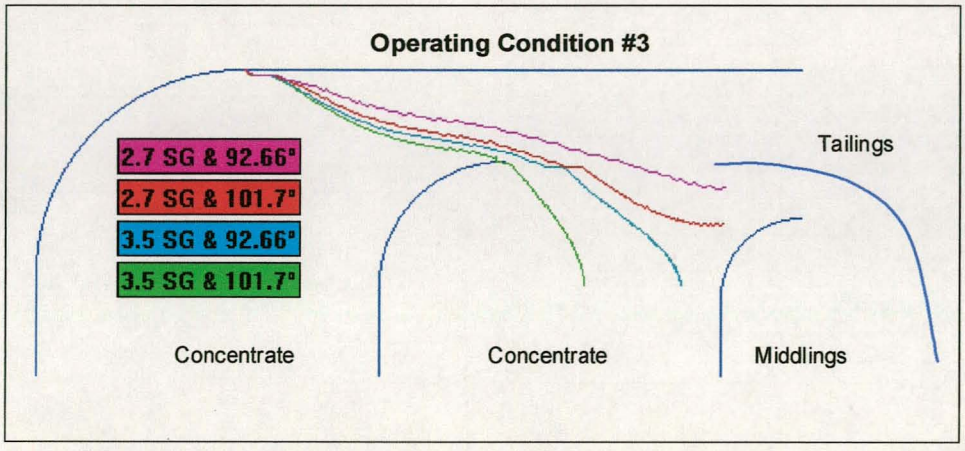

Figure 9-15: Particle trajectories for 3.38x1.04mm rods - operating condition #3

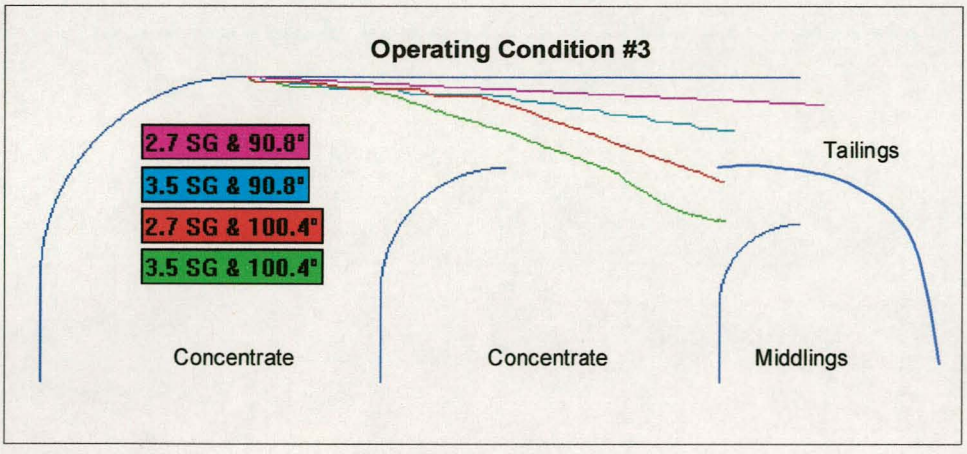

Figure 9-16: Particle trajectories for 1.98x1.04mm rods - operating condition #3

Although the experimental results for the 3.38mm x 1.04mm Rods suggest that the influence of the particle density on the trajectory of the particles increases as the equilibrium contact angle decreases, Figure 9-15 clearly shows that this is not entirely true. At a contact angle of 101.7°, the 3.5 SG particle comfortably reports to

the concentrate. By decreasing the contact angle to 92.66°, the particle trajectory is lifted, to a point where the particle can report either to the concentrate or middlings. However, under experimental conditions, a distribution of contact angles on the surface of the particle, as well as a distribution in bubble size exist resulting in the particles with an SG of 3.5 and contact angle of 92.66° reporting to the concentrate. Although a significant spread in particle trajectory therefore exits, the cell construction results in both types of particles reporting to the concentrate. The effect of equilibrium contact angle at high particle density is therefore masked.

The 1.98mm x 1.04mm rods are significantly lighter than the 3.38mm x 1.04 mm rods. The former particles are therefore floating at significantly higher positions in the froth (see Figure 9-16). Nonetheless, the spread in particle trajectories with a difference in contact angle is even more pronounced.

9.4 The Influence of Particle Mass on Particle Recovery

The experimental evidence from section 9.3 suggested that an upper and lower critical particle mass exist per particle shape. The force balance exerted on the particle in the froth is dependent on the particle mass. From equation 6-57, it is clear that the upward force component of the force balance exerted on a particle supported by the froth is dependent on the cross sectional surface area of the particle. However, the downward force component (equation 6-57) is dependent on the particle density and volume (i.e. mass). Therefore, to further investigate the influence of particle mass on the recovery of particles in the reverse froth flotation cell, particles of similar mass to cross sectional surface area ratios (M/A_0), had to be used at similar densities.

Based on visual observation of the behaviour of flat-shaped particles in the cell, it was observed that flat particles re-orientate upon breaking the bubble films so that the particle is floating with its smallest cross sectional area facing downwards (i.e. almost to assist the particle in falling through the froth). By comparing cubic and flat particles (essentially cubes that have been cut in half), the influence of particle mass can now be investigated for particles with similar M/A_0 ratios.

Two such comparisons were made between:

- Cubes of 3.05mm side length and flats of dimensions $L_f = W_f = 3.05$mm and $H_f = 1.52$mm.
- Cubes of 2.1mm side length and flats of dimensions $L_f = W_f = 2.1$mm and $H_f = 1.05$mm.

The particle properties for the flat particles with $L_f=W_f=3.05$mm and $H_f=1.52$mm are given in Table 9-5 together with the experimental results given in Figure 9-17. The experimental results of the 3.05mm cubes, in turn, are given in Figure 9-9, with the particle properties given in Table 9-2. Both these experimental sets of data were obtained under operating condition #3.

the concentrate. By decreasing the contact angle to 92.66°, the particle trajectory is lifted, to a point where the particle can report either to the concentrate or middlings. However, under experimental conditions, a distribution of contact angles on the surface of the particle, as well as a distribution in bubble size exist resulting in the particles with an SG of 3.5 and contact angle of 92.66° reporting to the concentrate. Although a significant spread in particle trajectory therefore exits, the cell construction results in both types of particles reporting to the concentrate. The effect of equilibrium contact angle at high particle density is therefore masked.

The 1.98mm x 1.04mm rods are significantly lighter than the 3.38mm x 1.04 mm rods. The former particles are therefore floating at significantly higher positions in the froth (see Figure 9-16). Nonetheless, the spread in particle trajectories with a difference in contact angle is even more pronounced.

9.4 The Influence of Particle Mass on Particle Recovery

The experimental evidence from section 9.3 suggested that an upper and lower critical particle mass exist per particle shape. The force balance exerted on the particle in the froth is dependent on the particle mass. From equation 6-57, it is clear that the upward force component of the force balance exerted on a particle supported by the froth is dependent on the cross sectional surface area of the particle. However, the downward force component (equation 6-57) is dependent on the particle density and volume (i.e. mass). Therefore, to further investigate the influence of particle mass on the recovery of particles in the reverse froth flotation cell, particles of similar mass to cross sectional surface area ratios (M/A_0), had to be used at similar densities.

Based on visual observation of the behaviour of flat-shaped particles in the cell, it was observed that flat particles re-orientate upon breaking the bubble films so that the particle is floating with its smallest cross sectional area facing downwards (i.e. almost to assist the particle in falling through the froth). By comparing cubic and flat particles (essentially cubes that have been cut in half), the influence of particle mass can now be investigated for particles with similar M/A_0 ratios.

Two such comparisons were made between:

- Cubes of 3.05mm side length and flats of dimensions L_f = W_f = 3.05mm and H_f =1.52mm.
- Cubes of 2.1mm side length and flats of dimensions L_f = W_f = 2.1mm and H_f =1.05mm.

The particle properties for the flat particles with L_f=W_f=3.05mm and H_f=1.52mm are given in Table 9-5 together with the experimental results given in Figure 9-17. The experimental results of the 3.05mm cubes, in turn, are given in Figure 9-9, with the particle properties given in Table 9-2. Both these experimental sets of data were obtained under operating condition #3.

Table 9-5: Particle properties for flats with L_f=W_f=3.05mm and H_f=1.52mm

Density [kg/m³]	Mass [mg]
3500	49.65
3300	46.81
3100	43.98
2900	41.14
2700	38.30
2600	36.88

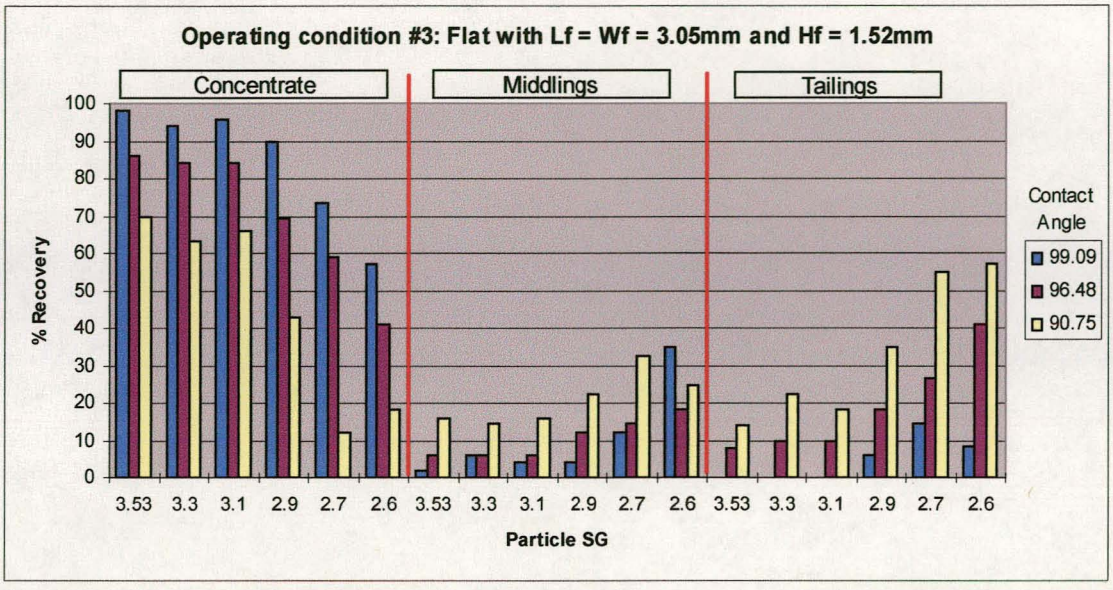

Figure 9-17: Behaviour of 3.05x3.05x1.52mm flats under operating condition #3

By comparing the experimental results for the large flats and cubes, it is clear that:

- With all other factors being constant, the mass of the particle has a critical effect on the trajectory, and subsequent recovery, of the particles.
- The lower the particle mass, the higher the particle would float in the froth phase of the reverse froth flotation cell, i.e. a decrease in particle mass would result in an increase in the loss of particles to the tailings or middlings.
- The mass of 3.05mm cubes has exceeded the critical mass. All particles therefore report to the concentrate irrespective of the particle density or contact angle. However, the mass of the flat-shaped particles is below this critical mass, resulting in:
  - A decrease in particle density resulting in an increase in particles lost to the tailings.
  - An in the equilibrium contact angle resulting in an increase in recovery to the concentrate.
  - An increase in the influence of particle contact angle with a decrease in particle density. Where there is only a difference of 28% in the recovery of particles to the concentrate for 3.5 SG particles of contact angles of 99.09° and 90.75°, the difference increases to 38% for 2.6 SG particles.

The particle properties for the flat particles with L_f=W_f=2.1mm and H_f=1.05mm are given in Table 9-6 while the experimental results are given in Figure 9-18. The experimental results of the 2.1mm cubes, in turn, are given in Figure 9-5, with the particle properties given in Table 9-1. Both these experimental sets of data were obtained under operating condition #3.

Table 9-6: Particle properties for flats with L_f=W_f=2.1mm and H_f=1.05mm

Density [kg/m³]	Mass [mg]
3500	16.21
3300	15.28
3100	14.35
2900	13.43
2700	12.50
2600	12.04

In comparing Figure 9-5 and Figure 9-18, it can be seen that:

- The recovery of the flat particles, with the same contact angle and density as cubic particles, has decreased. The flat particles are therefore floating at a higher position in the froth.
- Whereas an even spread of recoveries was obtained with the cubic particles throughout the concentrate, middlings and tailings, the flat shaped particle are predominantly reporting to the tailings.
- At medium (94.35°) to low (90.8°) contact angles virtually all the flat particles are reporting to the tailings. With cubic particles, however, a spread of recoveries was obtained at these contact angles, indicating that the time of bubble film thinning is still fast enough for the particle to settle through the froth. However, by comparing the respective mass of particles (Table 9-1 and Table 9-6), the masses of the flat particles are 50% lower than those of the cubic particles. Although the particle is therefore capable of bubble film thinning, and actually does rupture the bubble films, the upward force component of the force balance exerted on the particle in the froth will dominate. It is therefore unable to settle through the froth.
- At a high contact angle (100.39°) on the flat particles, some recovery is still possible to the middlings fraction (the limited recovery in the concentrate is due to a distribution of bubble size and contact angles present during the experimental conditions). Although the particle masses are still 50% lower than those of cubic particles, the bubble film rupture time, at these high contact angles, is fast enough so that the particle can break the bubble film at a higher rate than new films arrive at a level in the cell. Although the upward force component of the particles is still dominating the force balance on the particle, the particle can still settle through the froth.

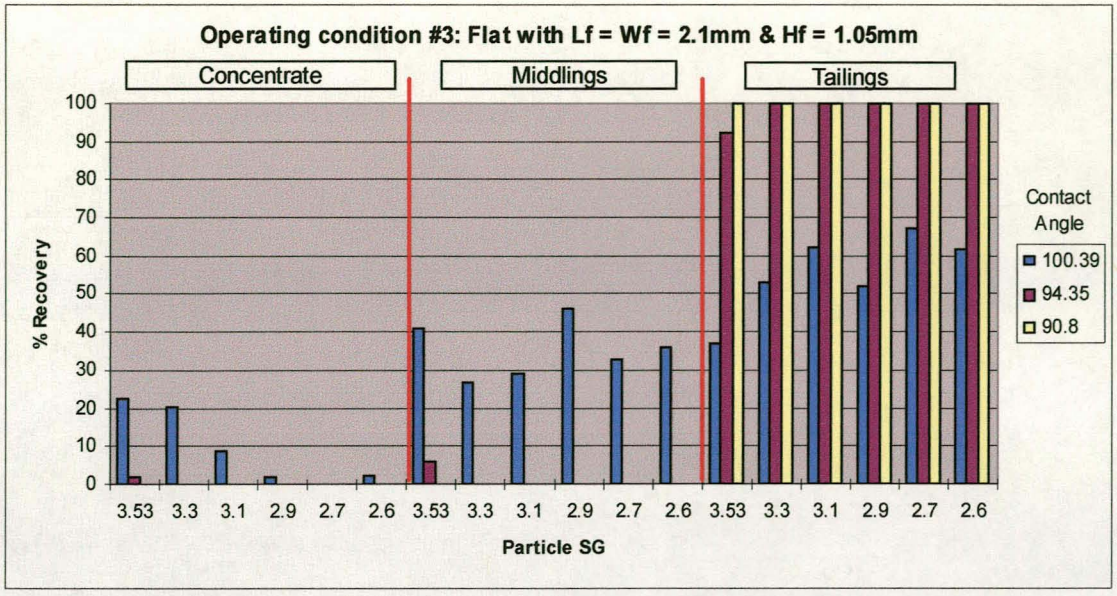

Figure 9-18: Behaviour of 2.1x2.1x1.05mm flats under operating condition #3

9.5 The Effect of Particle Shape and M/A_0 ratio on Particle Recovery

In section 9.4 the M/A_0 ratio is defined as the particle mass divided by the particle cross sectional area. Based on the experimental results in section 9.4, for particles with similar M/A_0 ratios (but different masses), the mass of the particle has a pronounced influence on the particle trajectory, and subsequent recovery, in the cell.

In the sensitivity analysis (section 8.8), the effect of particle shape on the particle trajectory was predicted by using the fundamental models described in section 5 and 6. All the particle manipulative variables were kept constant to isolate the effect of particle shape on the bubble film thinning rate. Under operating condition #3, Figure 8-32 was produced. For the benefit of easy reading this figure is reproduced as Figure 9-19 below.

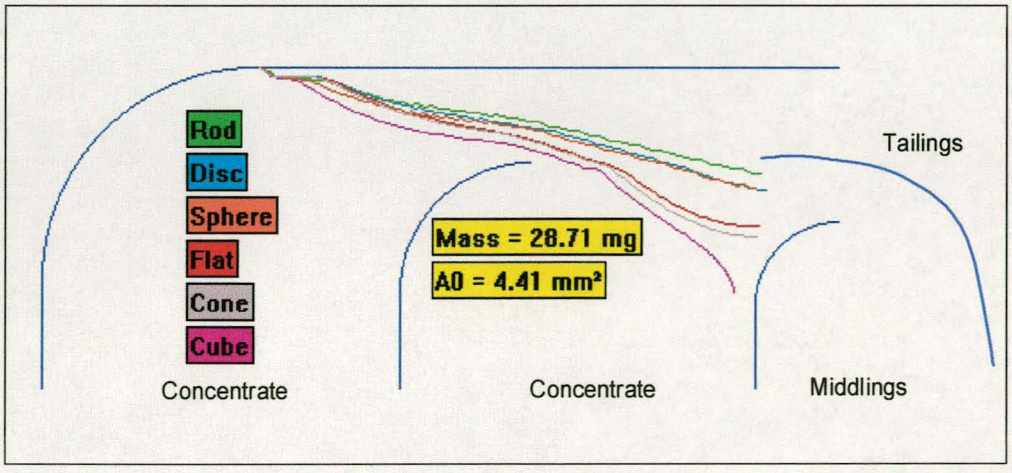

Figure 9-19: Influence of particle shape under operating condition #3 (Fig. 8-32)

From Figure 9-19 it is clear that for particles of various shapes, but of similar M/A_0 ratios and mass, a spread of particle trajectories occurs. This spread in trajectories is due to the effect of particle shape on the time of bubble film rupture. The fundamental models derived in sections 5 and 6 therefore predict that for particles of similar M/A_0 ratios, the particles will float in the order of:

- Rod
- Disc
- Sphere
- Flat
- Cone
- Cube

with a rod having the longest film thinning time (and subsequently floating at the highest trajectory) and the cube the shortest. This trend is similar to the results as obtained by Frye and Berg[18] in their analysis of the anti-foam action of solids.

Table 9-7 gives the M/A_0 ratios for the cubic and flat particles used in the experimental runs of section 9.4. Per particle shape, it would be expected that the recovery, per equilibrium contact angle, would be governed by the M/A_0 ratio. The higher the M/A_0 ratio, the more the particles would recover to the concentrate, while a decrease in the M/A_0 ratio would shift the recovery to the tailings. By comparing the experimental results obtained under operating condition #3, for the 3.05mm Cubes (figure 9-9) and the 2.1mm Cubes (figure 9-5), and the 3.05x1.52mm Flats (figure 9-17) and 2.1x1.05mm Flats (figure 9-18), it is clear that this conclusion holds.

Table 9-7: M/A_0 ratios per particle size & shape

Density [kg/m³]	3.05mm Cube	2.1mm Cube	3.05x1.52mm Flat	2.1x1.05mm Flat
3500	10.68	7.35	10.68	7.35
3300	10.07	6.93	10.07	6.93
3100	9.46	6.51	9.46	6.51
2900	8.85	6.09	8.85	6.09
2700	8.24	5.67	8.24	5.67
2600	7.93	5.46	7.93	5.46

From Table 9-7 it is further clear that the M/A_0 ratio of the 3.05mmx1.52mm flat particles is equal to the M/A_0 ratio for the 3.05mm cubes and in turn, the M/A_0 ratio of the 2.1mmx1.05mm flat particles is equal to the M/A_0 ratio for the 2.1mm cubes. Based purely on the M/A_0 ratio it would be expected that these particles would have similar recoveries. However, this is not the case as shown in Figure 9-17 vs. Figure 9-9 for 3.05mm particles.

Two factors cause the flat-shaped particles to float higher than the cubic particles. Based on the observations of Figure 9-19, the flat particles would have a longer film thinning time than the cubic particles. In addition, the mass of the cubic particles

are double that of the flat-shaped particles. It would therefore be expected that even though the M/A_0 ratio predicts that the cubes and flat-shaped particles would have similar recoveries, the effect of bubble film rupture time and overall mass would override this.

It was found that this combination of particle mass, M/A_0 ratio and bubble film thinning rate can be used to explain the recovery trends for every operating condition in the cell. For example, under operating condition #5:

- Figure 9-12 shows the experimental results for 3.05mm cubic particles.
- Figure 9-20 shows the experimental results for 1.04x3.38mm cylinders.
- Figure 9-21 shows the experimental results for flat particles where $L_f = W_f =$ 3.05mm and $H_f = 1.52$mm.
- Figure 9-22 shows the experimental results for disc shaped particles where $R_s =$ 0.65mm and $R_d = 1.1$mm.
- Figure 9-7 shows the experimental results for 2.1mm cubic particles.
- Figure 9-23 shows the experimental results for flat particles where $L_f = W_f =$ 2.1mm and $H_f = 1.05$mm.
- Figure 9-24 shows the experimental results for 1.04x1.98mm cylinders.

Table 9-8 shows the particle mass (in mg) for each of these particle shapes per density fraction, while Table 9-9 shows the respective M/A_0 ratios for each of these particle shapes, per density fraction.

Table 9-8: Particle mass [mg] per particle shape and density fraction

Density [kg/m³]	Cube 3.05	Rod 3.38 x 1.04	Flat 3.5 x 1.52	Disc 0.65 1.1	Cube 2.1	Flat 2.1 x 1.05	Rod 1.98 x 1.04
3500	99.30	40.20	49.65		32.41	16.21	23.35
3300	93.63		46.81		30.56	15.28	
3100	87.96	35.60	43.98	33.10	28.71	14.35	20.86
2900	82.28	33.31	41.14	30.97	26.86	13.43	19.51
2700	76.71	31.01	38.30		25.00	12.50	18.17
2600	73.71		36.88		24.08	12.04	

Table 9-9: M/A_0 ratio per particle shape and density fraction

Density [kg/m³]	Cube 3.05	Rod 3.38 x 1.04	Flat 3.5 x 1.52	Disc 0.65 1.1	Cube 2.1	Flat 2.1 x 1.05	Rod 1.98 x 1.04
3500	10.68	11.83	10.68		7.35	7.35	6.93
3300	10.07		10.07		6.93	6.93	
3100	9.46	10.48	9.46	7.28	6.51	6.51	6.14
2900	8.85	9.80	8.85	6.81	6.09	6.09	5.74
2700	8.24	9.13	8.24		5.67	5.67	5.35
2600	7.93		7.93		5.46	5.46	

If the particle recovery was purely based on the particle mass, the particle trajectories in the cell (and subsequent recovery to the concentrate) would have been in the order of:

1. Cubic particles with side length = 3.05mm.
2. Flat shaped particles where $L_f = W_f = 3.05$mm and $H_f = 1.52$mm.
3. Cylindrical particles where $R_{cyl} = 1.04$mm and $L_{cyl} = 3.38$mm.
4. Disc-shaped particles with $R_s = 0.65$mm and $R_d = 1.1$mm.
5. Cubic particles with side length = 2.1mm.
6. Cylindrical particles where $R_{cyl} = 1.04$mm and $L_{cyl} = 1.98$mm.
7. Flat shaped particles where $L_f = W_f = 2.1$mm and $H_f = 1.05$mm.

where the 3.05mm cubic particles would have had the steepest trajectory and highest recovery, and the 2.1mm x 1.05mm flat shaped particle the highest trajectory and subsequent losses to the tailings.

Similarly, if the particle recovery was purely based on this M/A_0 ratio per particle, the particle trajectories in the cell (and subsequent recovery to the concentrate) would have been in the order of:

1. Cylindrical particles where $R_{cyl} = 1.04$mm and $L_{cyl} = 3.38$mm.
2. Cubic particles where $S_{cube} = 3.05$mm and flat particles where $L_f = W_f = 3.05$mm and $H_f = 1.52$mm.
3. Disc-shaped particles with $R_s = 0.65$mm and $R_d = 1.1$mm.
4. Cubic particles where $S_{cube} = 2.1$mm and flat particles where $L_f = W_f = 2.1$mm and $H_f = 1.05$mm.
5. Cylindrical particles where $R_{cyl} = 1.04$mm and $L_{cyl} = 1.98$mm.

where the 3.38mm x 1.04mm cylindrical particles would have had the steepest trajectory and highest recovery, and the 1.98mm x 1.04mm cylindrical particles the highest trajectory and subsequent losses to the tailings.

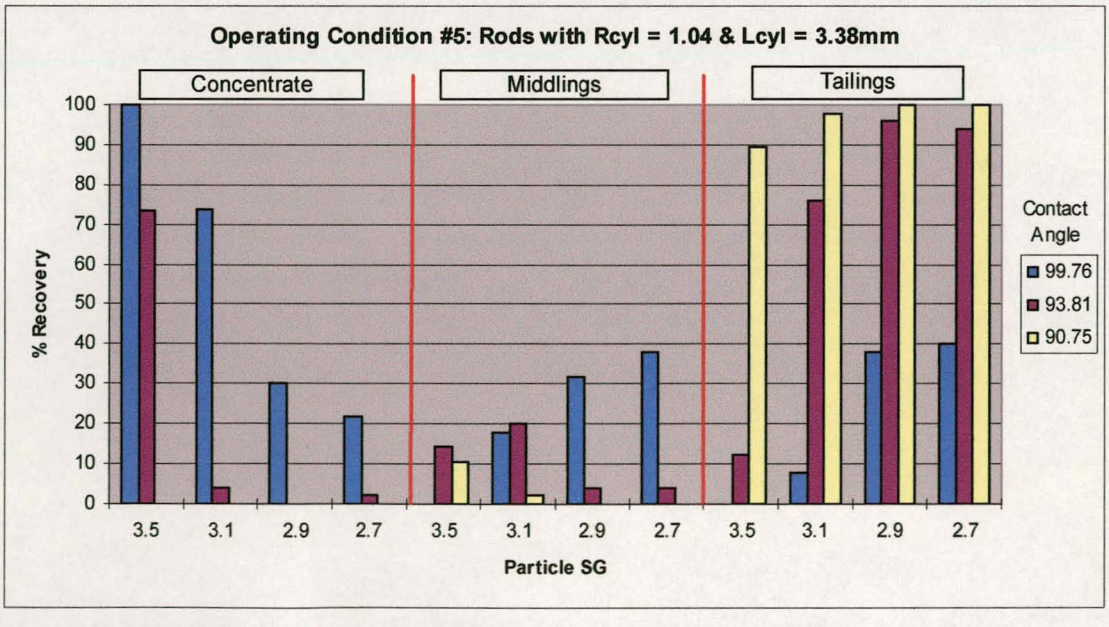

Figure 9-20: Behaviour of 3.38x1.04mm rods under operating condition #5

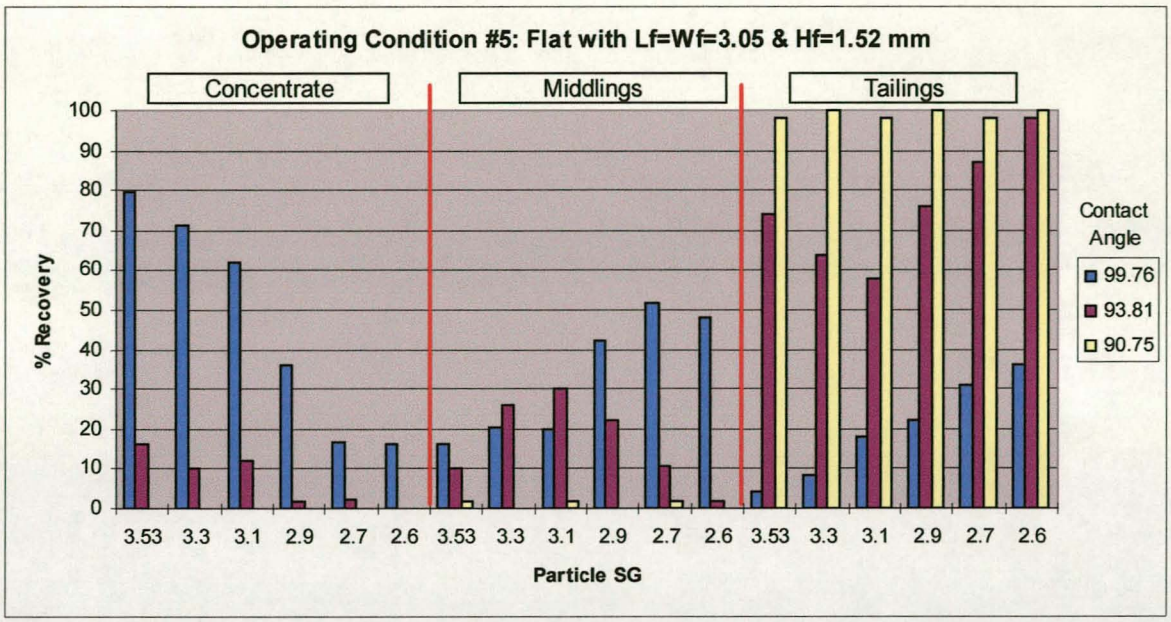

Figure 9-21: Behaviour of 3.05x3.05x1.52mm flats under operating condition #5

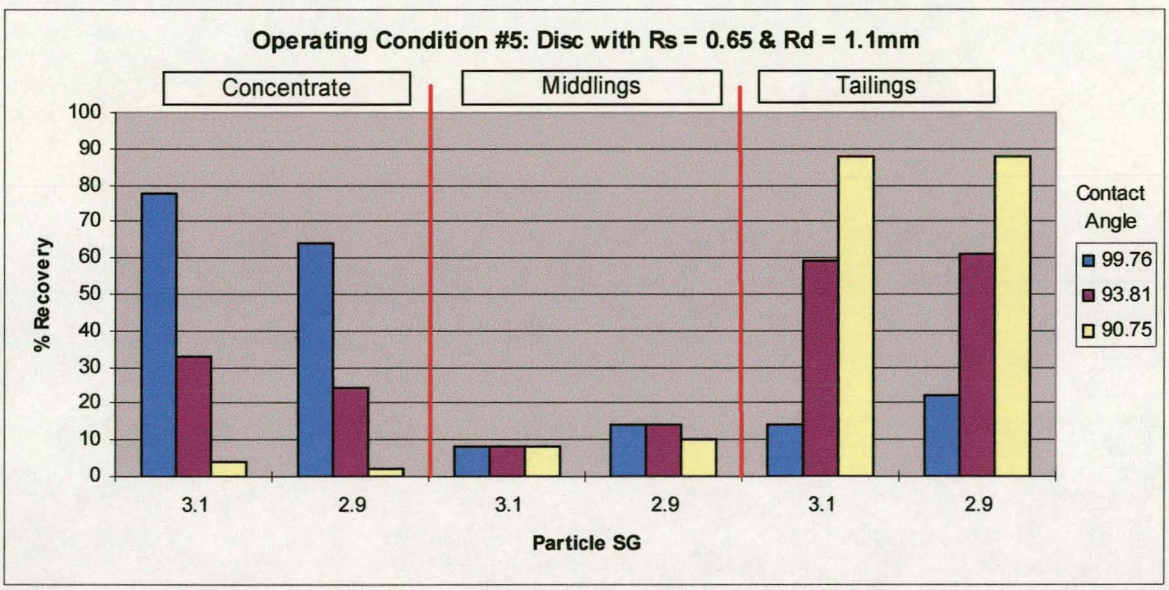

Figure 9-22: Behaviour of disc shaped particles under operating condition #5

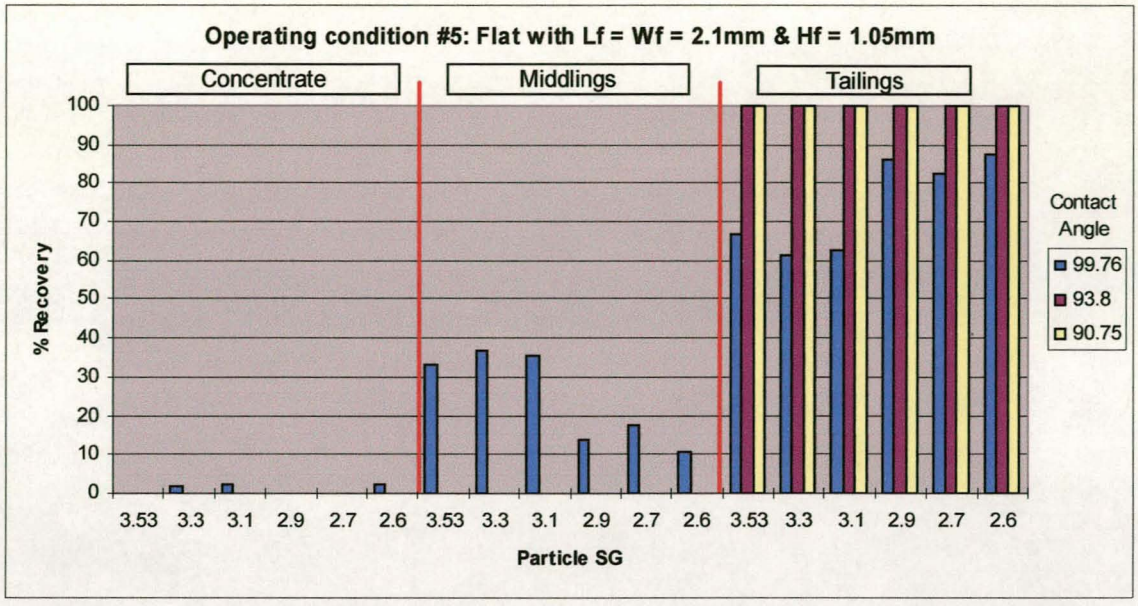

Figure 9-23: Behaviour of 2.1x2.1x1.05mm flats under operating condition #5

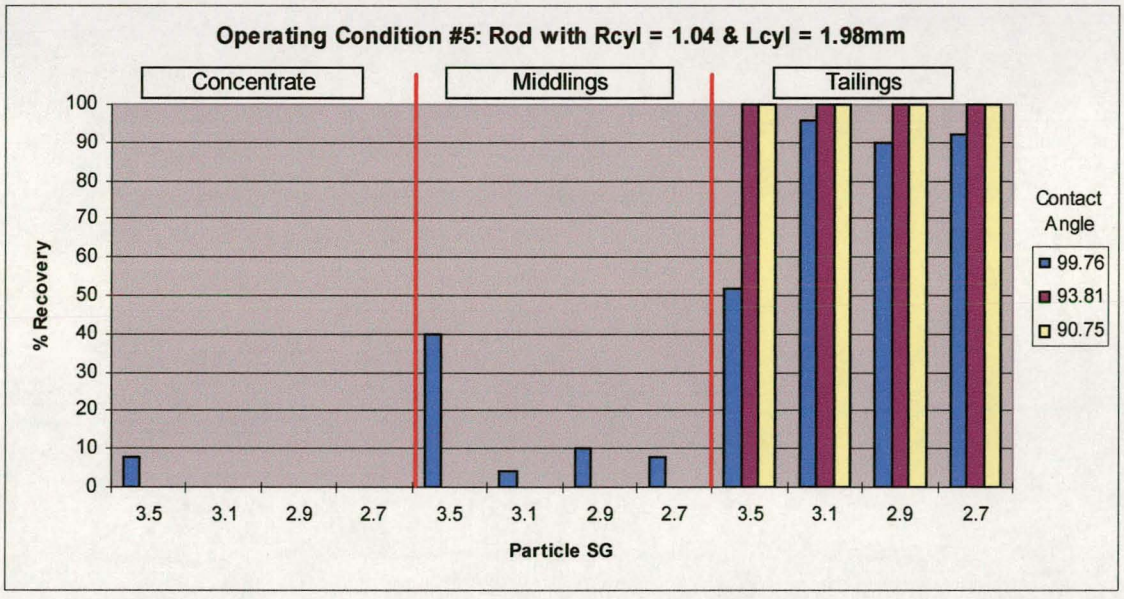

Figure 9-24: Behaviour of 1.98x1.04mm rods under operating condition #5

Based on the respective experimental results (see (Figures 9-12, 9-20, 9-21, 9-22, 9-7, 9-23 and 9-24) for operating condition #5, the order of particle recovery is:

1. Cubic particles where S_{cube} = 3.05mm.
2. Cylindrical particles where R_{cyl} = 1.04mm and L_{cyl} = 3.38mm.
3. Flat shaped particles where L_f = W_f = 3.05mm and H_f = 1.52mm.
4. Disc-shaped particles with R_s = 0.65mm and R_d = 1.1mm.
5. Cubic particles where S_{cube} = 2.1mm.
6. Flat shaped particles where L_f = W_f = 2.1mm and H_f = 1.05mm.
7. Cylindrical particles where R_{cyl} = 1.04mm and L_{cyl} = 1.98mm.

where the 3.05mm cubic particles have the steepest trajectory and highest recovery, and the 1.04mmx1.98mm rod shaped particles, the highest trajectory and subsequent losses to the tailings.

It is therefore clear that the particle recovery is not purely based on the particle mass, nor purely on the M/A_0 ratios, but rather a combination of these two parameters, coupled with the rate of bubble film rupture per particle shape (see Figure 9-19).

- The mass of the 3.05mm cubes is at least twice the mass of any other particle. It can therefore be expected that the downward force component of the force balance exerted on the particles will dominate the force balance. The 3.05mm cubes therefore have the steepest trajectory in the froth.
- Although the mass of the 3.38mm x 1.04mm rod-shaped particles is less than that of the 3.05mm x 1.52mm flat-shaped particles, the M/A_0 ratio is significantly higher. The net force downward would therefore be greater for the rod-shaped particles than for the flat-shaped particles. The rod-shaped particles therefore have a steeper trajectory in the froth, resulting in a higher recovery to the concentrate than for the flat-shaped particles.
- The disc-shaped particles will recover between the 3.05 x 1.52mm flat-shaped particles and the 2.1mm cubes due to their mass, as well as M/A_0 ratio being between that of the 3.05 x 1.52mm flat-shaped particles and the 2.1mm cubes.
- Both the mass and M/A_0 ratio of the 2.1mm cubes and 2.1 x 1.05mm flat-shaped particles result in the particles being recovered as number 5 and 6 respectively in the list.
- The mass of the 1.98 x 1.04mm rod-shaped particles is more than that of the 2.1 x 1.05mm flat-shaped particles. However, Table 9-9 shows that the M/A_0 ratio of these rod-shaped particles is significantly less than that of the flat-shaped particles. It can therefore be expected that the rod-shaped particles would have a flatter trajectory in the froth than the flat-shaped particles, leading to higher losses to the tailings.

9.6 Results Obtained with Harmony ROM Ore

The results obtained in sections 9.2 to 9.5 were seen as very encouraging, and the possibility of using the reverse froth flotation cell as an effective coarse particle flotation technique for sulphide bearing ores was subsequently investigated. Two samples were therefore prepared from Harmony Gold Mine ROM ore (see section 3.4.2). The properties of these samples are given in Table 9-10.

Table 9-10: Properties of Harmony ROM Samples

Size Fraction	Average Density [kg/m³]
+1.7mm -2.8mm	2820
+2.8mm -3.35mm	2760

9.6.1 Harmony ROM: +2.8mm -3.35mm fraction

The results of the sensitivity analysis (see sections 8.5, 8.6 and 8.7) together with the experimental results (see section 9.2), have repeatedly shown that by manipulating the air flowrate into the various compartments the trajectory of particles in the cell can be manipulated. This is mainly due to manipulating the froth velocity in the various froth areas, and subsequently affecting the force balance exerted on the particles in the froth. Two sets of experiments were therefore designed for this ore fraction:

- Determine the % mass and % sulphur recovery under operating conditions #1, #3, #4 and #5 without any addition of Xanthate. Under these conditions, the particles would separate purely on the basis of particle mass. The % sulphur recovery would therefore be due to mineral association with the various mass fractions.
- Determine the % mass and % sulphur recovery under the same four operating conditions, but with the addition of 500 gram per ton of Sodium Ethyl Xanthate and a conditioning time of 30 minutes. The objective with this set of experiments was to determine whether a concentrating effect can be obtained by rendering the exposed sulphide surfaces hydophobic with the addition of Xanthate.

For each experimental run, 100 grams of ore was hand-fed onto the froth bed. Although tedious and time consuming, particles were isolated in the froth, allowing the particles to separate on individual properties. By using an electro-magnetic vibrating feeder, particles formed agglomerates when entering the froth. These agglomerates then acted as single particles with increased mass. This combined particle mass would typically exceed the critical particle mass (see section 9.3), resulting in very poor separation. Virtually all such particles reported to the concentrate, irrespective of operating condition, particle mass or hydophobicity. However, by isolating the particles, the results as given in Table 9-11 were obtained.

From these results, the plot of % sulphur recovery vs. % mass recovery for the recovery to the concentrate is shown in Figure 9-25. The two curves correspond to the overall experimental conditions, i.e.:

- No Sodium Ethyl Xanthate addition
- 500 g/ton Sodium Ethyl Xanthate addition and 30 minutes conditioning time.

Table 9-11: Experimental results for Harmony ROM: -3.35mm+2.8mm

		No Xanthate addition		500 g/ton Xanthate addition	
Operating Condition	Reporting to:	% Mass Recovery	% Sulphur Recovery	% Mass Recovery	% Sulphur Recovery
Op Con #3	Concentrate	51.40	70.15	57.62	87.45
	Middlings	16.53	8.63	15.83	7.48
	Tailings	32.06	21.21	26.55	5.07
Op Con #1	Concentrate	42.38	62.35	48.49	75.63
	Middlings	11.22	5.80	10.14	3.89
	Tailings	46.39	31.85	41.37	20.48
Op Con #4	Concentrate	31.43	49.62	36.07	57.03
	Middlings	9.11	8.66	8.82	7.54
	Tailings	59.46	41.72	55.11	35.43
Op Con #5	Concentrate	29.29	45.31	32.93	49.48
	Middlings	7.52	8.64	5.45	6.00
	Tailings	63.19	46.05	61.62	44.52

From Figure 9-25 and Table 9-11 it can be seen that for the non-Xanthate condition:

- An increase in the liquid-froth interface level results in an increase in the mass recovery to the concentrate. This is in accordance with all the experimental results conducted on density tracers of various shapes and sizes (see section 9.2). As discussed, this effect is mainly due to an increase in the bubble size together with a decrease in the bubble film thickness. The froth is therefore incapable of supporting the particles, and the particles will fall through the froth under the influence of gravity.
- An increase in the respective air flowrates through the spargers located in sub-compartment A (operating condition #5) and sub-compartment B (operating condition #4) results in the % mass recovery to the concentrate to decrease when compared with the results of the operating conditions #1 and #3. This is to be expected due to the increase in the horizontal bubble velocity in the various cell compartments, as well as the increase in the upward force component of the force balance (due to the increase in the vertical velocity component).
- The components of the force balance, exerted by the bubble films on a particle, vary with operating condition. Since the % mass recovery varies per operating condition, it must be concluded that a distribution of particle masses exists in the feed sample.
- With an increase in the % mass recovery to the concentrate, the associated % sulphur recovery increases as well. However, the increase in % sulphur is not directly proportional to the increase in % mass. Therefore, a distribution of sulphur per particle mass fraction exists.

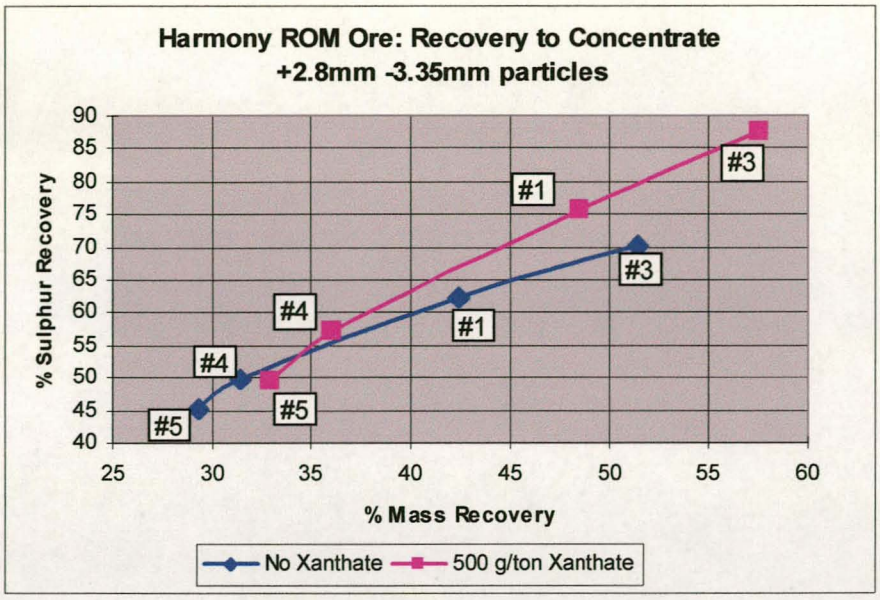

Figure 9-25: Recovery to concentrate for +2.8-3.35mm Harmony ROM

With the addition of 500 grams per ton Sodium Ethyl Xanthate:

- The % mass and % sulphur recovery again vary with operating condition (similar trends to the non-Xanthate condition). However, per operating condition, there has been an increase in the respective % mass and % sulphur recoveries. By pre-conditioning the particles with Xanthate, the sulphide present on the particle surface will be rendered hydrophobic. Since hydrophobic particles would act as bubble film breakers, it would be expected that the % sulphur recovery to the concentrate would increase. However, by preconditioning the particles with Xanthate, the overall mass of the particles still remains the same. If a particle has reported to the concentrate under the no Xanthate condition, it would be expected that the particle would still report to the concentrate (purely due to its mass). However, a particle (with sulphide on its surface) that reported to the middlings or tailings can now act as a bubble film breaker and report to the concentrate. The increase in % sulphur recovery therefore has to coincide with an increase in the % mass recovery.
- For the 500 g/ton Xanthate condition, the gradient in the line depicting % mass recovery vs. % sulphur recovery has increased. This means that although the % mass recovery increases by preconditioning the ore with Xanthate, a concentration effect takes place resulting in a relative increase in the sulphur recovery.

The reverse froth flotation cell produces three products (see Figure 3-4), i.e.:

- Concentrate
- Middlings
- Tailings

Figure 9-26 depicts the losses to the tailings (at various operating conditions) for the +2.8mm -3.35mm Harmony ROM ore. The figure is again based on the data as displayed in Table 9-11.

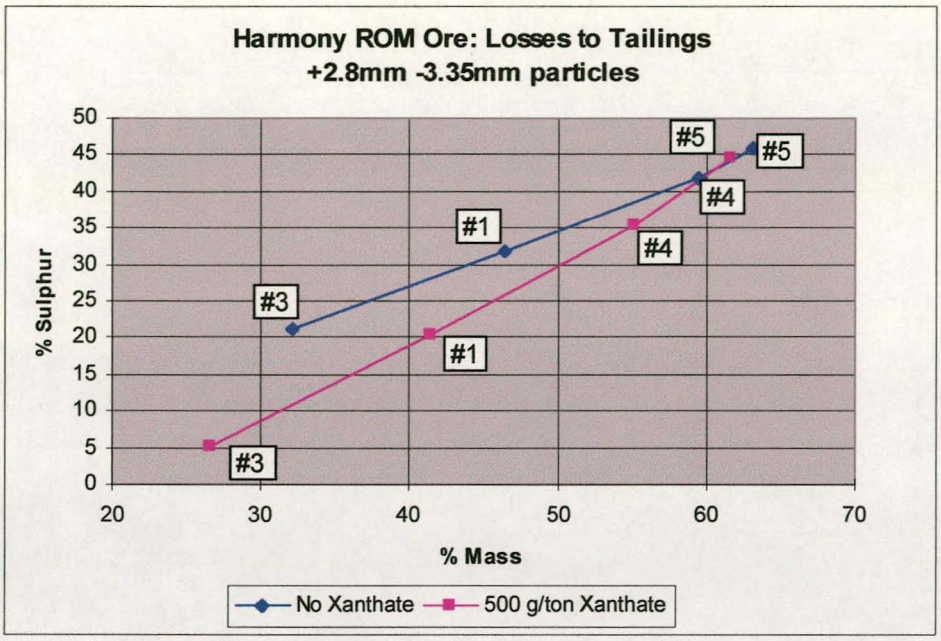

Figure 9-26: Recovery to tailings for +2.8-3.35mm Harmony ROM

As expected, Figure 9-25 displays the reverse trends as for Figure 9-26. What is prevalent, however, is that the "concentrating effect" by preconditioning the particles with Sodium Ethyl Xanthate seems to be even more pronounced. This is mainly due to a reduction in both the % mass and % sulphur reporting to the middlings under the Xanthate condition. This is mainly due to particles that were just not heavy enough to report to the concentrate with no Xanthate to be made hydrophobic, and therefore being able to break the bubble films and report to the concentrate.

9.6.2 Harmony ROM: +1.7mm -2.8mm fraction

The experimental work on the +2.8mm -3.35mm Harmony ROM ore fraction has shown that the % mass and % sulphur recoveries to the concentrate are dependent on the operating condition of the cell, as well as the preconditioning of particles with Sodium Ethyl Xanthate. The +1.7mm -2.8mm size fraction, however, showed poor recoveries to the concentrate, other than under operating condition #3. The reason for this is that the particles are too light, resulting in the upward force component to dominate the force balance. Although the particles can still break the bubble films (due to contact angle) they are not heavy enough to settle through the froth under gravity. Attempts were therefore made to operate the cell at significantly lower air flowrates and increased liquid-froth interface level. However, since all controls on the cell (i.e. re-circulating water) are manual, it was impossible to attain pseudo steady state conditions.

Under operating condition #3, however, limited particles did fall through the froth. It was therefore decided to investigate the influence of Xanthate addition, on the concentrating effect, as established under section 9.6.1. Four levels of Xanthate addition were tested. With each experimental set a preconditioning time of 30 minutes was used. The results of these experiments are given in Table 9-12, with graphical representations in Figures 9-27 and 9-28.

Table 9-12: Experimental results for Harmony ROM: -2.8mm+1.7mm

Xanthate Addition	Recovery to:	% Mass Recovery	% Sulphur Recovery
0 g/ton	Concentrate	14.71	28.75
	Middlings	3.80	6.91
	Tailings	81.48	64.34
200 g/ton	Concentrate	18.56	38.61
	Middlings	3.85	7.46
	Tailings	77.59	53.93
400 g/ton	Concentrate	20.32	40.68
	Middlings	3.10	4.78
	Tailings	76.58	54.54
800 g/ton	Concentrate	22.04	41.89
	Middlings	4.21	3.16
	Tailings	73.75	54.95

Figure 9-27 shows the % mass recovery vs. % sulphur recovery to the concentrate for the various levels of Xanthate addition. From Figure 9-27 it is clear that:

- An increase in Xanthate addition results in an increase in the % mass recovery as well as the % sulphur recovery to the concentrate.
- This increase in mass and sulphur recovery is not linear.
  - An increase of 3.85% mass recovery and 9.86% sulphur recovery is the result of increasing the Xanthate addition from 0 g/ton to 200 g/ton.
  - Increasing the Xanthate addition further from 200 g/ton to 400 g/ton results in a further increase of 1.76% in mass recovery and 2.07% in sulphur recovery.
  - Increasing the Xanthate addition even further to 800 g/ton results in a further increase of 1.72% in mass recovery and 1.21% in sulphur recovery.
- The greatest concentration effect is therefore obtained by the initial Xanthate addition. Increasing the dosage further results in smaller improvements in the concentration effect. An economically optimum Xanthate addition point therefore exists.

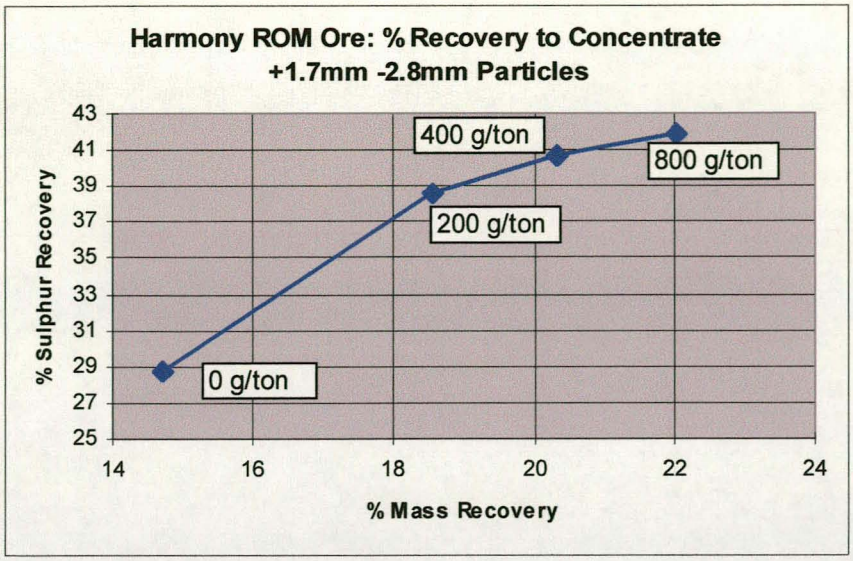

Figure 9-27: Recovery to concentrate for +1.7 -2.8mm Harmony ROM

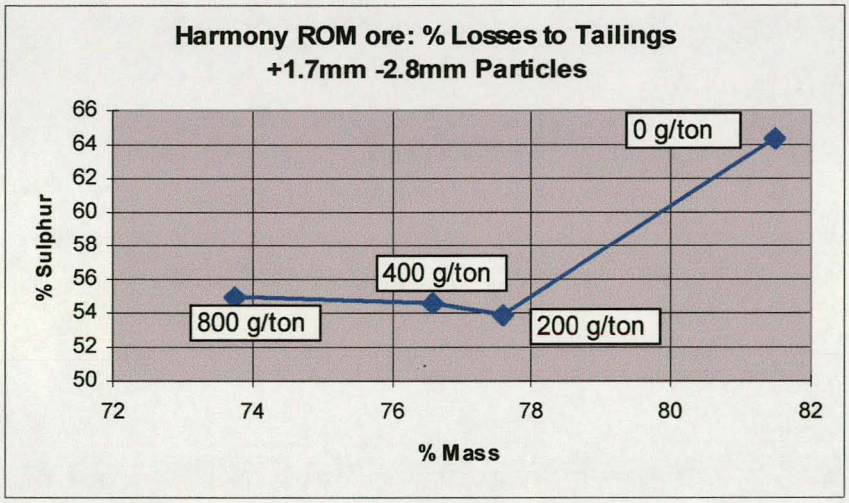

Figure 9-28: Losses to tailings for +1.7 -2.8mm Harmony ROM

Figure 9-28 shows the losses of the +1.7mm -2.8mm Harmony ROM ore to the tailings for an increase in Xanthate addition under operating condition #3. As expected from the previous discussions, an optimum point of Xanthate addition exists where the % sulphur lost to the tailings is minimised, together with the mass concentration effect. The main reason for this optimum point is the reduction in the % sulphur recovered to the middlings (see Table 9-12).

9.6.3 General discussion on coarse sulphide flotation

The results presented in section 9.6.1 and section 9.6.2 are very promising in terms of finding a coarse particle flotation technique for the pre-concentration of sulphide bearing minerals. However, it is recognised that several potential problems might exist with the technique:

- The pre-concentration of coarse sulphide bearing minerals is dependent on the liberation of sulphide, as well as the distribution of sulphide between the various particle mass fractions.
- Separation in the reverse froth flotation cell is primarily based on the particle mass, followed by the M/A_0 ratio of the particles. Once these criteria are satisfied, the effect of rate of bubble film rupture will become apparent. In principle, this means that reproducible results in terms of coarse sulphide flotation will only be obtained if:
  - Narrow size ranges are fed to the cell
  - The mineral distribution per size range remains constant
  - The mass distribution within each size range remains constant
  - The distribution of liberated sulphide per size fraction remains constant
- With any of these factors changing, cell performance will be drastically influenced. Therefore, since the composition of an ore body is never constant, it can be expected that the cell performance will vary for each ore type in an ore body.

9.7 Results Obtained with Orapa Recovery Tailings

The flotation cell was originally developed to answer a need in the diamond processing industry for the replacement of grease belts in the final recovery of fine (-3mm) diamonds. To test the applicability of the cell for this application, two samples of final recovery tailings were received from the Orapa Diamond Mine located in Botswana. The properties of these samples are given in Table 9-13.

Table 9-13: Properties of Orapa final recovery tailings

Size Fraction	Average Density [kg/m³]
+1.0mm -2.0mm (60% passing 1.72mm)	3820
+2.0mm -3.0mm (80% passing 2.36mm)	3760

Various experimental campaigns were launched with these particle fractions, the results of which are given elsewhere[34]. The main aim of these campaigns was to test various frothers as well as operational conditions, the scope of which falls outside this dissertation. However, once the optimum operational conditions were established, the ability of recovering diamonds from these feed products was tested. The respective samples were "spiked" with a 100 cubic density tracers of 3.5 SG. For the first sample, 2.1 mm and 1.0 mm cubic tracers were used, while 3.05 mm and 2.1 mm cubic tracers were used in the second sample. In addition, it was assumed that it would be possible to selectively render the diamond surface hydrophobic to a contact angle of 98°. The density tracers were therefore coated with candle wax, as described in section 3.4.5.1 of this dissertation.

Test runs for both particle size fractions were conducted under operating condition #3 and operating condition #5. The results of these tests are given in Table 9-14 below.

Table 9-14: Experimental results for spiked Orapa final recovery tails

	Recover to:	-3+2mm Tailings	3.05mm Cubes @98°	2.1mm Cubes @98°
Operating Condition #3	Concentrate	83	100	83
	Middlings	1.3	0	15
	Tailings	15.4	0	2
Operating Condition #5	Concentrate	54.5	100	26
	Middlings	1.8	0	56
	Tailings	43.7	0	18
		-2+1mm Tailings	2.1mm Cubes @98°	1.0mm Cubes @98°
Operating Condition #3	Concentrate	20.8	86	2
	Middlings	2.9	14	5
	Tailings	76.3	0	93
Operating Condition #5	Concentrate	5.2	30	0
	Middlings	3.8	54	0
	Tailings	91	16	100

9.7.1 -3+2mm Orapa tailings fraction

The recovery distributions to the concentrate, middlings and tailings for the -3+2mm Orapa tailings and spiked tracers are given in Figure 9-29. If the cubic density tracers resemble the valuable product, operating condition #3 would result in a 17% mass reduction with a possible loss of 17% of the valuable product. To counter this, it would be possible to accept the middlings fraction as concentrate. This strategy would result in a 15.4% mass reduction, with 2% of the valuable product being lost to the tailings. Due to the limited mass reduction, this operating condition would not work for the coarse size distribution.

Operating condition #5 was subsequently tested. Although a significant mass reduction (45.5%) was obtained, huge losses (74%) of valuable 2.1mm product could occur. By incorporating the middlings fraction as product, the mass reduction would increase to 43.7%, while losses of valuable 2.1mm product reduce to 18%. A significant mass reduction is therefore possible by treating coarse (-3+2mm) diamond concentrate. However, a possible loss of 18% of the fine valuable material could occur.

9.7.2 -2+1mm Orapa tailings fraction

A similar analysis was conducted for the -2+1mm Orapa tailings fraction. In this case, the tails were spiked with 2.1mm cubic density tracers and 1.0mm cubic density tracers. A SG of 3.5 was used for the density tracers together with a candle wax coating yielding a contact angle of ±98° on the surface of the tracers.

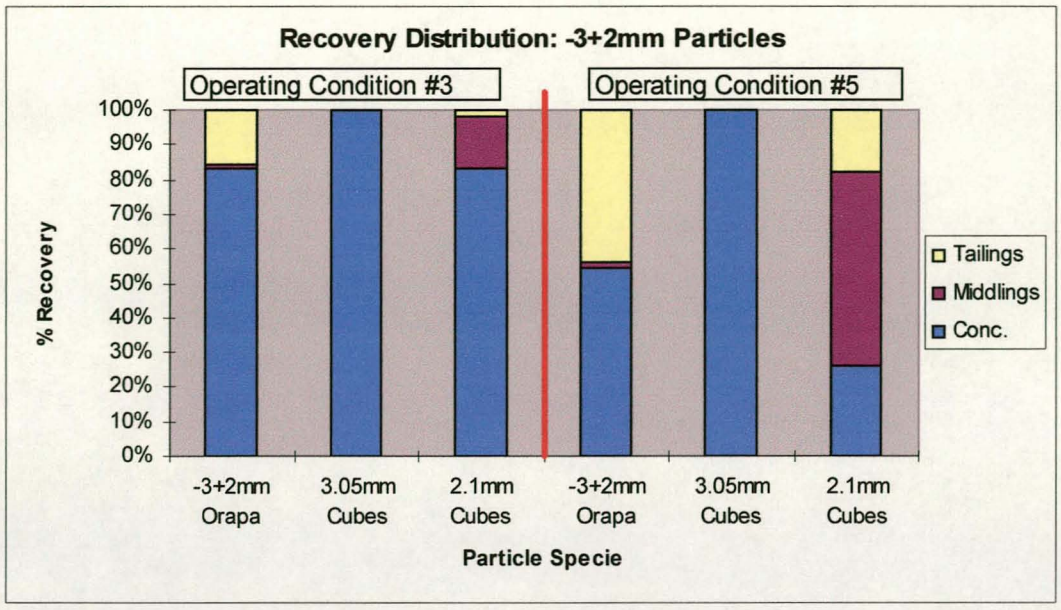

Figure 9-29: Recovery distribution for spiked -3+2mm Orapa tailings

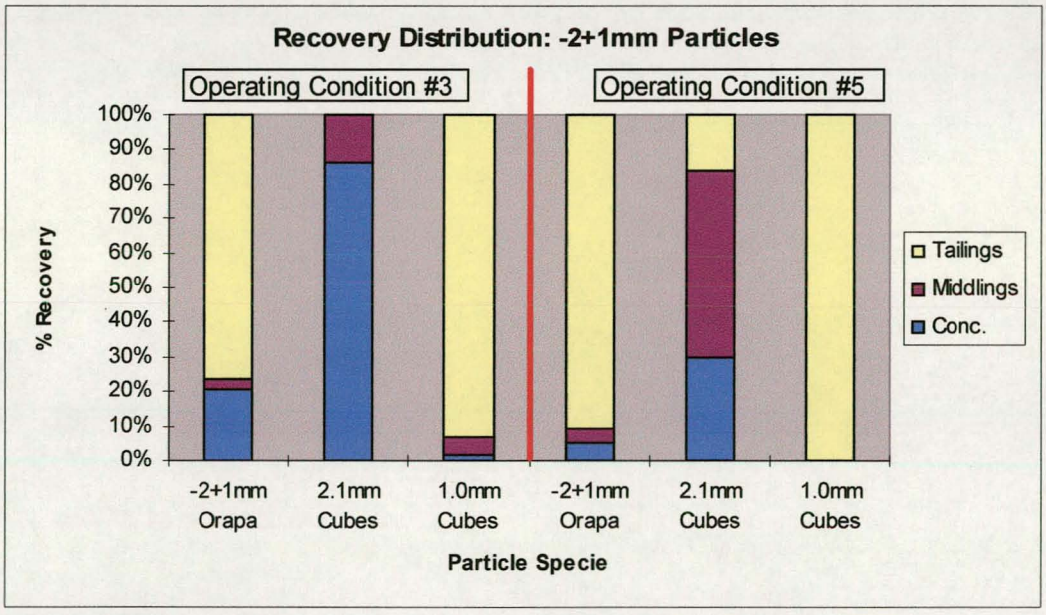

Figure 9-30: Recovery distribution for spiked -2+1mm Orapa tailings

Figure 9-30 shows the density distribution per operating condition for the various particles in the size fraction. Although a significant mass reduction would be possible under operating condition #3 for this size fraction, the potential loss of "valuable" material is significant. By accepting the middlings fraction as concentrate the mass reduction reduces to 76.3%, 100% of the upper size (2.1mm) valuable material is recovered, but the fine (1.0mm) valuable material recovery only increases to 7%. This poor recovery of "valuable" particles only worsens for operating condition #5 (see Figure 9-30).

9.7.3 General discussion on application in diamond processing

The results presented in sections 9.7.1 and 9.7.2 would indicate that the reverse froth flotation process is not suitable for the replacement of grease belts for fine diamond recovery. The major concern is the high potential losses of valuable material to the tailings. These losses are mainly due to the fact that the major separation process in the reverse froth flotation cell is based on particle mass. The surface properties of the particle only account for a secondary separation process.

This sensitivity towards particle mass would require the screening of feed material in very narrow size fractions. Not only is such screening difficult, but also the number of unit operations in the process would increase, resulting in unnecessary capital and operational costs.

9.8 Summary

The experimental results in this chapter showed that the behaviour of coarse particles in the froth phase of the cell is primarily dependent on the particle mass. In general, the higher the particle mass, the steeper its trajectory in the froth. In addition it was shown that particles would separate on the basis of contact angle as long as the particle mass is between an upper and lower critical limit. Outside of these limits, the force components acting on the particle will dominate the particle behaviour. Apart from these parameters, the M/A_0 ratio as well as the operational conditions of the cell, affects the particle behaviour.

Comparing the results with the dynamic model, it was found that the model is capable of predicting all the trends as identified during the experimental program. In addition, the model provided valuable assistance in explaining some of the experimental trends identified. Although the model predicts the "ideal trajectory" for a specific particle under specific operational conditions, the spread in experimental results could still be related to the model via the results of the sensitivity analysis in chapter 8.

10. CONCLUSIONS

A novel flotation technique for the recovery of coarse, hydrophobic particles from gravel was developed. Various operational problems were experienced with the original cell design. These problems prompted a major design review to be conducted. The outcome of this review culminated in a modified cell design, in which localised froth disturbances were eliminated.

The technique is based on the fact that coarse particles, if they are selectively rendered hydrophobic by conditioning, would act as bubble film breakers if the feed is introduced onto the surface of the froth. Such particles would settle through the froth under gravity to be recovered as an underflow product, while the gangue would be supported by the bubble films and be recovered as a float product. The process differs from conventional reverse flotation in that the separation is effected in the froth phase only. The process is therefore called "reverse froth flotation". The efficiency of the technique depends on the interaction between various particle and froth characteristics. In order to improve and optimise the process, a more fundamental understanding of the principles involved and interaction of parameters was required.

Visual observations of the behaviour of particles in the froth phase of the cell have shown that the particles are positioned in the froth at a level where they are best supported by the bubbles. This suggested that there is an optimum froth condition, at a particular bubble size, for the flotation of a particle of a certain size, shape and surface characteristics. Therefore, to understand and interpret the factors that influence the dynamic behaviour of particles, a fundamental model of the various mechanisms in the froth was developed. The aim of the model was not to predict the experimental observations exactly, but rather to simulate the observed trends in a qualitative manner. Variables could therefore be investigated in isolation, which is not always possible in experimental work.

Since the froth properties will be different at any position in the cell, the model predicts the trajectory of a particle over discrete time events. Various particle properties were taken into account, including surface properties, shape, size and density. To account for the change in nature of the froth, bubble flow streamlines were calculated. At any position on a streamline, the bubble size, thickness of bubble films, air hold-up and bubble velocity were modelled.

A comprehensive sensitivity analysis was conducted with the dynamic model. For the cell operational parameters, the following conclusions were drawn:

- Air flowrate:
  - Particles with identical properties will classify more to the tailings with an increase in air flowrate in sub-compartment A.
  - A secondary classification can be obtained by manipulating the air flowrate through sub-compartment B.

- Entrained water:
  - Manipulating the flow of liquid to the tailings and middlings respectively has a negligible influence on the trajectory of particles with identical properties.
  - The manipulation of water flows is an artificial constraint on the process. Due to the interaction of various parameters, particle trajectories should be evaluated under actual operating conditions.

Five operating conditions were therefore selected under which the effect of particle and operational parameters on the trajectory of particles in the reverse froth flotation cell were evaluated. The five conditions were based on manipulating the liquid-froth interface level and aeration rates. The following conclusions were drawn as to the effect of manipulating these cell operational parameters on the overall froth properties:

- An increase in the liquid-froth interface level, with all other manipulative parameters remaining constant, results in:
  - A smaller bubble size at the liquid froth interface
  - The height of the froth overflow over the splitter plate to increase
  - A less drained froth, i.e. the liquid flow to the tailings and middlings will increase
  - The air hold-up throughout the cell to decrease.
- The opposite effects are observed with a decrease in the liquid-froth interface.
- An increase in the air flowrate through the sparger in sub-compartment A results in:
  - A decrease in the air hold-up in froth areas #1 and #3.
  - A decrease in the bubble size at the liquid froth interface
  - The height of the froth overflow over the splitter plate to increase
  - A less drained froth, i.e. the liquid flow to the tailings and middlings will increase
- An increase in the air flowrate through the sparger in sub-compartment B results in:
  - A decrease in the air hold-up in froth areas #2 and #3.
  - An increase in the bubble size at the liquid froth interface
  - The height of the froth overflow over the splitter plate to increase
  - A less drained froth in froth area #2, i.e. the liquid flow to the middlings will increase

For each of the five operational conditions the effect of particle size was investigated with the dynamic model. Particles of similar shape and density, but of different physical dimensions were used, from which it was concluded that:

- Particles do classify on the basis of particle size in the reverse froth flotation cell.
- The extent of classification is dependent on:
  - the actual particle size
  - the liquid level in the froth, i.e. bubble size and entrained water
  - the air flowrate through the various spargers, i.e. the upward force exerted on the particles and the horizontal velocity bubbles in the froth.

- An increase in particle size results in an increase in the film rupture time and an increase in the downward force exerted by the particle on the supporting bubble films. At small particle sizes these effects can counteract each other, however, with large particles the effect of the particle mass, and subsequent downward force, will dominate.

The particle density was also varied during the sensitivity analysis. For this exercise, the particle shape, contact angle and physical dimensions were kept constant. Under the five operating conditions it was found that:

- The higher the particle density, the steeper the trajectory of the particle in the froth.
- The extent of the spread in trajectories is dependent on:
  - the actual particle density
  - the level of the liquid-froth interface, i.e. the air hold-up fraction in the froth
  - the horizontal froth velocity in the various froth areas, i.e. the air flowrate in the various sub-compartments.
- The classification in the froth based on particle density is dependent on the force balance the particle is subjected to while supported by the bubble films in the froth. An increase in particle mass results in the particle floating at a lower position in the froth, while an increase in the froth density has the opposite effect.

The last parameter investigated during the sensitivity analysis was the particle shape. The effect of particle shape on the film rupture time was isolated by selecting particles of similar mass and cross sectional area (M/A_0 ratio). From this exercise it was shown that:

- The particle shape has a pronounced effect on the trajectory of particles in the froth phase of the cell.
- Angular particles (cube, flat & cone) will float at a lower position in the froth while smooth particles will float at higher trajectories.
- The extent of the spread in trajectories is dependent on:
  - the actual particle shape
  - the level of the liquid-froth interface, i.e. the air hold-up fraction in the froth
  - the horizontal froth velocity in the various froth areas, i.e. the air flowrate in the various compartments.

The dynamic model predicts the particle trajectory under ideal conditions, i.e. no distribution in contact angle or bubble size. In practice, a distribution in both the particle contact angle and the bubble size at the liquid-froth interface exists. The influence of these distributions was therefore investigated. At first the dynamic model was used to vary the bubble size at the liquid-froth interface under each of the operating conditions. From this analysis it was concluded that:

- An increase in interface bubble size results in a lower particle trajectory, and vice versa.
- By increasing the interface height, the spread becomes more accentuated, but the trajectories as a whole are moved downwards, i.e. towards the concentrate

compartment. This is mainly due to more entrained water present in the froth, and an increase in bubble size at the liquid-froth interface.

- ➢ An increase in the air flowrate through the sparger located in sub-compartment B does not influence the classification in froth area #1. However, due to an increase in the horizontal froth velocity, the classification in froth area #2 is reduced.
- ➢ An increase in the air flowrate through the sparger located in sub-compartment A results in an overall increase in horizontal froth velocity. This increase causes the effect of bubble size to be less pronounced.

The effect of measured contact angle on the dynamic behaviour of particles was also simulated. From this study it was concluded that:

- ➢ Particles will float at a lower position in the froth with an increase in the equilibrium contact angle on the particle surface.
- ➢ The extent of the spread in trajectories is dependent on:
  - ➢ the actual equilibrium contact angle
  - ➢ the level of the liquid-froth interface, i.e. the air hold-up fraction in the froth
  - ➢ the horizontal froth velocity in the various froth areas, i.e. the air flowrate in the various compartments.

The sensitivity analysis has therefore shown that both the contact angle and bubble size distribution could effect the trajectory of the particles significantly. The spread in recoveries obtained under experimental conditions was therefore attributed to the distribution in bubble size and contact angles that exist in practice. However, it was found that the dynamic model was capable of predicting the ideal particle trajectories qualitatively. In addition, it provided a unique understanding of the interrelationship between the various parameters which otherwise would not have been gained by alternative modelling methods.

The experimental results conclusively showed that the behaviour of particles in the froth phase of the reverse froth flotation cell is primarily dependent on the particle mass (as predicted by the model). In general, the lower the particle mass, the higher the particle would float in the froth, i.e. a decrease in particle mass would result in an increase in the loss of particles to the tailings or middlings. The contact angle on the particle surface has only a secondary influence on the overall particle trajectory, in that a decrease in the equilibrium contact angle will result in more losses to the tailings. However, the particle contact angle has very little effect on the behaviour of large, high-density particles, as well as small, low-density particles.

Particles will therefore only separate on the basis of contact angle as long as the particle mass is between an upper and lower critical value. Any particle exceeding the upper critical mass limit will be too heavy and will fall through the froth irrespective of the contact angle. Similarly, the upward force component acting on a particle with mass less than the lower critical value will dominate the force balance. The particle will therefore remain supported by the froth, irrespective of the particle contact angle and bubble film rupture time. Should the particle mass be within

these mass limits it was found that the effect of the particle contact angle increases with a decrease in the particle mass.

It was further concluded that these mass limits are dependent on the operating conditions of the cell as well as the particle shape. The particle shape influences the mass to cross sectional surface area ratio (M/A_0). Where particles therefore have the same mass, the M/A_0 ratio would govern the particle trajectory. The higher the M/A_0 ratio, the more the particles would recover to the concentrate, while a decrease in the M/A_0 ratio would increase the losses to the tailings.

Two potential industrial applications for the process were evaluated, i.e:

- A coarse particle flotation technique for sulphide bearing ores
- The possible replacement of grease belts in the diamond mining industry for fine diamond recovery

As a coarse particle flotation technique for sulphide bearing ores, it was found that Xanthate pre-conditioning of the ore results in concentrating the sulphur bearing particles to the concentrate. By increasing the Xanthate addition, the relative % mass recovery as well as % sulphur recovery to the concentrate increases. This increase in mass and sulphur recovery, however, is not linear. The greatest concentration effect was obtained by the initial Xanthate addition. An economically optimum Xanthate addition point therefore exists.

These results were very promising in terms of finding a coarse particle flotation technique for the pre-concentration of sulphide bearing minerals. However, it is recognised that several potential problems might exist with the technique:

- The pre-concentration of coarse sulphide bearing minerals is dependent on the liberation of sulphide, as well as the distribution of sulphide between the various particle mass fractions.
- Separation in the reverse froth flotation cell is primarily based on the particles mass, followed by the M/A_0 ratio of the particles. Once these criteria are satisfied, the effect of rate of bubble film rupture will become apparent. In principle, this means that reproducible results in terms of coarse sulphide flotation will only be obtained if:
  - A narrow size ranges are fed to the cell
  - The mineral distribution per size range remains constant
  - The mass distribution within each size range remains constant
  - The distribution of liberated sulphide per size fraction remains constant
- With any of these factors changing, cell performance will be drastically influenced. Therefore, since the composition of an ore body is never constant, it can be expected that the cell performance will vary for each ore type in the ore body.

The results further indicated that the flotation process is not suitable for the replacement of grease belts for fine diamond recovery. The major concern is the high potential losses of valuable material to the tailings. These losses are mainly

due to the fact that the major separation process in the reverse froth flotation cell is based on particle mass. The surface properties of the particle only account for a secondary separation process.

The flotation community has struggled for many years to separate coarse particles using flotation froths. The "reverse froth flotation" technique, however, is capable of separating coarse particles on the basis of a combination of particle mass, hydrophobicity and mass to area ratio, and thereby providing a solution to the problem. In order to optimise the technique, the effect of physical parameters on the rupture of bubble films in the novel flotation cell has been characterised. Although only two industrial applications of the technique have been tested (with limited success), it is felt that the technique might find a unique application in the separation of coarse coal, as well as the separation of plastics from metals in the recycle industry.

11. REFERENCES

1. Ross, V.E., "Separation Method and Apparatus", SA Patent 93/5367, Apr. 28, 1993
2. Moxon, N.T. & Keast-Jones, R., The effect of collector emulsification using non-ionic surfactants on the flotation of coarse coal particles, *Int. J. Miner. Process.*, **18**, 1986, 21-32.
3. Moxon, N.T., Keast-Jones, R. & Aston, J.R., Increased coarse coal yield from flotation using non-ionic frothers, *Int. J. Miner. Process.*, **24**, 1988, 295-305.
4. Lloyd, P.J.D., The potential of integrating mining and extraction systems on the Witwatersrand, *Proceedings of the Eleventh Commonwealth Mining & Metallurgical Congress*, IMM, Hong Kong, 1987, 631-643.
5. Schubert, H., On optimum hydrodynamics of coarse particle flotation, *Aufbereitungs-technik*, **30** (11), 1989, 657-663.
6. Fuerstenau, D.W. & Raghavan, S., Flotation, M.C. Fuerstenau, ed., AIME, New York, 1976, 21
7. Fowkes, F.M., Industrial and Engineering Chemistry, **56**, 1964, 40.
8. Trahar, W.J., A rational interpretation of the role of particle size in flotation, *Int. J. Miner. Process.*, **8**, 1986, 289 - 327.
9. Gaudin, A.M., Groh, J.O. & Henderson, H.B., The effect of particle size on flotation. *Am. Inst. Min. Metall. Eng.*, Technical Publication No. 414.
10. Li, R., Hoberg, H. & Schneider, F.U., Investigations on the Influence of Particle Size in Flotation, *XVIII International Minerals Processing Congress*, Sydney, 23-28 May 1993. 689-697.
11. Dobby, G.S. & Finch, J.A., Particle Size Dependence in Flotation Derived from a Fundamental Model of the Capture Process, *Int. J. Miner. Process.*, **21**, 1987, 241-260.
12. Crawford, R., & Ralston, J., The Influence of Particle Size and Contact Angle in Mineral Flotation, *Int. J. Miner. Process.*, **23**, 1988, 1-24.
13. Livshitz, A. & Dudenkov, S.V., Some factors in flotation froth stability, *VII International Minerals Processing Conference*, Arbiter, D. ed. (New York, etc.: Gordon and Breach, 1965), 1964, 367 - 371.
14. Garrett, P.R., The effect of polytetrafluoroethylene particles on the foamability of aqueous surfactant solutions. *J. Colloid Interface Science.*, **69** (1), 1979, 107 - 121.
15. Dippenaar, A., The destabilization of froth by solids. I. The mechanism of film rupture, *Int. J. Miner. Process.*, **9**, 1982, 1-14.

16. Dippenaar, A., The destabilization of froth by solids. II. The rate determining step, *Int. J. Miner. Process.*, **9**, 1982, 15-27.
17. Hemmings, C.E., On the significance of flotation froth liquid lamella thickness, *Trans. Instn. Min. Metall. (Sect. C: Mineral Process. Extr. Metall.)*, **90**, 1981, C96-C102.
18. Frye, G.C.& Berg, J.C., Antifoam action by solid particles. *J. Colloid Interface Science.*, **127** (1), 1989, 222-238.
19. Taggart, A.F., Taylor, T.C. & Ince, C.R., Experiments with flotation reagents. *Trans. Am. Min. (Metall.),* **87**, 1930, 285-368
20. Adamson, A.W., Physical chemistry of Surfaces., 2nd Ed. Interscience, New York, 1967.
21. Neumann, A.W. & Good, R.J., Thermodynamics of Contact Angles, *J. Colloid Interface Science*, **38** (2), 1972, 341-358
22. Huh, C. & Reed, R.L., A method for estimating interfacial tensions and contact angles from sessile and pendant drop shapes, *Trans. Instn. Min. Metall. (Sect. C: Mineral Process. Extr. Metall.)*, **90** (2), 1983.
23. Allain, C., A new method for contact angle measurements of sessile drops, *J. Colloid Interface Science.*, **107**, 1985, 5-13.
24. Fort, T., A simple method for measuring solid-liquid contact angles, *J. Colloid Sci.*, **18**, 1963, 217-222.
25. Vold, R.D., Colloid and Interface chemistry, Addison-Wesley Publishing Company Inc., Massachusets, 1963, 121p.
26. Gutierrez Rodriques, J.A., Estimating the hydrophobicity of coal, *Colloids and Surfaces*, **12**, 1984, 1-25.
27. Billett, D.F., Ottewill, R.H., The dependence of contact angle on the adsorption of surface active agents, *Wetting. Soc. Chem. Ind.*, Monograph Series **25**, 1968, 253-271.
28. Hansen, J.O., Wetting of the diamond surface, Ph.D. thesis, University of Witwatersrand, 1986, 11-18.
29. Souheng, W.U., Polymer interface and adhesion, Marcel Dekker, Inc., 1982, 257p.
30. de Geddes, P.G., Wetting: Statics and Dynamics. *Rev. of Mod. Phys.*, **57** (3), 1985, 827-863.
31. Hanning, R.N. & Rutter, P.R. A simple method of determining contact angles on particles and their relevance to flotation, *Int. J. Miner. Process.*, **27**, 1989, 133-146.

32. Jiang, Z. & Holtham, P.N., Theoretical model of collision between particles and bubbles in flotation, *Trans. Instn. Min. Metall. (Sect. C: Mineral Process. Extr. Metall.)*, **95**, 1986, C187-C194.
33. Scheludko, A., Toshev, B.V. & Bojadjiev, D.T., Attachment of particles to a liquid surface (Capillary theory of flotation), *J. Chem. Soc. Faraday Trans.*, **1** (12), 2815-2828.
34. Van Dyk, W.A., The dynamic behaviour of coarse particles in flotation froths, De Beers Industrial Diamond Division Report, Diamond Research Laboratories, University of Stellenbosch, December 1993, 138p.
35. Adam, N.K., Solid surfaces, General properties, *The Physics and Chemistry of Surfaces.*, Adam, N.K. (ed), 3rd edition, Oxford University Press, 1944, 185p.
36. Laskowski, J. & Kitchener, J.A., The hydrophilic-hydrophobic transition on silica, *J. Colloid Interface Science*, **29** (4), 1969, 670-679.
37. Lamb, R.N. & Furlong, D.N., Controlled Wettability of Quartz Surfaces, *J. Chem. Soc. Faraday Trans.*, **1** (78), 1982, 61-73.
38. Blake, P. & Ralston, J., Controlled methylation of quartz particles. *Colloids and Surfaces.*, **15**, 1985, 101-118.
39. Crawford, R., Contact Angles on Particles and Plates, *Colloids and Surfaces*, **27**, 1987, 57-64.
40. Johansson, G. & Pugh, R.J., The influence of particle size and hydrophobicity on the stability of mineralized froths, *Int. J. Miner. Process*, **34**, 1992, 1-21.
41. Randall, E.W., Goodall, C.M., Fairlamb, P.M., Dold, P.L. & O'Connor, C.T., A method for measuring the sizes of bubbles in two and three-phase systems, *J. Phys. E: Sci. Instrum.*, **22**, 1989, 827-833.
42. Feng, D. & Aldrich, C., Relationship between bubble size distributions in the froth and bulk phases of flotation processes. Internal document: Department of Chemical Engineering, University of Stellenbosch, 1999.
43. The American Heritage® Concise Dictionary," *Microsoft® Encarta® 97 Encyclopedia*. The American Heritage® Concise Dictionary, Third Edition Copyright © 1994 by Houghton Mifflin Company. Electronic version licensed from and portions copyright © 1994 by INSO Corporation. All rights reserved.
44. Garrett, P.R., Understanding of foam generation and stability. *Chem. Eng. Science*, **48** (2), 1993, 367-392.
45. Malysa, K., Wet Foams: Formation, properties and mechanism of stability, *Adv. Colloid Interface Science*, **40**, 1992, 37-83

46. Ross, V.E., A mathematical model for the reverse flotation of fine diamond. DRL Report, Johannesburg, 1991.
47. Gibson, L.J., & Ashby, M.F., Cellular Solids – Structure and Properties. Pergamon Press, 1988.
48. Moys, M.H., A study of a plug-flow model for flotation froth behaviour, *Int. J. Miner. Process.*, **5**, 1978, 21-38
49. Hartland, S. & Barber, A.D., A model for a cellular foam, *Trans. Instn. Chem. Engrs*, **52**, 1974, 43-52.
50. Steiner, L., Hunkeler, R. & Hartland, S., Behaviour of dynamic cellular foams, *Trans. Instn. Chem. Engrs*, **55**, 1977, 153-163.
51. Orr, F.M. Jr, Scriven, L.E., & Rivas, A.P., Menisci in arrays of cylinders: numerical simulation by finite elements, *J. Colloid Interface Science*, **52** (3), 1975, 602-610.
52. Orr, F.M. Jr, Brown, R.A., & Scriven, L.E., Three dimensional menisci: numerical simulation by finite elements, *J Colloid Interface Science*, **60** (1), 1977, 137-147.
53. Orr, F.M. Jr, & Scriven, L.E., Menisci around plates and pins dipped in liquid: Interpretation of Wilhelmy Plate and solderability measurements, *J. Colloid Interface Science*, **60** (2), 1977, 402-405.
54. Boruvka, L. & Neumann, A.W., An analytical solution of the Laplace equation for the shape of liquid surfaces near a stripwise heterogeneous wall, *J. Colloid Interface Science*, **65** (2), 1978, 315-330.
55. Wong, H., Morris, S. & Radke, C.J., Three dimensional menisci in polygonal capillaries, *J. Colloid Interface Science*, **148** (2), 1992, 317-336.
56. Kralchevsky, P.A., Paunov, V.N., Denkov, N.D., Ivanov, I.B. & Nagayama, K., Energetical and force approaches to the capillary interactions between particles attached to a liquid-fluid interface, *J. Colloid Interface Science*, **155**, 1993, 420-437.
57. Schulze, H.J., Physico-chemical elementary processes in flotation. An analysis from the point of view of colloid science including process engineering considerations, Elsevier, New York, 1984, 185.

12. APPENDIX A: SOURCE CODE FOR LINES11.PAS

```
PROGRAM XY_VELOCITY;
{$N+}
USES crt,graph,Turbo3,fastttt,dos,winttt,keyttt,
     iottt,strngttt,menuttt,printer,parti3;
TYPE
 MATRIX=array[0..10,0..90,1..2] of Real;          {declare XY matrix size}
 MATRIX1=array[0..10,0..150,1..2] of Real;        {declare XY matrix size}
VAR
 r1,r2,r3,h1,h2,h3,l1,l2,                         {cell dimensions}
 k1,k2,k3,k4,kx,ky,                               {cell constants}
 theta,theta_crit1,theta_crit2,theta_crit3,       {angles around bends}
 x1,x2,x3,y1,y2,y3,x0,y0,                         {co-ordinates of lines}
 a,b,c,g,k,                                       {quadratic parameters}
 D1,D2,D3,                                        {length of flow area}
 x_vel,x_vel1,y_vel,theta_vel,D_vel,y_test,       {particle co-ordinates}
 x_velB,y_velB,theta_velB,
 theta_top,theta_bot,theta_dir,D_ratio,Area,      {velocity direction &}
 zj,Vel_XY,Vel_X,Vel_Y,Del_X_vel,Del_Y_vel,x_test, {magnitude}
 Ratio,RatioX,ScaleX,ScaleY,                      {draw parameters}
 X_Cor,Y_Cor,
 theta_par,G1A,G1B,v,qt,qtT,qtC2,                 {user input parameters}
 rho,sigma,mhu,db,db_int,h_int,
 del_crit,h_plate,
 eps,x_lip,aa,ab,ba,bb,A_eps,B_eps,               {air hold-up param.}
 kv,kv_1A,kv_1B,delta,                            {film thickness}
 R,xc,Beta,A_elip,B_elip,Rs,Rd,Wf,Lf,Hf,Scube,    {particle measurements}
 R_cyl,L_cyl,rho_par,eps_int,crit_mes,
 Cube_int,Flat_int,h_star,delta_h_star,           {film thinning}
 V1,V2,t_break,V_hold,delta_Pc,Q_dot,             {volume & break time}
 V_delta,tb_delta,t_fall,Vsettle,Del_Y,
 Vsettle_crit1,Vsettle_crit2,x_hou,y_hou,
 Vp,Ao,Dp,mhu_froth,rho_froth,                    {drag forces}
 Rep,CD,down_force,up_force,net_force,
 E_pos,E_fac,Fac_1A,Fac_1B,Fac_Split,             {position indicators}
 Fac_level                                        :Real;
 i,j,n,theta_deg,x_vert,M_count,N_count,          {counters}
 i_count,
 x_last,X_hold,Y_hold,j_ans,                      {holding parameters}
 MaxX,MaxY,X,Y,Radius,                            {draw parameters}
 X_Max,Y_Max,X_Min,Y_Min,color_count,
 GraphDriver,GraphMode,ErrorCode,
 main_choise,choise,error                         :Integer;
 m                                                :array[0..10] of Real;
```

```
 M1                                    :Menu_record;
 dfile                                 :text;
 file_name                             :string;
 Xasp,Yasp,Storage                     :Word;
 Image                                 :Pointer;
 XY_Cor1,XY_Cor2                       :Matrix;
 XY_Cor3                               :Matrix1;
 quit,quit1                            :Boolean;
CONST
 grav = 9.81;
 vz     = 40;                          {Vertical bubble velocity [cm/min]}
 vx     = 300;                         {Horizontal bubble velocity
[cm/min]}
 Lc     = 20;                          {Cell length [cm]}

{-------------------------------------------------------------------------------}

PROCEDURE Wait;                       {wait until keypressed}
VAR
 key : char;
BEGIN
 Sound(400);Delay(150);noSound;
 WriteCenter(25,white+blink,red,
 '************** PRESS ANY KEY TO PROCEED **************');
 Read(Kbd,key);
END;

{-------------------------------------------------------------------------------}

PROCEDURE Finish;                     {to end program}
Begin
 ClrScr;
 OnCursor;
 write('***************** END OF PROGRAM ******************');
 Halt;
End;

{-------------------------------------------------------------------------------}

PROCEDURE Title;                      {title of program}
Begin
 ClrScr;
 Offcursor;
 Speed:=1000;
 GrowFBox(10,4,70,16,white,green,2);
 WriteCenter(6,blue,green,'UNIVERSITY OF STELLENBOSCH');
```

```
 WriteCenter(7,blue,green,'DEPARTMENT: CHEMICAL ENGINEERING');
 WriteCenter(9,red,green,'PROGRAM TO DETERMINE THE DYNAMIC
BEHAVIOUR OF COARSE');
 WriteCenter(10,red,green,'PARTICLES IN THE REVERSE FROTH FLOTATION
CELL);
 WriteCenter(12,blue,green,'PROGRAMMER: W.A. VAN DYK');
 WriteCenter(14,blue,green,'DATE: OCTOBER 1998');
END;

{-------------------------------------------------------------------------------}

PROCEDURE Zero;                                    {zero all matrixes}
Begin
 D1:=0;
 D2:=0;
 D3:=0;
  FOR i:= 0 TO 10 DO
   Begin
    FOR j:= 0 TO 90 DO
     Begin
      For n:= 1 TO 2 DO
       Begin
        XY_Cor1[i,j,n]:=0;
        XY_Cor2[i,j,n]:=0;
        m[i]:=0;
       End;
     End;
   End;
  FOR i:= 0 TO 10 DO
   Begin
    FOR j:= 0 TO 150 DO
     Begin
      For n:= 1 TO 2 DO
       Begin
        XY_Cor3[i,j,n]:=0;
       End;
     End;
   End;
End;

{-------------------------------------------------------------------------------}

PROCEDURE Input;                                   {input of cell parameters}
var
 S1,S2,S3,S4,S5,S6,S7,S8,S9,S10,S11,S12,S13,S14    :string;
 retcode                                :integer;
```

```
Begin
 Box(6,1,76,21,white,black,2);
 Horizline(7,75,5,white,black,1);
 Offcursor;
 WriteCenter(3,yellow,black,'Provide the following information');
 WriteAT(9,7,white,black,'Weir radius #1');
 WriteAT(43,7,white,black,'Weir AB radius');
 WriteAT(9,9,white,black,'Weir BM radius');
 WriteAT(43,9,white,black,'Weir AB depth');
 WriteAT(9,11,white,black,'Weir BM depth');
 WriteAT(43,11,white,black,'Froth overflow height');
 WriteAT(9,13,white,black,'Comp. A width');
 WriteAT(43,13,white,black,'Comp. B width');
 WriteAt(9,15,white,black,'Splitter plate');
 WriteAt(43,15,white,black,'Value of Y0');
 WriteAt(9,17,white,black,'A coefficient');
 WriteAt(43,17,white,black,'A constant');
 WriteAt(9,19,white,black,'B coefficient');
 WriteAt(43,19,white,black,'B constant');
  S1:='90';
  S2:='55';
  S3:='35';
  S4:='40';
  S5:='65';
  S6:='5';
  S7:='150';
  S8:='150';
  S9:='41';
  S10:='0';
  S11:='0.268399';
  S12:='-0.046925';
  S13:='1.019322';
  S14:='0.198198';
   IO_Setfields(14);
   IO_Soundbeeper(true);
   IO_Allowesc(true);
    IO_DefineStr(1,14,2,14,2,29,7,S1,'###');
    IO_DefineStr(2,1,3,1,3,65,7,S2,'###');
    IO_DefineStr(3,2,4,2,4,29,9,S3,'###');
    IO_DefineStr(4,3,5,3,5,65,9,S4,'###');
    IO_DefineStr(5,4,6,4,6,29,11,S5,'###');
    IO_DefineStr(6,5,7,5,7,65,11,S6,'###');
    IO_DefineStr(7,6,8,6,8,29,13,S7,'###');
    IO_DefineStr(8,7,9,7,9,65,13,S8,'###');
    IO_DefineStr(9,8,10,8,10,29,15,S9,'####');
    IO_DefineStr(10,9,11,9,11,65,15,S10,'####');
```

```
    IO_DefineStr(11,10,12,10,12,29,17,S11,'########');
    IO_DefineStr(12,11,13,11,13,65,17,S12,'########');
    IO_DefineStr(13,12,14,12,14,29,19,S13,'########');
    IO_DefineStr(14,13,1,13,1,65,19,S14,'########');
   IO_DefineMsg(1,12,21,' Enter the radius of the cell wall of sub-compartment A
[mm] ');
   IO_DefineMsg(2,15,21,' Enter the radius of the weir AB [mm] ');
   IO_DefineMsg(3,15,21,' Enter the radius of the weir BM [mm] ');
   IO_DefineMsg(4,18,21,' Enter the depth from cell top to weir AB [mm] ');
   IO_DefineMsg(5,18,21,' Enter the depth from cell top to weir BM [mm] ');
   IO_DefineMsg(6,14,21,' Enter the depth from cell top to froth overflow [mm] ');
   IO_DefineMsg(7,23,21,' Enter width of sub-compartment A [mm] ');
   IO_DefineMsg(8,23,21,' Enter width of sub-compartment B [mm] ');
   IO_DefineMsg(9,16,21,' Enter height from cell top of splitter plate [mm] ');
   IO_DefineMsg(10,23,21,' Enter Y-position of steamlines [mm] ');
   IO_DefineMsg(11,19,21,' Enter the value of the hold-up A coefficient ');
   IO_DefineMsg(12,21,21,' Enter the value of the hold-up A constant ');
   IO_DefineMsg(13,19,21,' Enter the value of the hold-up B coefficient ');
   IO_DefineMsg(14,21,21,' Enter the value of the hold-up B constant ');
  Oncursor;
  IO_Edit(Retcode);
  IO_ResetFields;
   r1:=str_to_real(S1);
   r2:=str_to_real(S2);
   r3:=str_to_real(S3);
   h1:=str_to_real(S4);
   h2:=str_to_real(S5);
   h3:=str_to_real(S6);
   l1:=str_to_real(S7);
   l2:=str_to_real(S8);
   H_plate:=str_to_real(S9);
   y0:=str_to_real(S10);
   x0:=(r2-y0)*(-h3/(l1+l2-r1));
   aa:=str_to_real(S11);
   ab:=str_to_real(S12);
   ba:=str_to_real(S13);
   bb:=str_to_real(S14);
 End;

{-------------------------------------------------------------------------------}

PROCEDURE Define_Menu1;                    {The particle shape selection menu}
Begin
 With M1 do
  Begin
  Offcursor;
```

```
  Heading1:='Choise of Particle Shape';
  Heading2:='[Volumes of Revolution]';
  Topic[1]:='   Rod';
  Topic[2]:='   Cone';
  Topic[3]:='   Disc';
  Topic[4]:='   Ellipsoid';
  Topic[5]:='   Sphere';
  Topic[6]:='   Cube';
  Topic[7]:='   Flat';
  Topic[8]:='   Quit to DOS';
  TotalPicks:=8;
  PicksPerLine:=1;
  Addprefix:=1;
  TopleftXY[1]:=0;
  TopleftXY[2]:=5;
  Boxtype:=5;
   IF BaseOfScreen = $B800 THEN
    Begin
     Colors[1] := white;          {hi foreground}
     Colors[2] := red;           {hi background}
     Colors[3] := lightgray;      {lo foreground}
     Colors[4] := blue;          {lo background}
     Colors[5] := lightcyan;      {box colour}
    End
   ELSE
    Begin
     Colors[1] := white;          {hi foreground}
     Colors[2] := black;          {hi background}
     Colors[3] := black;          {lo foreground}
     Colors[4] := lightgray;      {lo background}
     Colors[5] := white;          {box colour}
    End;
  AllowEsc := false;           {inactivate the escape key}
  Margins := 5;
 End;
End;

{-------------------------------------------------------------------------------}

PROCEDURE Input_general;                    {Enter experimental conditions}
var
 S1,S2,S3,S4,S5,S6,S7,S8,S9,S10,S11,S12,S13,S14   :string;
 retcode                                  :integer;
  Begin
   ClrScr;
   Box(6,1,76,22,white,black,2);
```

```
Horizline(7,75,5,white,black,1);
Offcursor;
WriteCenter(3,white,black,'Provide the following information');
WriteAT(9,7,white,black,'Aeration rate A');
WriteAT(44,7,white,black,'Aeration rate B');
WriteAT(9,9,white,black,'Water flowrate T');
WriteAT(44,9,white,black,'Water flowrate M');
WriteAT(9,11,white,black,'Surface tension');
WriteAT(44,11,white,black,'Viscosity');
WriteAt(9,13,white,black,'Density');
WriteAT(44,13,white,black,'Bubble diameter');
WriteAT(9,15,white,black,'Contact Angle');
WriteAT(44,15,white,black,'Interface height');
WriteAT(9,17,white,black,'Integration steps');
WriteAT(44,17,white,black,'Integration steps');
WriteAT(9,19,white,black,'Critical thickness');
WriteAT(44,19,white,black,'Particle insert');
 S1:='23.81';
 S2:='18.39';
 S3:='17.69';
 S4:='20.60';
 S5:='0.063650';
 S6:='0.001026';
 S7:='1000';
 S8:='1.00765';
 S9:='96.0';
 S10:='0.485';
 S11:='1500';
 S12:='50';
 S13:='10';
 S14:='1';
  IO_Setfields(14);
  IO_Soundbeeper(true);
  IO_Allowesc(true);
   IO_DefineStr(1,14,2,14,2,29,7,S1,'#####');
   IO_DefineStr(2,1,3,1,3,64,7,S2,'#####');
   IO_DefineStr(3,2,4,2,4,29,9,S3,'#####');
   IO_DefineStr(4,3,5,3,5,64,9,S4,'#####');
   IO_DefineStr(5,4,6,4,6,29,11,S5,'########');
   IO_DefineStr(6,5,7,5,7,64,11,S6,'########');
   IO_DefineStr(7,6,8,6,8,29,13,S7,'####');
   IO_DefineStr(8,7,9,7,9,64,13,S8,'#######');
   IO_DefineStr(9,8,10,8,10,29,15,S9,'#####');
   IO_DefineStr(10,9,11,9,11,64,15,S10,'#####');
   IO_DefineStr(11,10,12,10,12,29,17,S11,'####');
   IO_DefineStr(12,11,13,11,13,64,17,S12,'####');
```

```
    IO_DefineStr(13,12,14,12,13,29,19,S13,'###');
    IO_DefineStr(14,13,1,13,1,64,19,S14,'###');
   IO_DefineMsg(1,16,22,' Enter the aeration rate in sub-compartment A [l/min] ');
   IO_DefineMsg(2,16,22,' Enter the aeration rate in sub-compartment B [l/min] ');
   IO_DefineMsg(3,16,22,' Enter the water flowrate to the tailings [cm^3/s] ');
   IO_DefineMsg(4,16,22,' Enter the water flowrate to middlings [cm^3/s] ');
   IO_DefineMsg(5,26,22,' Enter the surface tension [N/m] ');
   IO_DefineMsg(6,25,22,' Enter the liquid viscosity [Pa.s] ');
   IO_DefineMsg(7,25,22,' Enter the liquid density [kg/m^3] ');
   IO_DefineMsg(8,14,22,' Enter the bubble diameter at the froth interface [mm] ');
   IO_DefineMsg(9,22,22,' Enter the equilibrium contact angle [ø] ');
   IO_DefineMsg(10,19,22,' Enter the height of the froth interface [m] ');
   IO_DefineMsg(11,19,22,' Enter the number of integration steps for h* ');
   IO_DefineMsg(12,16,22,' Enter the number of integration steps for (V1+V2) ');
   IO_DefineMsg(13,21,22,' Enter the critical film thickness [æm] ');
   IO_DefineMsg(14,10,22,' Enter distance from cell lip where particle was inserted
[mm]');
  Oncursor;
  IO_Edit(Retcode);
  IO_ResetFields;
   G1A:=str_to_real(S1);
   G1B:=str_to_real(S2);
   qtT:=str_to_real(S3);
   qtC2:=str_to_real(S4);
   sigma:=str_to_real(S5);
   mhu:=str_to_real(S6);
   rho:=str_to_real(S7);
   db_int:=str_to_real(S8);
   db_int:=db_int/1000;
   theta_par:=str_to_real(S9);
   theta_par:=2*pi*theta_par/360;
   h_int:=str_to_real(S10);
   N_count:=str_to_int(S11);
   M_count:=str_to_int(S12);
   del_crit:=str_to_real(S13);
   x_vel1:=str_to_real(S14);
 Main_Choise:=1;
 Define_Menu1;
End;

{-------------------------------------------------------------------------------}

PROCEDURE Kv_input;                          {Enter velocity coefficients}
Var
 S1,S2        :string;
 retcode      :integer;
```

```
Begin
ClrScr;
 Box(14,3,64,18,white,black,2);
 Horizline(15,63,7,white,black,1);
 WriteCenter(5,white,black,'Please provide the following information');
 WriteAt(18,10,white,black,'Enter the kv value for sub-compartment A');
 WriteAt(18,12,white,black,'Enter the kv value for sub-compartment B');
 S1:='5.00';
 S2:='20.0';
 IO_setfields(2);
 IO_soundbeeper(true);
 IO_allowesc(true);
 IO_DefineStr(1,2,2,2,2,58,10,S1,'####');
 IO_DefineStr(2,1,1,1,1,58,12,S2,'####');
 IO_DefineMsg(1,23,18,' *** Press "END" to continue *** ');
 IO_DefineMsg(2,26,18,' *** Press "END" to continue *** ');
 OnCursor;
 IO_Edit(Retcode);
 Offcursor;
 IO_Resetfields;
 kv_1A:=Str_to_real(S1);
 kv_1B:=Str_to_real(S2);
End;

{-------------------------------------------------------------------------------}

FUNCTION tan(theta  :Real)      :Real;          {to compute the tan of theta}
Begin
 tan:=sin(theta)/cos(theta);
End;

{-------------------------------------------------------------------------------}

PROCEDURE Rod_dim;                          {Input dimensions of Rod particle}
Var
 S1,S2,S3     :string;
 retcode      :integer;
Begin
 ClrScr;
 Box(14,3,64,18,white,black,2);
 Horizline(15,63,7,white,black,1);
 WriteCenter(5,white,black,'Please provide the following information');
 WriteAt(20,10,white,black,'Enter the Rod radius (R) in [mm]');
 WriteAt(20,12,white,black,'Enter the Rod Length (L) in [mm]');
 WriteAt(20,14,white,black,'Enter the particle density [kg/m^3]');
 S1:='1.04';
```

```
 S2:='3.38';
 S3:='2000';
 IO_setfields(3);
 IO_soundbeeper(false);
 IO_allowesc(true);
 IO_DefineStr(1,3,2,3,2,56,10,S1,'######');
 IO_DefineStr(2,1,3,1,3,56,12,S2,'######');
 IO_DefineStr(3,2,1,2,1,56,14,S3,'####');
 IO_DefineMsg(1,22,18,' *** Press "END" to continue *** ');
 IO_DefineMsg(2,22,18,' *** Press "END" to continue *** ');
 IO_DefineMsg(3,22,18,' *** Press "END" to continue *** ');
 OnCursor;
 IO_Edit(Retcode);
 Offcursor;
 IO_Resetfields;
 R:=Str_to_real(S1);
 R_cyl:=Str_to_real(S1);
 L_cyl:=Str_to_real(S2);
 rho_par:=Str_to_real(S3);
 R:=R*1000;
 crit_mes:=L_cyl*1000;
 Force_Rod(R_cyl,L_cyl,Ao,Vp,Dp);
End;

{-------------------------------------------------------------------------------}

PROCEDURE Cone_dim;                    {Enter dimensions of conical particle}
Var
 S1,S2,S3       :string;
 retcode        :integer;
Begin
ClrScr;
 Box(14,3,64,18,white,black,2);
 Horizline(15,63,7,white,black,1);
 WriteCenter(5,white,black,'Please provide the following information');
 WriteAt(19,10,white,black,'Enter the cone radius (xc) in [mm]');
 WriteAt(19,12,white,black,'Enter the cone angle (á) in [ø]');
 WriteAt(19,14,white,black,'Enter the particle density [kg/m^3]');
 S1:='  1';
 S2:='45';
 S3:='3000';
 IO_setfields(3);
 IO_soundbeeper(false);
 IO_allowesc(true);
 IO_DefineStr(1,3,2,3,2,56,10,S1,'######');
 IO_DefineStr(2,1,3,1,3,56,12,S2,'##');
```

```
 IO_DefineStr(3,2,1,2,1,56,14,S3,'####');
 IO_DefineMsg(1,23,18,' *** Press "END" to continue *** ');
 IO_DefineMsg(2,26,18,' Enter angle smaller than 90ø');
 IO_DefineMsg(3,23,18,' *** Press "END" to continue *** ');
 OnCursor;
 IO_Edit(Retcode);
 Offcursor;
 IO_Resetfields;
 xc:=Str_to_real(S1);
 xc:=xc*1000;
 Beta:=Str_to_real(S2);
 Beta:=Beta*pi/180;
 rho_par:=Str_to_real(S3);
 crit_mes:=2*xc*tan(Beta);
 Force_Cone(xc,Beta,Ao,Vp,Dp);
End;

{-------------------------------------------------------------------------------}

PROCEDURE Disk_dim;                    {Enter dimension of disc particle}
Var
 S1,S2,S3       :string;
 retcode        :integer;
Begin
ClrScr;
 Box(14,3,64,18,white,black,2);
 Horizline(15,63,7,white,black,1);
 WriteCenter(5,white,black,'Please provide the following information');
 WriteAt(16,10,white,black,'Enter the disc end-radius (Rs) in [mm]');
 WriteAt(16,12,white,black,'Enter the disc width-radius (Rd) in [mm]');
 WriteAt(16,14,white,black,'Enter the particle density [kg/m^3]');
 S1:='0.5';
 S2:='1';
 S3:='3000';
 IO_setfields(3);
 IO_soundbeeper(false);
 IO_allowesc(true);
 IO_DefineStr(1,3,2,3,2,57,10,S1,'######');
 IO_DefineStr(2,1,3,1,3,57,12,S2,'######');
 IO_DefineStr(3,2,1,2,1,57,14,S3,'####');
 IO_DefineMsg(1,23,18,' *** Press "END" to continue *** ');
 IO_DefineMsg(2,23,18,' *** Press "END" to continue *** ');
 IO_DefineMsg(3,23,18,' *** Press "END" to continue *** ');
 OnCursor;
 IO_Edit(Retcode);
 Offcursor;
```

```
 IO_Resetfields;
 Rs:=Str_to_real(S1);
 Rs:=Rs*1000;
 Rd:=Str_to_real(S2);
 Rd:=Rd*1000;
 rho_par:=Str_to_real(S3);
 crit_mes:=2*Rs;
 Force_Disc(Rs,Rd,Ao,Vp,Dp);
End;

{-------------------------------------------------------------------------------------------------------}

PROCEDURE Elipsoid_dim;                    {Enter dimensions of ellipsoidal part}
Var
 S1,S2,S3        :string;
 retcode         :integer;
Begin
ClrScr;
 Box(14,3,64,18,white,black,2);
 Horizline(15,63,7,white,black,1);
 WriteCenter(5,white,black,'Please provide the following information');
 WriteAt(16,10,white,black,'Enter the ellipsoid x-radius (a) in [mm]');
 WriteAt(16,12,white,black,'Enter the ellipsoid y-radius (b) in [mm]');
 WriteAt(16,14,white,black,'Enter the particle density [kg/m^3]');
 S1:='0.5';
 S2:='1.0';
 S3:='3000';
 IO_setfields(3);
 IO_soundbeeper(false);
 IO_allowesc(true);
 IO_DefineStr(1,3,2,3,2,57,10,S1,'######');
 IO_DefineStr(2,1,3,1,3,57,12,S2,'######');
 IO_DefineStr(3,2,1,2,1,57,14,S3,'####');
 IO_DefineMsg(1,23,18,' *** Press "END" to continue *** ');
 IO_DefineMsg(2,23,18,' *** Press "END" to continue *** ');
 IO_DefineMsg(3,23,18,' *** Press "END" to continue *** ');
 OnCursor;
 IO_Edit(Retcode);
 Offcursor;
 IO_Resetfields;
 A_elip:=Str_to_real(S1);
 A_elip:=A_elip*1000;
 B_elip:=Str_to_real(S2);
 B_elip:=B_elip*1000;
 rho_par:=Str_to_real(S3);
 crit_mes:=2*B_elip;
```

```
 Force_Elip(A_elip,B_elip,Ao,Vp,Dp);
End;

{-------------------------------------------------------------------------------------------------}

PROCEDURE Sphere_dim;                    {Enter dimension of spherical particle}
Var
 S1,S2       :string;
 retcode     :integer;
Begin
ClrScr;
 Box(14,3,64,18,white,black,2);
 Horizline(15,63,7,white,black,1);
 WriteCenter(5,white,black,'Please provide the following information');
 WriteAt(20,10,white,black,'Enter the sphere radius (R) in [mm]');
 WriteAt(20,12,white,black,'Enter the particle density [kg/m^3]');
 S1:='0.75';
 S2:='2300';
 IO_setfields(2);
 IO_soundbeeper(false);
 IO_allowesc(true);
 IO_DefineStr(1,2,2,2,2,56,10,S1,'######');
 IO_DefineStr(2,1,1,1,1,56,12,S2,'####');
 IO_DefineMsg(1,22,18,' *** Press "END" to continue *** ');
 IO_DefineMsg(2,22,18,' *** Press "END" to continue *** ');
 OnCursor;
 IO_Edit(Retcode);
 Offcursor;
 IO_Resetfields;
 R:=Str_to_real(S1);
 R:=R*1000;
 rho_par:=Str_to_real(S2);
 crit_mes:=2*R;
 Force_Sphere(R,Ao,Vp,Dp);
End;

{-------------------------------------------------------------------------------------------------}

PROCEDURE Cube_dim;                      {Enter dimensions of cubic particle}
Var
 S1,S2,S3     :string;
 retcode      :integer;
Begin
ClrScr;
 Box(14,3,67,18,white,black,2);
 Horizline(15,66,7,white,black,1);
```

```
 WriteCenter(5,white,black,'Please provide the following information');
 WriteAt(16,10,white,black,'Enter the cube side length (Scube) in [mm]');
 WriteAt(16,12,white,black,'Enter the number of cube side increments');
 WriteAt(16,14,white,black,'Enter the particle density [kg/m^3]');
 S1:='1.0';
 S2:='100';
 S3:='3000';
 IO_setfields(3);
 IO_soundbeeper(false);
 IO_allowesc(true);
 IO_DefineStr(1,3,2,3,2,59,10,S1,'######');
 IO_DefineStr(2,1,3,1,3,59,12,S2,'######');
 IO_DefineStr(3,2,1,2,1,59,14,S3,'####');
 IO_DefineMsg(1,24,18,' *** Press "END" to continue *** ');
 IO_DefineMsg(2,27,18,' *** Only even numbers ***');
 IO_DefineMsg(3,24,18,' *** Press "END" to continue *** ');
 OnCursor;
 IO_Edit(Retcode);
 Offcursor;
 IO_Resetfields;
 Scube:=Str_to_real(S1);
 Cube_int:=Str_to_real(S2);
 rho_par:=Str_to_real(S3);
 crit_mes:=Scube*1000;
 Force_Cube(Scube,Ao,Vp,Dp);
End;

{-----------------------------------------------------------------------------------------------------------}

PROCEDURE Flat_dim;                          {Enter dimensions of flat particle}
Var
 S1,S2,S3,S4,S5   :string;
 retcode          :integer;
Begin
ClrScr;
 Box(14,3,64,20,white,black,2);
 Horizline(15,63,7,white,black,1);
 WriteCenter(5,white,black,'Please provide the following information');
 WriteAt(17,10,white,black,'Enter the flat length (Lf) in [mm]');
 WriteAt(17,12,white,black,'Enter the flat width (Wf) in [mm]');
 WriteAt(17,14,white,black,'Enter the flat height (Hf) in [mm]');
 WriteAt(17,16,white,black,'Enter the flat side increments ');
 WriteAt(17,18,white,black,'Enter the particle density [kg/m^3]');
 S1:='1.0';
 S2:='1.0';
 S3:='0.5';
```

```
 S4:='100';
 S5:='3000';
 IO_setfields(5);
 IO_soundbeeper(false);
 IO_allowesc(true);
 IO_DefineStr(1,5,2,5,2,56,10,S1,'######');
 IO_DefineStr(2,1,3,1,3,56,12,S2,'######');
 IO_DefineStr(3,2,4,2,4,56,14,S3,'######');
 IO_DefineStr(4,3,5,3,5,56,16,S4,'####');
 IO_DefineStr(5,4,1,4,1,56,18,S5,'####');
 IO_DefineMsg(1,23,20,' *** Press "END" to continue *** ');
 IO_DefineMsg(2,23,20,' *** Press "END" to continue *** ');
 IO_DefineMsg(3,23,20,' *** Press "END" to continue *** ');
 IO_DefineMsg(4,22,20,' *** Enter only even numbers *** ');
 IO_DefineMsg(5,23,20,' *** Press "END" to continue *** ');
 OnCursor;
 IO_Edit(Retcode);
 Offcursor;
 IO_Resetfields;
 Lf:=Str_to_real(S1);
 Wf:=Str_to_real(S2);
 Hf:=Str_to_real(S3);
 Flat_int:=Str_to_real(S4);
 rho_par:=Str_to_real(S5);
 crit_mes:=Hf*1000;
 Force_Flat(Lf,Wf,Hf,Ao,Vp,Dp);
End;

{-------------------------------------------------------------------------------}

PROCEDURE Input_dimensions;          {Request respective input dimensions}
Begin
ClrScr;
 Case Main_Choise of
 1 :Rod_dim;
 2 :Cone_dim;
 3 :disk_dim;
 4 :elipsoid_dim;
 5 :sphere_dim;
 6 :cube_dim;
 7 :flat_dim;
 8 :Finish;
 End;
End;

{-------------------------------------------------------------------------------}
```

```
PROCEDURE Constants;                    {calculate constants used}
Begin                                   {in all calculations}
 k1:=r3+h2-r1;
 k2:=r3+h2-h1-r2;
 k3:=l1+l2+r3-r1;
 k4:=l2+r3-r2;
End;

{-------------------------------------------------------------------------------}

FUNCTION Quadmin(a,b,c :Real) :Real;    {to solve quadratic equations}
var                                     {and return the minimum value}
 xa,xb   :Real;
  Begin
   xa:= (-b+sqrt(sqr(b)-4*a*c))/(2*a);
   xb:= (-b-sqrt(sqr(b)-4*a*c))/(2*a);
    IF xa < xb THEN
     Quadmin:= xa
    ELSE
     Quadmin:= xb;
  End;

{-------------------------------------------------------------------------------}

FUNCTION Quadmax(a,b,c :Real) :Real;    {to solve quadratic equations}
var                                     {and return the maximum value}
 xa,xb   :Real;
  Begin
   xa:= (-b+sqrt(sqr(b)-4*a*c))/(2*a);
   xb:= (-b-sqrt(sqr(b)-4*a*c))/(2*a);
    IF xa > xb THEN
     Quadmax:= xa
    ELSE
     Quadmax:= xb;
  End;

{-------------------------------------------------------------------------------}

PROCEDURE Cor_store1;                   {store x & y coordinates}
Begin                                   {of Froth Area #1}
 D1:=sqrt(sqr(y1-y2)+sqr(x1-x2));
  FOR i:= 0 TO 10 DO
   Begin
    m[i]:=(i/10)*D1;
    XY_Cor1[i,j,1]:=-(m[i]+sqrt(sqr(x2)+sqr(y2)))*cos(theta); {x-coordinate}
```

```
   XY_Cor1[i,j,2]:=(m[i]+sqrt(sqr(x2)+sqr(y2)))*sin(theta);  {y-coordinate}
  End;
End;

{-------------------------------------------------------------------------------}

PROCEDURE Cor_store2;                          {store x & y coordinates}
Begin                                          {of Froth Area #2}
 D2:=sqrt(sqr(y2-y3)+sqr(x2-x3));
  FOR i:= 0 TO 10 DO
   Begin
    m[i]:=(i/10)*D2;
    XY_Cor2[i,j,1]:=-(m[i]+r3)*cos(theta);    {x-coordinate}
    XY_Cor2[i,j,2]:=(m[i]+r3)*sin(theta);     {y-coordinate}
   End;
End;

{-------------------------------------------------------------------------------}

PROCEDURE Cor_store3;                          {store x & y coordinates}
Begin                                          {of Froth Area #3}
 D3:=sqrt(sqr(y1-y2)+sqr(x1-x2));
  FOR i:= 0 TO 10 DO
   Begin
    m[i]:=(i/10)*D3;
    XY_Cor3[i,j,1]:=x_vert;                    {x-coordinate}
    XY_Cor3[i,j,2]:=(m[i] + y2);               {y-coordinate}
   End;
End;

{-------------------------------------------------------------------------------}

PROCEDURE Lines_Comp1;                         {Compute coordinates of}
Begin                                          {streamlines in}
 kx:=k4-x0;                                    {Froth Area #1}
 ky:=k2+y0;
  theta_crit1:=Arctan((k1-ky)/(l1+l2+r3-kx));
  theta_crit2:=Arctan((r1+k1-ky)/(k3-kx));
  IF x0 = 0 THEN
  theta_crit3:= pi/2
  ELSE
  theta_crit3:=Arctan((r2-y0)/x0);
  IF theta_crit3 < 0 THEN
   Begin
    theta_crit3:=pi+theta_crit3;
   End;
```

```
FOR theta_deg:= 0 TO 90 DO                    {start of calculation}
 Begin
 j:=theta_deg;
 theta:=theta_deg*pi/180;
  IF theta < theta_crit1 THEN
   Begin
    x1:=kx-l1-l2-r3;
    y1:=-(tan(theta))*x1;
     a:=(1+sqr(tan(theta)));
     b:=2*x0-2*y0*tan(theta);
     c:=sqr(x0)+sqr(y0)-sqr(r2);
     x2:=Quadmin(a,b,c);
     y2:=-(tan(theta))*x2;
      Cor_store1;
   End;
  IF (theta >= theta_crit1) AND (theta <= theta_crit2) THEN
   Begin
    a:=(1+sqr(tan(theta)));
    b:=(2*tan(theta)*(k1-ky)-2*(kx-k3));
    c:=(sqr(kx-k3)+sqr(k1-ky)-sqr(r1));
    x1:=Quadmin(a,b,c);
    y1:=-tan(theta)*x1;
     a:=(1+sqr(tan(theta)));
     b:=2*x0-2*y0*tan(theta);
     c:=sqr(x0)+sqr(y0)-sqr(r2);
     x2:=Quadmin(a,b,c);
     y2:=-(tan(theta))*x2;
      Cor_store1;
   End;
  IF (theta > theta_crit2) AND (theta < theta_crit3) THEN
   Begin
    g:=(x0/(r2-y0));
    k:=(r1+k1-ky-(x0/(r2-y0)*(kx-k3)));
    x1:=-k/(tan(theta)+g);
    y1:=-(tan(theta))*x1;
     a:=(1+sqr(tan(theta)));
     b:=2*x0-2*y0*tan(theta);
     c:=sqr(x0)+sqr(y0)-sqr(r2);
     x2:=Quadmin(a,b,c);
     y2:=-(tan(theta))*x2;
      Cor_store1;
   End;
  IF (theta > theta_crit3) AND (theta_crit3 < pi/2) THEN
   Begin
    g:=(x0/(r2-y0));
    k:=(r1+k1-ky-(x0/(r2-y0)*(kx-k3)));
```

```
        x1:=-k/(tan(theta)+g);
        y1:=-(tan(theta))*x1;
         k:=(r2-y0+sqr(x0)/(r2-y0));
        x2:=-k/(tan(theta)+g);
        y2:=-(tan(theta))*x2;
         Cor_store1;
       End;
    End;
End;

{-------------------------------------------------------------------------------------------------}

PROCEDURE Lines_Comp2;                          {Compute coordinates of}
Begin                                           {streamlines of}
 IF k2 > 0 THEN                                 {Froth Area #2}
  Begin
   theta_crit1:= Arctan(k2/(l2+r3));
  End
 ELSE
  Begin
   theta_crit1:=0;
  End;
 theta_crit2:=Arctan((r2+k2)/k4);
  FOR theta_deg:= 0 TO 90 DO                    {start of calculation}
   Begin
   j:=theta_deg;
   theta:=theta_deg*pi/180;
    IF theta < theta_crit1 THEN
     Begin
      x2:=-(l2+r3);
      y2:=-(tan(theta))*x2;
       x3:=-r3*cos(theta);
       y3:=r3*sin(theta);
        Cor_store2;
     End;
    IF (theta >= theta_crit1) AND (theta <= theta_crit2) THEN
     Begin
      a:=(1+sqr(tan(theta)));
      b:=(2*k4+2*k2*(tan(theta)));
      c:=(sqr(k2)+sqr(k4)-sqr(r2));
      x2:=Quadmin(a,b,c);
      y2:=-(tan(theta))*x2;
       x3:=-r3*cos(theta);
       y3:=r3*sin(theta);
        Cor_store2;
     End;
```

```
   IF theta > theta_crit2 THEN
    Begin
     g:=(x0/(r2-y0));
     k:=r2-y0+sqr(x0)/(r2-y0)+ky+kx*x0/(r2-y0);
     x2:=-k/(tan(theta)+g);
     y2:=-(tan(theta))*x2;
      x3:=-r3*cos(theta);
      y3:=r3*sin(theta);
       Cor_store2;
    End;
  End;
End;

{-------------------------------------------------------------------------------}

PROCEDURE Lines_Comp3;                    {Computes coordinates of}
Begin                                     {streamlines in Froth Area #3}
 x_last:=0;
 IF x0 < 0 THEN
  Begin
   FOR x_vert:= 0 TO Trunc(-x0) DO
    Begin
     j:=x_vert;
      g:=(x0/(r2-y0));
      k:=(r1+k1-ky-(x0/(r2-y0)*(kx-k3)));
      x1:=x_vert;
      y1:=g*x1+k;
       a:=1;
       b:=-2*y0;
       c:=(sqr(y0)-sqr(r2)+sqr(x_vert+x0));
       y2:=Quadmax(a,b,c);
       x2:=x_vert;
        Cor_store3;
    End;
   x_last:=x_vert;
  End;
 FOR x_vert:= x_last TO Trunc(l2-r2-x0) DO
  Begin
   j:=x_vert;
    g:=(x0/(r2-y0));
    k:=(r1+k1-ky-(x0/(r2-y0)*(kx-k3)));
    x1:=x_vert;
    y1:=g*x1+k;
     k:=(r2-y0+sqr(x0)/(r2-y0));
     x2:=x_vert;
     y2:=g*x2+k;
```

```
    Cor_store3;
  End;
End;

{-------------------------------------------------------------------------------}

PROCEDURE Scale;                          {Scale {x0,y0} to {0,0} co-ordinates}
Begin
 FOR i:= 0 TO 10 DO
  Begin
   FOR j:= 0 TO 90 DO
    Begin
     XY_Cor1[i,j,1]:=XY_Cor1[i,j,1]-kx;
     XY_Cor1[i,j,2]:=XY_Cor1[i,j,2]+ky;
    End;
  End;
 FOR i:= 0 TO 10 DO
  Begin
   FOR j:= 0 TO 150 DO
    Begin
     XY_Cor3[i,j,1]:=XY_Cor3[i,j,1]-kx;
     XY_Cor3[i,j,2]:=XY_Cor3[i,j,2]+ky;
    End;
  End;
End;

{-------------------------------------------------------------------------------}

FUNCTION X_Calc(X_Cor :Real) :Integer;    {Calculates x co-ordinates for}
Begin                                     {screen display}
 X_Calc:=Trunc(RatioX*(ScaleX+X_Cor));
End;

{-------------------------------------------------------------------------------}

FUNCTION Y_Calc(Y_Cor :Real) :Integer;    {Calculates y co-ordinates for}
Begin                                     {screen display}
 Y_Calc:=Trunc(MaxY-Ratio*RatioX*(ScaleY+Y_Cor));
End;

{-------------------------------------------------------------------------------}

PROCEDURE Cell;                           {Plots the cell outline on the screen}
Begin
 SetColor(1);
 X:=X_Calc(0);
```

```
 Y:=Y_Calc(0);
 X_Max:=X;
  Radius:=Trunc(r3*RatioX);
  Y_Max:=Y+Radius;
  Arc(X,Y,90,180,Radius);
  Line(X-Radius,Y,X-Radius,MaxY);
  X_hold:=X;
   X:=X_Calc(-k4);
   Y:=Y_Calc(k2);
   Radius:=Trunc(r2*RatioX);
   Arc(X,Y,90,180,Radius);
   Line(X-Radius,Y,X-Radius,MaxY);
    X:=X_Calc(-k3);
    Y:=Y_Calc(k1);
    Radius:=Trunc(r1*RatioX);
    Arc(X,Y,90,180,Radius);
    Line(X-Radius,Y,X-Radius,MaxY);
    Line(X,Y-Radius,X_hold,Y-Radius);
    X_Min:=X-Radius;
    Y_Min:=Y-Radius;
End;

{-------------------------------------------------------------------------------------------------------}

PROCEDURE Drawlines;                    {Plots the flow profiles on the screen}
Begin
 Graphdriver := Detect;
 Initgraph(GraphDriver,GraphMode, 'C:\BP\BGI');
 ErrorCode:= GraphResult;
 SetBkColor(15);
 IF ErrorCode <> grOK THEN
  Begin
   DirectVideo := False;
   WriteLn('Graphics error: ',GraphErrorMsg(ErrorCode));
   Halt;
  End;
 GetAspectRatio(Xasp,Yasp);
  Ratio:=Yasp/Xasp;
   MaxX:=GetMaxX;
   MaxY:=GetMaxY;
 ScaleX:=1.3*l1+l2+r3;
 ScaleY:=1.5*r1;
RatioX:=MaxX/(2*l1+l2+r3);
 Cell;
  SetColor(1);
  FOR i:= 0 TO 10 DO
```

```
    Begin
     X:=X_Calc(XY_Cor1[i,0,1]);
     Y:=Y_Calc(XY_Cor1[i,0,2]);
     MoveTo(X,Y);
      FOR j:= 0 TO 89 DO
       Begin
        X:=X_Calc(XY_Cor1[i,j,1]);
        Y:=Y_Calc(XY_Cor1[i,j,2]);
        LineTo(X,Y);
       End;
    End;
   SetColor(1);
   FOR i:= 0 TO 10 DO
    Begin
     X:=X_Calc(XY_Cor2[i,0,1]);
     Y:=Y_Calc(XY_Cor2[i,0,2]);
     MoveTo(X,Y);
      FOR j:= 0 TO 90 DO
       Begin
        X:=X_Calc(XY_Cor2[i,j,1]);
        Y:=Y_Calc(XY_Cor2[i,j,2]);
        LineTo(X,Y);
       End;
    End;
   SetColor(1);
   FOR i:= 0 TO 10 DO
    Begin
     X:=X_Calc(XY_Cor3[i,0,1]);
     Y:=Y_Calc(XY_Cor3[i,0,2]);
     MoveTo(X,Y);
      FOR j:= 0 TO x_vert DO
       Begin
        X:=X_Calc(XY_Cor3[i,j,1]);
        Y:=Y_Calc(XY_Cor3[i,j,2]);
        LineTo(X,Y);
       End;
    End;
End;

{-------------------------------------------------------------------------------}

PROCEDURE Calc_theta_vel1A;                    {Calc θxy for Froth Area #1}
Begin
 IF (x_vel) = 0 THEN
  theta_vel:=pi/2
 ELSE
```

```
 theta_vel:=Arctan((y_vel)/(-x_vel));
 IF theta_vel < 0 THEN
  Begin
   theta_vel:=pi+theta_vel;
  End;
End;

{-------------------------------------------------------------------------------------------------}

PROCEDURE Calc_theta_vel1B;                    { Calc θxy for Froth Area #2}
Begin
 IF (x_velB) = 0 THEN
  theta_velB:=pi/2
 ELSE
  theta_velB:=Arctan((y_velB)/(-x_velB));
 IF theta_velB < 0 THEN
  Begin
   theta_velB:=pi+theta_vel;
  End;
End;

{-------------------------------------------------------------------------------------------------}

PROCEDURE Calc_eps;                            {Calculates the air hold-up}
Begin                                          {at any position in the cell}
 A_eps:=aa*zj+ab;
 B_eps:=ba*zj+bb;
  Eps:=A_eps*x_lip+B_eps;
End;

{-------------------------------------------------------------------------------------------------}

PROCEDURE Calc_epsint;                         {Calculates the air hold-up at the}
Begin                                          {Liquid/froth interface}
 zj:=0.75-(h2+r3+60)/1000;
 x_lip:=0;
 Calc_eps;
 Eps_int:=eps;
End;

{-------------------------------------------------------------------------------------------------}

PROCEDURE Test_Y;                              {Calculate test parameters}
Begin                                          {to estimate particle location}
 IF x_vel > -(r2+x0) THEN
 Begin
```

```
 IF x_vel < -x0 THEN
  Begin
   a:=1;
   b:=2*y0;
   c:=(sqr(y0)-sqr(r2)+sqr(x_vel+x0));
   y_test:=Quadmax(a,b,c);
  End
 ELSE
  Begin
   g:=(x0/(r2-y0));
   k:=(r2-y0+sqr(x0)/(r2-y0));
   y_test:=g*x_vel+k;
  End;
End
ELSE
 y_test:=y_vel;
End;

{-------------------------------------------------------------------------------------------------------}

PROCEDURE Scale_XY;                          {Scale {x0,y0} to {0,0}}
Begin
 x_velB:=x_vel-kx;
 y_velB:=y_vel+ky;
End;

{-------------------------------------------------------------------------------------------------------}

PROCEDURE Velocity_XY1B;                     {Calculate bubble velocity}
Begin                                        {at pos. xy in cell}
 IF k2 > 0 THEN                              {Froth Area #2}
  Begin
   theta_crit1:= Arctan(k2/(l2+r3));
  End
 ELSE
  Begin
   theta_crit1:=0;
  End;
 theta_crit2:=Arctan((r2+k2)/k4);
   IF theta_velB < theta_crit1 THEN
    Begin
     x1:=-(l2+r3);
     y1:=-(tan(theta_velB))*x1;
     theta_top:=pi/2;
      x2:=-r3*cos(theta_velB);
      y2:=r3*sin(theta_velB);
```

```
      theta_bot:=pi/2-theta_velB;
     End;
    IF (theta_velB >= theta_crit1) AND (theta_velB <= theta_crit2) THEN
     Begin
      a:=(1+sqr(tan(theta_velB)));
      b:=(2*k4+2*k2*(tan(theta_velB)));
      c:=(sqr(k2)+sqr(k4)-sqr(r2));
      x1:=Quadmin(a,b,c);
      y1:=-(tan(theta_velB))*x1;
      theta_top:=pi/2-Arctan((y1-k2)/-(x1+k4));
       x2:=-r3*cos(theta_velB);
       y2:=r3*sin(theta_velB);
       theta_bot:=pi/2-theta_velB;
     End;
    IF theta_velB > theta_crit2 THEN
     Begin
      g:=(x0/(r2-y0));
      k:=r2-y0+sqr(x0)/(r2-y0)+ky+kx*x0/(r2-y0);
      x1:=-k/(tan(theta_velB)+g);
      y1:=-(tan(theta_velB))*x1;
      theta_top:=Arctan(g);
       x2:=-r3*cos(theta_velB);
       y2:=r3*sin(theta_velB);
       theta_bot:=pi/2-theta_velB;
     End;
  zj:=0.75-(h2+r3-y_velB)/1000;
  x_lip:=(k3+x_velB)/1000;
   v:=(G1B*(1000/60)/((15)*(l2/10)))/100;          {m/sec}
   qt:=(qtC2/((15)*(l2/10)))/100;                  {m/sec}
   kv:=kv_1B;
   Calc_eps;
  D_vel:=sqrt(sqr(y1-y2)+sqr(x1-x2));
  Area:=D_vel*150;                                {in mm^2}
  Vel_XY:=G1B*(1000000/60)/(Area*eps*(1-0.99558*zj));  {mm/sec}
   X:=X_Calc(X_velB);
   Y:=Y_Calc(Y_velB);
  D_ratio:=(sqrt(sqr(y_velB-y2)+sqr(x_velB-x2))/D_vel);
End;

{-------------------------------------------------------------------------------------------------------------}

PROCEDURE Velocity_XY1A;                          {calculate bubble velocity}
Begin                                             {at pos. xy in cell}
 kx:=k4-x0;                                       {Froth Area #1}
 ky:=k2+y0;
 theta_crit1:=Arctan((k1-ky)/(l1+l2+r3-kx));
```

```
theta_crit2:=Arctan((r1+k1-ky)/(k3-kx));
 IF x0 = 0 THEN
  theta_crit3:= pi/2
 ELSE
  theta_crit3:=Arctan((r2-y0)/x0);
 IF theta_crit3 < 0 THEN
  Begin
   theta_crit3:=pi+theta_crit3;
  End;
     IF theta_vel < theta_crit1 THEN
      Begin
       x1:=kx-l1-l2-r3;
       y1:=-(tan(theta_vel))*x1;
        IF y_vel > y1 THEN
         Begin
          y_vel:=y1;
         End;
        IF x_vel < x1 THEN
         Begin
          x_vel:=x1;
         End;
       theta_top:=pi/2;
        a:=(1+sqr(tan(theta_vel)));
        b:=2*x0-2*y0*tan(theta_vel);
        c:=sqr(x0)+sqr(y0)-sqr(r2);
        x2:=Quadmin(a,b,c);
        y2:=-(tan(theta_vel))*x2;
        theta_bot:=pi/2-Arctan((y2+y0)/-(x2+x0));
         zj:=0.75-(h2+r3-ky-y_vel)/1000;
         x_lip:=(k3-kx+x_vel)/1000;
          v:=(G1A*(1000/60)/((l1/10)*(15)))/100;          {m/sec}
          qt:=(qtT/((l1/10)*(15)))/100;                   {m/sec}
          kv:=kv_1A;
          Calc_eps;
         D_vel:=sqrt(sqr(y1-y2)+sqr(x1-x2));
         Area:=D_vel*150;                                 {in mm^2}
         Vel_XY:=G1A*(1000000/60)/(Area*eps*(1-0.99558*zj)); {mm/sec}
          X_hou:=X_vel-kx;
          Y_hou:=Y_vel+ky;
          X:=X_Calc(X_hou);
          Y:=Y_Calc(Y_hou);
          D_ratio:=(sqrt(sqr(y_vel-y2)+sqr(x_vel-x2))/D_vel);
      End;
     IF (theta_vel >= theta_crit1) AND (theta_vel <= theta_crit2) THEN
      Begin
       Test_Y;
```

```
  IF y_vel < y_test THEN
   Begin
    Scale_XY;
    Calc_theta_vel1B;
    Velocity_XY1B;
   End
  ELSE
   Begin
    a:=(1+sqr(tan(theta_vel)));
    b:=(2*tan(theta_vel)*(k1-ky)-2*(kx-k3));
    c:=(sqr(kx-k3)+sqr(k1-ky)-sqr(r1));
    x1:=Quadmin(a,b,c);
    y1:=-tan(theta_vel)*x1;
     IF y_vel > y1 THEN
      Begin
       y_vel:=y1;
      End;
     IF x_vel < x1 THEN
      Begin
       x_vel:=x1;
      End;
    theta_top:=pi/2-Arctan((y1-(k1-ky))/-(x1-(kx-k3)));
     a:=(1+sqr(tan(theta_vel)));
     b:=2*x0-2*y0*tan(theta_vel);
     c:=sqr(x0)+sqr(y0)-sqr(r2);
     x2:=Quadmin(a,b,c);
     y2:=-(tan(theta_vel))*x2;
     theta_bot:=pi/2-Arctan((y2+y0)/-(x2+x0));
      zj:=0.75-(h2+r3-ky-y_vel)/1000;
      x_lip:=(k3-kx+x_vel)/1000;
       v:=(G1A*(1000/60)/((l1/10)*(15)))/100;          {m/sec}
       qt:=(qtT/((l1/10)*(15)))/100;                   {m/sec}
       kv:=kv_1A;
       Calc_eps;
      D_vel:=sqrt(sqr(y1-y2)+sqr(x1-x2));
      Area:=D_vel*150;                                 {in mm^2}
      Vel_XY:=G1A*(1000000/60)/(Area*eps*(1-0.99558*zj)); {mm/sec}
       X_hou:=X_vel-kx;
       Y_hou:=Y_vel+ky;
       X:=X_Calc(X_hou);
       Y:=Y_Calc(Y_hou);
       D_ratio:=(sqrt(sqr(y_vel-y2)+sqr(x_vel-x2))/D_vel);
   End;
 End;
IF (theta_vel > theta_crit2) AND (theta_vel < theta_crit3) THEN
 Begin
```

```
 Test_Y;
  IF y_vel < y_test THEN
   Begin
    Scale_XY;
    Calc_theta_vel1B;
    Velocity_XY1B;
   End
  ELSE
   Begin
    g:=(x0/(r2-y0));
    k:=(r1+k1-ky-(x0/(r2-y0)*(kx-k3)));
    x1:=-k/(tan(theta_vel)+g);
    y1:=-(tan(theta_vel))*x1;
     IF y_vel > y1 THEN
      Begin
       y_vel:=y1;
      End;
     IF x_vel < x1 THEN
      Begin
       x_vel:=x1;
      End;
    theta_top:=Arctan(g);
     a:=(1+sqr(tan(theta_vel)));
     b:=2*x0-2*y0*tan(theta_vel);
     c:=sqr(x0)+sqr(y0)-sqr(r2);
     x2:=Quadmin(a,b,c);
     y2:=-(tan(theta_vel))*x2;
     theta_bot:=pi/2-Arctan((y2+y0)/-(x2+x0));
      zj:=0.75-(h2+r3-ky-y_vel)/1000;
      x_lip:=(k3-kx+x_vel)/1000;
       v:=(G1A*(1000/60)/((l1/10)*(15)))/100;          {m/sec}
       qt:=(qtT/((l1/10)*(15)))/100;                   {m/sec}
       kv:=kv_1A;
       Calc_eps;
      D_vel:=sqrt(sqr(y1-y2)+sqr(x1-x2));
      Area:=D_vel*150;                                 {in mm^2}
      Vel_XY:=G1A*(1000000/60)/(Area*eps*(1-0.99558*zj)); {mm/sec}
       X_hou:=X_vel-kx;
       Y_hou:=Y_vel+ky;
       X:=X_Calc(X_hou);
       Y:=Y_Calc(Y_hou);
       D_ratio:=(sqrt(sqr(y_vel-y2)+sqr(x_vel-x2))/D_vel);
   End;
 End;
IF (theta_vel > theta_crit3) AND (theta_crit3 < pi/2) THEN
 Begin
```

```
        Test_Y;
         IF y_vel < y_test THEN
          Begin
           Scale_XY;
           Calc_theta_vel1B;
           Velocity_XY1B;
          End
         ELSE
          Begin
           g:=(x0/(r2-y0));
           k:=(r1+k1-ky-(x0/(r2-y0)*(kx-k3)));
           x1:=-k/(tan(theta_vel)+g);
           y1:=-(tan(theta_vel))*x1;
            IF y_vel > y1 THEN
             Begin
              y_vel:=y1;
             End;
            IF x_vel < x1 THEN
             Begin
              x_vel:=x1;
             End;
           theta_top:=Arctan(g);
            k:=(r2-y0+sqr(x0)/(r2-y0));
           x2:=-k/(tan(theta_vel)+g);
           y2:=-(tan(theta_vel))*x2;
           theta_bot:=Arctan(g);
            zj:=0.75-(h2+r3-ky-y_vel)/1000;
            x_lip:=(k3-kx+x_vel)/1000;
             v:=(G1A*(1000/60)/((l1/10)*(15)))/100;          {m/sec}
             qt:=(qtT/((l1/10)*(15)))/100;                   {m/sec}
             kv:=kv_1A;
             Calc_eps;
            D_vel:=sqrt(sqr(y1-y2)+sqr(x1-x2));
            Area:=D_vel*150;                                 {in mm^2}
            Vel_XY:=G1A*(1000000/60)/(Area*eps*(1-0.99558*zj)); {mm/sec}
             X_hou:=X_vel-kx;
             Y_hou:=Y_vel+ky;
             X:=X_Calc(X_hou);
             Y:=Y_Calc(Y_hou);
             D_ratio:=(sqrt(sqr(y_vel-y2)+sqr(x_vel-x2))/D_vel);
          End;
       End;
End;

{-------------------------------------------------------------------------------}
```

```
PROCEDURE Velocity_XYNext1A;                    {Calculate bubble velocity}
Begin                                           {at pos. xy in cell}
 IF (x0 < 0) AND (x_vel < -x0) THEN             {Froth Area #3}
  Begin
   g:=(x0/(r2-y0));
   k:=(r1+k1-ky-(x0/(r2-y0)*(kx-k3)));
   x1:=x_vel;
   y1:=g*x1+k;
    IF y_vel > y1 THEN
      Begin
       y_vel:=y1;
      End;
    IF x_vel < x1 THEN
      Begin
       x_vel:=x1;
      End;
   theta_top:=Arctan(g);
    a:=1;
    b:=-2*y0;
    c:=(sqr(y0)-sqr(r2)+sqr(x_vel+x0));
    y2:=Quadmax(a,b,c);
    x2:=x_vel;
    theta_bot:=pi/2-Arctan((y2+y0)/-(x2+x0));
 End
ELSE
  Begin
   g:=(x0/(r2-y0));
   k:=(r1+k1-ky-(x0/(r2-y0)*(kx-k3)));
   x1:=x_vel;
   y1:=g*x1+k;
    IF y_vel > y1 THEN
     Begin
      y_vel:=y1;
     End;
    IF x_vel < x1 THEN
     Begin
      x_vel:=x1;
     End;
   theta_top:=Arctan(g);
    k:=(r2-y0+sqr(x0)/(r2-y0));
    x2:=x_vel;
    y2:=g*x2+k;
    theta_bot:=Arctan(g);
  End;
zj:=0.75-(h2+r3-ky-y_vel)/1000;
x_lip:=(k3-kx+x_vel)/1000;
```

```
 v:=(G1A*(1000/60)/((l1/10)*(15)))/100;          {m/sec}
 qt:=(qtT/((l1/10)*(15)))/100;                   {m/sec}
 kv:=kv_1A;
 Calc_eps;
D_vel:=sqrt(sqr(y1-y2)+sqr(x1-x2));
Area:=D_vel*150;                                 {in mm^2}
Vel_XY:=G1A*(1000000/60)/(Area*eps*(1-0.99558*zj)); {mm/sec}
 X_hou:=X_vel-kx;
 Y_hou:=Y_vel+ky;
 X:=X_Calc(X_hou);
 Y:=Y_Calc(Y_hou);
D_ratio:=(sqrt(sqr(y_vel-y2)+sqr(x_vel-x2))/D_vel);
End;

{-------------------------------------------------------------------------------------------------}

PROCEDURE D_cor_XY;                              {Determine particle location}
Begin
 Calc_theta_vel1A;
 IF theta_vel < (pi/2) THEN
  Velocity_XY1A
 ELSE
  Begin
   Test_Y;
    IF y_vel < y_test THEN
     Begin
      Scale_XY;
      Calc_theta_vel1B;
      Velocity_XY1B;
     End
    ELSE
     Velocity_XYNext1A;
  End;
End;

{-------------------------------------------------------------------------------------------------}

PROCEDURE Vel_Control;                           {Calculate particle x,y velocity comp.}
Begin
 D_cor_XY;
 theta_dir:=theta_top*D_ratio+theta_bot*(1-D_ratio);
 Vel_X:=Vel_XY*cos(theta_dir);                    {mm/sec}
 Vel_Y:=Vel_XY*sin(theta_dir);                    {mm/sec}
End;

{-------------------------------------------------------------------------------------------------}
```

```
PROCEDURE Calc_Delta;                    {calculate bubble film thickness}
Begin
 db:=db_int*(1-0.99558*h_int)/(1-0.99558*zj);
 a:=1;
 b:=-(0.606*(1-eps)/eps*db+54.47*kv*mhu*v/(sqr(eps)*rho*db*grav));
 c:=0.0918*sqr((1-eps)/eps)*sqr(db)+16.506*kv*mhu*qt/(sqr(eps)*rho*grav);
 Delta:=Quadmax(a,b,c);
 Delta:=Delta*1000000;                   {in micron}
End;

{-------------------------------------------------------------------------------------------------}

PROCEDURE Break_time;                    {Calc. time for bubble film rupture}
Begin
 delta_h_star:=(delta/2-del_crit/2)/N_count;
 t_break:=0;
 V_hold:=0;
  FOR i_count := 1 TO N_count DO
   Begin
    h_star:=i_count*delta_h_star;
     Case Main_choise of
      1 :Rod(R,h_star,theta_par,sigma,V1,V2,delta_Pc,M_count);
      2 :Cone(V1,V2,Beta,xc,delta,h_star,theta_par,sigma,delta_Pc,M_count);
      3 :Disk(V1,V2,delta_Pc,Rs,Rd,delta,h_star,theta_par,sigma,M_count);
      4 :Elipsoid(V1,V2,delta_Pc,sigma,h_star,theta_par,delta,A_elip,
         B_elip,M_Count);
      5 :Sphere(V1,V2,delta_Pc,R,delta,h_star,theta_par,sigma,M_count);
      6 :Cube(V1,V2,delta_Pc,sigma,rho,rho_par,Scube,delta,h_star,theta_par,
         Cube_int);
      7 :Flat(V1,V2,delta_Pc,sigma,rho,rho_par,Lf,Hf,Wf,Flat_int,h_star,
         theta_par,delta);
      8 :Finish;
     End;
    Q_dot:=delta_Pc*sqr(delta)*delta*pi/3/(mhu);
     IF (V1+V2) < V_hold THEN
      Begin
       V_delta:=0;
      End
     ELSE
       V_delta:=V1+V2-V_hold;
    V_hold:=V1+V2;
    tb_delta:=V_delta/Q_dot;
    t_break:=t_break+tb_delta;
   End;
End;
```

```
{-------------------------------------------------------------------------------------------------------}

PROCEDURE Calc_forces;                    {Calc. force balance on particle}
Begin
 mhu_froth:=mhu;
 rho_froth:=(1-eps)*rho+eps*1.1614;
 Rep:=rho_froth*Abs(Vel_Y)*Dp/(mhu_froth*1000);
  IF Rep<=0.5 THEN
   CD:=24/Rep
  ELSE IF (Rep>0.5) AND (Rep<=1.0) THEN
   CD:=24/Rep + 1.5
  ELSE IF (Rep>1.0) AND (Rep<=10) THEN
   CD:=24/exp(0.8*ln(Rep))+0.4
  ELSE IF (Rep>10) AND (Rep<=500) THEN
   CD:=24/Rep*(1+0.15*exp(0.687*ln(Rep)))
  ELSE IF (Rep>500) THEN
   CD:=0.44;
 down_force:=Vp*rho_par*grav;
 up_force:=Vp*rho_froth*grav+CD*Ao*rho_froth*sqr(Y_vel/1000)/2;
 net_force:=down_force-up_force;
End;

{-------------------------------------------------------------------------------------------------------}

PROCEDURE New_XY;                         {Calc. new particle position in the froth}
Begin
 y_hou:=y_vel;
 Del_X_vel:=Vel_X*t_break;
 Del_Y_vel:=Vel_Y*t_break;
 X_vel:=X_vel+Del_X_vel;
 Y_vel:=Y_vel+Del_Y_vel;
 IF (D_ratio < 0.01) AND (x_vel > -(r2+x0)) AND (x_vel < -x0) THEN
  Begin
   a:=1;
   b:=2*x0;
   c:=sqr(y_hou-y0)-sqr(r2)+sqr(x0);
   x_test:=Quadmin(a,b,c);
    a:=1;
    b:=-2*y0;
    c:=(sqr(y0)-sqr(r2)+sqr(x_vel+x0));
    y_test:=Quadmax(a,b,c);
    IF (x_vel > x_test) AND (y_vel < y_test) THEN
     Begin
      x_vel:=x_test;
     End;
```

```
  End;
End;

{-------------------------------------------------------------------------------------------------}

PROCEDURE Fall;                          {Calc. particle fall time and new position}
Begin
  db:=db_int*(1-0.99558*h_int)/(1-0.99558*zj);
  {a:=net_force/(Vp*rho_par);
  b:=4*Vel_Y/1000;
  c:=-2*db;
  t_fall:=Quadmax(a,b,c);}
  t_fall:=sqrt(2*db*Vp*rho_par/net_force);
  Del_Y:=(db-Vel_Y*t_fall/1000)*1000;
  Y_vel:=Y_vel-Del_Y;
IF (x_vel > -(r2+x0)) AND (x_vel < -x0) THEN
 Begin
  IF y_vel < y2 THEN
   Begin
    y_vel:=y2;
   End;
 End;
End;

{-------------------------------------------------------------------------------------------------}

FUNCTION StopCon :boolean;                          {to repeat program for}
 VAR antw : char;                                   {different conditions}
Begin
 ClrScr;
 WriteLn;
 WriteLn('Do you want to repeat the program for different conditions ? -(Y/N)');
  Repeat
   Read(Kbd,antw)
  Until upcase (antw) IN ['J','Y','N'];
   IF upcase (antw) = 'N' THEN StopCon := true
                          ELSE StopCon := false;
End;

{-------------------------------------------------------------------------------------------------}

FUNCTION Beeindig :boolean;                         {to repeat program}
 VAR antw : char;
Begin
 ClrScr;
```

```
 WriteLn;
 WriteLn('Do you want to repeat the program ? -(Y/N)');
  Repeat
   Read(Kbd,antw)
  Until upcase (antw) IN ['J','Y','N'];
   IF upcase (antw) = 'N' THEN Beeindig := true
                          ELSE Beeindig := false;
End;

{-------------------------------------------------------------------------------}

BEGIN                                                    {main program}
 Titel;
 Wait;
 REPEAT
  ClrScr;
   Zero;
    Input;
     Constants;
      Lines_Comp1;
      Lines_Comp2;
      Lines_Comp3;
     Scale;
     DrawLines;
     ReadLn;
     RestoreCrtMode;
     SetGraphMode(GraphMode);
     Cell;
      Storage:=ImageSize(X_Min,Y_Min,X_Max,Y_Max);
      GetMem(Image,Storage);
      GetImage(X_Min,Y_Min,X_Max,Y_Max,Image^);
      color_count:=2;
      RestoreCrtMode;
      Factor1;
       REPEAT
        Input_general;
        Calc_epsint;
        ClrScr;
        DisplayMenu(M1,false,Main_choise,Error);
        Input_dimensions;
        kv_input;
        ClrScr;
          kx:=k4-x0;
          ky:=k2+y0;
          x_vel:=x_vel1;
          del_crit:=30*sqr(34827.85597*Vp*rho_par)*sqr(34827.85597*Vp*rho_par);
```

```
x_vel:=kx-k3+x_vel;
y_vel:=h2+r3-ky;
 X_hou:=X_vel-kx;
 Y_hou:=Y_vel+ky;
 X:=X_Calc(X_hou);
 Y:=Y_Calc(Y_hou);
  SetGraphMode(GraphMode);
  PutImage(X_Min,Y_Min,Image^,0);
  FreeMem(Image,Storage);
   MoveTo(X,Y);
   SetBkColor(0);
   SetColor(color_count);
    REPEAT
     Begin
      Vel_Control;
      LineTo(X,Y);
       Calc_Delta;

      IF (delta > crit_mes) THEN
       Begin
        t_break:=0.001;
        New_XY;
       End

      ELSE IF (delta < del_crit) THEN
       Begin
        Calc_forces;
          IF (down_force > up_force) THEN
           Begin
            Fall;
           End
          ELSE
           Begin
            t_break:=0.02;
            New_XY;
           End;
       End

      ELSE
       Begin
        Break_time;
        New_XY;
         Vel_Control;
         LineTo(X,Y);
         Calc_forces;
          IF (down_force > up_force) THEN
```

```
                Begin
                 Fall;
                End
               ELSE
                Begin
                 t_break:=0.02;
                 New_XY;
                End;
              End;
            End;
           UNTIL (x_lip*1000 > (k3-r3)) OR (y_vel < 0);
           Storage:=ImageSize(X_Min,Y_Min,X_Max,Y_Max);
           GetMem(Image,Storage);
           GetImage(X_Min,Y_Min,X_Max,Y_Max,Image^);
           color_count:=color_count+1;
           RestoreCrtMode;
          quit1:=StopCon;
      UNTIL quit1;
       CloseGraph;
      quit:=Beeindig;
 UNTIL quit;
 WriteLn;
 WriteLn('************* END OF PROGRAM ****************');
END.
```

13. APPENDIX B: SOURCE CODE FOR PARTI3.TPU

```
Unit Parti3;
{$N+}
Interface

USES crt,Turbo3,dos;

VAR
De,lamda,e_rat     :Real;                    {Local Variables to Unit}

CONST
gravt = 9.81;

{-------------------------------------------------------------------------------}
                                             {Declare all procedures in Unit}

PROCEDURE Rod(Var R,h_star,theta_par,sigma,V1,V2,delta_Pc:Real;
                    M_count:Integer);        {Calc V1+V2 & ΔPc for Rod}

PROCEDURE   Cone(Var   V1,V2,Beta,xc,delta,h_star,theta_par,sigma,delta_Pc
:Real;
                    M_count :Integer);       {Calc V1+V2 & ΔPc for Cone}

PROCEDURE Sphere(Var V1,V2,delta_Pc,R,delta,h_star,theta_par,sigma :Real;
                    M_count :Integer);       {Calc V1+V2 & ΔPc for Sphere}

PROCEDURE Disk(Var V1,V2,delta_Pc,Rs,Rd,delta,h_star,theta_par,sigma :Real;
                    M_count  :Integer);      {Calc V1+V2 & ΔPc for Disc}

PROCEDURE Elipsoid (VarV1,V2,delta_Pc,sigma,h_star,theta_par,delta,A_elip,
                    B_elip:Real; M_Count :Integer);  {Calc V1+V2 & ΔPc for
Ellipsoid}

PROCEDURE Cube(Var V1,V2,delta_Pc,sigma,rho,rho_par,Scube,delta,h_star,
                    theta_par,Cube_int :Real);   {Calc V1+V2 & ΔPc for Cube}

PROCEDURE Flat(Var V1,V2,delta_Pc,sigma,rho,rho_par,Lf,Hf,Wf,Flat_int,
                    h_star,theta_par,delta :Real);   {Calc V1+V2 & ΔPc for Flat}

PROCEDURE Force_Rod(Var R_cyl,L_cyl,Ao,Vp,Dp :Real);

PROCEDURE Force_Cone(Var xc,Beta,Ao,Vp,Dp : Real);

PROCEDURE Force_Disc(VAr Rs,Rd,Ao,Vp,Dp :Real);
```

```
PROCEDURE Force_Elip(Var A_elip,B_elip,Ao,Vp,Dp :Real);

PROCEDURE Force_Sphere(Var R,Ao,Vp,Dp :Real);

PROCEDURE Force_Cube(Var Scube,Ao,Vp,Dp :Real);

PROCEDURE Force_Flat(Var Lf,Wf,Hf,Ao,Vp,Dp :Real);


IMPLEMENTATION

{-------------------------------------------------------------------------------------------------}

PROCEDURE Rod(Var R,h_star,theta_par,sigma,V1,V2,delta_Pc:Real;
                    M_count:Integer);
VAR                                                 {Calc V1+V2 & ΔPc for Rod}
gamma,r_star1,R_star2,delta_a,
a_point,b_point                                         :Real;
k_count                                                 :Integer;
Begin
 V2:=0;
 gamma:=0;
 r_star1:=R;
  V1:=0;
  R_star2:=h_star/(1-sin(theta_par+gamma));
   delta_a:=h_star/M_count;
    FOR k_count:=1 TO M_count DO
     Begin
      a_point:=(k_count-0.5)*delta_a;
      b_point:=R_star2*sin(theta_par-pi/2)-
            SQRT(2*R_star2*a_point-sqr(a_point));
      V1:=V1+pi*(sqr(b_point)+2*b_point*R)*delta_a;
     End;
 delta_Pc:=sigma/(R_star2*1E-6);
End;

{-------------------------------------------------------------------------------------------------}

PROCEDURE Cone (Var V1,V2,Beta,xc,delta,h_star,theta_par,
                    sigma,delta_Pc :Real;
                    M_count :Integer);
VAR                                                 {Calc V1+V2 & ΔPc for Cone}
gamma,r_star1,R_star2,delta_a,a_point,b_point           :Real;
k_count,l_count                                         :Integer;
Begin
```

```
 V1:=0;
 V2:=0;
  gamma:=pi/2-Beta;
  r_star1:=(xc*sin(Beta)/cos(Beta)-delta/2+h_star)/(sin(Beta)/cos(Beta));
   R_star2:=h_star/(1-sin(theta_par+gamma));
    delta_a:=h_star/M_count;
     FOR k_count:=1 TO M_count DO
      Begin
       a_point:=(k_count-0.5)*delta_a;
       b_point:=R_star2*sin(theta_par-beta)-
              SQRT(2*R_star2*a_point-sqr(a_point));
       V1:=V1+pi*(sqr(b_point)+2*b_point*r_star1)*delta_a;
      End;
     FOR l_count:=1 TO M_count DO
      Begin
       a_point:=(l_count-0.5)*delta_a;
       b_point:=(xc*sin(Beta)/cos(Beta)-delta/2+a_point)/(sin(Beta)/cos(Beta));
       V2:=V2+pi*(sqr(r_star1)-sqr(b_point))*delta_a;
      End;
 delta_Pc:=sigma/(R_star2*1E-6);
End;

{-------------------------------------------------------------------------------------------------}

PROCEDURE Sphere(Var V1,V2,delta_Pc,R,delta,h_star,theta_par,sigma :Real;
                 M_count :Integer);
VAR                                          {Calc V1+V2 & ΔPc for Sphere}
r_star1,gamma,R_star2,delta_a,a_point,b_point      :Real;
k_count,l_count                                   :Integer;
Begin
 V1:=0;
 V2:=0;
  r_star1:=SQRT(sqr(R)-sqr(delta/2-h_star));
  gamma:=arctan(sqrt(1-sqr(r_star1/R))/(r_star1/R));
   R_star2:=h_star/(1-sin(theta_par+gamma));
    delta_a:=h_star/M_count;
     FOR k_count:=1 TO M_count DO
      Begin
       a_point:=(k_count-0.5)*delta_a;
       b_point:=R_star2*sin(theta_par+gamma-pi/2)-SQRT(2*R_star2*a_point-
sqr(a_point));
       V1:=V1+pi*(sqr(b_point)+2*b_point*r_star1)*delta_a;
      End;
     FOR l_count:=1 TO M_count DO
      Begin
       a_point:=(l_count-0.5)*delta_a;
```

```
      b_point:=SQRT(sqr(R)-sqr(delta/2-a_point));
      V2:=V2+pi*(sqr(r_star1)-sqr(b_point))*delta_a;
     End;
 delta_Pc:=sigma/(R_star2*1E-6);
End;

{-------------------------------------------------------------------------------------------}

PROCEDURE Disk(Var V1,V2,delta_Pc,Rs,Rd,delta,h_star,theta_par,sigma :Real;
                    M_count  :Integer);
VAR                                                    {Calc V1+V2 & ΔPc for Disc}
r_star1,R_star2,gamma,delta_a,a_point,b_point          :Real;
k_count,l_count                                        :Integer;
Begin
  V1:=0;
  V2:=0;
   r_star1:=SQRT(sqr(Rs)-sqr(delta/2-h_star));
   gamma:=arctan(sqrt(1-sqr(r_star1/Rs))/(r_star1/Rs));
    R_star2:=h_star/(1-sin(theta_par+gamma));
     delta_a:=h_star/M_count;
      FOR k_count:=1 TO M_count DO
       Begin
        a_point:=(k_count-0.5)*delta_a;
       b_point:=R_star2*sin(theta_par+gamma-pi/2)-SQRT(2*R_star2*a_point-
sqr(a_point));
       V1:=V1+pi*(sqr(b_point+r_star1+Rd)-sqr(r_star1+Rd))*delta_a;
      End;
     FOR l_count:=1 TO M_count DO
      Begin
       a_point:=(l_count-0.5)*delta_a;
       b_point:=SQRT(sqr(Rs)-sqr(delta/2-a_point));
       V2:=V2+pi*(sqr(r_star1+Rd)-sqr(b_point+Rd))*delta_a;
      End;
 delta_Pc:=sigma/(R_star2*1E-6);
End;

{-------------------------------------------------------------------------------------------}

PROCEDURE Elipsoid(Var V1,V2,delta_Pc,sigma,h_star,theta_par,delta,A_elip,
                    B_elip: Real; M_Count :Integer) ;
VAR                                                {Calc V1+V2 & ΔPc for Ellipsoid}
r_star1,R_star2,a_point,b_point,gamma,delta_a      :Real;
k_count,l_count                                    :Integer;
Begin
  V1:=0;
  V2:=0;
```

```
  r_star1:=A_elip*SQRT(1-sqr(delta/2-h_star)/sqr(B_elip));
  gamma:=Arctan(B_elip*(delta/2-h_star)/(A_elip*sqrt(sqr(B_elip)
        -sqr(delta/2-h_star))));
   R_star2:=h_star/(1-sin(theta_par+gamma));
    delta_a:=h_star/M_count;
     FOR k_count:=1 TO M_count DO
      Begin
       a_point:=(k_count-0.5)*delta_a;
       b_point:=R_star2*sin(theta_par+gamma-pi/2)-SQRT(2*R_star2*a_point-
sqr(a_point));
       V1:=V1+pi*(sqr(b_point)+2*b_point*r_star1)*delta_a;
      End;
     FOR l_count:=1 TO M_count DO
      Begin
       a_point:=(l_count-0.5)*delta_a;
       b_point:=A_elip*SQRT(1-sqr(delta/2-a_point)/sqr(B_elip));
       V2:=V2+pi*(sqr(r_star1)-sqr(b_point))*delta_a;
      End;
 delta_Pc:=sigma/(R_star2*1E-6);
End;

{-------------------------------------------------------------------------------}

PROCEDURE Cube(Var V1,V2,delta_Pc,sigma,rho,rho_par,Scube,delta,h_star,
                    theta_par,Cube_int :Real);
VAR                                              {Calc V1+V2 & ΔPc for Cube}
gamma,r_star1,r_star2,del_dp,test_hstar,
V_corners,Vol_rat,del_rho                :Real;
k_count,Cube_count                       :Integer;
Cube_Mat                          :array[0..200,1..5] of Real;
Begin
 V2:=0;
 gamma:=0;
 V1:=0;
  delta_Pc:=0;
  del_rho:=rho-1.1614;
   R_star2:=h_star/(1-sin(theta_par+gamma));
   R_star1:=sigma/(del_rho*gravt*h_star*(1E-6)-sigma/(R_star2*1E-6));
   R_star1:=Abs(R_star1*1E+6);
   del_dp:=Scube*1000/Cube_int;
   Cube_count:=Trunc(Cube_int/2);
   FOR k_count:=0 TO Cube_count DO
    Begin
     test_hstar:=sqr(R_Star1)-sqr(k_count*del_dp);
     IF test_hstar > 0 THEN
      Begin
```

```
      Cube_Mat[k_count,1]:=h_star-R_star1+sqrt(sqr(R_Star1)-
sqr(k_count*del_dp));
       IF Cube_Mat[k_count,1] < 0 THEN
        Begin
         Cube_Mat[k_count,1]:=0;
        End;
      End
     ELSE
      Begin
       Cube_Mat[k_count,1]:=0;
      End;
     Cube_Mat[k_count,3]:=Cube_Mat[k_count,1]/(1-sin(theta_par+gamma));
     IF (Cube_Mat[k_count,3] > 0) THEN
      Begin
       Cube_Mat[k_count,2]:=sigma*(1/(Cube_Mat[k_count,3]*(1E-
6))+1/(R_star1*(1E-6)));
      End
     ELSE
      Begin
       Cube_Mat[k_count,2]:=0;
      End;
      IF (Cube_Mat[k_count,2] < 0) THEN
       Begin
        Cube_Mat[k_count,2]:=0;
       End;

Cube_Mat[k_count,4]:=Cube_Mat[k_count,1]*Cube_Mat[k_count,3]*sin(theta_par-
pi/2)-
       (theta_par-
pi/2)/(2*pi)*pi*sqr(Cube_Mat[k_count,3])+0.5*(Cube_Mat[k_count,3]-
       Cube_Mat[k_count,1])*Cube_Mat[k_count,3]*sin(theta_par-pi/2);
     IF (Cube_Mat[k_count,4] < 0) THEN
      Begin
       Cube_Mat[k_count,4]:=0;
      End;
     Cube_Mat[k_count,5]:=Cube_Mat[k_count,4]*del_dp;
     V1:=V1+Cube_Mat[k_count,5];
    End;
    V_corners:=pi*Cube_Mat[Cube_count,3]*sqr(Cube_Mat[Cube_count,1])/2-
                  pi*sqr(Cube_Mat[Cube_count,1])*Cube_Mat[Cube_count,1]/3;
    IF (V_corners < 0) THEN
     Begin
      V_corners:=0;
     End;
   V1:=V1*8+V_corners;
   delta_Pc:=del_rho*gravt*h_star;
```

```
End;

{-------------------------------------------------------------------------------------------------}

PROCEDURE Flat(Var V1,V2,delta_Pc,sigma,rho,rho_par,Lf,Hf,Wf,Flat_int,
                    h_star,theta_par,delta :Real);
VAR                                                    {Calc V1+V2 & ΔPc for Flat}
gamma,r_star1,r_star2,del_dp,del_dpw,
test_hstar,test_hstar2,Vol_rat,h_star2,
V_corners1,V_corners2,V_corners,del_rho      :Real;
Flat_count,k_count,l_count                   :Integer;
Flat_Mat1,Flat_Mat2                          :array[0..200,1..5] of Real;
Begin
 V2:=0;
 gamma:=0;
 V1:=0;
 delta_Pc:=0;
 del_rho:=rho-1.1614;
  R_star2:=h_star/(1-sin(theta_par+gamma));
  R_star1:=sigma/(del_rho*gravt*h_star*(1E-6)-sigma/(R_star2*1E-6));
  R_star1:=Abs(R_star1*1E+6);
   del_dp:=Lf*1000/Flat_int;
   del_dpw:=Wf*1000/Flat_int;
   Flat_count:=Trunc(Flat_int/2);

  FOR k_count:=0 TO Flat_count DO
   Begin
    test_hstar:=sqr(R_Star1)-sqr(k_count*del_dp);
    IF test_hstar > 0 THEN
     Begin
      Flat_Mat1[k_count,1]:=h_star-R_star1+sqrt(sqr(R_Star1)-sqr(k_count*del_dp));
       IF Flat_Mat1[k_count,1] < 0 THEN
        Begin
         Flat_Mat1[k_count,1]:=0;
        End;
     End
    ELSE
     Begin
      Flat_Mat1[k_count,1]:=0;
     End;
    Flat_Mat1[k_count,3]:=Flat_Mat1[k_count,1]/(1-sin(theta_par+gamma));
    IF (Flat_Mat1[k_count,3] > 0) THEN
     Begin
      Flat_Mat1[k_count,2]:=sigma*(1/(Flat_Mat1[k_count,3]*(1E-6))+1/(R_star1*(1E-
6)));
     End
```

```
      ELSE
       Begin
        Flat_Mat1[k_count,2]:=0;
       End;
       IF (Flat_Mat1[k_count,2] < 0) THEN
        Begin
         Flat_Mat1[k_count,2]:=0;
        End;

Flat_Mat1[k_count,4]:=Flat_Mat1[k_count,1]*Flat_Mat1[k_count,3]*sin(theta_par-
pi/2)-
        (theta_par-pi/2)/(2*pi)*pi*sqr(Flat_Mat1[k_count,3])+0.5*(Flat_Mat1[k_count,3]-
        Flat_Mat1[k_count,1])*Flat_Mat1[k_count,3]*sin(theta_par-pi/2);
      IF (Flat_Mat1[k_count,4] < 0) THEN
       Begin
        Flat_Mat1[k_count,4]:=0;
       End;
      Flat_Mat1[k_count,5]:=Flat_Mat1[k_count,4]*del_dp;
      V1:=V1+Flat_Mat1[k_count,5];
     End;

   test_hstar2:=sqr(R_star1)-sqr(Wf/2);
   IF (test_hstar2 < 0) THEN
    Begin
     h_star2:=R_star1+Flat_Mat1[Flat_count,1];
    End
   ELSE
    Begin
     h_star2:=R_star1+Flat_Mat1[Flat_count,1]-sqrt(test_hstar2);
    End;

   FOR l_count:=0 TO Flat_count DO
    Begin
    test_hstar:=sqr(R_Star1)-sqr(l_count*del_dpw);
     IF test_hstar > 0 THEN
      Begin
       Flat_Mat2[l_count,1]:=h_star2-R_star1+sqrt(sqr(R_Star1)-
sqr(l_count*del_dpw));
       IF Flat_Mat2[l_count,1] < 0 THEN
        Begin
         Flat_Mat2[l_count,1]:=0;
        End;
      End
     ELSE
      Begin
       Flat_Mat2[l_count,1]:=0;
```

```
      End;
     Flat_Mat2[l_count,3]:=Flat_Mat2[l_count,1]/(1-sin(theta_par+gamma));
     IF (Flat_Mat2[l_count,3] > 0) THEN
      Begin
       Flat_Mat2[l_count,2]:=sigma*(1/(Flat_Mat2[l_count,3]*(1E-6))+1/(R_star1*(1E-
6)));
      End
     ELSE
      Begin
       Flat_Mat2[l_count,2]:=0;
      End;
      IF (Flat_Mat2[l_count,2] < 0) THEN
       Begin
        Flat_Mat2[l_count,2]:=0;
       End;
     Flat_Mat2[l_count,4]:=Flat_Mat2[l_count,1]*Flat_Mat2[l_count,3]*sin(theta_par-
pi/2)-
       (theta_par-pi/2)/(2*pi)*pi*sqr(Flat_Mat2[l_count,3])+0.5*(Flat_Mat2[l_count,3]-
       Flat_Mat2[l_count,1])*Flat_Mat2[l_count,3]*sin(theta_par-pi/2);
     IF (Flat_Mat2[l_count,4] < 0) THEN
      Begin
       Flat_Mat2[l_count,4]:=0;
      End;
     Flat_Mat2[l_count,5]:=Flat_Mat2[l_count,4]*del_dpw;
     V1:=V1+Flat_Mat2[l_count,5];
    End;

V_corners1:=pi*Flat_Mat1[Flat_count,3]*sqr(Flat_Mat1[Flat_count,1])/2-
            pi*sqr(Flat_Mat1[Flat_count,1])*Flat_Mat1[Flat_count,1]/3;
    IF (V_corners1 < 0) THEN
     Begin
      V_corners1:=0;
     End;
V_corners2:=pi*Flat_Mat2[Flat_count,3]*sqr(Flat_Mat2[Flat_count,1])/2-
            pi*sqr(Flat_Mat2[Flat_count,1])*Flat_Mat2[Flat_count,1]/3;
    IF (V_corners2 < 0) THEN
     Begin
      V_corners2:=0;
     End;
    V_corners:=(V_corners1+V_corners2)/2;
  V1:=V1*4+V_corners;
  delta_Pc:=del_rho*gravt*h_star;
End;

{-------------------------------------------------------------------------------}
```

```
PROCEDURE Force_Rod(Var R_cyl,L_cyl,Ao,Vp,Dp :Real);
Begin                                          {Calculate force balance}
 Vp:=pi*sqr(R_cyl)*L_cyl/1e9;                  {parameters for Rod}
 De:=2*R_cyl/1e3;
 Ao:=pi*sqr(R_cyl)/1e6;
 lamda:=2/3*(R_cyl+L_cyl)/L_cyl;
 Dp:=De/lamda;
End;

{-------------------------------------------------------------------------------------------------}

PROCEDURE Force_Cone(Var xc,Beta,Ao,Vp,Dp : Real);
Begin                                          {Calculate force balance}
 Vp:=2*pi/3*sqr(xc/1000)*xc/1000*(sin(Beta)/cos(Beta))/1e9; {parameters for Cone}
 Ao:=pi*sqr(xc/1000)/1e6;
 De:=2*xc/1e6;
 lamda:=sqrt(1+(sin(Beta)/cos(Beta)))/(sin(Beta)/cos(Beta));
 Dp:=De/lamda;
End;

{-------------------------------------------------------------------------------------------------}

PROCEDURE Force_Disc(VAr Rs,Rd,Ao,Vp,Dp :Real);
Begin                                          {Calculate force balance}
 Vp:=pi*Rd*Rs*(2*Rd+pi*Rs+4/3*sqr(Rs)/Rd)/1e18;  {parameters for Disc}
 De:=2*(Rd+Rs)/1e6;
 Ao:=pi*sqr(Rs+Rd)/1e12;
 lamda:=(2*sqr(Rd)+4*pi*Rd*Rs*(1-(Rd-Rs)/(Rd+Rs)))*(Rd+Rs)/(3*Rd*Rs*
      (2*Rd+pi*Rs+4/3*sqr(Rs)/Rd));
 Dp:=De/lamda;
End;

{-------------------------------------------------------------------------------------------------}

PROCEDURE Force_Elip(Var A_elip,B_elip,Ao,Vp,Dp :Real);
Begin                                          {Calculate force balance}
 IF B_elip < A_elip THEN                       {parameters for Ellipsoid}
  e_rat:=B_elip/A_elip
 ELSE
  e_rat:=A_elip/B_elip;
 Vp:=4*pi/3*sqr(A_elip)*B_elip/1e18;
 Ao:=pi*sqr(A_elip)/1e12;
 De:=2*A_elip/1e6;
 lamda:=(0.5+sqr(B_elip)/(4*sqr(A_elip)*e_rat)*ln((1+e_rat)/(1-e_rat)))
      *A_elip/B_elip;
 Dp:=De/lamda;
```

```
End;
{-------------------------------------------------------------------------------}

PROCEDURE Force_Sphere(Var R,Ao,Vp,Dp :Real);
Begin                                          {Calculate force balance}
 Vp:=4/3*pi*sqr(R)*R/1e18;                     {parameters for Sphere}
 Ao:=pi*sqr(R)/1e12;
 De:=2*R/1e6;
 lamda:=1;
 Dp:=De/lamda;
End;
{-------------------------------------------------------------------------------}

PROCEDURE Force_Cube(Var Scube,Ao,Vp,Dp :Real);
Begin                                          {Calculate force balance}
 Vp:=sqr(Scube)*Scube/1e9;                     {parameters for Cube}
 Ao:=sqr(Scube)/1e6;
 De:=Scube/1e3;
 lamda:=1;
 Dp:=De/lamda;
End;
{-------------------------------------------------------------------------------}

PROCEDURE Force_Flat(Var Lf,Wf,Hf,Ao,Vp,Dp :Real);
Begin                                          {Calculate force balance}
 Vp:=Lf*Wf*Hf/1e9;                             {parameters for Flat}
 Ao:=Lf*Wf/1e6;
 IF (Lf>Wf) AND (Wf>Hf) THEN
  De:=Wf/1e3
 ELSE IF (Lf>Hf) AND (Hf>Wf) THEN
  De:=Hf/1e3
 ELSE IF (Lf<Wf) AND (Lf<Hf) AND (Wf<=Hf) THEN
  De:=Wf/1e3
 ELSE IF (Lf<Wf) AND (Lf<Hf) AND (Hf<Wf) THEN
  De:=Hf/1e3
 ELSE
  De:=Lf/1e3;
 lamda:=1/3*(Lf*Wf+Lf*Hf+Hf*Wf)/(Lf*Wf*Hf)*(De*1000);
 Dp:=De/lamda;
End;
{-------------------------------------------------------------------------------}

END.
```

14. APPENDIX C: PHOTOGRAPHS OF EXPERIMENTAL SET-UP

Figure 14-1: Complete experimental set-up - original cell design

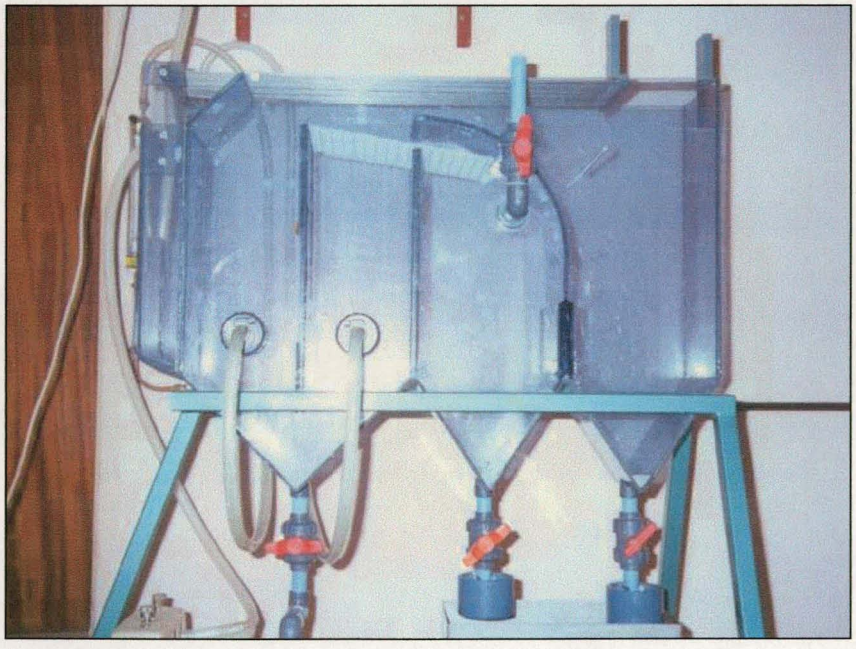

Figure 14-2: Front view of original cell design

Figure 14-3: Original cell in operation

Figure 14-4: Bent weirs in final cell design

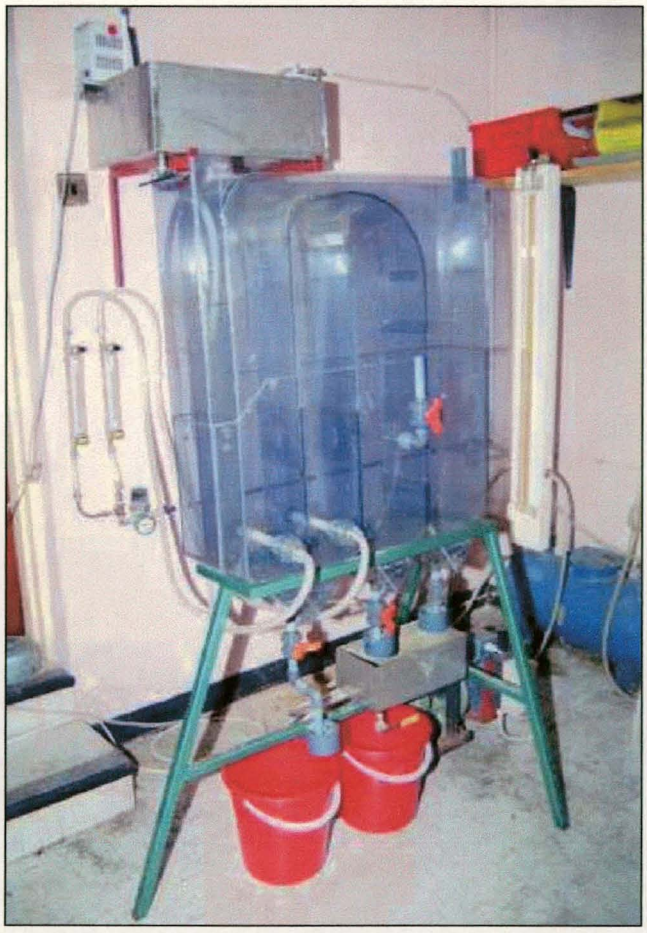

Figure 14-5: Complete experimental set-up - final cell design

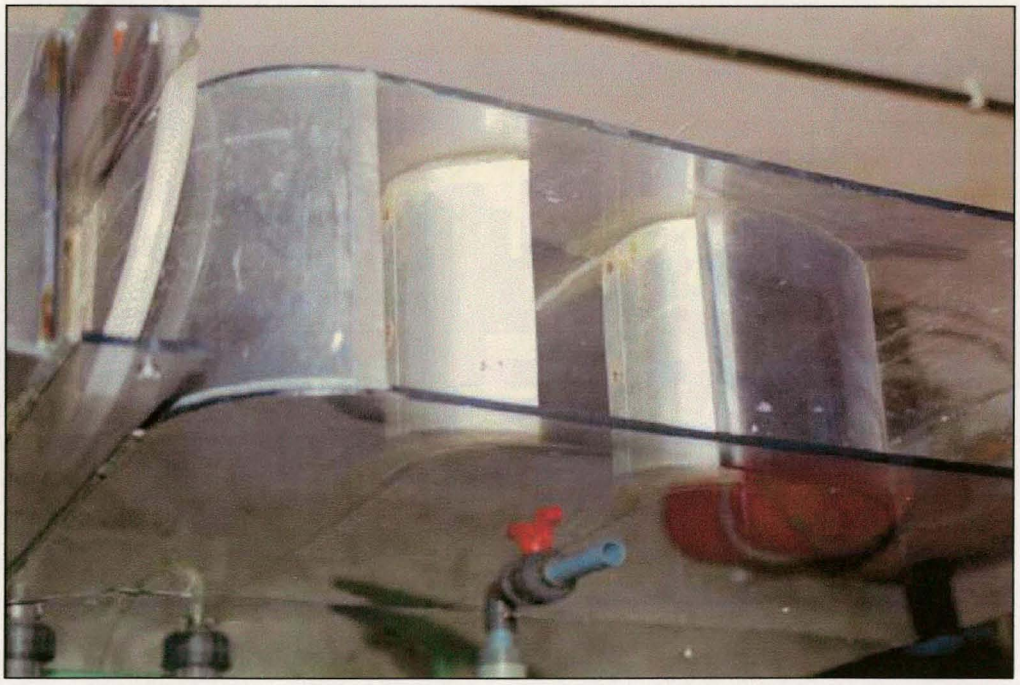

Figure 14-6: Top view of final cell design showing bent weir configuration

Figure 14-7: Front view of final cell design